UNIVERSITY OF OKLAHOMA

GRADUATE COLLEGE

MODELING AND ANALYSIS OF MULTIPLE LARGE SCALE HYDRAULIC FRACTURES IN ANISOTROPIC ROCK

A DISSERTATION

SUBMITTED TO THE GRADUATE FACULTY

in partial fulfillment of the requirements for the

Degree of

DOCTOR OF PHILOSOPHY

By

VARAHANARESH SESETTY
Norman, Oklahoma
2018

MODELING AND ANALYSIS OF MULTIPLE LARGE SCALE HYDRAULIC FRACTURES IN ANISOTROPIC ROCK

A DISSERTATION APPROVED FOR THE
MEWBOURNE SCHOOL OF PETROLEUM AND GEOLOGICAL ENGINEERING

BY

Dr. Ahmad Ghassemi, Chair

Dr. Matthew Pranter

Dr. Chandra Rai

Dr. Xingru Wu

Dr. Mashhad Fahes

Acknowledgements

I would like to express my sincere gratitude to Dr. Ahmad Ghassemi whom I've had privilege to learn from over the past 9 years. After finishing my Master's, Dr. Ahmad Ghassemi encouraged me to purse PhD in Petroleum Engineering and provided guidance throughout the journey. This work would not have been possible without his support and encouragement.

I would like to thank Dr. Matthew Pranter, Dr. Chandra Rai, Dr. Xingru Wu and Dr. Mashhad Fahes for serving as members of doctoral advisory committee. Their advice and suggestions contributed to significant improvement of this work. I would like to thank my colleagues Qian Gao, Yawei Li, Abhishek Agarwal and Kai Huang for wonderful memories at University of Oklahoma. Special thanks to Dr. Dharmendra Kumar for many useful and insightful discussions that contributed towards the betterment of this work.

Finally, I thank every member of my family and friends, especially, Krishna Gonthina, Mohan Reddy and Mohan Geddada for all their love, understanding and patience.

Table of Contents

List of Tables

List of Figures

Abstract

Shales and mudstones tend to exhibit strong anisotropy so that assuming mechanical isotropy in wellbore failure analysis and completion design strategies in shale can lead to inaccurate results. This dissertation focuses on developing numerical and semi-analytical fracture propagation models to study the behavior of hydraulic fractures near and away from the wellbore in anisotropic rock. In addition to elastic anisotropy, the effect of fracture toughness anisotropy on hydraulic fracture propagation is addressed. A numerical model based on 2D displacement discontinuity method (DDM) for fracture deformation is developed. Fluid flow inside the fractures is approximated using lubrication equation and is fully coupled with rock deformation. Natural fractures are modeled using joint elements that can account for elastic deformation (closure, shear) and plastic slip. Thus, hydraulic fracture propagation in a network of natural fracture can be simulated. In addition, to better approximate real hydraulic fracturing, a semi-analytical planar 3D (P3D) fracture height growth model is developed using the analytical plane strain solution for a line fracture in orthotropic rock to investigate the 3D aspects of rock anisotropy on hydraulic fracture propagation. The analytical expression for fracture deformation is derived using a singular elastic integral equation that relates fracture aperture with net pressure. The semi-analytical P3D model is combined with a 2D anisotropic displacement discontinuity (DD) method to enable simulation of multiple interacting hydraulic fractures in anisotropic formations (P3D-DD model). Moreover, recognizing the importance of using the proper fracture tip aperture solution for stability, accuracy and the speed of hydraulic fracture propagation numerical models, fracture tip solutions for both viscous- and toughness-dominated propagation regimes are derived for orthotropic rock for the first time. The fracture propagation algorithms in this work recognize the

regime of propagation at any given time during the injection so that the corresponding tip solution is implemented automatically allowing for correct pressure and fracture geometry calculations.

The models are applied to a number of problems of interest in reservoir geomechanics starting with the behavior of a pressurized crack. Analysis of a uniformly pressurized stationary fracture in an orthotropic rock indicates that fracture apertures and induced stresses around the fracture are functions of fracture orientation with respect to the rock's axes of elastic symmetry and its degree of modulus anisotropy (i.e., ratio of Young's modulus in the direction parallel to rock fabric to Young's modulus in the direction perpendicular to the rock fabric). The spatial extent of the induced normal stresses ("stress shadow") perpendicular to the fracture surface increases when the fracture is aligned with the direction of the least Young's modulus. Analysis of stress indicates a substantial increase in the stress shadow for anisotropic rock even with a degree of anisotropy as low as 1.9. Numerical simulations of large scale hydraulic fracture propagation indicate that the larger spatial extent of the induced stresses in anisotropic rock leads to early termination of the fractures emanating from the inner perforation clusters, resulting in fracture networks with dominant outer fractures. In the presence of fracture toughness anisotropy and under low differential stress conditions, the fractures deviate towards the plane of the least fracture toughness. Near the wellbore, fracture toughness anisotropy results in severe constriction of fracture apertures at the locations of fracture turning. This effect becomes more severe with increase in fracture toughness anisotropy and perforation misalignment angle.

Propagation of a single planar hydraulic fracture is considered in a vertical transversely isotropic rock (VTI) using the P3D model and the resultant fracture height, length and aperture distribution are compared with the isotropic case. The results indicate that isotropic fracture models tend to overestimate fracture height and underestimate fracture width. For a rock with degree of anisotropy

4, isotropic model underestimates the fracture aperture by 11% and overestimates the fracture height by 31% when compared to anisotropic model. Also, fracture aperture distribution in anisotropic rock tends to be more uniform compared to the isotropic case.

Numerical simulations of hydraulic fracture in the presence of natural fractures indicate that the induced stress component parallel to the hydraulic fracture surface plays a critical role in the evolution of the fracture network. Natural fracture segments that are at a low angle (with respect to hydraulic fracture) are affected the most by the hydraulic fracture's stress shadow. When the in-situ stress contrast is high (1000 psi), most of the natural fractures never mechanically open, however, they do experience slip. Under a low in-situ stress contrast (145 psi), segments of the natural fractures that are on the high angle side mechanically open. Under the condition of high in-situ stress contrast some natural fractures experienced bi-wing propagation due to higher shear stresses acting on the inclined natural fractures causing sufficient slip to initiate natural fracture propagation from both tips. The indication is that contrary to conventional wisdom in some cases a higher complexity may result under a high stress contrast. Fracture opening along the network shows drastic variation even under low in-situ stress contrast, where the lowest fracture apertures are observed along the natural fractures and at sites of fracture arrest.

Numerical analysis of propagation of dense parallel fracture strands show that closely spaced fracture strands can occur for a certain range of conditions and operational parameters. The in-situ stress contrast, perforations conditions, and injection rates exert a significant influence. Under the right conditions, closely-spaced fractures can extend to distances exceeding tens of feet from the wellbore. Early termination and/or coalescence of closely spaced fractures can also occur. Higher in-situ stress contrast and lower fracture toughness of rock appear to inhibit coalescence of closely spaced fractures .Propagation of dense fracture strands require higher net pressures inside fractures

to keep them open compared to a single fracture. The increase in net pressure inside the fractures is directly proportional to number of fracture strands. Also, it appears that an average increase in net pressure required to propagate multiple fractures can be related to net pressure for a single fracture, which might allow one to infer the number of fractures propagating simultaneously.

These results suggest that the spacing between the fractures for optimum growth in anisotropic rock must be different from isotropic rock for successful completion design of horizontal wells. Moreover, the numerical model can be used as a tool to improve interpretation of micro-seismic maps and injection pressure data.

1 Introduction

1.1 Motivation

Hydraulic fracturing of horizontal wells has been instrumental in unlocking oil and gas reserves from tight gas/oil sandstones and mudstones. Successful stimulation of these low to ultra-low permeability reservoirs greatly depends on the ability to create effective communication between the wellbore and the fracture network which provides the necessary surface area and flow pathway in the pay zone. One way to achieve maximum contact with the reservoir is to reduce the spacing between the perforation clusters during the stimulation treatment. However, fracture interactions and redundant energy input need to be considered in the process. On the other hand, communication between a wellbore and the fracture network is primarily controlled by the near wellbore fracture geometry.

Over the years, several numerical and analytical models have been developed to assist the design of hydraulic fracture treatments. The early models (Geertsma and deKlerk, 1961; Nordgren, 1972) considered single planar fracture from wellbore under plane strain condition. More sophisticated models (Palmer and Carroll, 1982; Vandamme and Curran, 1989; Ghassemi, 1997) were later developed to capture the evolution of hydraulic fracture in 3D. Subsequently, multiple interacting hydraulic fracture propagation models (Kumar and Ghassemi 2016; Weng et al., 2011) were proposed for treatment design analysis of multi-cluster multi-stage hydraulic fracturing techniques. All these models assume isotropic elastic behavior for rock. However, mudstones or shales are more often than not anisotropic. Laboratory measurements on core samples indicate a degree of modulus anisotropy (i.e., ratio of Young's modulus in the direction parallel to rock fabric to Young's modulus in the direction perpendicular to the rock fabric) of 1.4 to 4 in various shales (Suarez-Rivera et al., 2011; Sierra et al., 2010; Vachaparampil et al., 2016). In these experiments

the anisotropy of elastic properties of shale is attributed to the composition of the shale and preferred orientation of platy clay particles. The presence of micro-fractures and strong stress contrast can also lead to material anisotropy (Dewhurst and Siggins, 2006). In addition, the presence of natural fractures, bedding planes and planes of weaknesses induce mechanical anisotropy at large scale. For example, a rock mass with nearly orthogonal sets of natural fractures can be treated as an orthotropic rock (Goodman, 1976). Moreover, it is observed that mudstones also exhibit strong fracture toughness anisotropy. Fracture toughness measurements on Mancos shale indicates fracture toughness values in the direction perpendicular to bedding are 3.7 times higher than the values observed in the direction of bedding (Chandler et al., 2016). The effect of rock anisotropy on tensile and compressive failure of a deviated wellbore has been well studied analytically (Aadnoy, 1987; Ong and Roegiers, 1993; Vahid and Ghassemi, 2011). Also, an analytical solution (Chertov, 2012) for fracture apertures in anisotropic rock has been applied to optimize completions strategies in shale (Suarez-Rivera et al., 2011). This analytical solution is restricted to a single line fracture that is subjected to constant internal pressure in uniform far-field stress. In order to capture the complexity of hydraulic fracturing at large scale in anisotropic formations one needs more robust numerical model that relax the simplifying assumptions. Although considerable research effort has been devoted to laboratory experiments for measuring elastic properties of anisotropic rocks, at present hydraulic fracture propagation models that account for rock anisotropy (modulus and strength) are not available. Therefore, the effect of rock anisotropy on behavior of hydraulic fracture is largely unknown. This work focuses on developing numerical and advanced semi-analytical fracture propagation models to study the behavior of hydraulic fractures near and away from the wellbore in anisotropic rock. Additionally, the effect of natural fractures on hydraulic fracture propagation and multi-stage fracturing is addressed with

emphasis on the essential physics and the ability to predict treatment pressure. Finally, the model is extended to enable assessment of the conditions for the formation of fracture clusters or fracture swarms observed in the field studies.

1.2 Background

Chapter 1 Fracture propagation models that consider all aspects (length, height growth, non-planarity and poroelasticity) in 3D (Kumar and Ghassemi, 2016 and 2018; Gao and Ghassemi, 2017) are needed for comprehensive analyses and have been used to analyze multi-stage fracturing and the "Frac-Hit" phenomenon (Kumar and Ghassemi, 2017). However, because of increased computational cost, 2D and P3D (Simonson et al., 1978; Palmer and Carroll, 1983; Weng et al., 2011) models have been developed to reduce computational costs while addressing some of the shortcoming of early 2D semi-analytical models such as KGD and PKN which assume a fixed height. In fact, modeling fracture propagation at field scale by considering all aspects of a complex fracture in 3D may not be feasible with the existing computational resources. As a result, numerical models are often simplified by trading few aspects for others. For example, finite element methods (FEMs) (Fu et al., 2011) can be adopted for heterogeneous medium, however they are severely limited by memory allocation requirements. 3D boundary element models (BEMs) (Kumar and Ghassemi, 2016 and 2018) are faster than FEMs, however are mostly restricted to isotropic rocks. In discontinuous rock systems where complex fracture propagation is expected, 2D models based on displacement discontinuity can be considered as an alternative because HF/NF interactions in 3D are very challenging. For field scale applications, semi-analytical planar 3D (P3D) models (Dontsov, 2015; Kresse et al., 2013) or 2D boundary element based models are more suitable as they predict fracture characteristics (such as height, length, width and proppant placement) in a fraction of computation time required by 3D models. Many 2D and P3D models have been

developed in the last few decades **(**Palmer and Carroll, 1983; Weng et al., 2011; Dontsov, 2015**)**. The P3D models are unable to consider multiple fracturing while accounting for fracture interactions in a rigorous fashion. 2D DD models generally suffer from several restrictions regarding fracture propagation and HF/NF interactions as well as improper boundary conditions near the fracture tip. These restrictions result in unreliable and at time erroneous simulation outcomes such as net pressure, network geometry, and fracture length and trajectory which are remedied in this work.

1.2.1 Near Tip Hydraulic Fracture Behavior

The existing 2D boundary element methods for hydraulic fracturing are not only limited to isotropic rock but fail to capture the essentials of Linear Elastic Fracture Mechanics. That is, often time the critical conditions for fracture propagation is not enforced resulting in erroneous pressure and fracture geometries and multi-frac interaction scenarios. The fracture propagation problem according to LEFM theory assumes square root variation of opening displacement ($u \approx x^{1/2}$), near the fracture tips, where u is the opening near fracture tip and x is the distance from fracture tip. This behavior is modeled by a special fracture tip element in boundary element methods (Yan, 2004). In LEFM, fracture propagation is governed by a material property called fracture toughness which is related to fracture energy. But fracture energy is only one of the sources of energy dissipation mechanisms during hydraulic fracture propagation. Energy is also consumed to overcome the resistance of flow of viscous fluids in the fracture channel, which is called viscosity dissipation. If the viscous energy dissipation is significantly larger than the energy dissipated in creating new fracture surfaces, the fracture is assumed to be propagating under a viscosity dominated regime. In this scenario, fracture propagation is assumed to be completely governed by fluid dynamics of viscous flow and is independent of fracture toughness. This kind of behavior

could be observed when fluid is injected into pre-existing fractures (where fracture resistance is negligible) or flow of magma in fractures (Spence and Turcotte, 1985) or inducing hydraulic fractures using high viscous fluids in petroleum reservoirs. The existing 2D DD models cannot capture fracture propagation in the viscous regime. Also, when the near tip behavior of fluid driven fracture in different regimes is considered, it is done so in semi-analytical models or numerical schemes that are restricted to isotropic rock (Dontsov and Peirce, 2016; Lecampion and Desroches, 2015; Bunger et al., 2007). The effect of rock anisotropy on near tip behavior of a fracture driven by viscous fluid has not been addressed.

1.2.2 Simplified Fracture Models

As discussed previously, the computational time required for 3D models to simulate hydraulic fracture propagation at field scale make these model almost prohibitive for such applications. As a result, fast paced approximate planar 3D models (P3D) were developed. P3D models incorporate fracture height growth criterion based on the concept that hydraulic fractures are contained by the higher stresses in the layers above and below the payzone (Warpinski et al., 1982; Teufel and Clark, 1984). The analytical expression for height growth in these models is developed assuming that the mode-1 stress intensity factor at the fracture tips in the vertical plane is always in equilibrium with the fracture toughness of the rock (Simonson et al., 1978). However, the equilibrium fracture height growth models can only provide the excess fracture height growth into the higher stress layers bounding the payzone, and by default assume that the hydraulic fracture has a minimum height equal to the payzone thickness. Similarly to the PKN model, in the P3D modeling approach the fracture is discretized along its length into small elements, and an analytical expression is conventionally used to calculate the fracture apertures using the net pressure inside that element. Since the P3D model assumes that aperture of every fracture element is exclusively

related to the net pressure of that element alone, when used to solve for fracture growth in the lateral direction, it fails to take into account the interaction between fracture elements within a hydraulic fracture resulting in a lower system stiffness. As a result, a P3D model over/under estimate the fracture aperture and the predicted lateral growth.

To remedy this problem, Dontsov and Peirce (2015) proposed an enhanced P3D (EP3D) model that incorporates interaction between the hydraulic fracture elements along the length of the hydraulic fracture using a simplified 3D elastic integral equation in place of the analytical expression to relate fracture apertures with pressure. Their results indicate significant improvement in fracture length and aperture predictions, but at the cost of increased computational time. However, this and other P3D fracture propagation models mentioned above are restricted to planar fractures. Currently, only 2D DDM based models (Sesetty and Ghassemi, 2016; 2018a) can effectively consider multiple non planar fractures at the field scale. Although fracture propagation models based on 2D DDM are formulated on the assumption of infinite fracture height, one can incorporate a 3D correction factor to adjust the solution for problems with a fixed fracture height. The major drawback of 2D DDM model is its inability to simulate fracture height growth. On the other hand, P3D models consider fracture height growth but fail to take interaction between multiple fractures in to account. To address this issue one can couple the P3D model with 2D DDM (Kresse et al., 2013). The result is a P3D-DD model that considers the stress shadow between hydraulic fractures while at the same time considering height growth. Moreover, all existing P3D models to date neglect formation anisotropy.

1.2.3 Complex Fracture Networks

It is generally accepted that natural fractures exert a significant influence on hydraulic fracturing of unconventional plays. Micro-seismic events often associated with stimulation of these

reservoirs are attributed to shear displacement of natural fractures caused by induced stresses and pore pressure changes. As a result, complex fracture modeling in conjunction with micro-seismic imaging is useful for better estimation of the stimulated volume. However, current large scale hydraulic fracture models (Kresse et al., 2013; Wu, 2014; McClure, 2012) are either inherently incapable of handling complex hydraulic fracture natural fracture interactions or are based on unsubstantiated heuristic with insufficient lack of rigor. Although, the uncertainty in the characteristics of natural fracture properties is an often cited reason for neglecting the relevant physical processes in hydraulic fracture simulations, the fundamental issue is that hydraulic fracture propagation in the presence of natural fractures is a complex phenomenon and poses significant challenges to numerical modeling. The interaction between hydraulic fracture and natural fractures can create extensive fracture branching around the main hydraulic fracture which is at times referred to as an "off-balance" fracture growth (Daneshy 2003). A hydraulic fracture tip approaching a natural fracture can become arrested, or it can cross the natural fracture along its own path or become deflected into the natural fracture depending on the stress regime ahead of the fracture tip (Koshelev and Ghassemi 2003; Cook and Underwood 2001; Renshaw and Pollard 1995; Warpinski et al. 1987; Blanton 1982; Daneshy 1974). To properly account for this behavior it is necessary to analyze the stress field near the fracture tip accurately. Fracturing fluid flowing into a natural fracture can cause it to slip and dilate or to mechanically open. Various mechanisms that affect natural fracture activation are discussed in Daneshy (2016) and Weng et al. (2015). Continued fluid injection into natural fracture can result in formation of wing cracks (Kamali and Ghassemi 2016; Huang et al. 2013; Jung 2013; Ghassemi 2017; Min et al. 2010; Horii and Nemat-Nasser 1986; Nemat-Nasser and Horri 1983; Hoek and Bieniawksi 1984; Bombolakis 1973). Induced stresses due to fracture deformation combined with pore pressure changes in the reservoir

can induce slip (Safari and Ghassemi 2016) on isolated natural fractures (natural fractures that are not connected to hydraulic fracture). Natural fractures that are under high compressive normal stresses can act as channels for fluid diversion and experience slip, however, they may also remain mechanically closed and act as potential sites for proppant bridging.

Many numerical models have been developed in recent years to capture certain aspects of the above described complex interaction between natural and hydraulic fractures. These include the displacement discontinuity method (DDM) (Zhang et al. 2006, 2009; Sesetty and Ghassemi 2012) XFEM (Dahi-Taleghani and Olson, 2011) and DEM (Zhou et al. 2017) based models which have been mainly limited to few small scale fractures. 3D discrete fracture networks (Willis-Richards et al. 1996; Wang and Ghassemi 2011; Raihi and Damjanac 2013; Cheng and Ghassemi 2017) are more suitable for injection extraction problems and simulation of micro-seismicity in connected fracture networks rather than simulating hydraulic fracture propagation. Semi-analytical models (Weng et al. 2011) can be implemented at field scale but they fail to take into account the interaction between multiple fractures and are not suitable to model shear slip. A numerical model that fully couples fracture mechanics with fluid flow and considers all aspects of hydraulic/natural fracture interaction at field scale can be quite challenging in terms of numerical stability and computation time even in 2D. At present, most of the current literature on complex fracture networks is limited to the investigation of hydraulic fracture arrest/crossing behavior with natural fractures, and the associated fracture aperture evolution and injection pressure response with time. Stress distribution around fractures in the network, shear slip evolution, status of fracture elements (i.e., whether they are open/close/slip/stuck) have not been well reported.

1.2.4 Fracture Swarms

Current hydraulic fracture models assume single fracture per perforation cluster. This assumption stems from a simplified concept of the stress shadow that inhibit the growth of multiple parallel fractures under very tight spacing. Laboratory experiments (van de Ketterij and de Pater, 1999) performed on a perforated wellbore indicated poor connectivity of fractures emanating from perforations resulting in multi-strands rather than a single fracture. Out of the 21 experiments conducted, only two experiments exhibited good fracture connectivity near the wellbore, while the rest showed multiple fractures emanating from perforation cluster. The results also indicated that lower in-situ horizontal stress contrast favors connectivity between the fractures from individual perforations near the wellbore. Due to the limitation of sample size in laboratory experiments, the extent of lateral propagation observed by hydraulic fractures from individual perorations is not explored and is unknown. Multi-stranded fracture propagation at large scale (i.e. far from the wellbore) is also evident from mine-back experiments and cored intervals of hydraulically fractured rock. Warpinski et al., (1993) observed 30 hydraulic fractures over a span of just 4 ft. along the cored interval, far exceeding the number of perforation clusters which is two. Mine-back experiments in coal seams (Jeffrey et al., 1993) also indicated multiple fractures with spacing of just 1 ft. Core samples from hydraulic fracturing test site (HFTS) (Gale et al., 2018) and Eagle Ford field test (Raterman et al., 2017) indicated hydraulic fractures occurring in swarms. In Eagle Ford field test, fracture swarms of densities up to 60 fractures per 50 ft. of cored interval is observed. Physical observation of cores and image logs revealed that most of the fractures occurring in swarms are parallel to each other. Similar observations are made from core samples obtained from HFTS. Since the number of observed hydraulic fractures from HFTS and Eagle ford field test are much greater than perforations, multiple fractures emanating from a cluster of perforation cannot solely describe the behavior observed at far field. Presence of fracture swarms

affect all aspects of hydraulic fracture design such as treatment pressures, fracture widths, and length and proppant distribution (Ciezobka et al., 2018). Therefore, fracturing treatment design analysis performed using single fracture models can result in significant discrepancies between modeling output and field observations. Multiple fracture strands observed in early field test (Warpinski et al., 1993) were considered to be unusual (Nolte, 1993) and are attributed to the complexity of that specific reservoir (Mesaverde formation) citing re-opening of large number of micro-cracks that are aligned parallel to the fracture due to induced fracture tip stresses. On the contrary, the recent field studies (Ciezobka et al., 2018; Raterman et al., 2017) indicate that multi-strand hydraulic fracture propagation is a norm rather than an unusual occurrence. Therefore, it is imperative to understand the behavior of closely spaced multi-strand fracture propagation. The numerical study of propagation of two closely spaced parallel hydraulic fractures (Jeffery et al., 1987) indicated rise in the injection pressure compared to single fracture case. However, the two fracture analysis is not sufficient to understand the propagation of dense parallel fractures. Numerical modeling and analysis of this problem is lacking even in 2D mainly because of the complex numerical modeling capability required.

1.3 Objectives and Contributions

The objective of this work is to develop robust, multi-physics 2D and P3D hydraulic fracturing models that can simulate realistic hydraulic fracturing scenarios efficiently while capturing the impact of rock anisotropy and correctly accounting for near tip behavior, and HF/NF interactions in network stimulation.

The contributions of this work are:

- Development and verification of a 2D displacement discontinuity method (DDM) for anisotropic rock. The influence coefficients of DDM for orthotropic material are derived

using the Kelvin's fundamental solution for the problem of concentrated line force in an infinite orthotropic body (Rizzo and Shippy, 1970). The model is used to analyze the effect of rock anisotropy on induced stresses and displacements around a fracture.

- Development, verification and application of a fully coupled model based on 2D DDM for multiple hydraulic fracture propagation in isotropic and anisotropic rock. The model has been applied to clearly demonstrate the effects of rock anisotropy on fracture extension angle and path. In particular, near wellbore fracture tortuosity in anisotropic rock has been investigated.
- Development and implementation of self-similar fracture tip solutions for hydraulic fracture propagation in the viscous propagation regime in orthotropic rock, and improvement of the 2D DDM fracture propagation model to account for finite fracture height to enable simulation of field scale hydraulic fractures.
- Development of a fully coupled planar height growth fracture (P3D) propagation model for anisotropic rock and application to field-scale HF simulations.
- Development of a complex fracture network model based on 2D DDM that is capable of simulating reservoir scale hydraulic/natural fracture interaction.
- Investigation and analysis of the formation of dense parallel fracture strands observed in industry-sponsored field demonstration projects.

2 Displacement Discontinuity Method for Anisotropic Rock

2.1 Introduction to Material Anisotropy

Consider a material that is continuous, homogeneous and linearly elastic as in Figure 1-1. Based on Hooke's law, the six components of stress tensor (σ_{ij}) are related to strain tensor (e_{ij}) through material's elastic constants s_{ij} in the Cartesian coordinate system *xyz* as:

$$
\begin{aligned}
e_{xx} &= s_{11}\sigma_{xx} + s_{12}\sigma_{yy} + s_{13}\sigma_{zz} + s_{14}\sigma_{yz} + s_{15}\sigma_{xz} + s_{16}\sigma_{xy} \\
e_{yy} &= s_{21}\sigma_{xx} + s_{22}\sigma_{yy} + s_{23}\sigma_{zz} + s_{24}\sigma_{yz} + s_{25}\sigma_{xz} + s_{26}\sigma_{xy} \\
e_{zz} &= s_{31}\sigma_{xx} + s_{32}\sigma_{yy} + s_{33}\sigma_{zz} + s_{34}\sigma_{yz} + s_{35}\sigma_{xz} + s_{36}\sigma_{xy} \\
e_{yz} &= s_{41}\sigma_{xx} + s_{42}\sigma_{yy} + s_{43}\sigma_{zz} + s_{44}\sigma_{yz} + s_{45}\sigma_{xz} + s_{46}\sigma_{xy} \\
e_{xz} &= s_{51}\sigma_{xx} + s_{52}\sigma_{yy} + s_{53}\sigma_{zz} + s_{54}\sigma_{yz} + s_{55}\sigma_{xz} + s_{56}\sigma_{xy} \\
e_{xy} &= s_{61}\sigma_{xx} + s_{62}\sigma_{yy} + s_{63}\sigma_{zz} + s_{64}\sigma_{yz} + s_{65}\sigma_{xz} + s_{66}\sigma_{xy}
\end{aligned}
\qquad (2.1)
$$

The coefficients s_{ij} are elastic constants of the material and their relationship with engineering constants will be discussed later. The above equation shows a total of 36 independent elastic constants that can exist for an elastic material (to stay consistent with the literature (Lekhnitskii, 1963), we adopted a sign convention *of tension positive*; therefore contraction strains are negative). Inverting Eq. 2.1, we can obtain stress components in terms of strain components and elastic constants c_{ij} as in Eq. 2.2. Note that here constants c_{ij} are obtained through the inversion of Eq. 2.1 and they are represented in terms of s_{ij} .

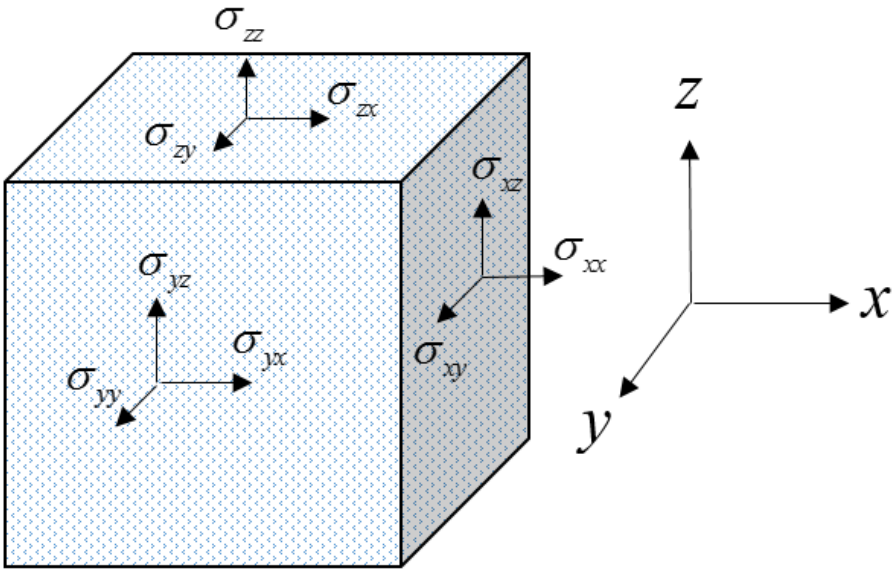

Figure 0-1. A linear elastic homogeneous material and stress tensor components acting on it in the Cartesian coordinate system *xyz*.

$$
\begin{aligned}
\sigma_{xx} &= c_{11}e_{xx} + c_{12}e_{yy} + c_{13}e_{zz} + c_{14}e_{yz} + c_{15}e_{xz} + c_{16}e_{xy} \\
\sigma_{yy} &= c_{21}e_{xx} + c_{22}e_{yy} + c_{23}e_{zz} + c_{24}e_{yz} + c_{25}e_{xz} + c_{26}e_{xy} \\
\sigma_{zz} &= c_{31}e_{xx} + c_{32}e_{yy} + c_{33}e_{zz} + c_{34}e_{yz} + c_{35}e_{xz} + c_{36}e_{xy} \\
\sigma_{yz} &= c_{41}e_{xx} + c_{42}e_{yy} + c_{43}e_{zz} + c_{44}e_{yz} + c_{45}e_{xz} + c_{46}e_{xy} \\
\sigma_{xz} &= c_{51}e_{xx} + c_{52}e_{yy} + c_{53}e_{zz} + c_{54}e_{yz} + c_{55}e_{xz} + c_{56}e_{xy} \\
\sigma_{xy} &= c_{61}e_{xx} + c_{62}e_{yy} + c_{63}e_{zz} + c_{64}e_{yz} + c_{65}e_{xz} + c_{66}e_{xy}
\end{aligned}
\tag{2.2}
$$

According to (Lekhnitskii, 1963), there exists a symmetry of the kind, $s_{ij} = s_{ji}$, between the elastic constants; therefore, the number of independent constants will be reduced to 21 from 36 as shown below in Eq. 2.3.

$$
\begin{aligned}
e_{xx} &= s_{11}\sigma_{xx} + s_{12}\sigma_{yy} + s_{13}\sigma_{zz} + s_{14}\sigma_{yz} + s_{15}\sigma_{xz} + s_{16}\sigma_{xy} \\
e_{yy} &= s_{12}\sigma_{xx} + s_{22}\sigma_{yy} + s_{23}\sigma_{zz} + s_{24}\sigma_{yz} + s_{25}\sigma_{xz} + s_{26}\sigma_{xy} \\
e_{zz} &= s_{13}\sigma_{xx} + s_{23}\sigma_{yy} + s_{33}\sigma_{zz} + s_{34}\sigma_{yz} + s_{35}\sigma_{xz} + s_{36}\sigma_{xy} \\
e_{yz} &= s_{14}\sigma_{xx} + s_{24}\sigma_{yy} + s_{34}\sigma_{zz} + s_{44}\sigma_{yz} + s_{45}\sigma_{xz} + s_{46}\sigma_{xy} \\
e_{xz} &= s_{15}\sigma_{xx} + s_{25}\sigma_{yy} + s_{35}\sigma_{zz} + s_{45}\sigma_{yz} + s_{55}\sigma_{xz} + s_{56}\sigma_{xy} \\
e_{xy} &= s_{16}\sigma_{xx} + s_{26}\sigma_{yy} + s_{36}\sigma_{zz} + s_{46}\sigma_{yz} + s_{56}\sigma_{xz} + s_{66}\sigma_{xy}
\end{aligned}
\tag{2.3}
$$

2.1.1 Axis of Elastic Symmetry

Consider a plane cut perpendicular to axis *z* of the material in Figure 2-1 as shown in Figure 2-2. Suppose, A is a point lying on the plane and an elastic constant that relates normal deformation at the point A in *x*-direction with normal stress component in *x*-direction is s_{11}. If every point in the plane *xy* exhibits the same elastic property in the *x*-direction then we call the axis *x* as axis of elastic symmetry. If a material consists of two axes of elastic symmetry, then the plane made by these two axes is called plane of elastic symmetry. The direction normal to the plane of elastic symmetry is referred as principal direction of elastic symmetry. For example, in Figure 2-2, if both *x*-axis and *y*-axis are the axes of elastic symmetry then, *xy* is the plane of elastic symmetry and *z*-axis will be the principal direction. The constitutive equations for the case where *x* and *y* are axes of elastic symmetry can be written as

$$
\begin{aligned}
e_{xx} &= s_{11}\sigma_{xx} + s_{12}\sigma_{yy} + s_{13}\sigma_{zz} + s_{16}\sigma_{xy} \\
e_{yy} &= s_{12}\sigma_{xx} + s_{22}\sigma_{yy} + s_{23}\sigma_{zz} + s_{26}\sigma_{xy} \\
e_{zz} &= s_{13}\sigma_{xx} + s_{23}\sigma_{yy} + s_{33}\sigma_{zz} + s_{36}\sigma_{xy} \\
e_{yz} &= s_{44}\sigma_{yz} + s_{45}\sigma_{xz} \\
e_{xz} &= s_{45}\sigma_{yz} + s_{55}\sigma_{xz} \\
e_{xy} &= s_{16}\sigma_{xx} + s_{26}\sigma_{yy} + s_{36}\sigma_{zz} + s_{66}\sigma_{xy}
\end{aligned}
\tag{2.4}
$$

Note that due to elastic symmetry, the number of independent elastic constants further reduced from 21 to 13 (see Lekhnitskii, (1963) for details).

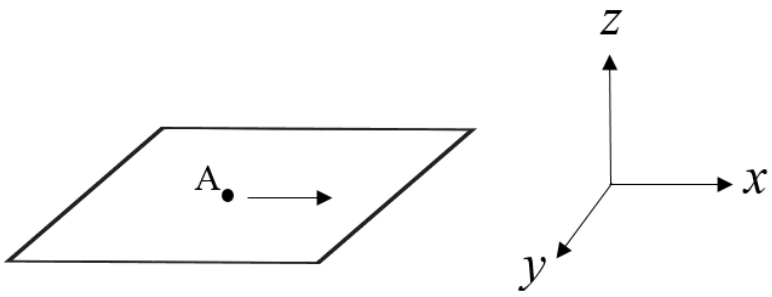

Figure 0-2. A plane cut perpendicular to axis *z* of the material in Figure 1. A is a point on the material and the arrow points towards *x*-axis.

2.1.2 Orthotropic Material

For a material such as indicated in Figure 2-1, if all the three orthogonal axes *x*, *y* and *z* are the axes of elastic symmetry then such a material is called orthotropic material. Based on the definitions given above, in an orthotropic material, there are three principal directions (*x*, *y* and *z*) and three planes of elastic symmetry (*xz*, *yz* and *xy*), all orthogonal to each other. Due to this elastic symmetry, the number of independent elastic constants in an orthotropic material will be reduced to 9 as in Eq. 2.5.

$$\begin{aligned} e_{xx} &= s_{11}\sigma_{xx} + s_{12}\sigma_{yy} + s_{13}\sigma_{zz} \\ e_{yy} &= s_{12}\sigma_{xx} + s_{22}\sigma_{yy} + s_{23}\sigma_{zz} \\ e_{zz} &= s_{13}\sigma_{xx} + s_{23}\sigma_{yy} + s_{33}\sigma_{zz} \\ e_{yz} &= s_{44}\sigma_{yz} \\ e_{xz} &= s_{55}\sigma_{xz} \\ e_{xy} &= s_{66}\sigma_{xy} \end{aligned} \qquad (2.5)$$

2.1.3 Relationship with Engineering Constants

The elastic constants s_{ij} are related to the engineering constants E_i (Young's modulus), G_{ij} (shear modulus) and v_{ij} (Poisson's ratio) in orthotropic rock material as follows:

$$
\begin{aligned}
&s_{11} = \frac{1}{E_x}, s_{22} = \frac{1}{E_y}, s_{33} = \frac{1}{E_z}, \\
&s_{12} = -\frac{v_{yx}}{E_y}, s_{13} = -\frac{v_{xz}}{E_x}, s_{23} = -\frac{v_{yz}}{E_y}, \\
&s_{44} = \frac{1}{2G_{yz}}, s_{55} = \frac{1}{2G_{xz}}, s_{66} = \frac{1}{2G_{xy}}
\end{aligned}
\tag{2.6}
$$

where E_i characterize the normal deformation of the material due to tension or compression in the direction i, G_{ij} characterize shears in the planes parallel to the plane ij and v_{ij} characterize contraction or expansion in the direction j when tensile or compressive load is applied in the direction i.

Notice that due to the symmetry of the elastic constants $s_{ij} = s_{ji}$ as indicated in Eq. 2.3, the following relationship between v_{ij} and v_{ji} must hold:

$$
\frac{v_{ij}}{E_i} = \frac{v_{ji}}{E_j} \tag{2.7}
$$

2.1.4 Transversely Isotropic Material

Suppose if any of the three planes of elastic symmetry of an orthotropic material possess an elastic symmetry such that for all the points lying in that plane, the elastic constants are equal in all the directions pointing within that plane, then such a material is called transversely isotropic material. In other words, one of the three planes of elastic symmetry must become an isotropic plane. In this case, the number of independent elastic constants will be reduced to only 5 as in Eq. 1.8. If the

plane *xy* in Figure 2-1, is taken to be the plane of isotropy, then stress-strain relationship from Eq. 2.5 can be written as

$$\begin{aligned} e_x &= s_{11}\sigma_{xx} + s_{12}\sigma_{yy} + s_{13}\sigma_{zz} \\ e_y &= s_{12}\sigma_{xx} + s_{11}\sigma_{yy} + s_{13}\sigma_{zz} \\ e_z &= s_{13}\sigma_{xx} + s_{13}\sigma_{yy} + s_{33}\sigma_{zz} \\ e_{yz} &= s_{44}\sigma_{yz} \\ e_{xz} &= s_{44}\sigma_{xz} \\ e_{xy} &= s_{66}\sigma_{xy} = (s_{11} - s_{12})2\sigma_{xy} \end{aligned} \tag{2.8}$$

2.1.5 Isotropic Material

A material is considered isotropic if it exhibits same elastic properties in every direction at every point. In this case, the number of independent elastic constants will be reduced to 2 and Eq. 2.8 becomes (in terms of engineering constants)

$$\begin{aligned} e_x &= \frac{1}{E}\sigma_{xx} - \frac{\nu}{E}\sigma_{yy} - \frac{\nu}{E}\sigma_{zz} \\ e_y &= -\frac{\nu}{E}\sigma_{xx} + \frac{1}{E}\sigma_{yy} - \frac{\nu}{E}\sigma_{zz} \\ e_z &= -\frac{\nu}{E}\sigma_{xx} - \frac{\nu}{E}\sigma_{yy} + \frac{1}{E}\sigma_{zz} \\ e_{yz} &= \frac{1}{2G}\sigma_{yz} \\ e_{xz} &= \frac{1}{2G}\sigma_{xz} \\ e_{xy} &= \frac{1}{2G}\sigma_{xy} \end{aligned} \tag{2.9}$$

where

$$G = \frac{E}{2(1+\nu)}$$

2.2 Plane Problems

Often we are involved with many 3D problems that can be approximated in two dimensions (i.e., in a plane). Such an approximation eases the mathematical difficulty and allows one to construct analytical solutions which are exact and computationally fast, and also decreases computational burden during numerical analysis. In this work we deal mostly with 2D problems and we will state the conditions under which such analysis holds. We will also propose some corrections to 2D solutions to incorporate 3D effects. Plane problems can be generalized into two categories. They are:

2.2.1 Plane Stress

In a plane stress condition we restrict our attention to the stress components in a single plane. All other stress components are assumed to be zero. For example, if plane *xy* (see Figure 2-1) is considered to be in the state of plane stress, we take $\sigma_{zz} = \sigma_{xz} = \sigma_{yz} = 0$, and the constitutive relation for orthotropic material given in Eq. 2.5 becomes

$$\begin{aligned} e_{xx} &= s_{11}\sigma_{xx} + s_{12}\sigma_{yy} \\ e_{yy} &= s_{12}\sigma_{xx} + s_{22}\sigma_{yy} \\ e_{zz} &= s_{13}\sigma_{xx} + s_{23}\sigma_{yy} \\ e_{xy} &= s_{66}\sigma_{xy} \end{aligned} \tag{2.10}$$

The relationship in terms of strain components can be obtained by inverting Eq. 2.10 and the result is given in Eq. 2.11.

$$\begin{aligned} \sigma_{xx} &= c_{11}e_{xx} + c_{12}e_{yy} \\ \sigma_{yy} &= c_{12}e_{xx} + c_{22}e_{yy} \\ \sigma_{xy} &= c_{66}e_{xy} \end{aligned} \tag{2.11}$$

where

$$c_{11} = \frac{s_{22}}{s_{11}s_{22} - s_{12}^2}$$
$$c_{12} = \frac{-s_{12}}{s_{11}s_{22} - s_{12}^2}$$
$$c_{22} = \frac{s_{11}}{s_{11}s_{22} - s_{12}^2}$$
$$c_{66} = 1/\, s_{66}$$

2.2.2 Plane Strain

In a plane strain condition we assume that all strain components are zero except for a single plane. For example, if plane *xy* is considered to be in the state of plane strain, we take $e_{zz} = e_{xz} = e_{yz} = 0$, and the constitutive relation for orthotropic material given in Eq. 2.5 becomes

$$\begin{aligned} e_{xx} &= \frac{s_{11}s_{33} - s_{13}^2}{s_{33}}\sigma_{xx} + \frac{s_{12}s_{33} - s_{13}s_{23}}{s_{33}}\sigma_{yy} \\ e_{yy} &= \frac{s_{12}s_{33} - s_{13}s_{23}}{s_{33}}\sigma_{xx} + \frac{s_{22}s_{33} - s_{23}^2}{s_{33}}\sigma_{yy} \\ e_{xy} &= s_{66}\sigma_{xy} \end{aligned} \tag{2.12}$$

Inverting the above equation gives the stress components in terms of strain components and elastic constants c_{ij} as:

$$\begin{aligned} \sigma_{xx} &= c_{11}e_{xx} + c_{12}e_{yy} \\ \sigma_{yy} &= c_{12}e_{xx} + c_{22}e_{yy} \\ \sigma_{xy} &= c_{66}e_{xy} \end{aligned} \tag{2.13}$$

where

$$c_{11} = \frac{s_{22}s_{33} - s_{23}^2}{s_{33}s_0^2}$$
$$c_{12} = \frac{-(s_{12}s_{33} - s_{13}s_{23})}{s_{33}s_0^2}$$
$$c_{22} = \frac{s_{11}s_{33} - s_{13}^2}{s_{33}s_0^2}$$
$$c_{66} = 1/s_{66}$$

2.3 Transformation Equations

2.3.1 Elastic Constants

Consider an orthotropic material where *x*, *y* and *z* are axes of elastic symmetry such as shown in Figure 2-3. If the elastic constants s_{ij} for this material that relate the stress-strain components at a point in the coordinate system *xyz* are given, then the elastic constants $\overline{s}_{ij}$ that relate stress-strain components in the coordinate system $\overline{xyz}$ which is obtained by rotating the system *xyz* about axis *z* by β degrees (as in Figure 2-3) are given by following expressions (Lekhnitskii, 1963):

$$\begin{aligned}
\overline{s}_{11} &= s_{11}\cos^4\beta + (2s_{12} + s_{66})\sin^2\beta\cos^2\beta + s_{22}\sin^4\beta \\
\overline{s}_{12} &= (s_{11} + s_{22} - 2s_{12} - s_{66})\sin^2\beta\cos^2\beta + s_{12} \\
\overline{s}_{22} &= s_{11}(\sin^4\beta) + (2s_{12} + s_{66})\sin^2\beta\cos^2\beta + s_{22}\cos^4\beta \\
\overline{s}_{66} &= 4(s_{11} + s_{22} - 2s_{12} - s_{66})\sin^2\beta\cos^2\beta + s_{66} \\
\overline{s}_{16} &= \left(s_{22}\sin^2\beta - 2s_{11}\cos^2\beta + (2s_{12} + s_{66})(\cos^2\beta - \sin^2\beta)\right)\sin\beta\cos\beta \\
\overline{s}_{26} &= \left(2s_{22}\cos^2\beta - 2s_{11}\sin^2\beta - (2s_{12} + s_{66})(\cos^2\beta - \sin^2\beta)\right)\sin\beta\cos\beta \qquad (2.14) \\
\overline{s}_{45} &= (s_{44} - s_{55})\cos\beta\sin\beta + s_{45}(\cos^2\beta - \sin^2\beta) \\
\overline{s}_{13} &= s_{13}\cos^2\beta + s_{23}\sin^2\beta \\
\overline{s}_{36} &= 2(s_{23} - s_{13})\cos\beta\sin\beta \\
\overline{s}_{23} &= s_{13}\sin^2\beta + s_{23}\cos^2\beta \\
\overline{s}_{11} &= s_{33}
\end{aligned}$$

Notice that after the rotation of coordinate system, new elastic constants $\bar{s}_{16}, \bar{s}_{26}, \bar{s}_{36}, \bar{s}_{45}$ appeared. This is because the new coordinate axes $\bar{x}$ and $\bar{y}$ are not the axes of elastic symmetry. Therefore, in this coordinate system, the stress-strain relationships in terms of the new elastic constants can be expressed as in Eq. 2.15 which are similar to Eq. 2.4.

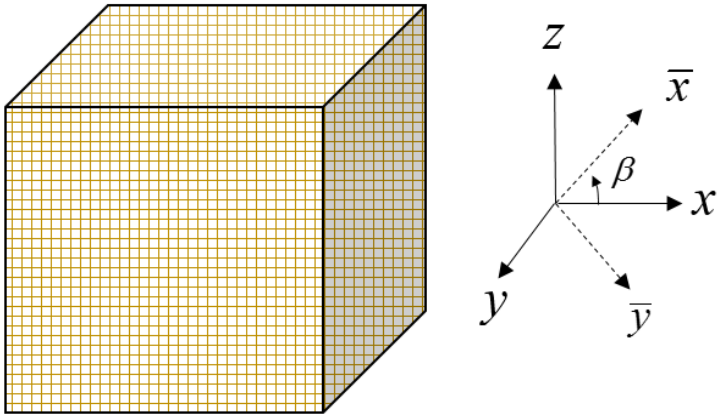

Figure 0-3. An orthotropic material with three axes of elastic symmetry *x*, *y* and *z*. $\bar{x}$ and $\bar{y}$ are the new coordinate axes that are obtained after rotating the coordinate system *xyz* about axis *z* by β degrees.

$$
\begin{aligned}
e_{\bar{x}\bar{x}} &= \bar{s}_{11}\sigma_{\bar{x}\bar{x}} + \bar{s}_{12}\sigma_{\bar{y}\bar{y}} + \bar{s}_{13}\sigma_{zz} + \bar{s}_{16}\sigma_{\bar{x}\bar{y}} \\
e_{\bar{y}\bar{y}} &= \bar{s}_{12}\sigma_{\bar{x}\bar{x}} + \bar{s}_{22}\sigma_{\bar{y}\bar{y}} + \bar{s}_{23}\sigma_{zz} + \bar{s}_{26}\sigma_{\bar{x}\bar{y}} \\
e_{zz} &= \bar{s}_{13}\sigma_{\bar{x}\bar{x}} + \bar{s}_{23}\sigma_{\bar{y}\bar{y}} + \bar{s}_{33}\sigma_{zz} + \bar{s}_{36}\sigma_{\bar{x}\bar{y}} \\
e_{\bar{y}z} &= \bar{s}_{44}\sigma_{\bar{y}z} + \bar{s}_{45}\sigma_{\bar{x}z} \\
e_{\bar{x}z} &= \bar{s}_{45}\sigma_{\bar{y}z} + \bar{s}_{55}\sigma_{\bar{x}z} \\
e_{\bar{x}\bar{y}} &= \bar{s}_{16}\sigma_{\bar{x}\bar{x}} + \bar{s}_{26}\sigma_{\bar{y}\bar{y}} + \bar{s}_{36}\sigma_{zz} + \bar{s}_{66}\sigma_{\bar{x}\bar{y}}
\end{aligned}
\qquad (2.15)
$$

Under the condition of plane $\bar{x}\bar{y}$ in the state of plane strain,

$$e_{\bar{y}z} = 0; e_{\bar{x}z} = 0; e_{zz} = 0 \qquad (2.16)$$

Substituting the above values in Eq. 2.15 gives

$$
\begin{aligned}
e_{\bar{x}\bar{x}} &= \left(\bar{s}_{11} - \frac{\bar{s}_{13}^2}{\bar{s}_{33}}\right)\sigma_{\bar{x}\bar{x}} + \left(\bar{s}_{12} - \frac{\bar{s}_{13}\bar{s}_{23}}{\bar{s}_{33}}\right)\sigma_{\bar{y}\bar{y}} + \left(\bar{s}_{16} - \frac{\bar{s}_{13}\bar{s}_{36}}{\bar{s}_{33}}\right)\sigma_{\bar{x}\bar{y}} \\
e_{\bar{y}\bar{y}} &= \left(\bar{s}_{12} - \frac{\bar{s}_{23}\bar{s}_{13}}{\bar{s}_{33}}\right)\sigma_{\bar{x}\bar{x}} + \left(\bar{s}_{22} - \frac{\bar{s}_{23}^2}{\bar{s}_{33}}\right)\sigma_{\bar{y}\bar{y}} + \left(\bar{s}_{26} - \frac{\bar{s}_{23}\bar{s}_{36}}{\bar{s}_{33}}\right)\sigma_{\bar{x}\bar{y}} \\
e_{\bar{x}\bar{y}} &= \left(\bar{s}_{16} - \frac{\bar{s}_{36}\bar{s}_{13}}{\bar{s}_{33}}\right)\sigma_{\bar{x}\bar{x}} + \left(\bar{s}_{26} - \frac{\bar{s}_{36}\bar{s}_{23}}{\bar{s}_{33}}\right)\sigma_{\bar{y}\bar{y}} + \left(\bar{s}_{66} - \frac{\bar{s}_{36}^2}{\bar{s}_{33}}\right)\sigma_{\bar{x}\bar{y}}
\end{aligned}
\tag{2.17}
$$

The above equation can be inverted to represent stress components in terms of strain components and material constants $\bar{c}_{ij}$ as in Eq. 2.18.

$$
\begin{aligned}
\sigma_{\bar{x}\bar{x}} &= \bar{c}_{11}e_{\bar{x}\bar{x}} + \bar{c}_{12}e_{\bar{y}\bar{y}} + \bar{c}_{16}e_{\bar{x}\bar{y}} \\
\sigma_{\bar{y}\bar{y}} &= \bar{c}_{12}e_{\bar{x}\bar{x}} + \bar{c}_{22}e_{\bar{y}\bar{y}} + \bar{c}_{26}e_{\bar{x}\bar{y}} \\
\sigma_{\bar{x}\bar{y}} &= \bar{c}_{16}e_{\bar{x}\bar{x}} + \bar{c}_{26}e_{\bar{y}\bar{y}} + \bar{c}_{66}e_{\bar{x}\bar{y}}
\end{aligned}
\tag{2.18}
$$

The inverted coefficients $\bar{c}_{ij}$ are given in Appendix A.

If plane $\bar{x}\bar{y}$ is considered to be in the state of plane stress, the following stress components will be zero.

$$\sigma_{\bar{y}z} = 0; \sigma_{\bar{x}z} = 0; \sigma_{\bar{z}z} = 0$$

Following the procedure described above, the coefficients $\bar{c}_{ij}$ for the case of plane stress can be obtained and these are given in Appendix A.

2.3.2 Stresses

The stress components in the coordinate system $\bar{x}\bar{y}z$ are related to the stress components in the system *xyz* as follows (only listed plane $\bar{x}\bar{y}$ components)

$$
\begin{aligned}
\sigma_{\bar{x}\bar{x}} &= \sigma_{xx}\cos^2\beta + 2\sigma_{xy}\sin\beta\cos\beta + \sigma_{yy}\sin^2\beta \\
\sigma_{\bar{y}\bar{y}} &= \sigma_{xx}\sin^2\beta - 2\sigma_{xy}\sin\beta\cos\beta + \sigma_{yy}\cos^2\beta \\
\sigma_{\bar{x}\bar{y}} &= -(\sigma_{xx} - \sigma_{yy})\sin\beta\cos\beta + \sigma_{xy}(\cos^2\beta - \sin^2\beta)
\end{aligned}
\tag{2.19}
$$

2.4 Equilibrium and Compatibility Conditions

Consider a differential element of a continuous material in two dimensions (in the plane *xy*) and stresses acting on it in *x*-direction as in Figure 2-4. If we consider the balance of traction vectors in the *x*-direction we get (assuming zero body forces and inertial forces)

$$-\sigma_{xx}dy + (\sigma_{xx} + \frac{\partial \sigma_{xx}}{\partial x}dx)dy - \sigma_{yx}dx + (\sigma_{yx} + \frac{\partial \sigma_{yx}}{\partial y}dy)dx = 0$$

or

$$\frac{\partial \sigma_{xx}}{\partial x} + \frac{\partial \sigma_{yx}}{\partial y} = 0 \qquad (2.20)$$

Similarly considering stresses in *y*-direction we get,

$$\frac{\partial \sigma_{xy}}{\partial x} + \frac{\partial \sigma_{yy}}{\partial y} = 0 \qquad (2.21)$$

The above equation is referred as equilibrium condition of a static material and the stress tensor at any point in the material is confined by this condition. To ensure rotational equilibrium of the element, σ_{xy} must be equal to σ_{yx} .

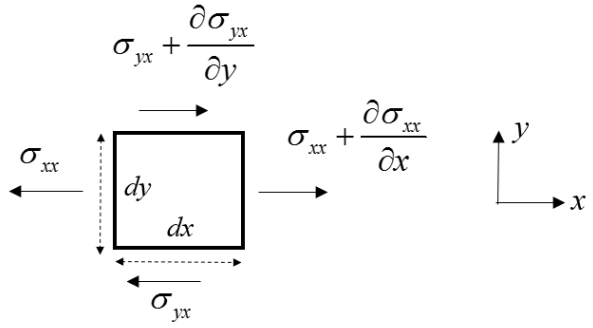

Figure 0-4. An infinitesimal stress element with stress components acting in the direction *x*.

If we assume that the displacements in a material can be expressed by a smooth continuous differentiable function $u(x, y)$ in the plane *xy*, then at any point in the plane, the normal and shear strains can be expressed as

$$e_{xx} = \frac{\partial u_x}{\partial x};\ e_{yy} = \frac{\partial u_y}{\partial x};\ e_{xy} = e_{yx} = \frac{1}{2}\left(\frac{\partial u_x}{\partial y} + \frac{\partial u_y}{\partial x}\right) \tag{2.22}$$

These three strains are related by Eq. 2.23, which is called compatibility condition.

$$\frac{\partial^2 e_{yy}}{\partial x^2} + \frac{\partial^2 e_{xx}}{\partial x^2} = \frac{2\partial^2 e_{xy}}{\partial x \partial y} \tag{2.23}$$

Finally, substituting stress-strain relations in equilibrium equations and using definitions from Eq. 2.22 we obtain a partial differential equation which can be solved for a given boundary conditions for stresses and displacements in an elastic material. Analytical solutions can be obtained for some simple boundary values problems, however, for more complex and realistic problems obtaining an analytical solution poses extreme mathematical difficulty. In these cases we approximate the continuous system as discrete system using numerical finite element or boundary element methods.

2.5 Fundamental Solution

Fundamental singular solutions for elasticity problems have been employed to develop boundary element methods using superposition principle. Analytical solution for concentrated line force in an infinite orthotropic elastic material was used to develop fictitious stress method (Crouch and Starfield, 1983) for orthotropic material. Similarly, analytical solution for unit displacement discontinuity in an infinite elastic isotropic material was used to develop displacement discontinuity method (Crouch, 1976). Brady and Bray, (1978) extended analytical solution for concentrated line force in an isotropic material to the case of opposing concentrated line forces separated by a small distance (i.e. dipole) in order to solve problems pertaining to thin elongated excavations without the need to model hanging walls and footwalls separately in numerical analysis. In boundary element technique, the basic idea is to discretize the material only along its boundary and use the fundamental solutions (which are singular) to find strength of singularities

that has to be distributed along the boundary surface such that the total stress/displacement on each boundary element is equal to a known value. Following Brady and Bray, (1978) and Kimence and Erguven, (2005), in this work we use fundamental solution for concentrated line force in an infinite elastic orthotropic material to develop two dimensional displacement discontinuity method for orthotropic material by establishing relationship between dipole stresses and displacement discontinuities.

2.5.1 Concentrated Line Source

Consider an infinite orthotropic elastic material that is subjected to a line load of magnitude *P* per unit length (N/m) extending along axis *z* through $-\infty < z < \infty$ as shown in Figure 2-5. This problem can be evaluated under plane strain condition with plane *xy* being in the state of plane strain as the loading conditions on planes perpendicular to *z*-axis does not vary; that is

$$\frac{\partial P}{\partial z} = 0;$$

Due to the symmetry of loading conditions along axis *z*, the strain components

$$e_{zz} = \frac{\partial u_z}{\partial z} = 0;\ e_{xz} = 0;\ e_{yz} = 0$$

If *x*, *y* and *z* are the three axes of elastic symmetry of the orthotropic material, then the stresses and displacements at any point in the plane *xy* due to the load *P* is given as (Rizzo and Shippy, 1970)

$$\begin{aligned} u_x &= P_{\bar{x}} h_{11} + P_{\bar{y}} h_{12} \\ u_y &= P_{\bar{x}} h_{21} + P_{\bar{y}} h_{22} \\ \sigma_{xx} &= P_{\bar{x}} I_{11} + P_{\bar{y}} I_{12} \\ \sigma_{yy} &= P_{\bar{x}} I_{21} + P_{\bar{y}} I_{22} \\ \sigma_{xy} &= P_{\bar{x}} I_{31} + P_{\bar{y}} I_{32} \end{aligned} \qquad (2.24)$$

where $P_{\bar{x}}$ and $P_{\bar{y}}$ are force components in the direction of some local coordinate axes $\bar{x}$ and $\bar{y}$ respectively (see Figure 2-5), and h_{ij}, I_{ij} are displacement and stress functions (for example, h_{22} gives displacement in *y* direction for unit force component in $\bar{y}$ direction and I_{11} gives stress in *x* direction for unit force component in $\bar{x}$ direction) respectively in the local coordinate system $\bar{x}\bar{y}z$ (these are given in Appendix B). The displacements are taken positive if a material point moves in the direction of positive axis (only positive axes are shown in Figure 2-5).

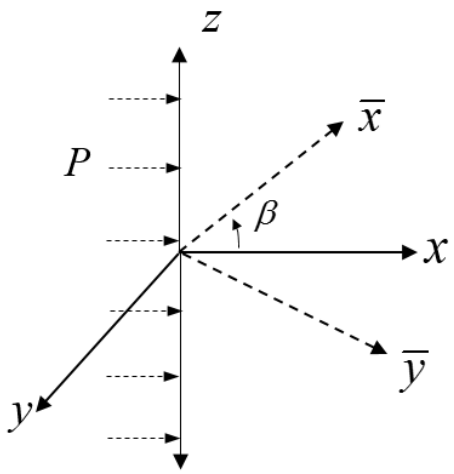

Figure 0-5. Concentrated line load of magnitude *P* acting through $-\infty < z < \infty$ in the plane *xy*. $\bar{x}$ and $\bar{y}$ are the new coordinate axes that are obtained after rotating the coordinate system *xyz* about axis *z* by β degrees.

2.5.2 Dipole Load

A dipole load constitutes of two opposing concentrated line loads of equal magnitude that are separated by an infinitesimally small distance. If the stress or displacement at a point $r(x, y)$ (see Figure 2-6) in the plane *xy* due to a concentrated line load of magnitude P_y per unit length is given as

$$s(x, y) = P_y . f(x, y) \qquad (2.25)$$

where $s(x,y)$ denotes stress or displacement at a point $r(x,y)$ and $f(x,y)$ denotes the corresponding influence function which is continues and differentiable.

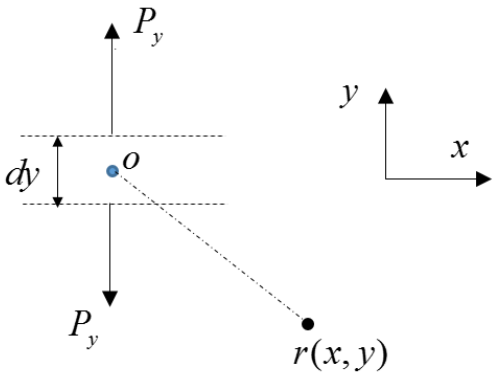

Figure 0-6. Two concentrated line loads of same magnitude P_y acting in *y*-direction and separated by a small distance *dy*. Origin *o* is at the mid-point of *dy*. $r(x,y)$ is an arbitrary point located in the plane *xy*.

Then for the pair of opposite line concentrated loads P_y per unit length, separated by a small distance *dy* (see Figure 6), the stress or displacement at a point $r(x,y)$ in the plane *xy* is given as (Brady and Bray, 1978)

$$s(x,y) = (P_y.f(x,y) + P_y.\frac{f(x,y)}{\partial y}\frac{dy}{2}) - (P_y.f(x,y) - P_y.\frac{f(x,y)}{\partial y}\frac{dy}{2})$$

or (2.26)

$$s(x,y) = dy.P_y.\frac{f(x,y)}{dy}$$

where *dy* is twice the distance between the origin *o* and point of load application. For infinitesimally small distance *dy* (that can be almost viewed as a point) the product, $dy.P_y$, which is represented by Q_y (as in Eq. 2.27) is defined as dipole stress or dipole intensity per unit length

(as in electric dipoles where electric charge substitutes load). Note that when the two forces are concentric, the dipole moment about the origin *o* is zero.

$$Q_y = dy.P_y \tag{2.27}$$

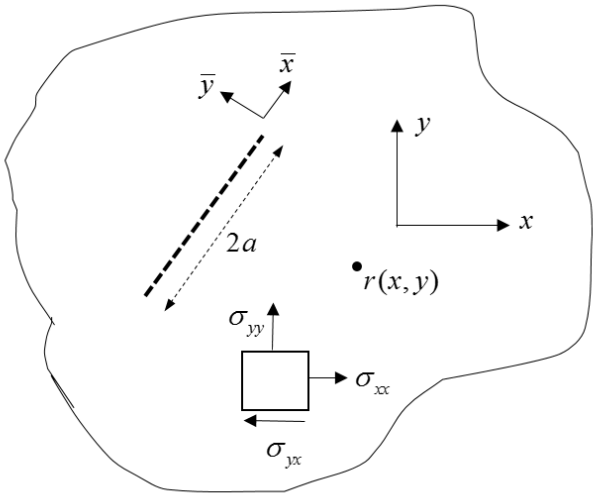

Figure 0-7. *xy* plane view of an infinite orthotropic material with a thin slit of length 2*a*. *x*, *y* and *z* (pointing outwards) are the three axes of elastic symmetry of the material. $\bar{x}$ and $\bar{y}$ are the local coordinate axes of the slit. Figure also show far-field stress tensor components in the plane *xy*.

2.6 Displacement Discontinuity Method

Consider an infinite elastic orthotropic material with thin slit of length 2*a* and subjected to far-field stresses σ_{xx}, σ_{yy} and σ_{xy} in the plane *xy* as shown in Figure 2-7. To find the influence functions to evaluate induced stresses and displacements at an arbitrary point $r(x, y)$ in the plane *xy* due to the slit, we divide the problem in to two steps. In the first strep we assume that the slit experiences only normal strain due to external loading while all other strains are restricted. Then the particular solutions for stresses and displacements due to normal strain are developed. In the next step we follow similar procedure to develop particular solutions for stresses and

displacements for the case where only shear strain is non-zero. These two particular solutions that satisfy different boundary conditions on the slit can be combined to arrive at the complete solution for the general stress condition considered in the Figure 2-7.

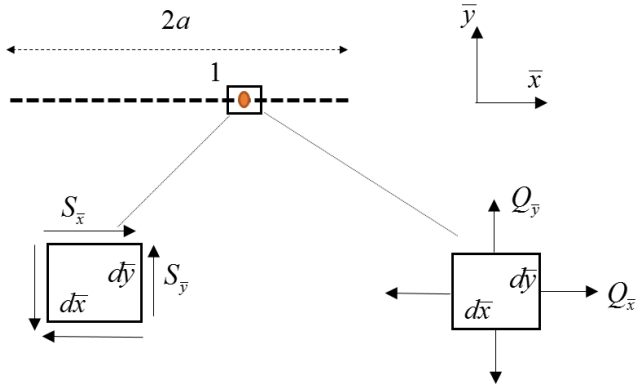

Figure 0-8. $\bar{x}\bar{y}$ plane view of Figure 2-7. Point 1 (represented by orange dot) is a differential element on the slit where normal dipole stresses $Q_{\bar{x}}$, $Q_{\bar{y}}$, and shear dipoles stresses $S_{\bar{x}}$, $S_{\bar{y}}$ are applied.

As indicated above, first let us consider the following boundary condition at a point 1 on slit (see Figure 2-8)

$$e_{\bar{i}\bar{j}} = 0,\ e_{\bar{y}\bar{y}} \neq 0 \tag{2.28}$$

Let the normal strain $e_{\bar{y}\bar{y}}$ is associated with the dipole stress $Q_{\bar{y}}$ per unit length as shown in the Figure 2-8. The stresses and displacements at a point $r(x, y)$ in the plane *xy* due to this dipole stress is obtained by applying Eq. 2.26 to Eq. 2.24, which yields

$$\begin{aligned} &u_x = Q_{\bar{y}} \frac{\partial h_{12}}{\partial \bar{y}},\ u_y = Q_{\bar{y}} \frac{\partial h_{22}}{\partial \bar{y}} \\ &\sigma_{xx} = Q_{\bar{y}} \frac{\partial I_{12}}{\partial \bar{y}}, \sigma_{yy} = Q_{\bar{y}} \frac{\partial I_{22}}{\partial \bar{y}}, \sigma_{xy} = Q_{\bar{y}} \frac{\partial I_{32}}{\partial \bar{y}} \end{aligned} \tag{2.29}$$

However, the dipole stress $Q_{\bar{y}}$ will induce contraction strain ($e_{\bar{x}\bar{x}}$) in the $\bar{x}$ direction and shear strain ($e_{\bar{x}\bar{y}}$) according to Eq. 2.17. To cancel the induced strain $e_{\bar{x}\bar{x}}$, we introduce another dipole stress of intensity $Q_{\bar{x}}$ in the $\bar{x}$ direction as shown in Figure 2-8. From Eq. 2.18, if $e_{\bar{x}\bar{x}}, e_{\bar{x}\bar{y}} = 0$, $Q_{\bar{x}}$ is related to $Q_{\bar{y}}$ through elastic constants as

$$Q_{\bar{x}} = \frac{\bar{c}_{12}}{\bar{c}_{22}} Q_{\bar{y}} \tag{2.30}$$

Now the stresses and displacements at a point $r(x, y)$ in the plane *xy* due to dipole stress $Q_{\bar{x}}$ is obtained using Eqs. 2.24, 2.26& 2.30 which are given Eq. 2.31.

$$\begin{aligned} u_x &= \frac{\bar{c}_{12}}{\bar{c}_{22}} Q_{\bar{y}} \frac{\partial h_{11}}{\partial \bar{x}}, \; u_y = \frac{\bar{c}_{12}}{\bar{c}_{22}} Q_{\bar{y}} \frac{\partial h_{21}}{\partial \bar{x}} \\ \sigma_{xx} &= \frac{\bar{c}_{12}}{\bar{c}_{22}} Q_{\bar{y}} \frac{\partial I_{11}}{\partial \bar{x}}, \sigma_{yy} = \frac{\bar{c}_{12}}{\bar{c}_{22}} Q_{\bar{y}} \frac{\partial I_{21}}{\partial \bar{x}}, \sigma_{xy} = \frac{\bar{c}_{12}}{\bar{c}_{22}} Q_{\bar{y}} \frac{\partial I_{31}}{\partial \bar{x}} \end{aligned} \tag{2.31}$$

Similarly, to cancel out induced shear strain ($e_{\bar{x}\bar{y}}$), we must consider two shear dipoles stresses $S_{\bar{x}}$ and $S_{\bar{y}}$ (note that two shear dipoles must be acting together as a single shear dipole would cause rotation of a stress element) acting on the slit as shown in Figure 2-8. The stresses and displacements at a point $r(x, y)$ in the plane *xy* due to the these two dipole stresses are

$$\begin{aligned} u_x &= S_{\bar{x}} \frac{\partial h_{11}}{\partial \bar{y}} + S_{\bar{y}} \frac{\partial h_{12}}{\partial \bar{x}} \\ u_y &= S_{\bar{x}} \frac{\partial h_{21}}{\partial \bar{y}} + S_{\bar{y}} \frac{\partial h_{22}}{\partial \bar{x}} \\ \sigma_{xx} &= S_{\bar{x}} \frac{\partial I_{11}}{\partial \bar{y}} + S_{\bar{y}} \frac{\partial I_{12}}{\partial \bar{x}} \\ \sigma_{yy} &= S_{\bar{x}} \frac{\partial I_{21}}{\partial \bar{y}} + S_{\bar{y}} \frac{\partial I_{22}}{\partial \bar{x}} \\ \sigma_{xy} &= S_{\bar{x}} \frac{\partial I_{31}}{\partial \bar{y}} + S_{\bar{y}} \frac{\partial I_{32}}{\partial \bar{x}} \end{aligned} \tag{2.32}$$

From Eq. 2.18, if $e_{\bar{x}\bar{x}}, e_{\bar{x}\bar{y}} = 0$, the shear dipole stress $S_{\bar{x}}$ is related to normal dipole stress $Q_{\bar{y}}$ as

$$S_{\bar{x}} = \frac{\bar{c}_{26}}{\bar{c}_{22}} Q_{\bar{y}} \tag{2.33}$$

Due to rotational equilibrium, the shear dipole stress $S_{\bar{y}}$ must be equal to $S_{\bar{x}}$. Substituting Eq. 2.33 in Eq. 2.32 gives

$$\begin{aligned}
u_x &= \frac{\bar{c}_{26}}{\bar{c}_{22}} Q_{\bar{y}} \frac{\partial h_{11}}{\partial \bar{y}} + \frac{\bar{c}_{26}}{\bar{c}_{22}} Q_{\bar{y}} \frac{\partial h_{12}}{\partial \bar{x}} \\
u_y &= \frac{\bar{c}_{26}}{\bar{c}_{22}} Q_{\bar{y}} \frac{\partial h_{21}}{\partial \bar{y}} + \frac{\bar{c}_{26}}{\bar{c}_{22}} Q_{\bar{y}} \frac{\partial h_{22}}{\partial \bar{x}} \\
\sigma_{xx} &= \frac{\bar{c}_{26}}{\bar{c}_{22}} Q_{\bar{y}} \frac{\partial I_{11}}{\partial \bar{y}} + \frac{\bar{c}_{26}}{\bar{c}_{22}} Q_{\bar{y}} \frac{\partial I_{12}}{\partial \bar{x}} \\
\sigma_{yy} &= \frac{\bar{c}_{26}}{\bar{c}_{22}} Q_{\bar{y}} \frac{\partial I_{21}}{\partial \bar{y}} + \frac{\bar{c}_{26}}{\bar{c}_{22}} Q_{\bar{y}} \frac{\partial I_{22}}{\partial \bar{x}} \\
\sigma_{xy} &= \frac{\bar{c}_{26}}{\bar{c}_{22}} Q_{\bar{y}} \frac{\partial I_{31}}{\partial \bar{y}} + \frac{\bar{c}_{26}}{\bar{c}_{22}} Q_{\bar{y}} \frac{\partial I_{32}}{\partial \bar{x}}
\end{aligned} \tag{2.34}$$

Finally, the stresses and displacements at a point $r(x, y)$ due to dipole stresses $Q_{\bar{x}}, Q_{\bar{y}}, S_{\bar{x}}$ and $S_{\bar{y}}$ is obtained by combining Eqs. 2.29, 2.31& 2.34, which yields

$$\begin{aligned}
u_x &= Q_{\bar{y}} \frac{\partial h_{12}}{\partial \bar{y}} + \frac{\bar{c}_{12}}{\bar{c}_{22}} Q_{\bar{y}} \frac{\partial h_{11}}{\partial \bar{x}} + \frac{\bar{c}_{26}}{\bar{c}_{22}} Q_{\bar{y}} \frac{\partial h_{11}}{\partial \bar{y}} + \frac{\bar{c}_{26}}{\bar{c}_{22}} Q_{\bar{y}} \frac{\partial h_{12}}{\partial \bar{x}} \\
u_y &= Q_{\bar{y}} \frac{\partial h_{22}}{\partial \bar{y}} + \frac{\bar{c}_{12}}{\bar{c}_{22}} Q_{\bar{y}} \frac{\partial h_{21}}{\partial \bar{x}} + \frac{\bar{c}_{26}}{\bar{c}_{22}} Q_{\bar{y}} \frac{\partial h_{21}}{\partial \bar{y}} + \frac{\bar{c}_{26}}{\bar{c}_{22}} Q_{\bar{y}} \frac{\partial h_{22}}{\partial \bar{x}} \\
\sigma_{xx} &= Q_{\bar{y}} \frac{\partial I_{12}}{\partial \bar{y}} + \frac{\bar{c}_{12}}{\bar{c}_{22}} Q_{\bar{y}} \frac{\partial I_{11}}{\partial \bar{x}} + \frac{\bar{c}_{26}}{\bar{c}_{22}} Q_{\bar{y}} \frac{\partial I_{11}}{\partial \bar{y}} + \frac{\bar{c}_{26}}{\bar{c}_{22}} Q_{\bar{y}} \frac{\partial I_{12}}{\partial \bar{x}} \\
\sigma_{yy} &= Q_{\bar{y}} \frac{\partial I_{22}}{\partial \bar{y}} + \frac{\bar{c}_{12}}{\bar{c}_{22}} Q_{\bar{y}} \frac{\partial I_{21}}{\partial \bar{x}} + \frac{\bar{c}_{26}}{\bar{c}_{22}} Q_{\bar{y}} \frac{\partial I_{21}}{\partial \bar{y}} + \frac{\bar{c}_{26}}{\bar{c}_{22}} Q_{\bar{y}} \frac{\partial I_{22}}{\partial \bar{x}} \\
\sigma_{xy} &= Q_{\bar{y}} \frac{\partial I_{32}}{\partial \bar{y}} + \frac{\bar{c}_{12}}{\bar{c}_{22}} Q_{\bar{y}} \frac{\partial I_{31}}{\partial \bar{x}} + \frac{\bar{c}_{26}}{\bar{c}_{22}} Q_{\bar{y}} \frac{\partial I_{31}}{\partial \bar{y}} + \frac{\bar{c}_{26}}{\bar{c}_{22}} Q_{\bar{y}} \frac{\partial I_{32}}{\partial \bar{x}}
\end{aligned} \tag{2.35}$$

As a second step, consider the following boundary condition at point 1 on the slit.

$$e_{\bar{i}\bar{j}} = 0,\ e_{\bar{x}\bar{y}} \neq 0 \tag{2.36}$$

Let $S_{\bar{x}}$ and $S_{\bar{y}}$ are the two shear dipole stresses associated with the shear strain $e_{\bar{x}\bar{y}}$. Due to rotational equilibrium $S_{\bar{x}}$ must be equal to $S_{\bar{y}}$. Following the procedure described above, the displacements and stresses at a point $r(x, y)$ due to these two shear dipole stresses can be expressed as

$$\begin{aligned}
u_x &= S_{\bar{x}} \frac{\partial h_{11}}{\partial \bar{y}} + S_{\bar{x}} \frac{\partial h_{12}}{\partial \bar{x}} \\
u_y &= S_{\bar{x}} \frac{\partial h_{21}}{\partial \bar{y}} + S_{\bar{x}} \frac{\partial h_{22}}{\partial \bar{x}} \\
\sigma_{xx} &= S_{\bar{x}} \frac{\partial I_{11}}{\partial \bar{y}} + S_{\bar{x}} \frac{\partial I_{12}}{\partial \bar{x}} \\
\sigma_{yy} &= S_{\bar{x}} \frac{\partial I_{21}}{\partial \bar{y}} + S_{\bar{x}} \frac{\partial I_{22}}{\partial \bar{x}} \\
\sigma_{xy} &= S_{\bar{x}} \frac{\partial I_{31}}{\partial \bar{y}} + S_{\bar{x}} \frac{\partial I_{32}}{\partial \bar{x}}
\end{aligned} \tag{2.37}$$

The shear dipole stresses will induce normal strains $e_{\bar{x}\bar{x}}$ and $e_{\bar{y}\bar{y}}$ according to stress-strain relationship (Eq. 2.17). Therefore, to cancel out these strains, additional dipole stresses must be imposed. In order to nullify $e_{\bar{x}\bar{x}}$, dipole stress $Q_{\bar{x}}$ is imposed as in Figure 2-8. From Eq. 2.18, if $e_{\bar{x}\bar{x}}, e_{\bar{y}\bar{y}} = 0$, then $Q_{\bar{x}}$ is related to $S_{\bar{x}}$ as follows

$$Q_{\bar{x}} = \frac{\bar{c}_{16}}{\bar{c}_{66}} S_{\bar{x}} \tag{2.38}$$

In the same manner, to nullify $e_{\bar{y}\bar{y}}$, the dipole stress $Q_{\bar{y}}$ is applied as shown in Figure 2-8. From stress-strain relations in Eq. 2.18, $Q_{\bar{y}}$ is related to $S_{\bar{x}}$ as

$$Q_{\bar{y}} = \frac{\bar{c}_{26}}{\bar{c}_{66}} S_{\bar{x}} \tag{2.39}$$

Now, the stresses and displacements at an arbitrary point in the plane *xy* due to the dipole stresses, $Q_{\bar{x}}$ and $Q_{\bar{y}}$ can be written as (using Eqs. 2.37, 2.38& 2.39)

$$
\begin{aligned}
u_x &= \frac{\bar{c}_{16}}{\bar{c}_{66}} S_{\bar{x}} \frac{\partial h_{11}}{\partial \bar{x}} + \frac{\bar{c}_{26}}{\bar{c}_{66}} S_{\bar{x}} \frac{\partial h_{12}}{\partial \bar{y}} + S_{\bar{x}} \frac{\partial h_{11}}{\partial \bar{y}} + S_{\bar{x}} \frac{\partial h_{12}}{\partial \bar{x}} \\
u_y &= \frac{\bar{c}_{16}}{\bar{c}_{66}} S_{\bar{x}} \frac{\partial h_{21}}{\partial \bar{x}} + \frac{\bar{c}_{26}}{\bar{c}_{66}} S_{\bar{x}} \frac{\partial h_{22}}{\partial \bar{y}} + S_{\bar{x}} \frac{\partial h_{21}}{\partial \bar{y}} + S_{\bar{x}} \frac{\partial h_{22}}{\partial \bar{x}} \\
\sigma_{xx} &= \frac{\bar{c}_{16}}{\bar{c}_{66}} S_{\bar{x}} \frac{\partial I_{11}}{\partial \bar{x}} + \frac{\bar{c}_{26}}{\bar{c}_{66}} S_{\bar{x}} \frac{\partial I_{12}}{\partial \bar{y}} + S_{\bar{x}} \frac{\partial I_{11}}{\partial \bar{y}} + S_{\bar{x}} \frac{\partial I_{12}}{\partial \bar{x}} \\
\sigma_{yy} &= \frac{\bar{c}_{16}}{\bar{c}_{66}} S_{\bar{x}} \frac{\partial I_{21}}{\partial \bar{x}} + \frac{\bar{c}_{26}}{\bar{c}_{66}} S_{\bar{x}} \frac{\partial I_{22}}{\partial \bar{y}} + S_{\bar{x}} \frac{\partial I_{21}}{\partial \bar{y}} + S_{\bar{x}} \frac{\partial I_{22}}{\partial \bar{x}} \\
\sigma_{xy} &= \frac{\bar{c}_{16}}{\bar{c}_{66}} S_{\bar{x}} \frac{\partial I_{31}}{\partial \bar{x}} + \frac{\bar{c}_{26}}{\bar{c}_{66}} S_{\bar{x}} \frac{\partial I_{32}}{\partial \bar{y}} + S_{\bar{x}} \frac{\partial I_{31}}{\partial \bar{y}} + S_{\bar{x}} \frac{\partial I_{32}}{\partial \bar{x}}
\end{aligned}
\qquad (2.40)
$$

In order to establish relation between dipole stresses and displacement discontinuities, we follow the two step procedure described above (i.e. separating the normal and shear strain components). In the first step, we assume all strain components are zero except $e_{\bar{y}\bar{y}}$ (Eq. 2.28). For this condition, using stress strain relationship (Eq. 2.18), the normal strain $e_{\bar{y}\bar{y}}$ can be related to normal stress $\sigma_{\bar{y}\bar{y}}$ as

$$\sigma_{\bar{y}\bar{y}} = \bar{c}_{22} e_{\bar{y}\bar{y}} \qquad (2.41)$$

For unit stress element, Eq. 2.41 is equivalent to

$$Q_{\bar{y}} = \bar{c}_{22} D_{\bar{y}} \qquad (2.42)$$

where $D_{\bar{y}}$ is called normal displacement discontinuity which represents difference between the displacements of the opposite surfaces of the slit at point 1 in the direction $\bar{y}$.

Similarly, considering the boundary condition from Eq. 2.36 and stress strain relationship from Eq. 2.18, shear dipole stress $S_{\bar{x}}$ can be related to shear displacement discontinuity $D_{\bar{x}}$ as

$$S_{\bar{x}} = \bar{c}_{66} D_{\bar{x}} \tag{2.43}$$

Substituting Eqs. 2.42& 2.43 into Eqs. 2.35& 2.40 and using superposition, the stresses and displacements in the plane *xy* are given as

$$\begin{aligned}
u_x &= D_{\bar{x}} \left(\int_{-a}^{a} u_{x,s}(\bar{x}-\varepsilon, \bar{y})\, \mathrm{d}\varepsilon \right) + D_{\bar{y}} \left(\int_{-a}^{a} u_{x,n}(\bar{x}-\varepsilon, \bar{y})\, \mathrm{d}\varepsilon \right) \\
u_y &= D_{\bar{x}} \left(\int_{-a}^{a} u_{y,s}(\bar{x}-\varepsilon, \bar{y})\, \mathrm{d}\varepsilon \right) + D_{\bar{y}} \left(\int_{-a}^{a} u_{y,s}(\bar{x}-\varepsilon, \bar{y})\, \mathrm{d}\varepsilon \right) \\
\sigma_{xx} &= D_{\bar{x}} \left(\int_{-a}^{a} \sigma_{xx,s}(\bar{x}-\varepsilon, \bar{y})\, \mathrm{d}\varepsilon \right) + D_{\bar{y}} \left(\int_{-a}^{a} \sigma_{xx,n}(\bar{x}-\varepsilon, \bar{y})\, \mathrm{d}\varepsilon \right) \\
\sigma_{yy} &= D_{\bar{x}} \left(\int_{-a}^{a} \sigma_{yy,s}(\bar{x}-\varepsilon, \bar{y})\, \mathrm{d}\varepsilon \right) + D_{\bar{y}} \left(\int_{-a}^{a} \sigma_{yy,s}(\bar{x}-\varepsilon, \bar{y})\, \mathrm{d}\varepsilon \right) \\
\sigma_{xy} &= D_{\bar{x}} \left(\int_{-a}^{a} \sigma_{xy,s}(\bar{x}-\varepsilon, \bar{y})\, \mathrm{d}\varepsilon \right) + D_{\bar{y}} \left(\int_{-a}^{a} \sigma_{xy,n}(\bar{x}-\varepsilon, \bar{y})\, \mathrm{d}\varepsilon \right)
\end{aligned} \tag{2.44}$$

In the above equations the integrals are evaluated analytically and the subscripts *n* (normal) and *s* (shear) are adopted to distinguish between the induced stress and displacement contributions from normal and shear displacement discontinuities. Finally, the problem is posed by discretizing the boundary of interest into N small linear elements of length 2a. The fundamental solution for each element is superimposed such that the specified (stress/displacement) boundary condition is satisfied at all the elements. This procedure will result in linear system of equations with 2N unknowns corresponding to induced stresses or displacements as in Eq. 2.45.

$$\begin{aligned}
\overset{i}{u}_s &= \sum_{j=1}^{N} \overset{ij}{B}_{ss} \overset{j}{D}_s + \sum_{j=1}^{N} \overset{ij}{B}_{sn} \overset{j}{D}_n \\
\overset{i}{u}_n &= \sum_{j=1}^{N} \overset{ij}{B}_{ns} \overset{j}{D}_s + \sum_{j=1}^{N} \overset{ij}{B}_{nn} \overset{j}{D}_n \\
\overset{i}{\sigma}_s &= \sum_{j=1}^{N} \overset{ij}{A}_{ss} \overset{j}{D}_s + \sum_{j=1}^{N} \overset{ij}{A}_{sn} \overset{j}{D}_n \\
\overset{i}{\sigma}_n &= \sum_{j=1}^{N} \overset{ij}{A}_{ns} \overset{j}{D}_s + \sum_{j=1}^{N} \overset{ij}{A}_{nn} \overset{j}{D}_n
\end{aligned} \tag{2.45}$$

The coefficients $\overset{ij}{A}_{ss}$, $\overset{ij}{B}_{ss}$ etc. are called influence functions for stresses and displacements. For example, $\overset{ij}{A}_{ss}$ gives shear stress at *i*th element due to unit shear displacement discontinuity at *j*th element. By specifying the known values of stresses or displacements at each element on the boundary, the unknown normal and shear displacement discontinuities can be found by solving the 2N system of equations in Eq. 2.45. The evaluated displacement discontinuities can then be used to find stress or displacement distribution in the material. Note that due to the sign convention followed for displacements (i.e. displacements are positive for material points that move in the direction of positive axis), the positive normal displacement discontinuity indicates slit surfaces move towards each other while negative normal displacement discontinuity indicates slit surfaces move away from each other similar to the convention adopted in Crouch and Starfield, (1983).

Note that assuming constant displacement discontinuities over the entire length of an element can give erroneous results for fracture opening and ride near the tips. According to linear elastic fracture mechanics, near the fracture tip, opening and ride various (Barenblatt, 1962) in the order $r^{1/2}$, where r is distance measured from the fracture tip (the near tip behavior of a fracture will be discussed in detail in the upcoming chapters). Although one can incorporate this effect in the solution of displacement discontinuity method by discretizing fracture tip regions into very fine size elements, such a procedure is not a complete remedy and moreover it is computationally expensive. Therefore, in order to improve the accuracy of displacement discontinuities near the fracture tips, we use displacement discontinuity elements with a square root shape function shown in Eq. 2.46.

$$D_{\bar{y},t} = D_{\bar{y}}\left(\frac{\xi + a}{a}\right)^{1/2}$$
$$D_{\bar{x},t} = D_{\bar{x}}\left(\frac{\xi + a}{a}\right)^{1/2} \qquad (2.46)$$

where $D_{\bar{y}}$ and are normal and shear displacement discontinues respectively at the mid points of the fracture tip elements, and $D_{\bar{y},t}$ and $D_{\bar{x},t}$ represent normal and displacement discontinuity variation over the element of length 2*a*. ξ is distance along the fracture tip element which is measured from origin *o* and is taken positive in the direction of positive $\bar{x}$ axis. Now, the influence functions for tip elements can be obtained by replacing constant displacement discontinuities $D_{\bar{y}}$ and $D_{\bar{y}}$ in Eq. 2.44 with $D_{\bar{y},t}$ and $D_{\bar{x},t}$ from Eq. 2.46 and subsequent numerical integration. Finally, it should be noted that Eq. 2.45 is applicable to both plane strain and plane stress problem, simply by altering the material constants $\bar{c}_{ij}$ which are listed in Appendix A.

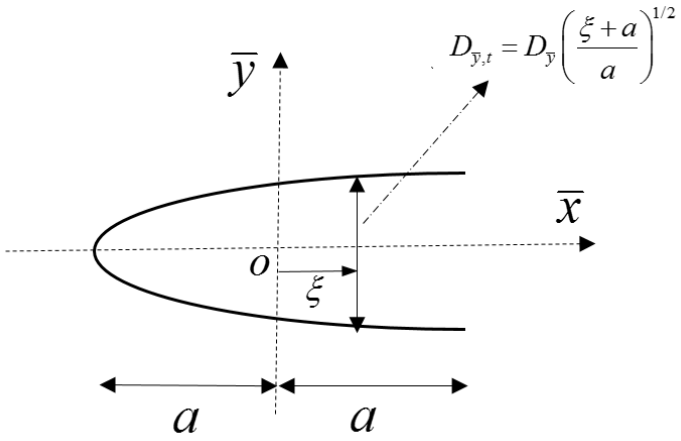

Figure 0-9. Fracture tip element with square root variation of displacement discontinuities.

2.7 Fictitious Stress Method

In problems pertaining to large excavations, tunnels and cavities (such as wellbore), tangential stresses on the boundary walls is one of the primary components of the solution to evaluate failure. Although displacement discontinuity method can be employed to solve such problems, however,

in order to evaluate tangential stresses on the boundaries, it is required to calculate derivatives of the tangential displacement components, which can affect accuracy of the computed results. For these problems, a more suitable boundary element method is fictitious stress method where evaluation of tangential stresses on the boundaries is straightforward (note that fictitious stress method cannot model thin slits/cracks due to its inability to distinguish between two opposing surfaces). The fictitious stress method for an isotropic elastic material is developed using fundamental solution for concentrated line force in an infinite isotropic elastic material. Analogously it is extended to orthotropic material using the fundamental solution for line force in an orthotropic material. Similar to displacement discontinuity method, in fictitious method the boundary of interest is discretized into small elements where singularities (i.e. fictitious stresses) are distributed such that the boundary condition on each element is satisfied. Unlike displacements discontinuities which represent relative displacement of crack surfaces in normal and tangential directions, the fictitious stresses as the name indicates does not have any physical meaning. The influence coefficients for fictitious stress method for both isotropic and orthotropic materials can be found in Crouch and Starfield, (1983), therefore not repeated here.

If we consider an infinite orthotropic elastic material with *1-2-3* as material's axes of elastic symmetry containing a cavity '*c*' and a fracture '*f*' as shown in the Figure 2-10. If the boundary of the cavity '*c*' is discretized into *M* line elements and fractures '*f*' into *N* line elements, then using superposition the induced normal (σ_n^i) and shear (σ_s^i) stresses acting on the surface of each element can be expressed as (Crouch and Starfield, 1983)

$$\begin{aligned}\sigma_n^i &= \sum_{j=1}^{M}(A_{ns}^{ij}P_s^j + A_{nn}^{ij}P_n^j) + \sum_{j=M+1}^{M+N}(A_{ns}^{ij}D_s^j + A_{nn}^{ij}D_n^j)\\ \sigma_s^i &= \sum_{j=1}^{M}(A_{ss}^{ij}P_s^j + A_{sn}^{ij}P_n^j) + \sum_{j=M+1}^{M+N}(A_{ss}^{ij}D_s^j + A_{sn}^{ij}D_n^j) \quad (i=1,M+N),\end{aligned} \tag{2.47}$$

where the terms P_n, P_s represent fictitious stresses acting on the surface of the cavity 'c' and D_n, D_s represent displacement discontinuities of fracture elements. The terms A_{ns}^{ij}, etc., are boundary stress influence coefficients which give normal/shear stress at the midpoint of i^{th} element due to the unit fictitious stress or displacement discontinuity at j^{th} element. Their expressions for, $1 \le j \le M$ can be found in Crouch and Starfield, (1983) and for, $M+1 \le j \le N$ are given above in Eq. 2.44. The linear combination of the influences of the fictitious stresses and the displacement discontinuities gives stresses on any given cavity/fracture element or at any point in the material. Numerical simulations relating to this geometry will be discussed in detail in the subsequent chapters.

2.8 Verification of anisotropic displacement discontinuity method

The anisotropic displacement discontinuity (ADDM) method is verified against analytical plane strain solution (Azhdari et al., 1999) for a problem of line fracture subjected to uniform far-field tension and shear. For verification purpose two different cases are considered. In Case-1, the line fracture is subjected to only far-field tensile stress (σ_{xx}) of magnitude 1 MPa perpendicular to fracture surface (see Figure 2-10). Whereas in Case-2, the line fracture is subjected to only far-field shear stress (σ_{xy}) of magnitude 1 MPa. The two axes of elastic symmetry in the plane *xy* are represent by 1 and 2 and they can be rotated in the plane *xy*. The angle of axis 1 with respect to axis *x* is given by ψ degrees. Figure 2-11 shows the comparison between fracture normal opening and fracture ride along axis *y* obtained from analytical plane strain solution and ADDM, for a line fracture of length 1 m for the cases 1 and 2 and for two different ψ of 0^0 and 45^0. The material is orthotropic and its elastic constants are given in Table 2-1 (note that these values do not belong to any specific material, they are chosen for the purpose of ADDM verification). In the numerical

model, the fracture length along *y*-axis is discretized into 50 equal sized elements and square root elements (see Figure 2-9) are used at fracture tips. The results indicate excellent match between ADDM and analytical solution.

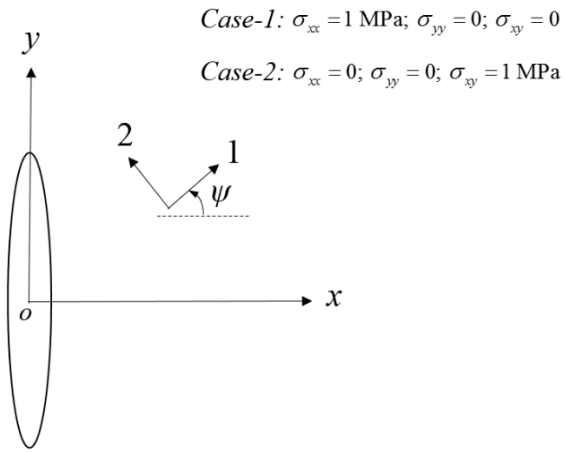

Figure 0-10. *xy* plane strain consideration of a line fracture in an infinite orthotropic material. 1 and 2 are axes of elastic symmetry and ψ is angle between axis 1 and axis *x*.

Table 0-1. Elastic constants for orthotropic material.

E_1	E_2	E_3	G_{12}	ν_{21}	ν_{32}	ν_{31}
40 MPa	25 MPa	10 MPa	7.5 MPa	0.12	0.18	0.05

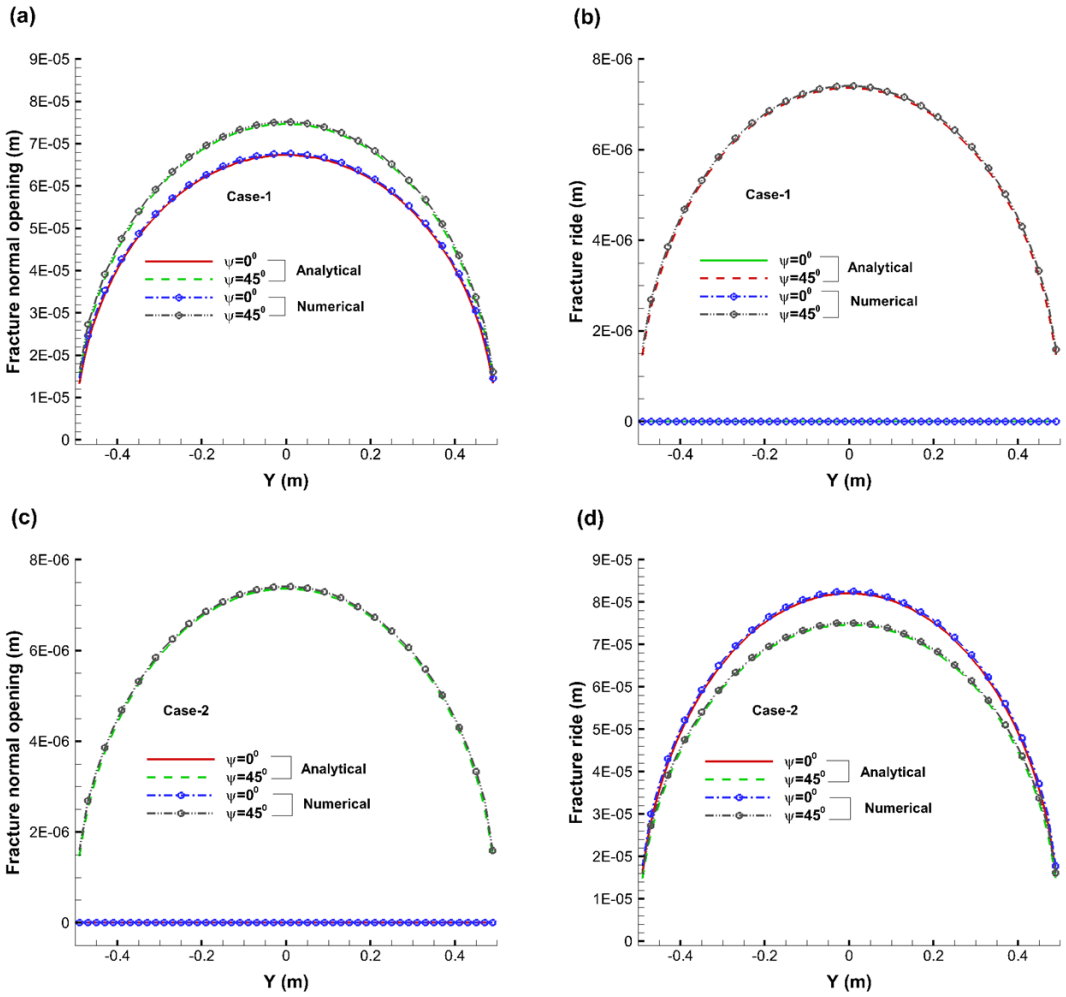

Figure 0-11. Comparison between analytical (Azhdari et al., 1999) and numerical ADDM solutions for fracture normal opening and fracture ride along axis *y* for cases 1 and 2 and for different ψ (see Figure 11).

2.9 Verification of Anisotropic Fictitious Stress Method

Anisotropic fictitious stress method is verified by comparing the numerical results with analytical solution of the circular hole in an infinite elastic orthotropic plane under uniaxial tension at infinity given by Green and Taylor (1945). The problem is considered in plane stress with material properties for spruce board given in Table 2-2. The problem is solved for both cases of tension applied parallel and perpendicular to the axis y (see inset in Figure 2-12). The circular hole is

discretized into 100 equal sized elements. The numerically obtained tangential stresses at the wall of circular hole and stresses along the axes parallel and perpendicular to the direction of applied tension are compared with the analytical solution in Figures 2-12& 2-13. The results indicate excellent agreement between numerical and analytical solution.

Table 0-2. Elastic constants for spruce board.

E_x	E_y	G_{xy}	ν_{xy}
645.16 KPa	17035.77 KPa	869.57 KPa	0.0213

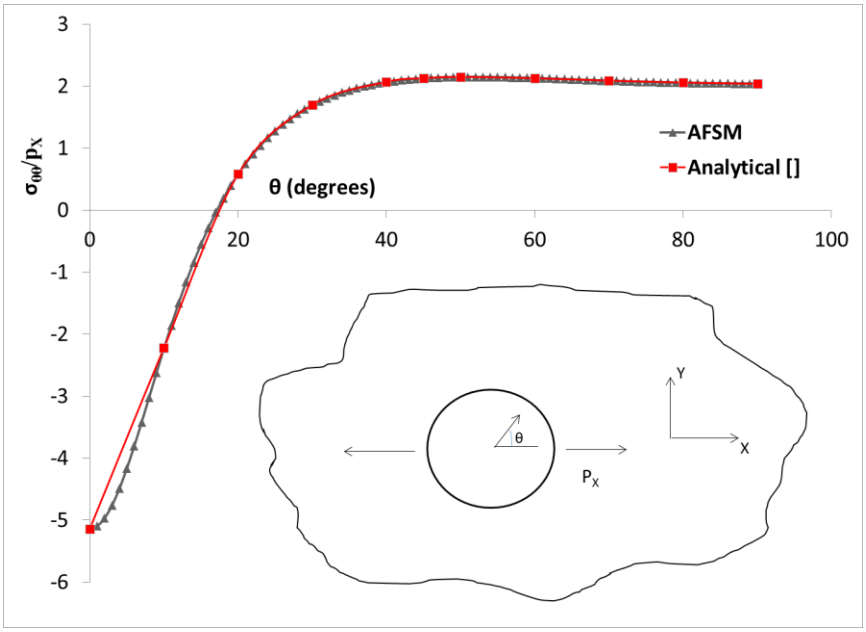

Figure 0-12. Comparison of tangential stresses between analytical solution [12] and AFSM along the wall of the cavity in the spruce board when tension is applied perpendicular to the grains.

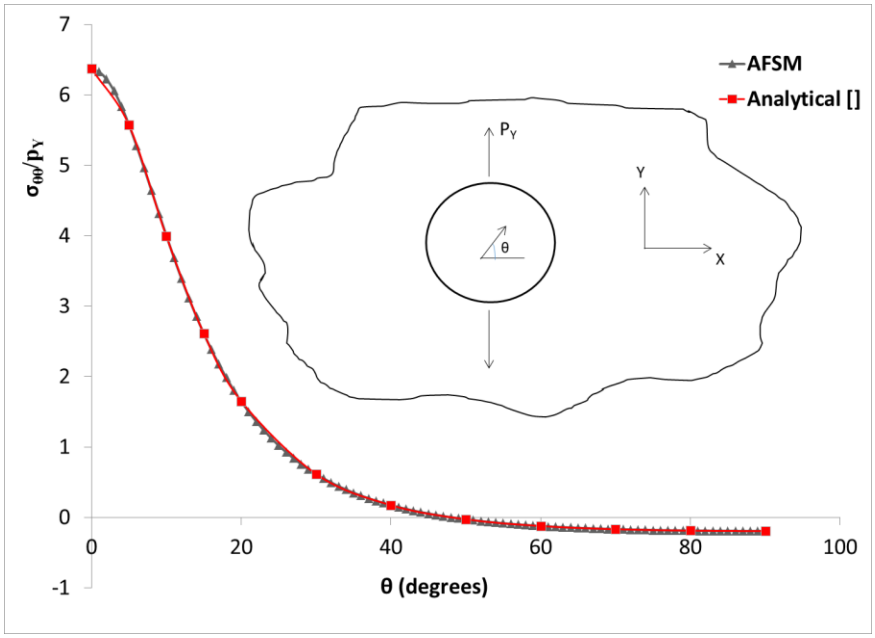

Figure 0-13. Comparison of tangential stresses between analytical solution and AFSM along the wall of the cavity in the spruce board when tension is applied parallel to the axis *y*.

3 Effect of Rock Anisotropy on Induced Stresses and Displacements around a Fracture

In this chapter we study the effect of rock anisotropy on fracture opening, induced stresses and displacements around a pressurized fracture. Consider a transversely isotropic rock with planes of isotropy (planes 1-3) tilted at an angle ϕ with respect to the horizontal plane X-Y as indicated in the Figure 3-1a. Suppose *'f'* is a rectangular fracture with height H (parallel to the vertical principal stress σ_V or axis Z) and length L (parallel to the maximum horizontal principal stress σ_H or axis X). It is assumed that the height of the fracture *'f'* is contained to the reservoir layer thickness, H, due to the stress barriers acting in the outer layers (Warpinski et al., 1982; Teufel and Clark, 1984) and that the fracture propagates only along its length. Under this scenario (when $L/H \gg 1$) it is appropriate to consider plane strain (YZ plane). Figure 3-1b shows YZ- plane view of Figure 11a with origin located at the midpoint of fracture height H.

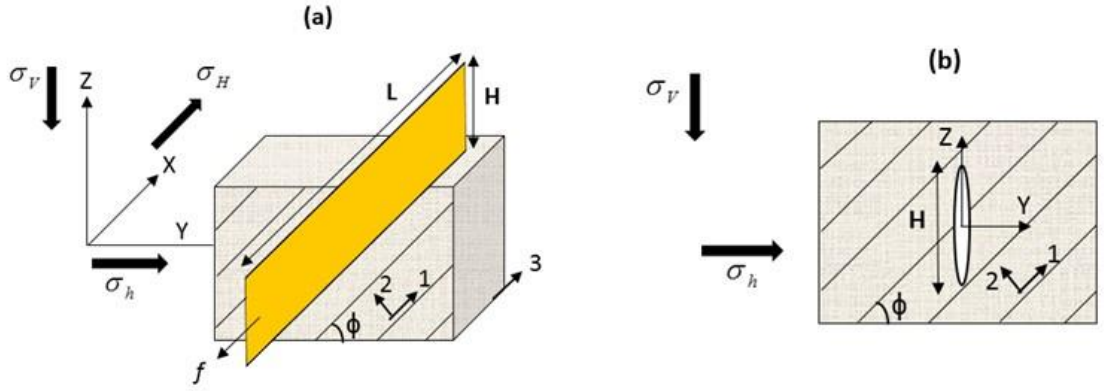

Figure 0-14. (a) Transversely isotropic body with bedding planes tilting at ϕ . 'f' is a vertical fracture with height H and length L, where, $L/H \gg 1$, (b) the Z-Y plane view of Figure 11a.

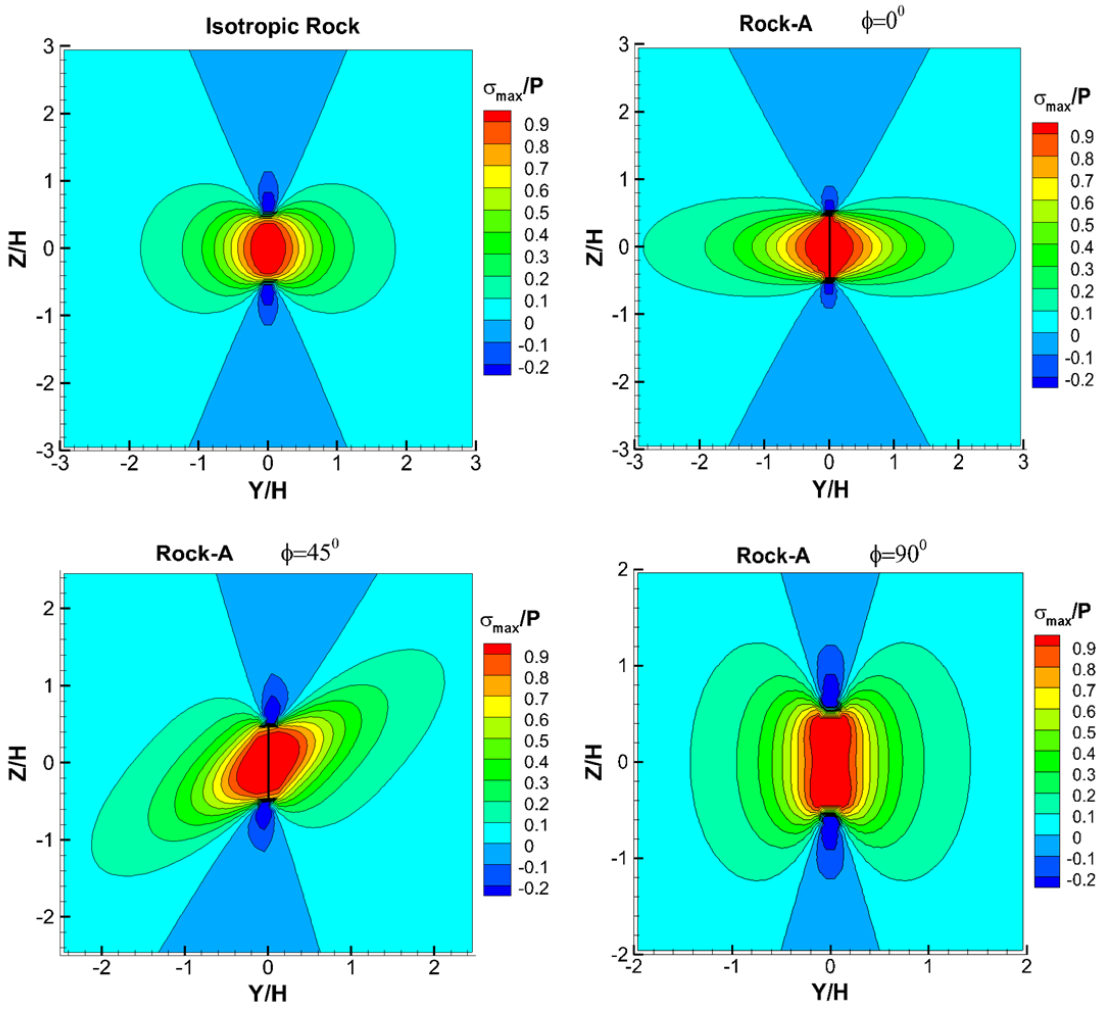

Figure 0-15. Normalized local maximum principal stress distribution in Rock-A around a vertical fracture (in the plane Z-Y, see Figure-11b) with an internal net pressure (P) for different bedding dip (ϕ).

For numerical analysis, two transversely isotropic rocks Rock-A and Rock-B are considered and will be used throughout this work. Rock-A is an argillaceous shale with a degree of anisotropy (i.e., the ratio of Young's modulus parallel to bedding planes and Young's modulus perpendicular to bedding planes) 4, and its anisotropic elastic constants are listed in Table 3-1. Rock-B is Woodford shale with a degree of anisotropy 1.88, and its anisotropic elastic constants are listed in Table 3-2. The elastic constants given in Tables 3-1& 3-2 are static measurements in a laboratory

on core scale specimens. In the following analysis, to highlight the impact of rock anisotropy, isotropic results are also presented. Isotropic results are obtained using the Young's modulus in the direction of minimum principal horizontal stress and isotropic Poisson's ratio v_{13} assuming that fracture always opens against minimum principal horizontal stress. Considering a single vertical plane strain fracture '*f*' of height H with uniform internal pressure P, the induced stresses and fracture displacement discontinuities are reported for rocks with different anisotropic elastic properties and for different angles (ϕ) of the isotropic planes (i.e., bedding planes) with respect to the vertical fracture.

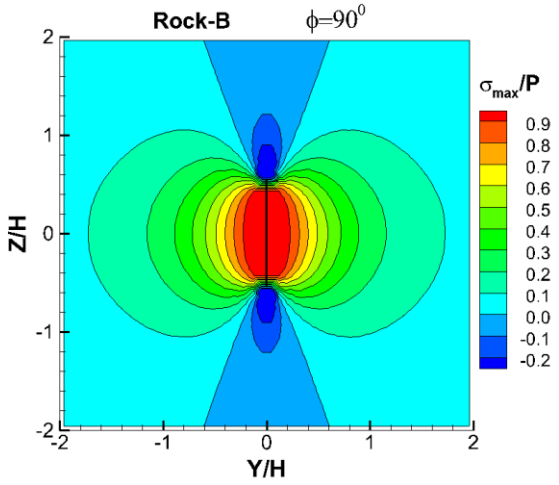

Figure 0-16. Normalized maximum principal stress distribution in Rock-B (lower degree of anisotropy of 1.88) around a vertical fracture (in the plane Z-Y, see Figure-11) with an internal net pressure (P) for dip ϕ =90^0.

Figure 3-2 shows the normalized maximum principal stress curves around the vertical fracture '*f*' (see Figure 3-1a) for different ϕ in Rock-A. The results indicate that if Rock-A is treated as isotropic, these curves appear like circles and the maximum principal stress attains its largest value along the line Z=0 (i.e., passing through the midpoint of fracture height). Considering anisotropy of Rock-A, when ϕ =0^0 (this case corresponds to a vertical fracture in a vertical transversely

isotropic rock, VTI), the principal stress curves appear like ellipses with major axis parallel to the direction of maximum Young's modulus (i.e., E_1). As a result, the stress shadow reach in the direction perpendicular to the fracture surface is larger than isotropic case. Also, the maximum principal stress attains the largest value along the line Z=0 similar to isotropic case. For the case $\phi = 45^0$ (this case corresponds to a vertical fracture in a tilted transversely isotropic rock. TTI), the principal stress curves have a complex shape.

Table 0-3. Properties of Rock-A

E_1 (GPa)	E_3 (GPa)	E_2 (GPa)	ν_{13}	ν_{12}	G_{12} (GPa)	K_{IC} (MPa.m$^{0.5}$)	E_1/E_2
40	40	10	0.15	0.185	7.45	2	4.0

Table 0-4. Properties of Rock-B

E_1 (GPa)	E_3 (GPa)	E_2 (GPa)	ν_{13}	ν_{12}	G_{12} (GPa)	K_{IC} (MPa.m$^{0.5}$)	E_1/E_2
19.6	19.6	10.4	0.166	0.25	5.0	2	1.88

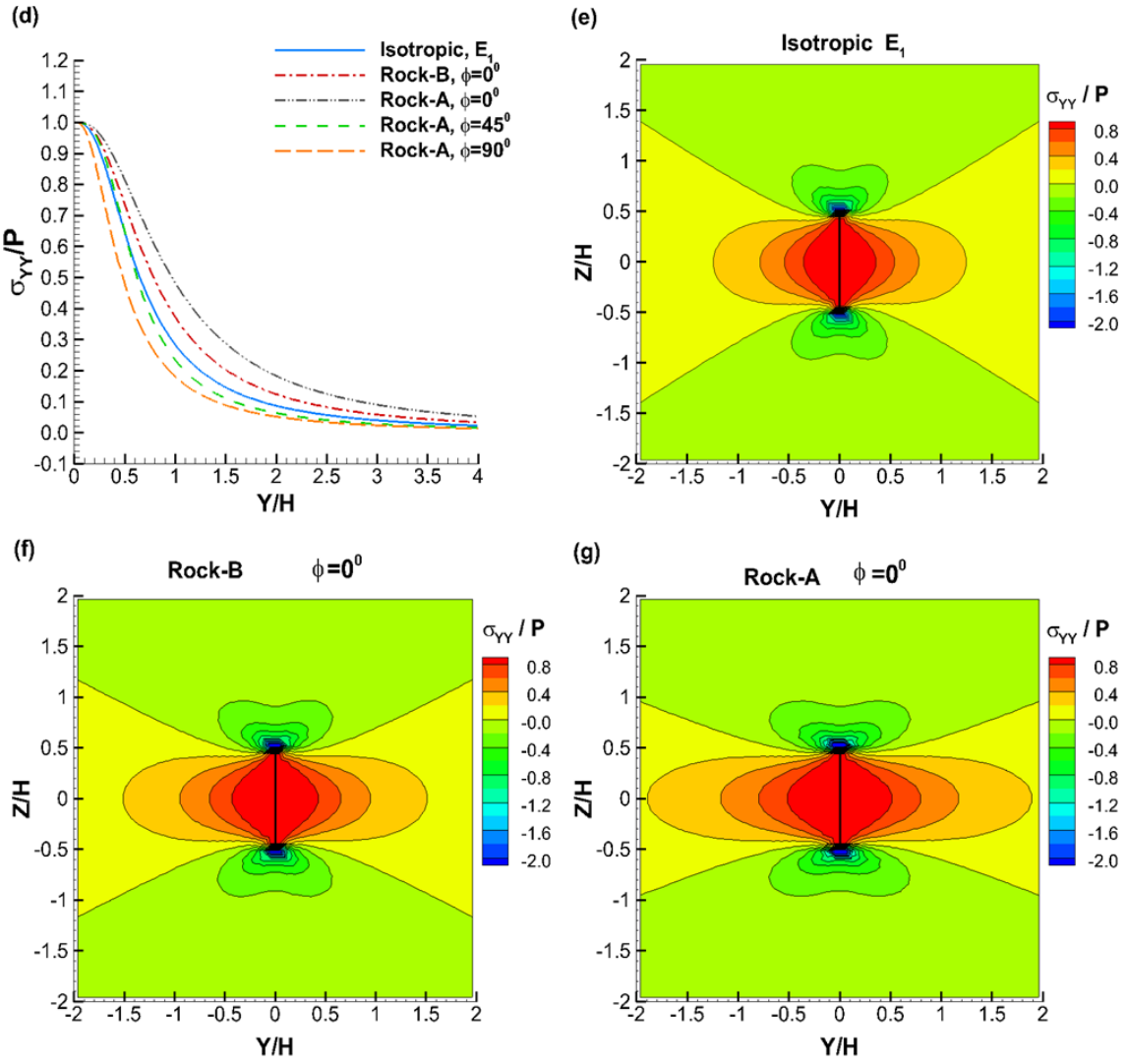

Figure 0-17. Z-Y plane strain analysis of a rectangular fracture (shown in Figure 11) subjected to a constant internal net pressure, P. Normalized induced stress component σ_{YY} , (d) along the line Z=0, (e) in the plane Z-Y for isotropic rock, (f) anisotropy Rock B, (g) anisotropic Rock A.

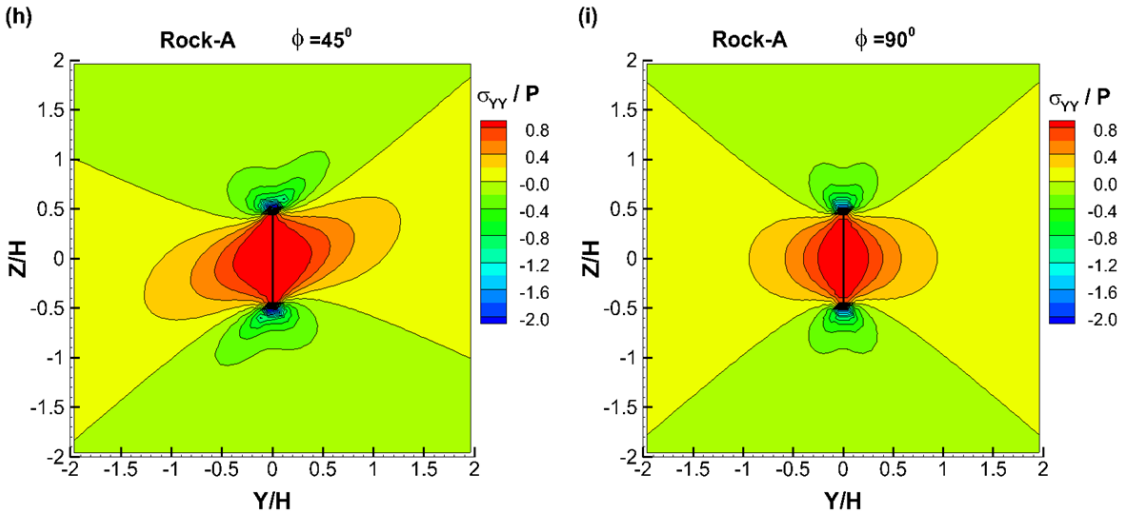

Figure 0-18. (h) For anisotropic Rock A and bedding dip 45^0, (i) anisotropic Rock-A and bedding dip 90^0.

In this case, the largest value of the local maximum principal stress is not attained along the line Z=0. It is oriented towards the direction of the maximum Young's modulus. This can result in asymmetric fracture growth which will be illustrated in the following chapters. When $\phi = 90^0$ (corresponding to a vertical fracture in a horizontal transversely isotropic rock, HTI), very near to the fracture surface, the principal stress curves have a complex shape (near the fracture surface, they appear like butterfly wing and away they become kidney shaped). Similar to the previous case, the largest value of the local maximum principal stress is not attained along the line Z=0. According to Lekhnitskii (1963), the principal stress curves are fourth-order equations (Eq. 3.1) in terms of Y and Z coordinates, with rock elastic constants as coefficients. Depending on the elastic constants, the shape these stress curves can change. For example, in Rock-A when $\phi = 90^0$, the curves appear like ovals as shown in Figure 3-2. However, in Rock-B when $\phi = 90^0$, the curves attain almost circular shape (away from the fracture) and the local maximum principal stress attains its largest value along the line Z=0 according to Figure 3-3 (unlike case of Rock-A).

$$\beta_{11}y^4 + (2\beta_{12} + \beta_{66})y^2z^2 + \beta_{22}y^4 + \frac{P}{\pi}(\mu_1 + \mu_2)\sqrt{\beta_{11}\beta_{22}}(y^2 + z^2)z = 0 \qquad (3.1)$$

Where *y* and *z* are coordinates in plane YZ (see Figure 3-1a), β_{ij} are elastic constants for an anisotropic material and their relationship with engineering constants is given in Eq. (chapter-1). μ_1 and μ_2 are the two complex roots of the characteristic equation (Eq. C.6 in Appendix C) with positive imaginary parts.

Now, the principal stress curves around a plane strain fracture attain their greatest value along the line Z=0 (see Figure 3-1) if

$$2\beta_{12} + \beta_{66} > 1.5\beta_{22}$$
$$or \qquad (3.2)$$
$$2\beta_{12} + \beta_{66} = 1.5\beta_{22},\ 8\beta_{11} - 3\beta_{22} \geq 0$$

From Eqs. 3.1& 3.2, we can see that depending on the elastic constants of the rock, the shape of principal stress curves around a fracture can change. For example, in Rock-B when ϕ =90^0, the principal stress curves attain almost circular shape (away from the fracture) and the maximum principal stress attains its largest value along the line Z=0 according to Figure 3-3 as the properties of Rock-B satisfied Eq. 2. On the other hand in Rock-A when ϕ =90^0, the curves appear like ovals as shown in Figure 3-2, and the greatest value of principal stress around the fracture is no longer along the line Z=0 since the properties of Rock-A did not satisfy Eq. 3.2.

The induced stresses around a fracture influences the propagation of adjacent fractures. The above analysis indicates that rock anisotropy can impact the induced stress state around a fracture significantly. If we consider propagation of multiple parallel fractures interacting with each other (as this is one of the prominent techniques of creating large scale fractures in unconventional

reservoirs), the induced stress components in the direction perpendicular to the fracture surface (i.e., Y component according to Figure 3-1a) plays a prominent role in governing the fracture propagation. Due to this reason in this chapter we restricted our attention to stress component σ_{YY}. The effect of rock anisotropy on other stress components and their role on fracture propagation will be discussed in the following chapters dealing with complex fracture networks.

Figure 3-4d shows normalized values of induced stresses in Y-direction along the line Z=0 for different anisotropic rocks and bedding plane dip ϕ from ZY plane strain analysis of the fracture '*f*' indicated in Figure 3-1 that is subjected to a constant internal net pressure P. The results indicate a gradual increase in σ_{YY} with increase in degree of anisotropy when fracture height is perpendicular to the direction of maximum Young's modulus E_1 (i.e. $\phi = 0^0$). For example at Y=H, the σ_{YY} along the line Z=0 from isotropic approximation is 0.29P. Whereas in the case of anisotropic rock with a degree of anisotropy 1.88 (Rock-B), the σ_{YY} value is 0.38P. For anisotropic rock with a degree of anisotropy 4 (Rock-A), σ_{YY} is increased to 0.49P, a 69% increase over its value for isotropic rock. This effect is reversed with increase in bedding dip. When degree of anisotropy is 4 and bedding plane dip is 45^0, σ_{YY} at Y=H is 0.24P. For vertical bedding ($\phi = 90^0$), σ_{YY} is 0.18P which is 38% decrease over its value for isotropic case. Figures 3-4e-3-5i show distribution of normalized induced stresses in the Y-direction around the vertical fracture '*f*' in the plane ZY. There results clearly indicate an increase in the spatial extent of induced stresses with increase in degree of rock anisotropy when fracture height is perpendicular to the direction of maximum Young's modulus E_1 ($\phi = 0^0$). This is an important finding as the increase in induced stresses perpendicular to the fracture surface can negatively impact the growth of closely spaced

multiple parallel fractures. On the other hand when bedding planes are tilted (ϕ =45^0), the induced stresses perpendicular to the fracture surface rotated towards the direction of maximum Young's modulus as indicated in Figure 3-5h. This is similar to the behavior of maximum principal stress distribution around a fracture in the case of inclined bedding planes as in Figure 3-2. When fracture height is parallel to the direction of maximum Young's modulus E_1 (ϕ =90^0), Figure 3.5i indicates shrinkage in spatial extent of induced σ_{YY} compared to isotropic case.

Figures 3-6a, 3-6b and 3-6c shows dimensionless values of normal displacement discontinuity D_n (i.e. fracture opening) along the fracture Z-axis for different anisotropic rocks and bedding dip angles, obtained from the plane strain (YZ) analysis of the fracture '*f*' (Figure 3-1) that is subjected to a constant internal net pressure P. These results corresponds to the net pressure of 1 MPa. As discussed before, the isotropic solution is obtained by using the Young's modulus parallel to minimum principal stress and isotropic plane Poisson's ratio ν_{13}. Figure 3-6a suggests that when the fracture height is perpendicular to the direction of maximum Young's modulus E_1 (ϕ =0^0), the isotropic approximation underestimates fracture opening. At the midpoint of fracture height (i.e. Z=0), the fracture opening (D_n) from isotropic approximation of Rock A is 4.9E-5*x*H. When rock anisotropy is accounted the fracture opening observed at Z=0 is 7.4E-5*x*H, which is a 51% increase over isotropic approximation. However, this behavior reverses with increase in bedding plane dip as indicated by Figures 3-6b and 3-6c. When bedding planes are dipping at an angle of 45^0, isotropic approximation overestimates the fracture opening at Z=0 by 9% in the Rock A (Figure 3-4b). For a complete vertical bedding (i.e. ϕ =90^0), isotropic solution overestimated fracture opening at Z=0 by 32% in Rock A (Figure 3-6c). It will be shown later that the erroneous estimation of fracture apertures by isotropic model affect both fracture length and height predictions.

Another interesting aspect of rock anisotropy is that a fracture under pure mode-1 loading experiences shear displacement discontinuity (ride) when it is inclined with respect to the rock's axes of elastic symmetry. This behavior is shown in Figure 3-6d, where the fracture ride is zero for the cases $\phi = 0^0$ and 90^0, however, non-zero for the case $\phi = 45^0$ in Rock-A when a vertical plane strain fracture '*f*' is subjected to a constant internal net pressure P (see Figure 3-1a). We can explain this behavior by looking at the displacement plots in the directions Y and Z around the fracture in Rock-A for different ϕ indicated in Figure 3-7 (positive displacements are taken in the direction of positive axes). The results show that when bedding planes are inclined with respect to the fracture height (i.e., $\phi = 45^0$), the points on the negative side of fracture surface (left side) moved upwards (i.e., towards the direction of lower Young's modulus) and the points on the positive side of fracture surface (right side) moved downwards (i.e., towards the direction of lower Young's modulus) resulting in non-zero shear displacement discontinuity or fracture ride. It will be shown later that the non-zero shear ride observed under pure mode-1 loading (as in the example considered in this chapter) does not induce mode-2 stress singularity at the fracture tips.

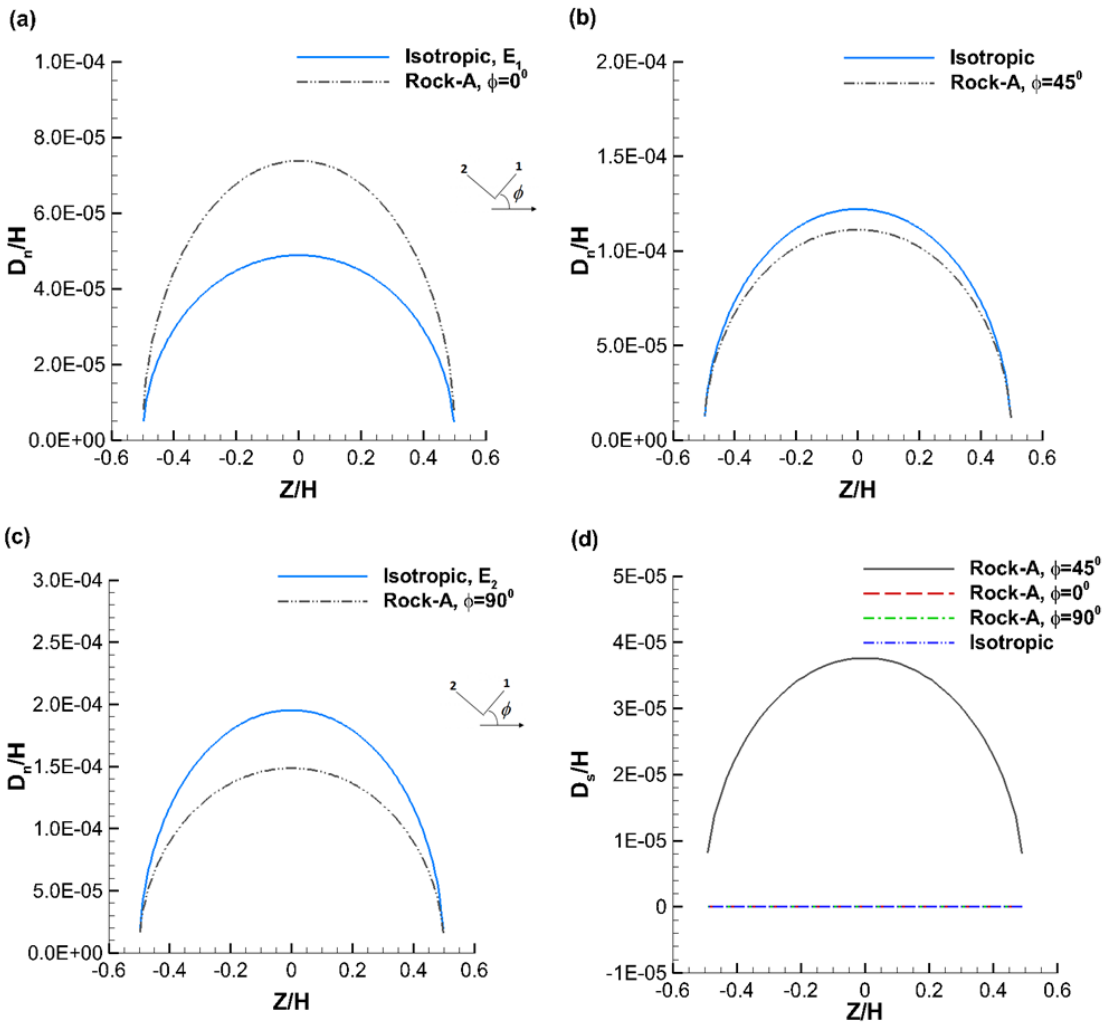

Figure 0-19. ZY plane strain analysis of a rectangular fracture (shown in Figure 11) subjected to a constant internal net pressure, P. (a-c) Dimensionless normal fracture opening (D_n) along the fracture Z-axis for various degrees of rock anisotropy and bedding dip (ϕ) with an internal net pressure (P) of 1 MPa. (d) Dimensionless fracture ride (D_s).

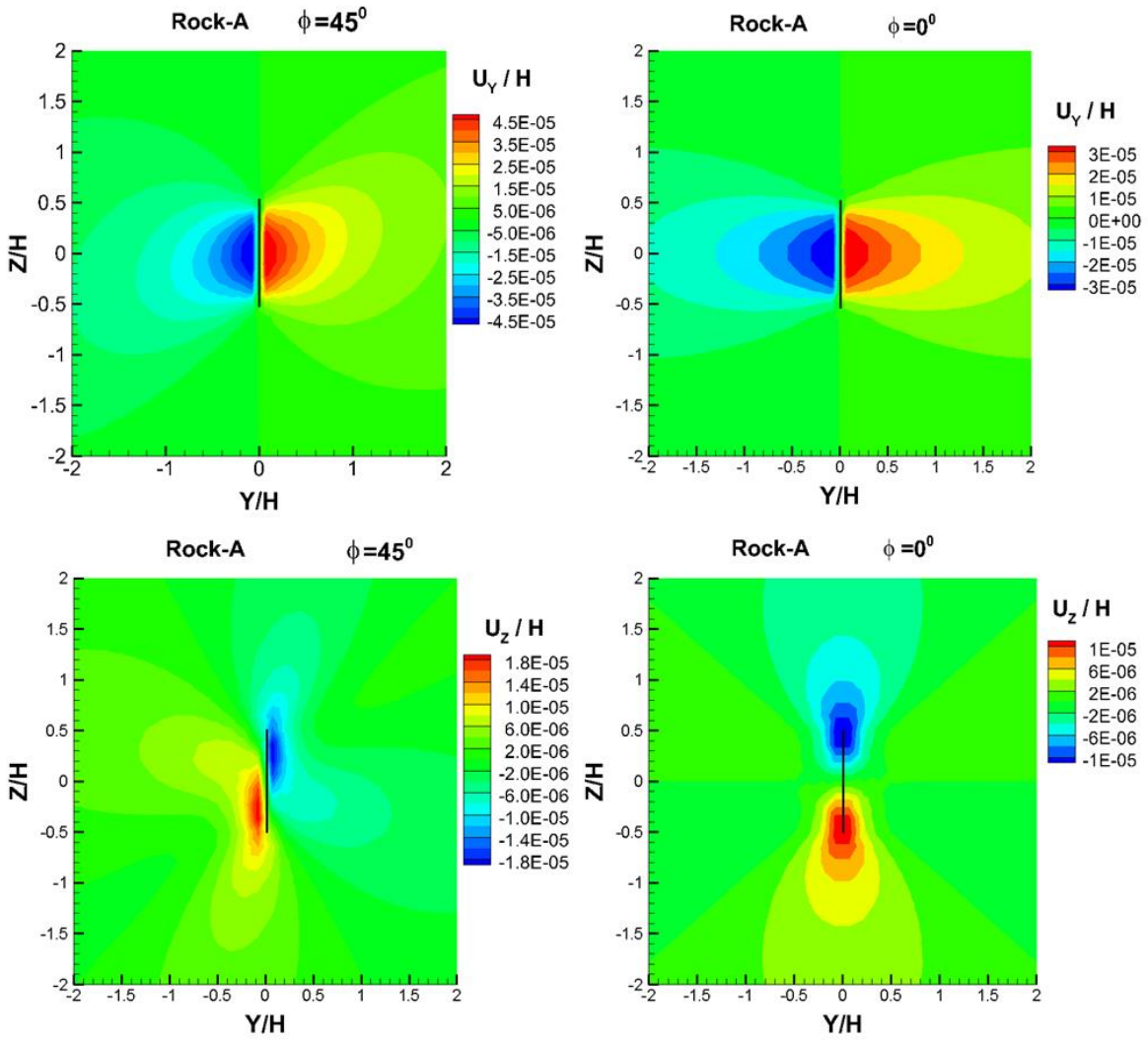

Figure 0-20. Z-Y plane strain analysis of a rectangular fracture (shown in Figure 11) subjected to a constant internal net pressure, P of 1 MPa. Normalized displacement distribution in the directions Y and Z in Rock A for different ϕ . Displacements are taken positive in the positive directions of coordinate axes.

4 Near Tip Processes in Fluid Driven Fracture and Analytical Solutions

Hydraulic fractures are driven by fluid injection. Therefore, the evolution of a hydraulic fracture is controlled not only by the rock elastic and fracture properties, but also by fluid properties. Early work by Barenblatt, (1962), Spence and Sharp, (1983), Spence and Turcotte, (1985) and Lister, (1990) followed by Desroches et al. (1994), recognized that the shape of a fracture tip in a rock with zero fracture toughness is different from the case where the rock fracture toughness is non-zero. In this chapter, first we will review and discuss the effect of fracture toughness of the rock and the fluid viscosity on the near tip fracture opening and pressure field in an isotropic rock. The second part of the chapter deals with developing global and near-tip self-similar solutions for anisotropic rock, and their use in building an efficient numerical hydraulic fracture propagation simulator that can automatically implement appropriate boundary conditions near the fracture tip depending on the properties of rock and fluid.

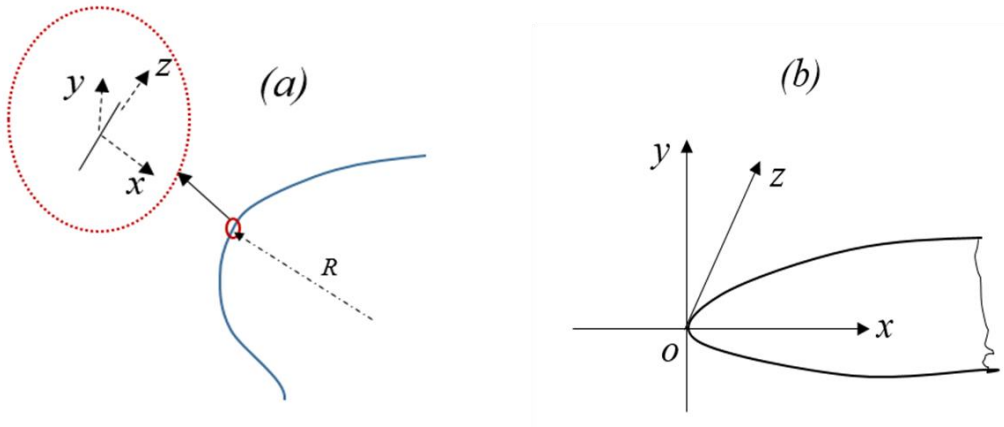

Figure 0-21. (a) Edge of an irregular-shaped fracture with inset showing a local fracture segment, (b) *xy* plane view of fracture edge with origin at fracture tip.

4.1 Governing Equations

Consider a fracture in the plane *xz* with an arbitrary shape with zero shear loading. Figure 4-1a shows the edge of such a fracture and a small segment of it having a radius of curvature R. If the length scale associated with the segment is small enough compared to length scale of radius R, we can approximate the curved segment as a straight line shown in the inset of Figure 4-1a. The deformation in the vicinity of such a segment can be considered to be within the plane *xy* (i.e. $dw(z)/dz = 0$), also the fracture dimension in the direction perpendicular to the edge (i.e. *x*-axis) becomes irrelevant and therefore can be taken infinite. Therefore, the resulting elastic integral equation that relates fracture apertures $w(x)$ with net fluid pressure inside the fracture $p(x)$ corresponds to a plane strain semi-infinite fracture (Barenblatt, 1962):

$$p(x) = \frac{E'}{4\pi}\int_0^\infty \frac{w'(s)ds}{x-s}, \qquad E' = \frac{E}{1-\nu^2} \tag{4.1}$$

Where, E is Young's modulus, ν is Poisson's ratio and *x* is distance from the fracture tip to a point along the fracture (see Figure 4-1b).

The above equation can be inverted for *w*' (see Appendix C):

$$dw(x)/dx = \frac{4}{\pi E'\sqrt{x}}\int_0^\infty \frac{p(s)ds}{\sqrt{s}} - \frac{4}{\pi E'}\int_0^\infty \sqrt{\frac{x}{s}}\,\frac{p(s)}{x-s}\,ds \tag{4.2}$$

Noting that the first integral on the R.H.S of the above equation is the definition of mode-1 stress intensity factor (Rice, 1968),

$$K_I = \sqrt{\frac{2}{\pi}}\int_0^\infty \frac{p(s)ds}{\sqrt{s}} \tag{4.3}$$

and integrating the Eq. 4.2 with respect to *x* using the tip boundary condition *w*(0)=0 and Eq. 4.3, gives

$$w(x) = \frac{4K_1\sqrt{2x}}{\sqrt{\pi}E'} + \frac{4}{\pi E'}\int_0^{\infty}\left(\ln\left|\frac{\sqrt{x}+\sqrt{s}}{\sqrt{x}-\sqrt{s}}\right| - 2\sqrt{\frac{x}{s}}\right)p(s)ds \tag{4.4}$$

At distances very close to the fracture tip, the above equation is reduced to,

$$w(x)_{x\to 0} \approx \frac{4K_1\sqrt{2x}}{\sqrt{\pi}E'} + O(x^{3/2}) \tag{4.5}$$

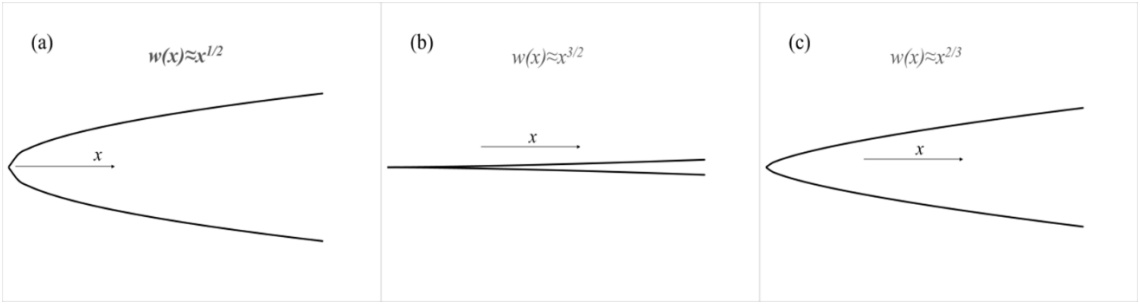

Figure 0-22. Fracture opening profiles very near the tip of a fluid driven semi-infinite fracture in a rock with, (a) non-zero fracture toughness and fluid with negligible viscosity, (b) zero fracture toughness and fluid with negligible viscosity, and (c) zero fracture toughness and high viscous fluid.

If the fracture is driven by a viscous fluid, there exists a fluid front inside the fracture. Assuming that the fracture tip and fluid front coincide (i.e. the fluid-lag is zero) the continuity equation can be expressed as,

$$\frac{\partial w(x)}{\partial t} + \frac{\partial q(x)}{\partial x} = 0 \tag{4.6}$$

However, recognizing that the reference coordinate system *x-y-z* is at the fracture tip and so it moves in term as the fracture propagates (see Figure 4-1(b)), the following convective derivative (Eq. 4.7) is applied to Eq. 4.6

$$\frac{\partial f(x,t)}{\partial t} = \frac{\partial f(x,t)}{\partial t} - \frac{\partial x}{\partial t}\frac{\partial f(x,t)}{\partial x} \tag{4.7}$$

which results in

$$\frac{\partial w(x)}{\partial t} - \frac{\partial x}{\partial t}\frac{\partial w(x)}{\partial x} + \frac{\partial q(x)}{\partial x} = 0 \tag{4.8}$$

where $q(x)$ is fluid flux. Very near to the fracture tip, the term $\partial w(x)/\partial t$ is negligible (Detournay and Peirce, 2014) compared to the term $\partial w(x)/\partial x$ and noting that $\partial x/\partial t$ is fracture velocity V, we obtain

$$V\frac{\partial w(x)}{\partial x} = \frac{\partial q(x)}{\partial x} \tag{4.9}$$

Integrating the above equation with the tip boundary conditions of: $q(0) = 0, w(0) = 0$, gives:

$$q(x) = w(x).V \tag{4.10}$$

The above equation physically means that, very near the fracture tip, the average velocity (i.e. $q(x)/w(x)$) of the fluid is equal to the fracture velocity *V*. The continuity equation (Eq. 10) combined with cubic law (Eq. 4.11) gives the lubrication equation (Eq. 4.12) in terms of fracture velocity.

$$q(x) = \frac{w^3(x)}{12\mu}\frac{dp}{dx} \tag{4.11}$$

$$\frac{w^2(x)}{\mu'}\frac{\partial p}{\partial x} = V \tag{4.12}$$

Where μ is fluid viscosity and $\mu' = 12\mu$. Substituting the near tip solution of *w*(*x*) from Eq. 4.5 in the lubrication equation (Eq. 4.12), and after integration, the behavior of fluid pressure very near to the fracture tip is,

$$p(x)_{x\to 0} \approx \ln(x) \tag{4.13}$$

Note that the logarithmic singularity in pressure distribution is the direct consequence of the term $x^{1/2}$ from Eq. 4.5. However, if the rock has zero fracture toughness, the logarithmic singularity disappears since the first term in Eq. 4.5 must be zero (since, stress concentration cannot exist in a rock with zero fracture toughness). In this case, the fracture opening and fluid pressure very near

the tip takes the following form (see Appendix C) for a semi-infinite fracture (Desroches et al., 1994),

$$w(x)_{x\to 0} \approx 2^{1/3}3^{5/6}\left(\frac{\mu' V}{E'}\right)^{1/3} x^{2/3} \tag{4.14}$$

$$p(x)_{x\to 0} \approx -2^{-2/3}3^{-2/3}\left(E'^{2}\,\mu' V\right)^{1/3} x^{-1/3} \tag{4.15}$$

Where V is the velocity of fracture which is also the velocity of fluid front (because of zero fluid-lag). Note that the above equations are independent of fracture toughness since it is assumed zero from the outset. Therefore, a fracture driven by a viscous fluid in a zero toughness rock assumes a fracture tip of shape in the order $x^{2/3}$ and fluid pressure with singularity ($-x^{-1/3}$), where x is the distance measured from fracture tip.

Figure 4-2 shows comparison between the fracture shapes very near the fracture tip for various cases of rock fractures toughness and fluid viscosity. If fracture toughness of the rock is non-zero and the fluid viscosity is zero, the aperture profile is of order $x^{1/2}$ near the fracture tip according to Eq. 4.5 and the corresponding shape of fracture tip is shown in Figure 4-2a. In this case, the fracture assumes round shape near the tip. On the other hand, if both fracture toughness of the rock and fluid viscosity are zero, the aperture profile near the fracture is in the order $x^{3/2}$ from Eq. 4.5. In this case the fracture tip takes on a cusp shape where the two surfaces of the fracture close smoothly as shown in Figure 4-2b. Figure 4-2c shows the shape of the fracture tip in a zero toughness rock with non-zero viscosity fluid and zero fluid lag. In this case, the aperture profile near the fracture tip is of order $x^{2/3}$ from Eq. 4.14.

Note that for the case of viscous fluid driven fracture, the solution for the pressure distribution near the fracture tip in rocks with both zero (Eq. 4.15) and non-zero (Eq. 4.13) fracture toughness indicates singularity at the fracture tip. But infinite pressure is not physically plausible. To resolve

the infinite negative pressure at the tips, one can assume a small region of fluid lag near the fracture tip where the absolute pressure is taken to be either zero or equal to the rock pore pressure. This is similar to envisioning fracture process zone in LEFM to resolve the theoretical infinite stresses near the fracture tip.

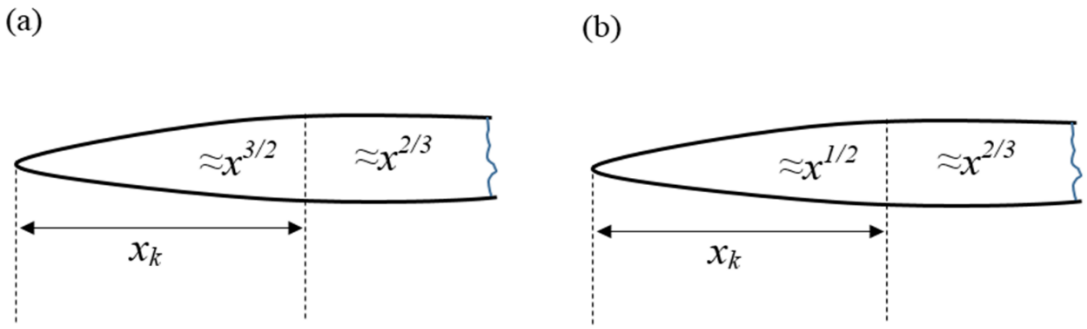

Figure 0-23. Fracture opening profiles near the tip of a semi-infinite fracture driven by a non-zero viscous fluid in a rock with (a) zero fracture toughness, and (b) non-zero fracture toughness. x_k denotes the distance along the fracture from the tip where LEFM tip solution is valid.

Consider a fracture driven by a viscous fluid in a rock with zero fracture toughness. Let x_k be the distance from the fracture tip along which LEFM aperture solution (Eq. 4.5) is valid. The existence of fluid-lag region (as discussed above) where viscous fluid is not penetrated indicates that fracture aperture profile near the tip (i.e. $x \le x_k$) should be of order $x^{3/2}$ from Eq. 4.5. Whereas away from the region of fluid lag, aperture profile should be of order 2/3 from Eq. 4.14. Therefore, fracture opening profile varies from $x^{3/2}$ to $x^{2/3}$ with increasing distance from the fracture tip as shown in Figure 4-3a. For the same case, however, with non-zero fracture toughness rock, in the vicinity of fracture tip, LEFM dictates that fracture aperture profile must be of order $x^{1/2}$ (i.e. $x \le x_k$) from Eq. 4.5. It will be shown later that far from the fracture tip, the aperture profile will be of order 2/3

from Eq. 4.14 as indicated in Figure 4-3b. Note that the distance x_k in Figure can extend beyond the region of fluid-lag (see below for more details).

The solution of fracture aperture and pressure very near the fracture tip (from Eqs. 4.14& 4.15) are for the limiting case of a hydraulic fracture in a rock with zero fracture toughness. This limiting tip solution can be used to construct a numerical model or self-similar solution to model fracture propagation in rocks with zero fracture toughness. For a more general case where the rock fracture toughness is non-zero, the near tip fracture aperture profile is depicted in Figure 4-3b. Typically in any numerical model, the fracture is discretized into small elements and the boundary conditions (i.e., fracture tip aperture or pressure solution) are applied on the fracture tip element. If the length of fracture tip element is less than x_k (see Figure 4-3) then it is appropriate to use LEFM aperture solution as tip aperture boundary condition. On the other hand, if the length of the tip element is greater than x_k it is appropriate to use zero fracture toughness aperture solution as tip aperture boundary condition. As will be shown later, x_k depends on rock and fluid properties and evolves with time (which means x_k is not a fixed value). Therefore, in order to construct a numerical model that can use appropriate tip boundary conditions, it is imperative to evaluate the parameter x_k. In what follows next, we will discuss self-similar solution of fracture opening near the tip, to obtain a physical interpretation of the length x_k shown in Figure 4-3.

Once x_k can be evaluated, then the correct tip solution may be used in a numerical algorithm for fracture propagation using displacement discontinuity method. The technique is implemented in a 2D DD procedure. Finally, the fracture tip solutions obtained for isotropic body are extended to anisotropic case for use in anisotropic DD fracture model.

4.2 Near Tip Self-Similar Solution

The set of governing equations (given previously) for a semi-infinite fracture steadily propagating with a constant velocity *V* and without a fluid lag, in an impermeable rock with non-zero fracture toughness are repeated below for convenience:

$$p(x) = \frac{E'}{4\pi}\int_0^{\infty} \frac{w'(s)ds}{x-s} \tag{4.11}$$

$$\frac{w^2(x)}{\mu'}\frac{\partial p}{\partial x} = V \tag{4.12}$$

$$w(x)_{x\to 0} \approx \frac{K'\sqrt{x}}{E'},$$

$$w(x)_{x\to \infty} \approx 2^{1/3}3^{5/6}\left(\frac{\mu' V}{E'}\right)^{1/3} x^{2/3},$$

$$K' = 4\sqrt{\frac{2}{\pi}}K_{IC} \tag{4.16}$$

$$E' = \frac{E}{1-\nu^2}$$

$$\mu' = 12\mu$$

Here *x* denotes the distance along the fracture interior measured from fracture tip (see Figure 4-1). Notice that the near tip solution for a semi-infinite fracture in zero fracture toughness rock (Eq. 4.14& 4.15) becomes the exterior solution or the solution at infinity (Eq. 4.16) for hydraulic fracture in a rock with non-zero fracture toughness as shown by Garagash and Detournay, (2000). Using this fact, the self-similar tip solution for the general case of viscous fluid driven fracture in a non-zero fracture toughness solid is constructed.

To reduce the above equations into dimensionless form (the advantage of reducing the governing equations into dimensionless form is that the near tip solution once obtained, will be in a self-

similar form. The self-similarity here means that the solution is independent of time and material properties), let

$$\begin{aligned} x &= L_* \xi \\ w(x) &= W_* \bar{W} \\ p(x) &= P_* \bar{P} \end{aligned} \tag{4.17}$$

Where L_*, W_* and P_* are characteristic length, aperture and pressure, respectively with their respective dimensions. The terms $\bar{W}$, $\bar{P}$ and ξ are dimensionless aperture, pressure, and distance from the fracture tip, respectively.

Substituting Eq. 4.17 into the governing equations (Eq. 4.1, 4.12& 4.16) gives:

$$P_* \bar{P}(\xi) = \frac{E' W_*}{4\pi L_*} \int_0^\infty \frac{\bar{W}'(s) ds}{\xi - s} \tag{4.18}$$

$$\frac{W_*^2 P_* \bar{W}^2(\xi)}{\mu' L_*} \frac{d\bar{P}}{d\xi} = V \tag{4.19}$$

$$\frac{E' W_*}{K' \sqrt{L_*}} \bar{W}(\xi)_{\xi \to 0} \approx \sqrt{\xi} \tag{4.20}$$

Now choose

$$\frac{W_*}{\sqrt{L_*}} = \frac{K'}{E'} \tag{4.21}$$

So that Eq. 4.20 becomes:

$$\bar{W}(\xi)_{\xi \to 0} \approx \sqrt{\xi} \tag{4.22}$$

Substituting Eq. 4.21 in Eq. 4.19 gives

$$\frac{K'^2 P_* \bar{W}^2(\xi)}{E'^2 \mu'} \frac{d\bar{P}}{d\xi} = V \tag{4.23}$$

Now choose

$$P_* = \frac{E'^2 \mu' V}{K'^2} \tag{4.24}$$

So that Eq. 4.23 becomes:

$$\bar{W}^2(\xi)\frac{d\bar{P}}{d\xi} = 1 \tag{4.25}$$

Similarly choosing L_* and W_* as

$$\begin{aligned} L_* &= \frac{K'^6}{E'^4 \mu'^2 V^2} \\ W_* &= \frac{K'^4}{E'^3 \mu' V} \end{aligned} \tag{4.26}$$

And substituting Eq. 4.26 in Eq. 4.18 gives:

$$\bar{P}(\xi) = \frac{1}{4\pi}\int_0^\infty \frac{\bar{W}'(s)ds}{\xi - s} \tag{4.27}$$

and finally by putting W* and l* into Eq. 4.16 (part b):

$$\bar{W}(\xi)_{\xi\to\infty} \approx 2^{1/3}3^{5/6}\xi^{2/3} \tag{4.28}$$

Therefore, Eqs. 4.22, 4.25, 4.27& 4.28 are a set of governing equations in dimensionless form for a semi-infinite fracture propagating with a constant velocity *V* with no fluid lag in an isotropic medium. The solution for the fracture aperture and pressure very near to the fracture tip ($_{\xi\to 0}$) including the higher order terms in dimensionless form is given (Garagash and Detournay, 2000) as:

$$\begin{aligned} \bar{W}(\xi)_{\xi\to 0} &\approx \sqrt{\xi} + 4\pi\xi + \frac{128}{3}\xi^{3/2}\ln\xi + O(\xi^{3/2}) \\ \bar{P}(\xi)_{\xi\to 0} &\approx \ln\xi + 5.504 - 16\pi\xi^{1/2} - \frac{256}{3}\xi\ln\xi + O(\xi) \end{aligned} \tag{4.29}$$

Note that the first term in the aperture solution (Eq. 4.29) is the imposed LEFM boundary condition (Eq. 4.22). The corresponding term in the pressure solution is, $\ln \xi$ obtained by substituting $\bar{W} \approx \sqrt{\xi}$ in the lubrication equation and carrying out the integration to solve for the pressure. The remaining terms in the solution are obtained using the procedure in see Garagash and Detournay, (2000) for more details).

Far from the fracture tip, $\xi \to \infty$, the aperture and pressure solutions in dimensionless form including the higher order terms are given as:

$$\begin{aligned} \bar{W}(\xi)_{\xi\to\infty} &\approx 2^{1/3}3^{5/6}\xi^{2/3} + 0.0371887\xi^{0.138673} + O(\xi^{0.138673}) \\ \bar{P}(\xi)_{\xi\to\infty} &\approx -2^{-2/3}3^{-2/3}\xi^{-1/3} + 0.0371887\frac{0.138673\cot(0.138673\pi)}{4}\xi^{-0.86133} + O(\xi^{-0.86133}) \end{aligned} \quad (4.30)$$

Again the first term in the aperture solution (Eq. 4.30) is the imposed zero fracture toughness boundary condition (Eq. 4.28). The corresponding term ($-\xi^{-1/3}$) in the pressure solution is obtained through lubrication equation (see Garagash and Detournay, (2000) for more details on complete solution).

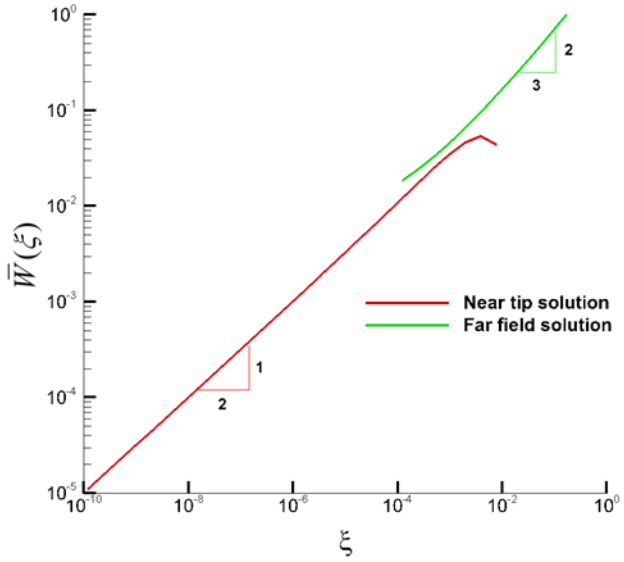

Figure 0-24. Log-log plot of the near tip self-similar solution (Eqs. 4.29& 4.30) for dimensionless fracture aperture $\bar{W}$ for the two different limiting solutions as a function of dimensionless distance ξ from the fracture tip in a rock with non-zero fracture toughness. From the fracture tip up to the dimensionless distance $\xi \leq (1\times10^{-4})$, the aperture profile is dominated by LEFM solution (i.e., $\xi^{1/2}$) and then begin to diverge. Beyond the distance $\xi \geq (1e-2)$, the aperture profile is dominated by zero toughness solution (i.e., $\xi^{2/3}$).

Figure 4-4 shows dimensionless aperture ($\bar{W}$) variation over dimensionless distance (ξ) from fracture tip in a semi-infinite fracture. We see that from the fracture tip to the dimensionless distance $\xi \leq (1e-4)$, the aperture profile is dominated by the LEFM solution (i.e. $\xi^{1/2}$). Let us call this distance as ξ_k, therefore, $\xi_k = (1e-4)$. This corresponds to the dimensional quantity x_k in Figure 4-3b. Beyond the distance $\xi \geq (1e-2)$, the aperture profile is dominated by zero toughness solution (i.e. $\xi^{2/3}$). In the region $(1e-4) \leq \xi \leq (1e-2)$ there is no clear dominating aperture profile. We call this region as intermediate region where the aperture profile is given by combined LEFM and zero fracture toughness solutions.

Note that the logarithmic singularity in pressure solution at the fracture tip from Eq. 4.29 indicates the need for the presence of fluid lag as discussed previously. However, the fluid lag is not considered in the construction of self-similar solutions near the tip since it introduces dependence of solution on material properties therefore can't be considered and so is ignored. Such an approximation is not very off from the reality as in a typical hydraulic fracture, the length of the fluid lag zone tends to be vanishingly small according to Garagash, (2004).

As we saw previously, the near tip aperture is either the LEFM or the viscous solution up to a distance x_k measured from the tip. When modeling, this distance need be determined to allow the correct near tip solution to be implemented. From Figure 4-4, we can find that the dimensionless distance ξ_k from fracture tip where the LEFM solution is applicable. Through the scaling parameter L_* (Eq. 4.26) in Eq. 4-17a and using $\xi_k = 1e-4$ we can obtain physical quantity x_k as,

$$x_k = \frac{(1e-4)K'^6}{E'^4 \mu'^2 V^2} \tag{4.31}$$

Let ξ_μ be the dimensionless distance from fracture tip where the zero fracture toughness (or the viscous) solution begins to apply. From Figure 4-4, we see that this distance in dimensionless quantity is $\xi = (1e-2)$. Through the scaling parameter L_*, we can obtain physical quantity x_μ as,

$$x_\mu = \frac{(1e-2)K'^6}{E'^4 \mu'^2 V^2} \tag{4.32}$$

If we take the following input values for a typical hydraulic fracture in an unconventional reservoir,

$K = 2$ MPa.m$^{1/2}$, $E' = 30$ GPa, $\mu = 1$ cP, $V = 0.5$ m.s^{-1}

The characteristic length will be L_* =2319 m and from Eqs. 4.29& 4.30, we obtain

x_k = 0.23 m

x_μ =23 m

If the injection fluid is a thick gel with viscosity 100 cP instead of water (1 cP) and keeping the remaining input parameters same, we find

x_k =2.3x10^{-5} m

x_μ =2.3x10^{-3} m

Note that the physical quantities x_k , x_μ corresponds to the distances from the tip of a semi-infinite fracture. This may seem unrealistic, however, for typical input parameters for hydraulic fractures, these values are several orders of magnitude smaller than the typical length of a hydraulic fracture which is finite not semi-infinite. As a result, the near tip behavior of a hydraulic fracture can be adequately described using the solutions derived for a semi-infinite fracture. Since, the velocity of a fracture propagating with constant injection rate decreases with time due to increase in fracture length and storage, the parameter x_k (Eq. 4.31), which defines the region near the fracture tip where LEFM solution is valid, expands with time.

4.3 Fracture Propagation Regimes

During fracture propagation, if the viscous dissipation due to fluid flow inside the fracture is negligible compared to the energy expended in creating the new rock surface, then the fracture propagation will be in toughness dominated regime. On the other hand, if the energy expended in creating the new rock surface is negligible compared to the viscous energy losses due to fluid flow inside the fracture, then the fracture propagation will be in viscous dominated regime. Without explicitly calculating the energy losses, we can use the semi-infinite fracture tip solutions to find the regime of fracture propagation in a numerical model. For typical input parameters considered

in the previous section, we find x_k =0.23 m for injecting water with a viscosity of 1 cP. Therefore, in any numerical model with these input parameters and for a given time period (where velocity is a constant), the distance from the fracture tip to the first node of the tip element must be less than or equal to 0.23 m with the LEFM tip solution (Eq. 4.5) as the tip solution. Since the fracture propagation in this case is dominated by rock fracture toughness, we call the mode of fracture propagation as toughness dominated. If the injection fluid is a gel with viscosity of 100 cP, we find x_k =2.3x10^{-5} m. Since it is impractical to use a tip element that small in any numerical model, so instead, the zero fracture toughness tip solution is used as the tip aperture boundary condition. In the latter case, the fracture propagation in this case is independent of fracture toughness and we call the mode of fracture propagation as viscosity dominated.

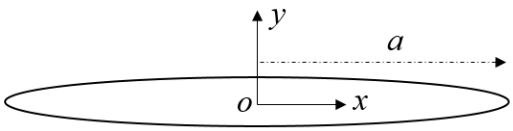

Figure 0-25. A symmetrical line fracture in plane strain condition with half-length *a,* and origin *o* at fracture center.

4.4 Semi-Analytical Solution for Plane Strain Fracture in Viscous Regime

Consider a plane strain fracture of length 2*a* in an infinite elastic isotropic rock as shown in Figure 4-5. The elastic integral equation relating the net pressure *p(x)* inside the fracture with fracture apertures *w(x)* is (Barenblatt, 1962),

$$p(x,t) = \frac{E'}{4\pi} \int_{-a}^{a} \frac{w'(s,t)ds}{x-s} \tag{4.43}$$

$$\frac{\partial w(x,t)}{\partial t} + \frac{\partial q(x,t)}{\partial x} = 0 \tag{4.44}$$

Combining the continuity equation (Eq. 4.44) and cubic law (Eq. 4.11), gives the governing equation for fluid flow as,

$$\frac{\partial w(x,t)}{\partial t} = \frac{\partial}{\partial x}\left(\frac{w^3(x,t)}{\mu'} \frac{\partial p(x,t)}{\partial x} \right) \tag{4.45}$$

Global mass balance dictates,

$$\int_{-a}^{a} w(x,t)dx = Q_0 t \tag{4.46}$$

At the fracture tip, both aperture and flux are zero

$$w(x,t) = 0,\ q(x,t) = 0\ \{x = \pm a\} \tag{4.47}$$

If the rock has zero fracture toughness, the mode-1 stress intensity factor at tips must be zero; therefore,

$$\int_{0}^{a} \frac{p(x,t)dx}{\sqrt{a^2 - x^2}} = 0 \tag{4.48}$$

To reduce the above equations into dimensionless form let,

$$\begin{aligned} x &= \hat{L}\bar{x} \\ a &= \hat{L}\lambda(\tau) \\ t &= \hat{T}\tau \\ w(x,t) &= \hat{L}\bar{W}(\bar{x},\tau) \\ p(x,t) &= \hat{P}\bar{P}(\bar{x},\tau) \end{aligned} \tag{4.49}$$

Where $\hat{L}$, $\hat{T}$ and $\hat{P}$ are characteristic length, time and pressure respectively with their respective dimensions. These can be derived following the procedure given above and they are given as,

$$\begin{aligned} \hat{L} &= \sqrt{\frac{\mu' Q_0}{E'}} \\ \hat{T} &= \frac{\mu'}{E'} \\ \hat{P} &= E' \end{aligned} \tag{4.50}$$

Substituting the Eq. 4.49 in Eqs. 4.43, 4.45& 4.46 gives,

$$\bar{P}(\bar{x},\tau)=\frac{1}{4\pi}\int_{-\lambda(t)}^{\lambda(t)}\frac{\bar{W}'(\bar{s},\tau)d\bar{s}}{\bar{x}-\bar{s}} \tag{4.51}$$

$$\frac{\partial\bar{W}(\bar{x},\tau)}{\partial\tau}=\frac{\partial}{\partial\bar{x}}\left(\bar{W}^3(\bar{x},\tau)\frac{\partial\bar{P}(\bar{x},\tau)}{\partial\bar{x}}\right) \tag{4.52}$$

$$\int_{-\lambda(\tau)}^{\lambda(\tau)}\bar{W}(\bar{x},\tau)\partial\bar{x}=\tau \tag{4.53}$$

If we express, the dimensionless pressure, aperture and length in power law form (Spence and Turcotte, 1985) as

$$\begin{aligned}\bar{W}(\bar{x},\tau)&=k\tau^{1/3}W_{\xi}(\xi)\\ \bar{P}(\bar{x},\tau)&=\tau^{-1/3}P_{\xi}(\xi)\\ \lambda(\tau)&=k\tau^{2/3}\end{aligned} \tag{4.54}$$

where

$$\xi=\frac{\bar{x}}{\lambda(\tau)} \tag{4.55}$$

and substituting in Eq. 4.51 gives

$$P_{\xi}(\xi)=\frac{1}{4\pi}\int_{-1}^{1}\frac{W'_{\xi}(\eta)d\eta}{\xi-\eta} \tag{4.56}$$

Since ξ is time dependent dimensionless coordinate (Eq. 4.55), the lubrication equation must be modified accordingly using the convective derivative (Eq.4.7)

From Eq. 4.55,

$$\frac{\partial}{\partial\bar{x}}=\frac{\partial}{\lambda(t)\partial\xi} \tag{4.57}$$

Using Eq. 4.7 and Eq. 4.57 in Eq. 4.52 we obtain,

$$\frac{\partial \bar{W}(\bar{x},\tau)}{\partial \tau} - \frac{1}{\lambda(\tau)} \frac{\partial \lambda(\tau)}{\partial \tau} \frac{\partial \bar{W}(\bar{x},\tau)}{\partial \bar{x}} = \frac{1}{\lambda^2(\tau)} \frac{\partial}{\partial \bar{x}} \left(\bar{W}^3(\bar{x},\tau) \frac{\partial \bar{P}(\bar{x},\tau)}{\partial \bar{x}} \right) \tag{4.58}$$

Substituting Eq. 4.54 in Eq. 4.58 gives,

$$\frac{1}{3} W_\xi(\xi) - \frac{2}{3} \xi \frac{\partial W_\xi(\xi)}{\partial \xi} = \frac{\partial}{\partial \xi} \left(W_\xi^3(\xi) \frac{\partial P_\xi(\xi)}{\partial \xi} \right) \tag{4.59}$$

The constant *k* is obtained by substituting Eq. 4.54 in Eq. 4.3 as,

$$k = \left[\int_{-1}^{1} W_\xi(\xi) d\xi \right]^{-1/2} \tag{4.60}$$

and the boundary condition is

$$W_\xi(\pm 1) = 0 \tag{4.61}$$

Here $W_\xi(\xi)$ and $P_\xi(\xi)$ are self-similar fracture aperture and pressure that are independent of time. The method of solving Eqs. 4.56, 4.59& 4.60 with condition (Eq. 4.61) for $W_\xi(\xi)$, $P_\xi(\xi)$ and *k* is first proposed by Spence and Sharp, (1985) for the case where fracture toughness is non-zero. However, Carbonell and Detournay, (1998) reported inconsistencies in the solutions obtained by Spence and Sharp, (1965) especially for problems with low fracture toughness and improvised it for the case where fracture toughness of the rock is zero by explicitly using the near tip zero toughness solution (Eq. 4.14). The solution method first expresses fracture aperture ($W_{\xi(\xi)}$) as polynomial expansion up to Nth order accuracy as,

$$W_\xi(\xi) = \left(1 - \xi^2\right)^{2/3} \sum_{n=1}^{N} A_n C_{2n-2}^{1/6}(\xi) + B F_w(\xi) \tag{4.62}$$

where $C_n^{\lambda}(x)$ are Gegenbauer polynomials, which can be expressed in terms of Jacobi polynomials. Notice that zero fracture toughness near tip solution of order 2/3 (Eq. 4.14) is explicitly used in the expansion of $W_{\xi}(\xi)$.

Using lubrication equation (Eq. 4.59), the self-similar solution for net pressure ($P_{\xi}(\xi)$) is given as,

$$P_{\xi}(\xi) = \sum_{n=1}^{N} A_n G_n(\xi) + BF_p(\xi) \tag{4.63}$$

where

$$n=1, G_n(\xi) = \frac{\alpha}{4\pi(1-\alpha)} B(\tfrac{1}{2},\alpha)\ {}_2F_1(\tfrac{1}{2}-\alpha,1;2-\alpha;1-\xi^2) + \frac{\alpha}{2}\cot\pi\alpha\,|\xi|\left(1-\xi^2\right)^{\alpha-1}$$

$$n>1, G_n(\xi) = \frac{(2\alpha-1)(2n-1)}{4\pi(n-1+\alpha)} B(\tfrac{1}{2}-n,\alpha+n)\left[\alpha\xi^2\ {}_2F_1(\tfrac{5}{2}-n-\alpha,n;\tfrac{3}{2};\xi^2) - \frac{1}{2}\ {}_2F_1(\tfrac{3}{2}-n-\alpha,n-1;\tfrac{1}{2};\xi^2)\right]$$

where ${}_pF_q(a_1..a_p,1;b_1..b_q;x)$ is hypergeometric function and $B(p,q)$ is Beta function.

The term $F_p(\xi)$ is included in the solution (Eq. 4.63) to satisfy the condition of discontinuous pressure gradient at the inlet and is given by

$$F_p(\xi) = 2 - \pi|\xi| \tag{4.64}$$

The corresponding term in aperture solution is

$$F_w(\xi) = 4\sqrt{1-\xi^2} + 2\xi^2 \ln\left|\frac{1-\sqrt{1-\xi^2}}{1+\sqrt{1-\xi^2}}\right| \tag{4.65}$$

The terms A_n, B and k are constants and the method of evaluating these can found in Spence and Sharp. For the problem defined above, these values are listed in Adachi and Detournay, (2002) up to n=7.

4.5 Semi-Analytical Solution for Plane Strain Fracture in Toughness Regime

If we assume that the viscous dissipation inside the fracture due to fluid flow is negligibly small, the equilibrium condition near the fracture tip gives (Sneddon and Lowengrub, 1969, Spence and Turcotte, 1985),

$$-p(x,t)_{x\to a+} = \frac{K_{IC}}{\sqrt{2\pi(x-a)}} \tag{4.66}$$

where $p(x,t)$ is net pressure inside the fracture, the negative sign here indicates that the tensile stresses are taken negative. Substituting Eq. 4.49 in the above equation gives,

$$-\bar{P}(\bar{x},\tau)E' = \frac{K_{IC}}{\sqrt{2\pi(\bar{x}\hat{L}-\lambda(\tau)\hat{L})}} \tag{4.67}$$

Defining dimensionless toughness parameter γ as

$$\gamma = \frac{K_{IC}}{E'\sqrt{\hat{L}\pi}} \tag{4.68}$$

And substituting in Eq. 4.67 gives

$$\bar{p}(x,\tau)_{x\to\lambda(\tau)+} = -\frac{\gamma}{\sqrt{2(\bar{x}-\lambda(\tau))}} \tag{4.69}$$

Finally, using self-similarity variables from Eq. 4.54 in Eq. 4.69, we obtain,

$$P(\xi)_{\xi\to 1+} = -\frac{\gamma}{\sqrt{2k(\xi-1)}} \tag{4.70}$$

The elasticity (Eq. 4.56) and lubrication (Eq. 4.59) equations are solved with the boundary conditions (Eqs. 4.61& 4.70) and the solution expanded up to first order accuracy is given as (Spence and Turcotte, 1985),

$$W_{\xi}(\xi) = A_1(1-\xi^2)^{1/2} + \frac{B\xi^2}{4}\ln\left[\frac{1-\sqrt{1-\xi^2}}{1+\sqrt{1+\xi^2}}\right] \tag{4.71}$$

Compare this solution with the solution for zero fracture toughness rock (Eq. 62) where the leading term in aperture expansion is of order 2/3 (In fact this is the major difference between the solution techniques of Spence and Sharp, (1985) and Carbonell and Detournay, (1998)) . When dimensionless fracture toughness, $\gamma >> 1$, the coefficients A and B are given as,

$$\begin{aligned} A_1 &\approx 1.4646\gamma^{4/3} \\ B &\approx 0.2331\gamma^{-8/3} \\ k &\approx 0.46619\gamma^{-2/3} \end{aligned} \tag{4.72}$$

Note that in this limit, the coefficient B in Eq. 4.71 goes to zero and the fracture assumes an elliptical shape (Eq. 4.73) as in the case of a fracture subjected to uniform internal fluid pressure,

$$W_{\xi}(\xi) \approx A_1(1-\xi^2)^{1/2} \tag{4.73}$$

Combining Eqs. 4.72, 4.73 and Eqs. 4.49, 4.50& 4.54, the fracture aperture at injection location and fracture half-length in this limit are given as,

$$\begin{aligned} w(0) &= 2.167596\gamma^{2/3}\left(\frac{\mu' Q_0^{\,3}}{E'}\right)^{1/6} t^{1/3} \\ a &= 0.293681\gamma^{-2/3}\left(\frac{E' Q_0^{\,3}}{\mu'}\right)^{1/6} t^{2/3} \end{aligned} \tag{4.74}$$

Although it is not apparent, it is worth noting that the above results are independent of fluid viscosity.

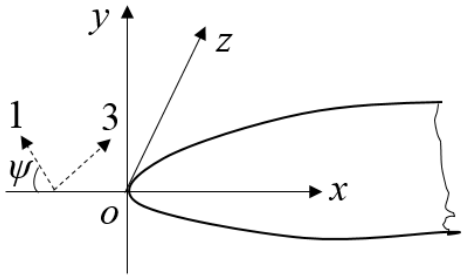

Figure 0-26. Tip region of a semi-infinite fracture in plane strain condition with origin at fracture tip. 1-3 are principal axes of the orthotropic material.

4.6 Fracture Tip Region in Anisotropic Rock

4.6.1 Governing Equations

Consider an infinite elastic homogeneous orthotropic body with three principal axes of elastic symmetry in the directions 1-2-3. As discussed previously, to study the deformation near the edge of a fracture, a problem of semi-infinite fracture in plane strain condition is considered as indicated in Figure 4-6. Assuming that fracture is free of far-field shear loading, the elastic integral equation that relates fracture aperture $w(x)$ with net fluid pressure inside the fracture $p(x)$ is given as,

$$p(x) = 2\text{Real}\left(\frac{1}{2\pi i b_{11}} \int_{-a}^{a} \frac{1}{x-\xi} \left[\frac{-\mu_1 r'(\xi) + w'(\xi)}{\hat{\mu}_1} + \frac{-\mu_2 r'(\xi) + w'(\xi)}{\hat{\mu}_2} \right] d\xi \right) \tag{4.79}$$

where

$$\hat{\mu}_1 = (\mu_1 - \mu_2)(\mu_1 - \mu_3)(\mu_1 - \mu_4)$$
$$\hat{\mu}_2 = (\mu_2 - \mu_1)(\mu_2 - \mu_3)(\mu_2 - \mu_4)$$

μ_1 and μ_2 are the complex roots of characteristic equation (Eq. 4.80) with positive imaginary parts.

$$b_{11}\mu^4 - 2b_{16}\mu^3 + (2b_{12} + b_{66})\mu^2 - 2b_{26}\mu + b_{22} = 0 \tag{4.80}$$

$$b_{ij} = a_{ij} - \frac{a_{i3}a_{j3}}{a_{33}}$$

where a_{ij} denote material constants in the fracture coordinate system *x-y-z.* For simplicity we restrict ourselves to the case (with significant practical interest, see also discussion) where the material's principal axes coincide with fracture axes (i.e. ψ=0). In this case Eq. 4.79 is reduced to Eq. 4.81 as the fracture ride $r(x)$ is zero.

$$p(x) = \frac{\hat{\mu}_1 + \hat{\mu}_2}{\hat{\mu}_1 \hat{\mu}_2} 2\text{Real}\left(\frac{1}{2\pi i b_{11}} \int_{0}^{\infty} \frac{w'(s)}{x-s} ds \right) \tag{4.81}$$

Let the two complex roots (μ_1, μ_2) be

$$\begin{aligned} \mu_1 &= \alpha_1 + i\beta_1 \\ \mu_2 &= \alpha_2 + i\beta_2 \end{aligned} \tag{4.82}$$

and substituting in Eq. 4.81, we obtain,

$$p(x) = \frac{\Delta_1}{b_{11}\pi\Delta_0}\int_0^\infty \frac{w'(s)}{x-s}\,ds \tag{4.83}$$

where

$$\begin{aligned} \Delta_1 &= 2(\beta_1 + \beta_2) \\ \Delta_0 &= 4\beta_1\beta_2\left(\left(\alpha_1 - \alpha_2\right)^2 + \left(\beta_1 + \beta_2\right)^2\right) \end{aligned} \tag{4.84}$$

Note that when principal axes of the material 1-2-3 coincide with the fracture axes *x-y-z*, the real part of the roots (μ_1, μ_2) takes the value $\alpha_1 = \alpha_2 = 0$.

The Eq. 4.83 can be inverted for *w'* (see Appendix-C)

$$w'(x) = \frac{b_{11}\Delta_0}{\pi\Delta_1\sqrt{x}}\int_0^\infty \frac{p(s)ds}{\sqrt{s}} - \frac{b_{11}\Delta_0}{\pi\Delta_1}\int_0^\infty \sqrt{\frac{x}{s}}\,\frac{p(s)}{x-s}\,ds \tag{4.85}$$

Here we use the fact that the stress intensity factors at fracture tip in anisotropic body are independent of material properties (Sih et al., 1965) and are identical to isotropic case if the loads acting on fracture surface are self-balancing (i.e. the load at a point on the upper surface of the fracture should be exactly equal and opposite in direction to the load at corresponding point on the lower surface of the fracture).

Therefore, in anisotropic body the mode-1 stress intensity factor is

$$K_I = \sqrt{\frac{2}{\pi}}\int_0^\infty \frac{p(s)ds}{\sqrt{s}} \tag{4.86}$$

Substituting Eq. 4.86 into Eq. 4.85 and integrating with respect to *x* with condition $w(0) = 0$ gives,

$$w(x) = \frac{b_{11}\Delta_0 K_1\sqrt{2x}}{\sqrt{\pi}\Delta_1} + \frac{b_{11}\Delta_0}{\pi\Delta_1}\int_0^\infty \left(\ln\left|\frac{\sqrt{x}+\sqrt{s}}{\sqrt{x}-\sqrt{s}}\right| - 2\sqrt{\frac{x}{s}} \right) p(s)ds \tag{4.87}$$

The limiting behavior of the above equation at distances very close to the fracture tip is

$$w(x)_{x\to 0} \approx \frac{b_{11}\Delta_0 K_1\sqrt{2x}}{\sqrt{\pi}\Delta_1} + O(x^{3/2}) \tag{4.88}$$

The above equation indicates that very close to the fracture tip, fracture aperture is of order 1/2, and 3/2, in an anisotropic rock with non-zero and zero fracture toughness respectively similar to isotropic case.

If the fracture is driven by viscous fluid in a zero fracture toughness anisotropic rock, the near tip fracture apertures can be written as

$$\begin{aligned} w(x)_{x\to 0} &\approx 2^{-1/3}3^{5/6}\left(\frac{\mu' V}{E'}\right)^{1/3} x^{2/3}, \\ p(x) &= 2^{2/3}3^{-2/3}\left(E'^2\,\mu' V\right)^{1/3} x^{-1/3}, \\ E' &= \frac{\Delta_1}{b_{11}\Delta_0} \\ \mu' &= 12\mu \end{aligned} \tag{4.89}$$

4.7 Self-Similar Fracture Tip Solution in Orthotropic Rock

Noting the similarity between the elasticity equations for isotropic (Eq. 4.1) and anisotropic (Eq. 4.83) bodies, one can straightforwardly use the solutions developed for isotropic body for anisotropic case while modifying only the characteristic dimensions. In this section the governing equations for fracture propagation in anisotropic body are reduced to dimensionless form so that the resultant equations are equivalent to the governing equations for isotropic body, and the corresponding characteristic dimensions are given.

Let us express Eq. 4.83 as

$$p(x) = \frac{4E'}{4\pi}\int_0^{\infty} \frac{w'(s)}{x-s}\,ds$$
$$E' = \frac{\Delta_1}{b_{11}\Delta_0} \tag{4.90}$$

The lubrication equation defining fluid flow is

$$\frac{w^2(x)}{\mu'}\frac{\partial p}{\partial x} = V \tag{4.12}$$

Boundary conditions near (Eq. 4.88) and far (Eq. 4.89) from the fracture tip are,

$$w(x)_{x\to 0} \approx \frac{K'\sqrt{x}}{E'},$$
$$w(x)_{x\to \infty} \approx 2^{-1/3}3^{5/6}\left(\frac{\mu' V}{E'}\right)^{1/3} x^{2/3}, \tag{4.91}$$
$$K' = K_{IC}\sqrt{\frac{2}{\pi}}$$
$$\mu' = 12\mu$$

To make the above equations dimensionless, let us introduce

$$x = L_* \xi$$
$$w(x) = W_* \bar{W} \tag{4.92}$$
$$p(x) = P_* \bar{P}$$

with ξ, $\bar{W}$, $\bar{P}$ denoting dimensionless values of distance from fracture tip, fracture aperture and fluid pressure. The terms L_*, W_*, P_* are characteristic dimensions of length, aperture and pressure respectively.

Substituting Eq. 4.92 into Eqs.4. 90, 4.12& 4.91, we obtain

$$P_* \bar{P}(\xi) = \frac{4E'W_*}{4\pi L_*}\int_0^{\infty} \frac{\bar{W}'(s)ds}{\xi - s} \tag{4.93}$$

$$\frac{W_*^2 P_* \bar{W}^2(\xi)}{\mu' L_*}\frac{d\bar{P}}{d\xi} = V \tag{4.94}$$

$$\frac{E'W_*}{K'\sqrt{L_*}}\bar{W}(\xi)_{\xi\to 0} \approx \sqrt{\xi} \tag{4.95}$$

Take

$$\frac{W_*}{\sqrt{L_*}} = \frac{K'}{E'} \tag{4.96}$$

so that Eq. 4.95 becomes

$$\bar{W}(\xi)_{\xi\to 0} \approx \sqrt{\xi} \tag{4.97}$$

Putting Eq. 4.96 in Eq. 4.94 gives

$$\frac{K'^2 P_* \bar{W}^2(\xi)}{E'^2 \mu'} \frac{d\bar{P}}{d\xi} = V \tag{4.98}$$

Take

$$P_* = \frac{E'^2 \mu' V}{K'^2} \tag{4.99}$$

so that Eq. 4.98 becomes

$$\bar{W}^2(\xi) \frac{d\bar{P}}{d\xi} = 1 \tag{4.100}$$

Similarly choosing L_* and W_* as

$$\begin{aligned} L_* &= \frac{16K'^6}{E'^4 \mu'^2 V^2} \\ W_* &= \frac{4K'^4}{E'^3 \mu' V} \end{aligned} \tag{4.101}$$

and substituting in Eq. 4.93 gives

$$\bar{P}(\xi) = \frac{1}{4\pi} \int_0^\infty \frac{\bar{W}'(s) ds}{\xi - s} \tag{4.102}$$

and finally

$$\bar{W}(\xi)_{\xi\to\infty} \approx 2^{-1/3}3^{5/6}\xi^{2/3} \tag{4.103}$$

The solution to Eqs. (4.97, 4.100, 4.102& 4.103) is given in Eqs. 4.29& 4.30, and plotted in Figure 4 which shows that up to dimensionless distance $\xi \le (1e-4)$ from fracture tip, fracture aperture has square root variation and beyond the distance $\xi \ge (1e-2)$ from fracture tip, fracture aperture varies in the order 2/3. The physical variable x_k (see Figure 4-3) for orthotropic rock can be written as

$$x_k = \frac{(1e-4)16K'^6}{E'^4\mu'^2V^2} \tag{4.104}$$

For elastic constants given in Table 3-2 (close to Woodford shale, Sierra et al., 2010), and taking the following typical values for the remaining parameters

$K = 2$ MPa.m$^{1/2}$, $\mu = 1$ cP, $V = 0.5$ m.s^{-1}

give

x_k = 1.86 m

Which indicates that up to 1.86 m from the fracture tip, fracture aperture is dominated by LEFM square root tip solution (Eq. 4.88).

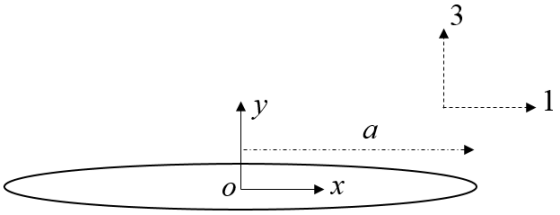

Figure 0-27. A symmetrical line fracture in plane strain condition with half-length *a*, in an orthotropic medium. 1-3 are principal axes of the material.

4.8 Semi-Analytical Solution for Plane Strain Fracture in Viscous Regime in Orthotropic Rock

The governing equations for a finite hydraulic fracture in plane strain condition propagating in a zero fracture toughness orthotropic medium can be reduced to dimensionless form as in Eqs. (56, 59, 60& 61) with solution given by Eqs 62& 63. Following the procedure given above, the characteristic dimensions of length, time and pressure for orthotropic body can be deduced as

$$\hat{L} = \sqrt{\frac{\mu' Q_0}{4E'}}$$
$$\hat{T} = \frac{\mu'}{4E'} \qquad (4.105)$$
$$\hat{P} = 4E'$$

with

$$E' = \frac{\Delta_1}{b_{11}\Delta_0}$$
$$\mu' = 12\mu$$

4.9 Semi-Analytical Solution for Plane Strain Fracture in Toughness Regime in Orthotropic Rock

As stated earlier, if the loading on fracture surface is self-balancing, the stress intensity factors at fracture tip becomes independent of material properties in an anisotropic body, therefore in the case of large fracture toughness, the following equation (Eq. 4.106) can be used as a boundary condition to solve the governing Eqs. (4.56, 4.59, 4.60& 4.61).

$$-p(x,t)_{x\to a+} = \frac{K_{IC}}{\sqrt{2\pi(x-a)}} \qquad (4.106)$$

where *a* denotes half-length of the fracture and *x* is distance along the fracture with origin at the fracture center (see Figure 4-7).

Using Eq. 4.105, the Eq. 4.106 is reduced to,

$$\bar{p}(x,\tau)_{x\to\lambda(\tau)+} = -\frac{\gamma}{\sqrt{2(\bar{x}-\lambda(\tau))}} \tag{4.107}$$

$$\gamma = \frac{K_{IC}}{E'\sqrt{\hat{L}\pi}} \tag{4.108}$$

where γ is defined as dimensionless fracture toughness.

Finally, using self-similarity variables from Eq. 4.54 in Eq. 4.107, we obtain,

$$P(\xi)_{\xi\to 1+} = -\frac{\gamma}{\sqrt{2k(\xi-1)}} \tag{4.109}$$

The solution to this problem (i.e. Eqs. 4.56, 4.59, 4.60, 4.61& 4.109) in dimensionless form in the limit $\gamma >> 1$ is given in Eqs. 4.72& 4.73.

Using Eqs, 4.54& 4.105 the solution for fracture aperture at injection point and half-length as function of time in physical variables can be expressed as,

$$\begin{aligned} w(0) &= 1.72049\gamma^{2/3}\left(\frac{\mu' Q_0{}^3}{E'}\right)^{1/6} t^{1/3} \\ a &= 0.37\gamma^{-2/3}\left(\frac{E' Q_0{}^3}{\mu'}\right)^{1/6} t^{2/3} \end{aligned} \tag{4.110}$$

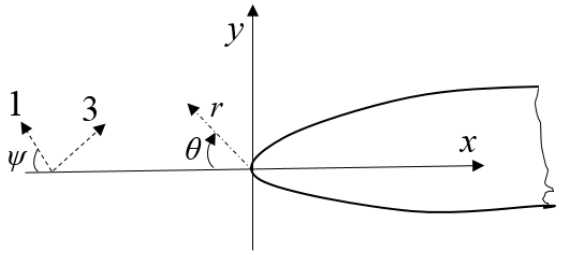

Figure 0-28. Tip region of a plane strain fracture in an orthotropic medium. *r*, θ constitute polar coordinate system near the fracture tip.

4.10 Fracture Oriented Arbitrarily with respect to Rock's Principal Axes

In previous sections, a simplified case was assumed where fracture axes were parallel to material's principal axes to decouple fracture normal displacement discontinuity from shear displacement discontinuity in Eq. 4.79 The resultant Eq. 4.81 is simple to evaluate near tip behavior. However, for ψ other than zero (see Figure 4-8), the shear and normal displacements are coupled and the resulting elastic integral equation is much complex to invert. Therefore, to examine the validity of LEFM tip solution (i.e. $w(x) \approx x^{1/2}$) for the case of a fracture oriented arbitrarily with respect to material's principal axes, we consider the analytical solution for near tip displacements given by Sih et al. (1965).

4.10.1 Toughness Solution

For the fracture configuration shown in Figure 4-8, the displacements in the local *x*-axis (*u*) and *y*-axis (*v*) at a small distance *r* from fracture tip is given as

$$u(r,\theta) = K_I\sqrt{\frac{2r}{\pi}}\,\mathrm{Re}\left[\frac{(\mu_1 p_2\omega_2 - \mu_2 p_1\omega_1)}{\mu_1-\mu_2}\right] + K_2\sqrt{\frac{2r}{\pi}}\,\mathrm{Re}\left[\frac{(p_2\omega_2 - p_1\omega_1)}{\mu_1-\mu_2}\right]$$
$$v(r,\theta) = K_I\sqrt{\frac{2r}{\pi}}\,\mathrm{Re}\left[\frac{(\mu_1 q_2\omega_2 - \mu_2 q_1\omega_1)}{\mu_1-\mu_2}\right] + K_2\sqrt{\frac{2r}{\pi}}\,\mathrm{Re}\left[\frac{(q_2\omega_2 - q_1\omega_1)}{\mu_1-\mu_2}\right] \qquad (4.111)$$

where

$$p_i = b_{11}\mu_i^2 + b_{12} - b_{16}\mu_i$$
$$q_i = b_{12}\mu_i + \frac{b_{22}}{\mu_i} - b_{26}$$
$$\omega_i = \sqrt{\cos\theta + \mu_i \sin\theta}$$
$$i = (1,2)$$

θ is measured from the axis of fracture tip and taken positive in clockwise direction. μ_1 and μ_2 are complex roots of the characteristic Eq. 4.80 with positive imaginary parts.

Now, the displacement discontinuity near the fracture tip can be expressed as

$$\begin{aligned} D_n(r)_{r\to 0} &= v(r,\pi) - v(r,-\pi) \\ D_s(r)_{r\to 0} &= u(r,\pi) - u(r,-\pi) \end{aligned} \tag{4.112}$$

Substituting Eq. 4.111 into Eq. 4.112 and noting that ω_i takes the values $(0,-i)$ and $(0,i)$ as θ approaches π and $-\pi$ respectively, we obtain

$$\begin{aligned} D_s(r)_{r\to 0} &= 2\sqrt{\frac{2r}{\pi}}\left(H_{11}K_I + H_{12}K_{II}\right), \\ D_n(r)_{r\to 0} &= 2\sqrt{\frac{2r}{\pi}}\left(H_{21}K_I + H_{22}K_{II}\right), \end{aligned} \tag{4.113}$$

where

$$\begin{aligned} H_{11} &= \mathrm{Im}\left(\frac{\mu_2 p_1 - \mu_1 p_2}{\mu_1 - \mu_2}\right), \\ H_{12} &= \mathrm{Im}\left(\frac{p_1 - p_2}{\mu_1 - \mu_2}\right), \\ H_{21} &= \mathrm{Im}\left(\frac{\mu_2 q_1 - \mu_1 q_2}{\mu_1 - \mu_2}\right), \\ H_{22} &= \mathrm{Im}\left(\frac{q_1 - q_2}{\mu_1 - \mu_2}\right), \end{aligned} \tag{4.114}$$

When K_{II} =0 (which is the case when shear loading on the fracture is zero), near the fracture tip from Eq. 4.113, aperture is given by

$$w(x)_{x\to 0} = 2\sqrt{\frac{2x}{\pi}}\left(H_{21}K_I\right) \tag{4.115}$$

Finally, it is worth noting that for the special case considered in the previous section (i.e. ψ =0), the equation for near tip fracture aperture for arbitrarily oriented fracture (i.e. Eq. 4.115) will be reduced to Eq. 4.88,

This can be shown by expressing the complex roots as

$$\mu_1 = i\beta_1,\ \mu_2 = i\beta_2 \tag{4.116}$$

and substituting in Eq. 4.114 gives

$$H_{21} = b_{22}\frac{(\beta_1 + \beta_2)}{\beta_1\beta_2} \tag{4.117}$$

For the special case considered, the following property holds (Azhdari et al. 1999),

$$(\beta_1\beta_2)^2 = \frac{b_{22}}{b_{11}} \tag{4.118}$$

From Eqs. 4.117& 4.118, we obtain

$$H_{21} = \beta_1\beta_2(\beta_1 + \beta_2) \tag{4.119}$$

and

$$w(x) = 2\sqrt{\frac{2x}{\pi}}\beta_1\beta_2(\beta_1 + \beta_2)K_I \tag{4.120}$$

which is same as Eq. 4.88.

Therefore, the results (Eq. 4.115& 4.88) indicate that for an arbitrarily oriented fracture in an anisotropic body with non-zero fracture toughness, near the fracture tip, the aperture has square root variation similar to isotropic case.

4.10.2 Viscous Solution

The zero toughness near tip solution for a semi-infinite fracture propagating steadily with velocity V is derived (Appendix C) for the special case, where the axes of a fracture coincides with material's axes of elastic symmetry. In this special case, the shear dislocation density function $r'(\xi)$ is zero when fracture is free of shear stress, therefore the general form of elasticity equation (Eq. 4.79) is reduced to Eq. 4.83, which is easy to deal mathematically. For a more general case where fracture axes are at arbitrarily angle with respect to the axes of elastic symmetry, it is much

harder to obtain solution for elasticity equation (Eq. 4.79), since the shear dislocation density function $r'(\xi)$ will be non-zero. Without going through the complicated mathematical analysis to obtain near tip solution for general elasticity equation (Eq. 4.79), in this section, we will seek the conditions under which it is appropriate to use the near tip zero toughness solution obtained for the special case to a general case.

Consider a symmetrical fracture of length 2a with uniform net pressure P in plane strain condition in an infinite orthotropic body as shown in Figure 4-7. We will consider a case where the directions of elastic symmetry 1 and 3 are not aligned with the fracture axis *x*. For such a general case of fracture configuration, if $\alpha_1 + i\beta_1$ and $\alpha_2 + i\beta_2$ are the two complex roots of the characteristic equation (Eq. 4.80), the solution of fracture aperture is given as (Azhdari et al. 2000),

$$w(x) = 2b_{11}\sqrt{a^2 - x^2}P\left[\beta_1\left(\alpha_2^2 + \beta_2^2\right) + \beta_2\left(\alpha_1^2 + \beta_1^2\right)\right] \tag{4.121}$$

For the special case, based on the elasticity equation (Eq. 4.83), the solution for fracture aperture if the pressure inside the fracture is constant can be written as,

$$w(x) = 2b_{11}\sqrt{a^2 - x^2}P\left[\frac{\beta_1\beta_2\left(\left(\alpha_1 - \alpha_2\right)^2 + \left(\beta_1 + \beta_2\right)^2\right)}{\left(\beta_1 + \beta_2\right)}\right] \tag{4.122}$$

If we rewrite the terms inside the bracket of Eq. 4.121 as,

$$\frac{\left(\beta_1\alpha_2^2 + \beta_2\alpha_1^2\right)\left(\beta_1 + \beta_2\right) + \beta_1\beta_2\left(\beta_1 + \beta_2\right)^2}{\beta_1 + \beta_2} \tag{4.123}$$

and comparing Eq. 4.123 with the corresponding term in Eq. 4.122 shows that Eqs. 4.121& 4.122 are equal if,

$$\left(\beta_1\alpha_2^2 + \beta_2\alpha_1^2\right)\left(\beta_1 + \beta_2\right) = \beta_1\beta_2(\alpha_1 - \alpha_2)^2 \tag{4.124}$$

or

$$C = \left(\alpha_1\beta_2 + \alpha_2\beta_1\right)^2 = 0 \qquad (4.125)$$

Therefore, the general (Eq. 4.121) and special (Eq. 4.122) solutions for fracture aperture will converge if the constant C from Eq. 4.125 is negligible.

We will now consider numerical examples to study the error associated with approximating the fracture apertures for a general case with the solution obtained for special case (Eq. 4.122). For this, two rocks (Rock-A& Rock-B) are considered which are transversely isotropic. Rock-A has degree of anisotropy (E_1 / E_3) 4, and its properties listed in Table 3-1 are closely related to argillaceous shale (Suarez-Rivera et al. 2011). Rock-B has degree of anisotropy (E_1 / E_3) 1.8 and its properties listed in Table 3-2 belong to Woodford shale (Sierra et al. 2010). Figure 4-9 shows comparison of aperture profile over the entire fracture length in dimensionless values obtained from complete (Eq. 121) and approximate (Eq. 122) solutions for various values of ψ in Rock-A with P=1 MPa. The corresponding results for Rock-B are shown in Figure 4-10.

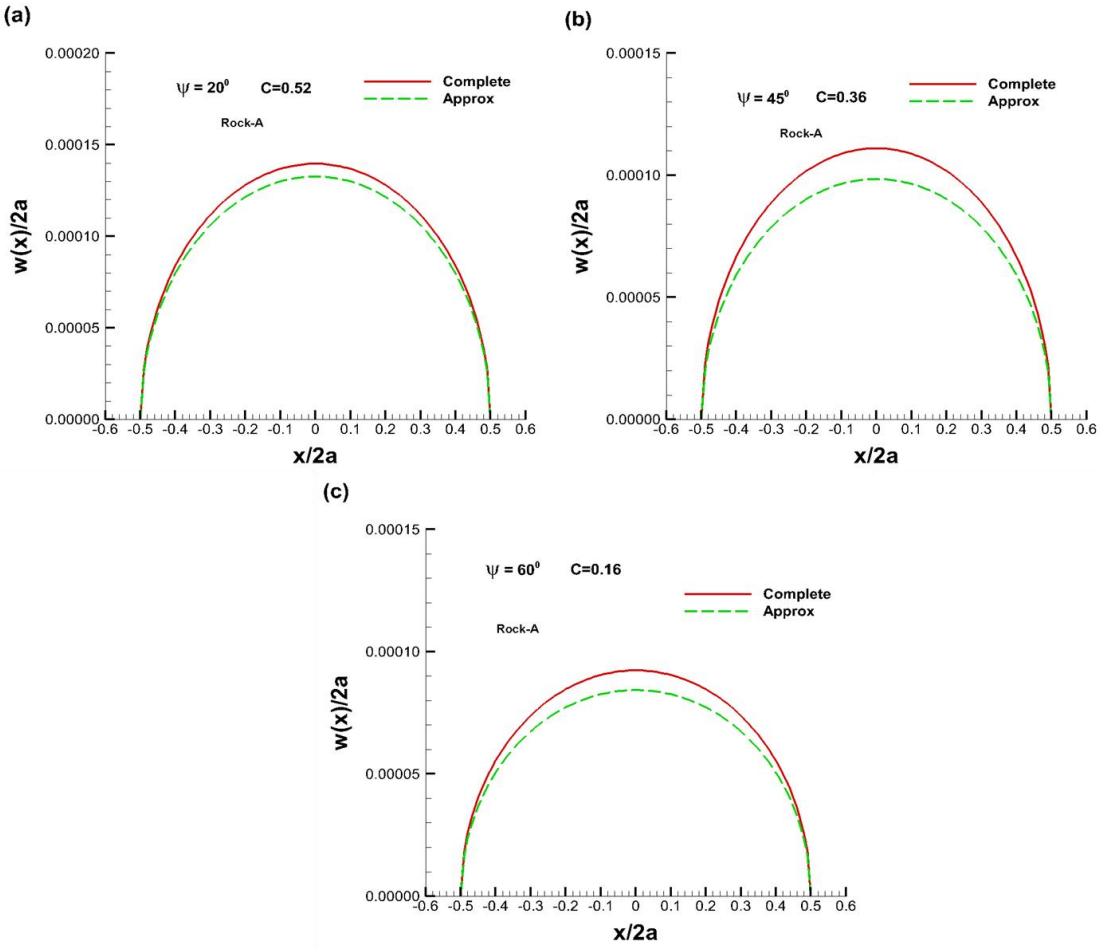

Figure 0-29. Comparison of fracture opening profiles between complete (Eq. 4.121) and approximate (Eq. 4.122) solutions for various orientations of fracture with respect to material's axes of elastic symmetry (see Figure 4-7) in Rock-A with properties given in Table 3-1. The net pressure P inside the fracture is 1 MPa.

The results indicate that considerable difference between the two solution is observed in Rock-A especially for ψ =45^0. In Rock-B, the difference between the two solutions is very small. This can be attributed to very low values of C (Eq. 125) observed in this Rock. Interestingly in both rocks, very near to the tip (i.e. up to 10% of fracture half-length from the tip) the difference between the two solutions is very small. In the region covering up to 5% of the fracture half-length from the tip, the difference between the solutions is almost negligible.

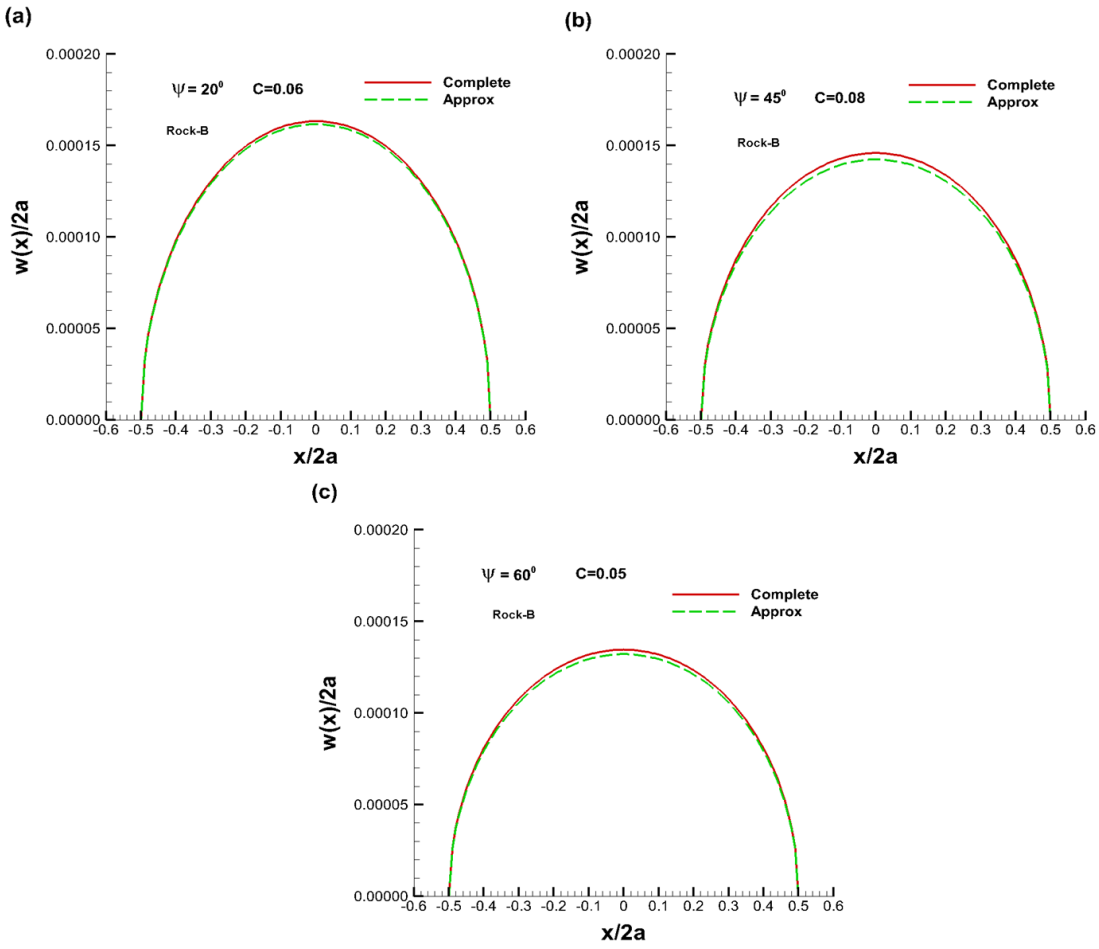

Figure 0-30. Comparison of fracture opening profiles between complete (Eq. 4.121) and approximate (Eq. 4.122) solutions for various orientations of fracture with respect to material's axes of elastic symmetry (see Figure 4-7) in Rock-B with properties given in Table 3-2. The net pressure P inside the fracture is 1 MPa.

Since we are only interested in finding the applicability of zero toughness near tip solution derived for the special case to a general case, it appears appropriate to ignore the influence of shear dislocation density $r'(\xi)$ in Eq. 79 on the near tip solution. Moreover, the loss of accuracy in global solution due to such approximation would be much smaller for materials like Rock-B, where the values of constant C are very small. Although, the above analysis is carried out with a uniformly pressurized fracture for simplicity, however, we may expect similar behavior in the case of viscous

fluid driven fracture considering that much of the fracture length has close to constant pressure, while significant pressure drop is limited to the region close to the fracture tips.

4.11 Summary

The near tip behavior of an arbitrary shape planar fracture driven by viscous fluid is considered through semi-infinite plane strain fracture in isotropic and anisotropic rocks with zero and non-zero fracture toughness. The global and near tip self-similar solutions for fracture aperture and pressure are extended to anisotropic rock for the special case where the fracture axes coincide with material's principal axes. This special case has significant practical importance considering that most shales are transversely isotropic rocks. Therefore, if the hydraulic fracture is vertical and bedding planes are horizontal, the fracture axes coincides with material's principal axes. In isotropic rock with non-zero fracture toughness, near the tip of fluid driven fracture, aperture varies from the order 1/2 to 2/3 with increase in distance from fracture tip. A similar behavior is observed in anisotropic rock for the special case considered. For more general case where a fracture is oriented arbitrarily with respect to material's principal axes, in a non-zero fracture toughness rock, the near tip aperture is of order 1/2 as in isotropic case. However, owing to the mathematical difficulty, the far-field solution (i.e. vicious solution) for the general case is not yet available.

The fracture propagation algorithm based on evolving fracture tip theory is dependent on fracture velocity (if propagation is in viscous regime) which is a priori unknown. Although one can include fracture velocity in the solution implicitly by inverting the zero toughness solution as shown previously, this algorithm has certain limitations on the kind of problems it can be applied to solve. Since, the zero fracture toughness solution (or viscous solution) is constructed based on the assumption that fracture surfaces have discontinuity of normal displacement only, in situations where fracture propagation is dominated by mixed mode, this solution is not applicable. Also, its

validity in rock with anisotropic fracture toughness is questionable. Therefore, the viscous solution from Eq. 4.14 is appropriate only for planar fracture or when radius of fracture curvature is very large compared to the scale of tip element where Eq. 4.14 is applied as boundary condition. More difficulties arise when complex fracture networks are considered, as the number of fracture tips that are subjected to different far-field stresses propagating at any given instant could be many. As a result, the propagation algorithm based on fracture front iteration could be inefficient and may not be stable. On the other hand, for problems where the aforementioned limitations does not exist, the viscous solution offer great computational advantage since the region of validity of viscous solution near the tip is much larger compared to LEFM solution. Therefore, this allows one to use larger size tip elements where viscous solution is used as boundary condition. Moreover, for rock and fluid properties typically associated with petroleum applications, the LEFM tip solution is adequate as a tip boundary condition irrespective of the regime of fracture propagation (see Sesetty and Ghassemi, 2017a), therefore, in these problems the choice of near tip boundary condition is a matter of convenience rather based on near tip physics.

5 Coupled Numerical Model for Fracture Propagation

5.1 Fracture Propagation Algorithm

5.1.1 Viscous Regime

In order to use fracture tip solution for viscous regime (Eq. 4.89) one needs to evaluate fracture tip velocity. If we fix the fracture length increment (dL) at any given time step, then the mass balance provides the time increment (dt) as output. Similarly, if we fix the time increment, the mass balance provides the length increment of the fracture as output. Since either time or length is an unknown for each solution step, the fracture velocity (i.e. dL/dt) is a priori unknown and is a part of the solution. One way to evaluate the fracture tip velocity is to use the lubrication Equation (Eq. 4.12), near the tip. However, such an approximation for fracture tip velocity can result in serious errors because near the tip the aperture approaches zero and pressure approaches a singularity. An alternative way is to make use of the zero fracture toughness aperture solution to eliminate the explicit use of V in the tip solution as given in Peirce and Detournay, (2008).

5.1.2 Toughness Regime

Implementing fracture tip solution for toughness regime is relatively easier compared to fracture tip solution for viscous regime. We consider the initial conditions of the problem are given (i.e., the initial fracture size and apertures), and let *dt* be the time increment for the next solution. Using a no flow boundary condition at the fracture tips (Eq. 4.47) solve the coupled problem (Eqs. 4.43& 4.45) for new fracture apertures and pressures. Evaluate stress intensity factors at all fracture tips. Using a bracketing method find *dt* such that the stress intensity factor at least at one of the fracture tips is within the tolerance of fracture toughness. For the fractures that met the propagation condition (i.e. $K_I=K_{IC}$), add a new element and move the problem to the next time step. It is clear

from the above discussion that the accuracy of this algorithm depends on the accuracy of stress intensity factors evaluated based on numerical solution. In this work, constant displacement discontinuity method is used to solve fracture deformation problem with special square root elements at fracture tips. The mode-1 stress intensity factor is evaluated using Eq. 4.5 by replacing *w(x)* with fracture tip element normal displacement discontinuity and *x* with half-length of fracture tip element.

5.2 Verification

In this section the numerical method for coupled fracture propagation problem is verified against semi-analytical solutions for two limiting cases that corresponds to viscous regime and toughness regime. Figure 5-1 (a, b) shows comparison of self-similar fracture aperture and net pressure profiles obtained semi-analytically (Eqs. 4.62& 4.63) and numerically for the case of a line fracture (see Figure 4-6) under plane strain condition propagating in zero fracture toughness isotropic medium. The results for orthotropic body are shown in Figure 5-1 (c, d). Note that the self-similar solutions for fracture aperture and pressure in both isotropic and orthotropic bodies is same. For numerical case, the elastic integral equations (Eq. 4.43& 4.83) are approximated using constant displacement discontinuity method, while finite difference method is used to approximate lubrication equation (Eq. 4.45). In all the numerical examples considered in this work, a uniform mesh with element size 0.2 m is used unless stated otherwise. The results show excellent match between semi-analytical and numerical solutions. On the other hand, when fracture toughness of the rock is significantly high, the numerical solution is compared with the limiting analytical solution from Eq. 4.74 with the input E'=28.8 GPa and Q_0=8.83e-4 m^2/s. Figure 5-2 shows excellent match between numerical and analytical solutions in this limiting case as well, which

reflects the high accuracy achieved in stress intensity factor evaluation trough special square root elements.

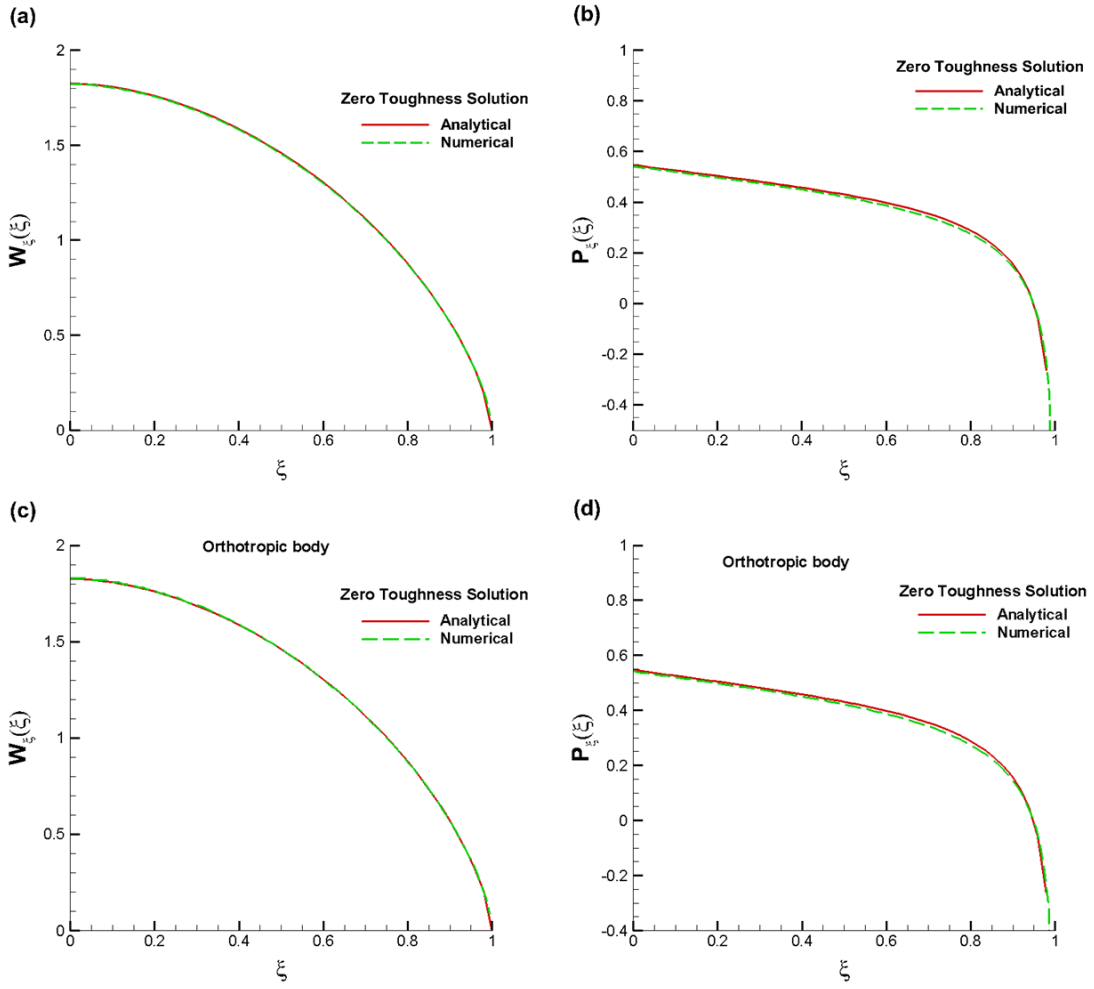

Figure 0-31. Verification of numerical model with the limiting case zero fracture toughness self-similar analytical solution for isotropic body (a, b) and orthotropic body (c, d). Note that self-similar solution does not change between isotropic and anisotropic bodies.

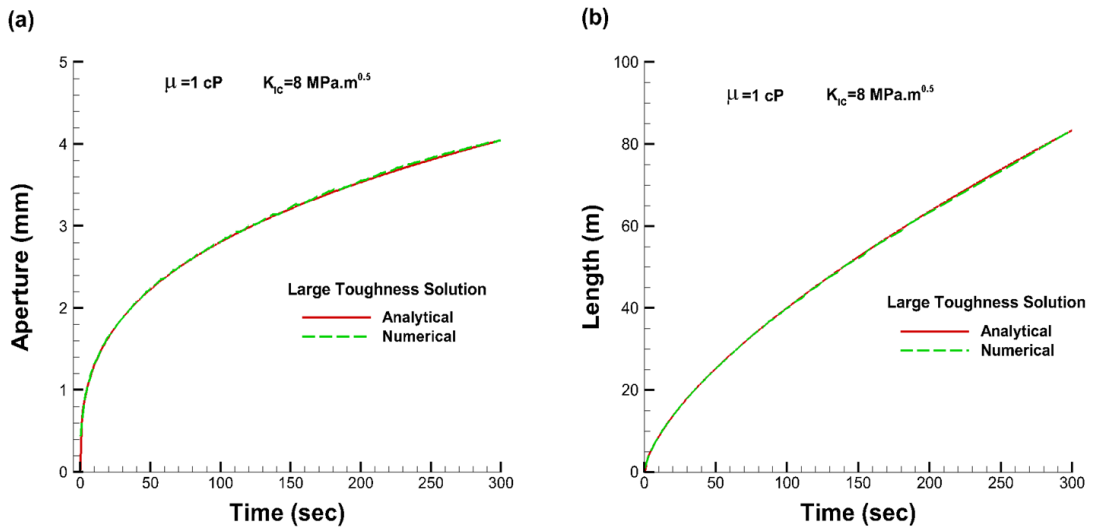

Figure 0-32. Verification of numerical model with analytical large fracture toughness solution for isotropic rock.

5.3 Comparison with KGD solution

The fundamental difference between the KGD solution (Khristianovitch; Geertsma and Haafkens, 1979; Geertsma and DeKlerk, 1969) and the self-similar solutions for the limiting cases (i.e., zero fracture toughness and large fracture toughness) given earlier is in the boundary conditions used to solve to the governing equations for fracture propagation. Initial work by Zheltov and Khristianovitch, (1955) suggested the existence of fluid-lag near the fracture tips in order avoid indefinite tensile stresses near the fracture tips associated with LEFM solution. He assumed that a fracture with un-wetted region near the fracture tips closes smoothly (as in the case $w \approx x^{3/2}$ in Figure 2b). In such cases, the aperture profile near the fracture tip is,

$$\left.\frac{dw}{dx}\right|_{x\to+a,-a} = 0 \qquad (5.1)$$

The above condition (i.e. zero slope) is used to solve the elasticity equation (Eq. 4.43). This boundary condition also implies that the rock has negligible fracture toughness as discussed

previously (see Eq. 4.5). Moreover, the effect of fracture storage on flux changes inside the fracture is ignored. Therefore, the continuity equation (Eq. 4.44) is simplified to,

$$\frac{dq}{dx} = 0 \tag{5.2}$$

Using the conditions (Eqs. 5.1& 5.2), the elasticity equation for a symmetrical line fracture under plane strain condition (Eq. 4.43) and fluid flow (Eq. 4.11) are solved for fracture aperture, pressure and length. The aperture estimate at injection point and fracture half-length are given as,

$$\begin{aligned} w(0) &= 0.979224\left(\frac{\mu' Q_0^{\,3}}{E'}\right)^{1/6} t^{1/3} \\ a &= 0.64704\left(\frac{E' Q_0^{\,3}}{\mu'}\right)^{1/6} t^{2/3} \end{aligned} \tag{5.3}$$

Note that the above expressions are independent of fracture toughness; therefore, we can consider KGD solution as an approximate zero fracture toughness solution or viscous solution. Also, in KGD solution, consideration of un-wetted region near the tip is simply theoretical and is not included in the final solution (Eq. 5.3), since the aperture and length integrations are carried out in the limit of the fluid approaching the tip.

Using the relationship between physical variables and dimensionless constants (Eqs. 4.49, 4.50& 4.54) and the self-similar solution for the case of zero fracture toughness from Eq. 4.62, the fracture aperture at the injection point and fracture half-length can be expressed as

$$\begin{aligned} w(0) &= 1.123294\left(\frac{\mu' Q_0^{\,3}}{E'}\right)^{1/6} t^{1/3} \\ a &= 0.61524\left(\frac{E' Q_0^{\,3}}{\mu'}\right)^{1/6} t^{2/3} \end{aligned} \tag{5.4}$$

Let us call this solution as a true solution for the case where fracture toughness can be ignored. Comparing the above solution with the KGD solution (Eq. 5.3) indicates that these differ only by

a constant multiplication factor. Figure 5-3 shows comparison between KGD solution, true solution and numerical solution for the input E'=28.8 GPa and Q_0=8.83e-4 m^2/s.

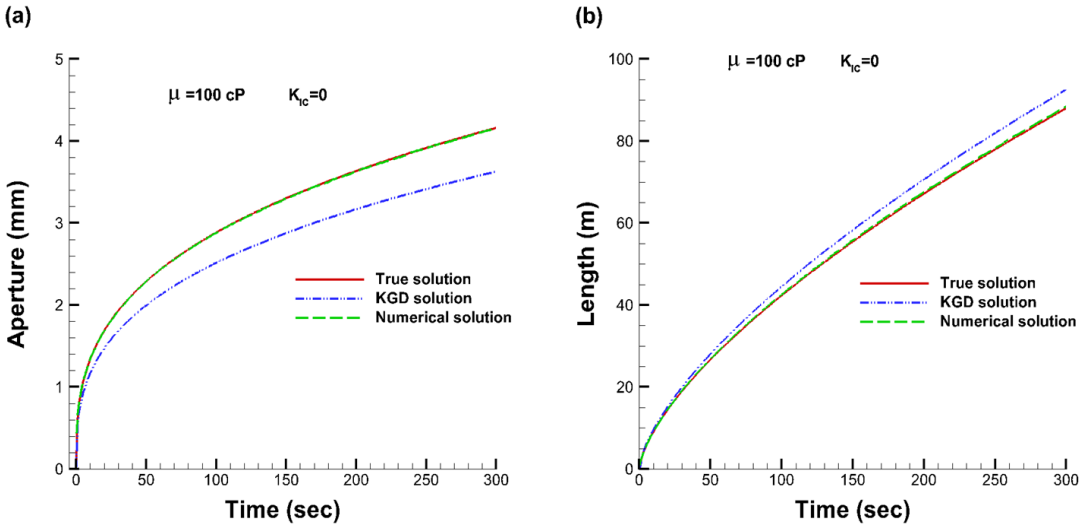

Figure 0-33. Comparing numerical solution with true and KGD solutions.

The results indicate that KGD solution is significantly off from the true solution especially the estimation of fracture aperture. The use of simplified continuity equation (Eq. 5.2), tip boundary condition (Eq. 5.1) instead of Eq. 4.14 can be the cause of the error associated with KGD solution. Note that most literature do not illustrate these differences in solutions.

6 Effect of Rock Anisotropy on Fracture Extension Angle and Path

Consider a straight fracture that is in plane strain condition in an infinite orthotropic body. The *x-y* plane view of the orthotropic body is shown in Figure 6-1, where the directions of axes of elastic symmetry are represented by 1 and 2. The angle between material's axis 1 and the coordinate axis *x* is represented by ψ. The angle between fracture major axis and *x*-axis is denoted by γ. The fracture extension angle is measured from fracture tip axis as shown in Figure 6-1, and is denoted by ω. All angles are taken positive in anticlockwise direction. Since, in a typical anisotropic rock, the maximum value of fracture toughness ($K_{IC,\max}$) occurs (Chandler et al. 2015) in the plane perpendicular to the direction of maximum Young's modulus (typically the direction of rock fibers/bedding planes) and minimum value of fracture toughness ($K_{IC,\min}$) is observed in the plane parallel to the direction of maximum Young's modulus, the two extrema values $K_{IC,\max}$ and $K_{IC,\min}$ are related through an elliptical equation to find fracture toughness in any arbitrary plane. Assuming that anisotropic body is linearly elastic, homogeneous and brittle in nature, in this chapter we will review some well recognized criterions available to evaluate fracture propagation angle in an orthotropic body. These criterions are straight forward extensions of the theories developed for isotropic body based on linear elastic fracture mechanics.

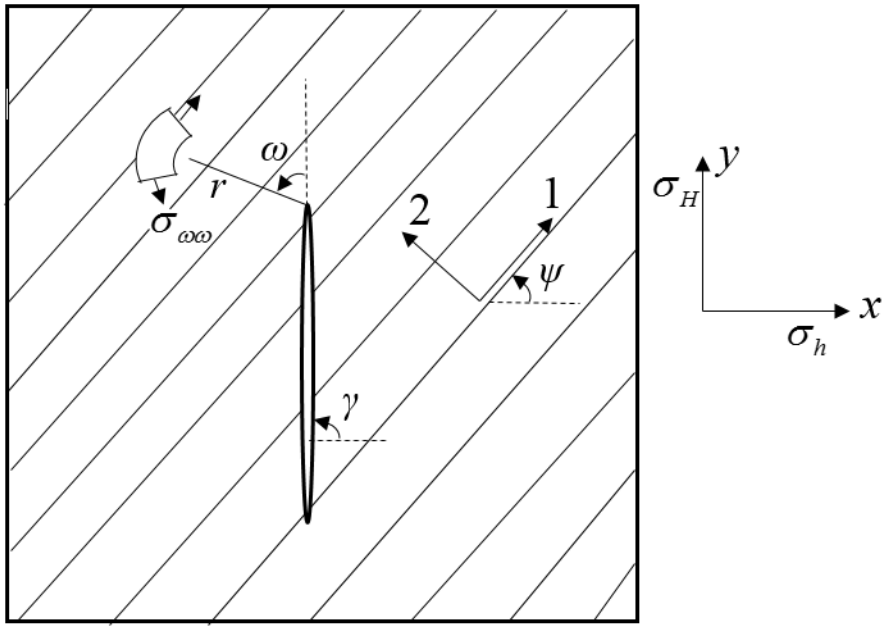

Figure 0-34. Cross-section of an infinite orthotropic body showing *x*-*y* plane view with a straight fracture in plane strain condition. The angle between fracture axis and *x*-axis is γ. The direction of material fibers or bedding planes (black parallel lines) is indicated by axis 1 and its angle with respect to *x*-axis is indicated by ψ. Fracture tip extension angle is measured from tip axis is indicated by ω. All angles are taken positive counterclockwise.

6.1 Criterions for Fracture Extension Angle

6.1.1 Maximum Energy Release Rate Criterion

This criterion is initially postulated by Griffith for isotropic body and is extended to anisotropic case by Sih et al 1965. Suppose *U* is the surface energy (i.e. energy required to break the internal bonds to create new surface) of the fracture and *W* is the decrease in strain energy due to fracture extension, then the fracture equilibrium condition implies that

$$\frac{\partial U}{\partial l} = \frac{\partial W}{\partial l} \tag{6.1}$$

where ∂W defines strain energy release due to extension of fracture by length ∂l and ∂U denotes energy required to form the new fracture surface. Since *U* can be expressed in terms of surface

tension (which is treated as constant for a given material), we consider $\partial U / \partial l$ as a material property.

We can also express the energy release due to fracture extension in terms of fracture toughness of the material. The energy (δA) release due to extension of fracture by a small amount (δl) can be expressed as (Barenblatt, 1962)

$$\delta A = \int_{\delta l} \sigma u_n \partial l \tag{6.2}$$

where u_n denotes normal displacements σ is tensile stress field and over the elongation δl. For isotropic body, under pure mode-1 loading (after substituting the corresponding displacement and stress expressions in Eq. 6.2) we get,

$$\delta A = \frac{2\pi(1-v^2)K_1^2 \delta l}{E} \tag{6.3}$$

where K_I is mode-1 stress intensity factor, *v* is Poisson's ratio and *E* is Young's modulus. Now the fracture equilibrium condition (Eq. 6.1) can be written as

$$\frac{\delta W}{\delta l} = \frac{\delta A}{\delta l} = \frac{2\pi(1-v^2)K_{IC}^2}{E} \tag{6.4}$$

where K_{IC} is called critical stress intensity factor or fracture toughness which is a material property. The corresponding equation (as Eq. 6.4) for anisotropic body is rather complicated however can be evaluated (see Azdhari, 1999) with the stress and displacement terms near the tip given in Appendix C. The fracture is assumed to propagate by a length δl in the direction where δA from Eq. 6.2 is maximum.

6.1.2 Minimum Strain Energy Density Criterion

This criterion is postulated by Sih, (1974), also called the S-criterion states that fracture tip propagates in the direction where the strain energy density has the lowest value. The strain energy density can be expressed as

$$\frac{dW}{dV} = \frac{1}{2}\left(\sigma_x \varepsilon_x + \sigma_y \varepsilon_y + \sigma_{xy} \varepsilon_{xy}\right) \tag{6.5}$$

where σ_i and ε_i are near tip stress and strain fields in the coordinate system *x-y-z* (see Figure 6-1). Using the equations of stress-strain relationship in orthotropic body and expressions for stress distribution near the fracture tip from Appendix C, the strain energy density function in Eq. 6.5 can be written in terms of stress intensity factors and material elastic constants and it can be evaluated for a given fracture extension angle ω. Fracture propagation begins when strain energy density term in Eq. 6.5 reaches its critical value $dW_c / \partial V$ which is obtained by replacing stress intensity factors in Eq. A1-A3 with their critical values. In this criterion the directional variation of material strength can be easily incorporated (Ye and Ayari, 1994).

6.1.3 Maximum Tangential Stress Criterion

Another hypothesis for fracture propagation that is based on near tip stress field states that fracture tip extends in the direction perpendicular to the maximum tangential stress (i.e. principal value) (Erdogan and Sih, 1962; Saouma et al., 1987). The near tip stresses in the coordinate frame *x-y-z* for anisotropic body are given in Appendix C. For isotropic body these stresses can be found in (Erdogan and Sih, 1962) and the direction of fracture propagation is given as (Stone and Babuska, 1997)

$$\omega(K_I, K_{II}) = \begin{cases} 0 & if\ K_{II} = 0 \\ 2\arctan\left(\dfrac{\dfrac{K_I}{K_{II}} - \mathrm{sgn}(K_{II})\sqrt{\left(\dfrac{K_I}{K_{II}}\right)^2 + 8}}{4} \right) & if\ K_{II} \neq 0 \end{cases} \tag{6.6}$$

However, in the case of anisotropic body, due to the complexity of stress equations (Appendix C) a simple analytical expression for fracture propagation angle (such as Eq. 6) cannot be obtained. Instead, a numerical approach (such as bisection method) is considered to find the direction that corresponds to the maximum value of tangential stress around the fracture tip.

For a given fracture under load, if K_I and K_{II} are mode-1 and mode-2 stress intensity factors respectively and ω is the fracture propagation angle, then the hypothesis states that in isotropic body, fracture is in equilibrium condition when

$$\sigma_{\omega\omega}(2\pi r)^{1/2} = \cos\frac{\omega}{2}\left[K_I \cos^2\frac{\omega}{2} - \frac{3}{2}K_{II}\sin\omega \right] = K_{IC} \tag{6.7}$$

or

$$\frac{\cos\dfrac{\omega}{2}\left[K_I \cos^2\dfrac{\omega}{2} - \dfrac{3}{2}K_{II}\sin\omega \right]}{K_{IC}} = 1 \tag{6.8}$$

Using the equations for near tip stress field in an orthotropic body in the coordinate system x-y-z (Eq. A1-A3) and equation of stress transformation (Eq. A4), the tangential stress distribution around the tip of a fracture in an orthotropic body can be expressed as (Saouma et al., 1987),

$$\sigma_{\omega\omega} = \frac{1}{(2\pi r)^{1/2}}\left[K_I\,\mathrm{Re}\left[A\left(\mu_1 B - \mu_2 C\right)\right] + K_{II}\,\mathrm{Re}\left[A\left(B - C\right)\right]\right] \tag{6.9}$$

where

$$A = \frac{1}{\mu_1 - \mu_2}$$
$$B = \left(\mu_2 \sin\omega + \cos\omega\right)^{3/2} \tag{6.10}$$
$$C = \left(\mu_1 \sin\omega + \cos\omega\right)^{3/2}$$

μ_1 and μ_2 are the complex roots of the characteristic equation (Eq. A6) with positive imaginary parts.

In anisotropic body, one has to account the directionally varying material strength. Therefore, if ω is fracture propagation angle, the fracture equilibrium condition can be expressed as

$$\sigma_\omega (2\pi r)^{1/2} = K_I \,\mathrm{Re}\left[A\left(\mu_1 B - \mu_2 C\right)\right] + K_{II}\,\mathrm{Re}\left[A\left(B - C\right)\right] = K_{IC,\max}\cos^2(\psi+\omega) + K_{IC,\min}\sin^2(\psi+\omega) \tag{6.11}$$

or

$$\frac{K_I \,\mathrm{Re}\left[A\left(\mu_1 B - \mu_2 C\right)\right] + K_{II}\,\mathrm{Re}\left[A\left(B - C\right)\right]}{K_{IC,\max}\cos^2(\psi+\omega) + K_{IC,\min}\sin^2(\psi+\omega)} = 1 \tag{6.12}$$

where $K_{IC,\max}$, $K_{IC,\min}$ denotes maximum and minimum fracture toughness values of the material and an elliptical equation is used to find fracture toughness in an arbitrary plane. Note that when ψ and ω are zero (see Figure 6-1), the fracture is perpendicular to the direction of bedding planes/fibers and the fracture toughness value becomes maximum $K_{IC,\max}$ in Eqs. 6.11& 6.12. The fracture propagation angle ω is obtained by maximizing Eq. 6.12 or its normalized equivalent given below,

$$\sigma^*_{\omega\omega} = \frac{\mathrm{Re}\left[A\left(\mu_1 B - \mu_2 C\right)\right] + \dfrac{K_{II}}{K_1}\mathrm{Re}\left[A\left(B - C\right)\right]}{\dfrac{K_{IC,\max}}{K_{IC,\min}}\cos^2\omega + \sin^2\omega} \tag{6.13}$$

In fracture propagation algorithm, if stress intensity factors K_I and K_{II} at a fracture tip are given, first the fracture propagation angle ω is obtained using Eq. 6.6 for isotropic body or maximizing Eq. 6.12/6.13 in anisotropic body. The condition for fracture extension can be verified by substituting ω, K_I and K_{II} in Eqs. 6.8 and 6.12 for isotropic and anisotropic bodies respectively. Finally, it should be noted that there is no clear consensus on single criterion among those discussed above that adequately describes fracture propagation path in anisotropic body, since it was observed that for the same input parameters different criterions produce different results. For example, fracture propagation path considered using energy release rate criterion indicated non-planar growth when a planar fracture subjected to pure mode-1 loading is inclined with respect to material's axes of elastic symmetry, whereas, the other criterions indicated co-linear growth for the same problem (Azdhari, 1996; Laubie, 2013). Similarly, fracture propagation angle under mixed mode loading evaluated using strain energy density method is different from that obtained using maximum tangential stress method (Gdoutos and zacharopoulos, 1989). In addition, the lack of extensive experimental studies demonstrating the effect of fracture strength anisotropy on fracture propagation especially in rocks makes it difficult to choose a single criterion. However, the few available experiments on rock samples (Ke et al. 2008; Luo et al. 2018) favor the maximum tangential stress criterion which will be discussed below in greater detail. Also, experiments on composite fibers with significant strength anisotropy (Beuth et al., 1986) revealed that only maximum tangential stress theory provides relatively better accuracy in predicting the fracture extension angle when compared to the other theories. Due to these reasons, as well as due to the mathematical simplicity in evaluating fracture extension angle, in this work we adopt maximum tangential stress criterion. Since the hypotheses for fracture propagation direction is based only on the near tip stress field, the effect of the fracture loading kind on fracture propagation direction is

contributed only through the stress intensity factors. As a result, in fluid driven fractures, the effect of viscosity (and the resulting pressure gradient inside the fracture) on fracture propagation direction is captured through only stress intensity factors.

6.2 Effect of Rock Anisotropy on Fracture Extension Angle

In this section we will study the effect of material elastic anisotropy and material strength anisotropy on fracture extension angle (ω) using maximum tangential stress criterion. First the distribution of normalized tangential stresses ($\sigma^*_{\omega\omega}$ from Eq. 6.13) around a fracture tip is investigated for different orientations of fracture with respect to axes of elastic symmetry for a case where mode-2 stress intensity factor K_{II} is zero. The material chosen is argillaceous shale which is a transversely isotropic rock with degree of anisotropy 4 (defined as the ratio of Young's modulus parallel to the bedding, E_1 and Young's modulus perpendicular to the bedding, E_2). For simplicity we name this rock as Rock-A and its elastic properties are given in Table 6-1. We also define degree of toughness anisotropy (TA) which is the ratio of maximum ($K_{IC,\max}$) and minimum ($K_{IC,\min}$) fracture toughness values. If material has uniform fracture toughness then TA is one.

Table 0-5. Properties of Rock-A

E_1 (GPa)	E_3 (GPa)	E_2 (GPa)	ν_{13}	ν_{12}	G_{12} (GPa)	$K_{IC,max}$ (Mpa.m$^{1/2}$)
40	40	10	0.15	0.185	7.45	2.0

Table 0-6. Properties of Rock-E

E_1 (GPa)	E_3 (GPa)	E_2 (GPa)	ν_{13}	ν_{12}	G_{12} (GPa)
60	60	10	0.15	0.25	7.93

Table 0-7. Properties of Rock-B

E_1 (GPa)	E_3 (GPa)	E_2 (GPa)	ν_{13}	ν_{12}	G_{12} (GPa)
19.6	19.6	10.4	0.166	0.25	5.0

Figure 2a shows normalized tangential stress distribution ($\sigma^*_{\omega\omega}$) around a fracture tip in Rock-A for various ψ when K_{II} =0 and TA=1. The results indicate that stress distribution is symmetric around the fracture tip in anisotropic rock only when fracture is aligned with one of the axes of elastic symmetry (i.e. ψ =0^0/90^0). However, it appears that the location of maximum tangential stress remained unchanged at zero degrees except for the case of ψ =90^0. When ψ =0^0 (i.e. fracture perpendicular to bedding), the distribution of $\sigma^*_{\omega\omega}$ is characterized by sharp increase at ω =0^0. On the other hand when ψ =90^0 (i.e. fracture parallel to bedding), the distribution of $\sigma^*_{\omega\omega}$ has the shape of a plateau near ω =0^0, and the maximum value of $\sigma^*_{\omega\omega}$ slightly shifted away from ω =0^0 to ω =6.2^0/-6.2^0. Figure 6-2(b) shows distribution of $\sigma^*_{\omega\omega}$ for different TA when ψ =0^0. The results indicate that with increase in fracture toughness anisotropy, the chances of co-linear fracture propagation is reducing as the location of maximum $\sigma^*_{\omega\omega}$ shifted from ω =0^0 in uniform toughness rock to ω =-65.5^0/65.5^0 in rock with TA=4. On the other hand when ψ =90^0, the changes of co-linear propagation increases significantly with increase in fracture toughness anisotropy according to Figure 6-2c. Therefore, in this case fracture will propagate along the bedding planes/fibers.

Figure 6-3 shows fracture extension angle ω as a function of ψ in Rock-A for different values of toughness anisotropy when a fracture is subjected to pure mode-1 loading (K_{II} / K_I =0), mixed mode loading (K_{II} / K_I =1) and mode-2 dominated loading (K_{II} / K_I =10). The results indicate that when fracture toughness is uniform and mode-2 stress intensity factor K_{II} =0, co-linear fracture propagation occurs in Rock-A for all ψ <86^0.

When ψ =90^0 the fracture extension angle becomes zero only with increase in TA. In all other cases, we found that fracture extension angle is non-zero. Under mixed mode and mode-2 dominated loading it appears that even moderate increase in toughness anisotropy (i.e. TA=2) causes considerable change in fracture extension angles. We also observed that under mixed mode and mode-2 dominated loading, the orientation of fracture with respect to the axes of elastic symmetry (i.e. ψ) has considerable effect on fracture extension angles even when TA=1. It is interesting to note that, in all the loading types considered, there exists a ψ , where the fracture extension angle ω is same for degrees of toughness anisotropy (which is represented by an intersection point of all the lines in Figure 6-3). Finally it is worth noting that in isotropic rock, based on Eq. 6.6, fracture extension angle ω for cases K_{II} / K_I =0 is 0^0, K_{II} / K_I =1 is -53.13^0 and K_{II} / K_I =10 is -68.63^0.

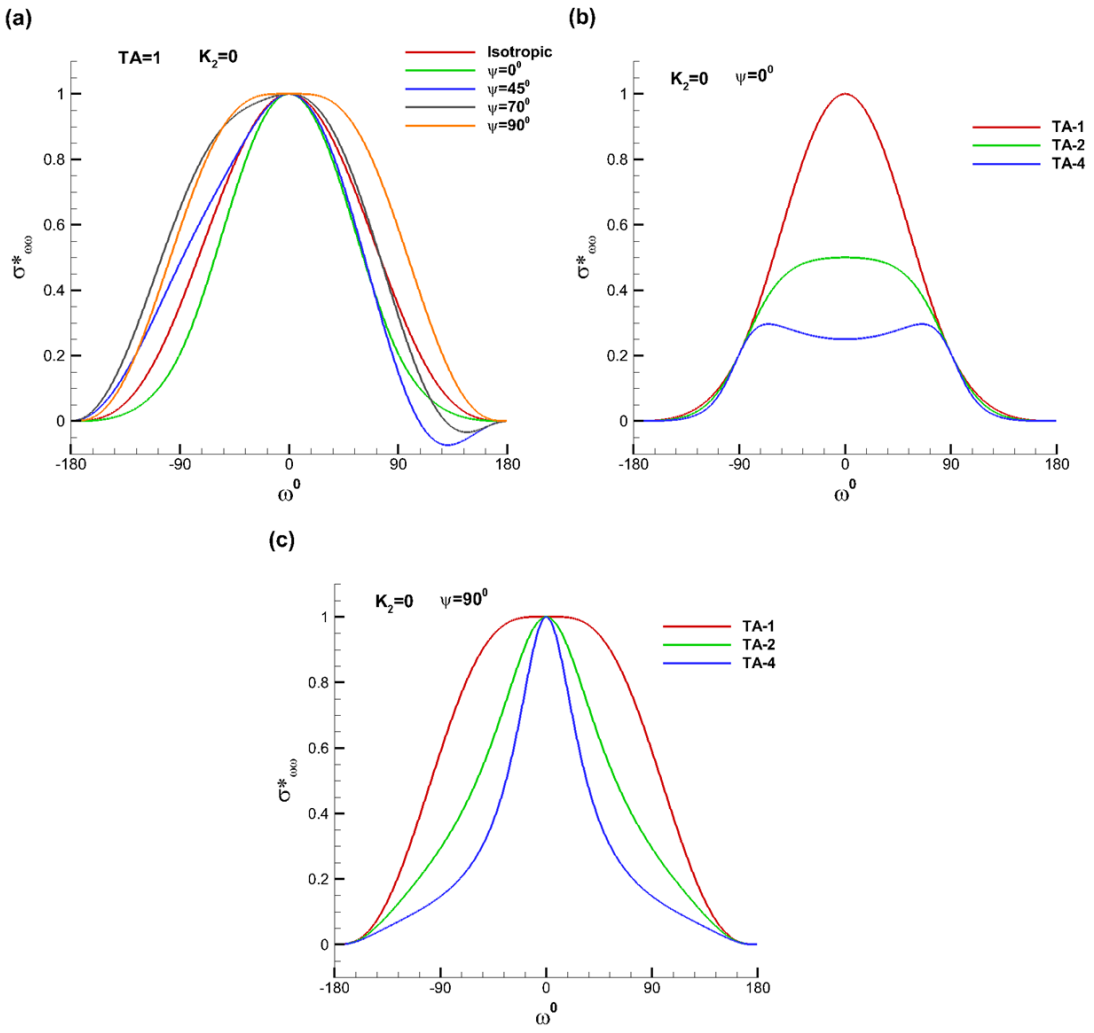

Figure 0-35. Distribution of normalized $\sigma^*_{\omega\omega}$ around the fracture tip in Rock-A which is subjected to pure mode-1 loading. (a) Shows the effect of ψ when rock fracture toughness is uniform (TA=1), (b) the effect of degree of fracture toughness anisotropy (TA) for cases ψ =0^0, (c) and for ψ =90^0.

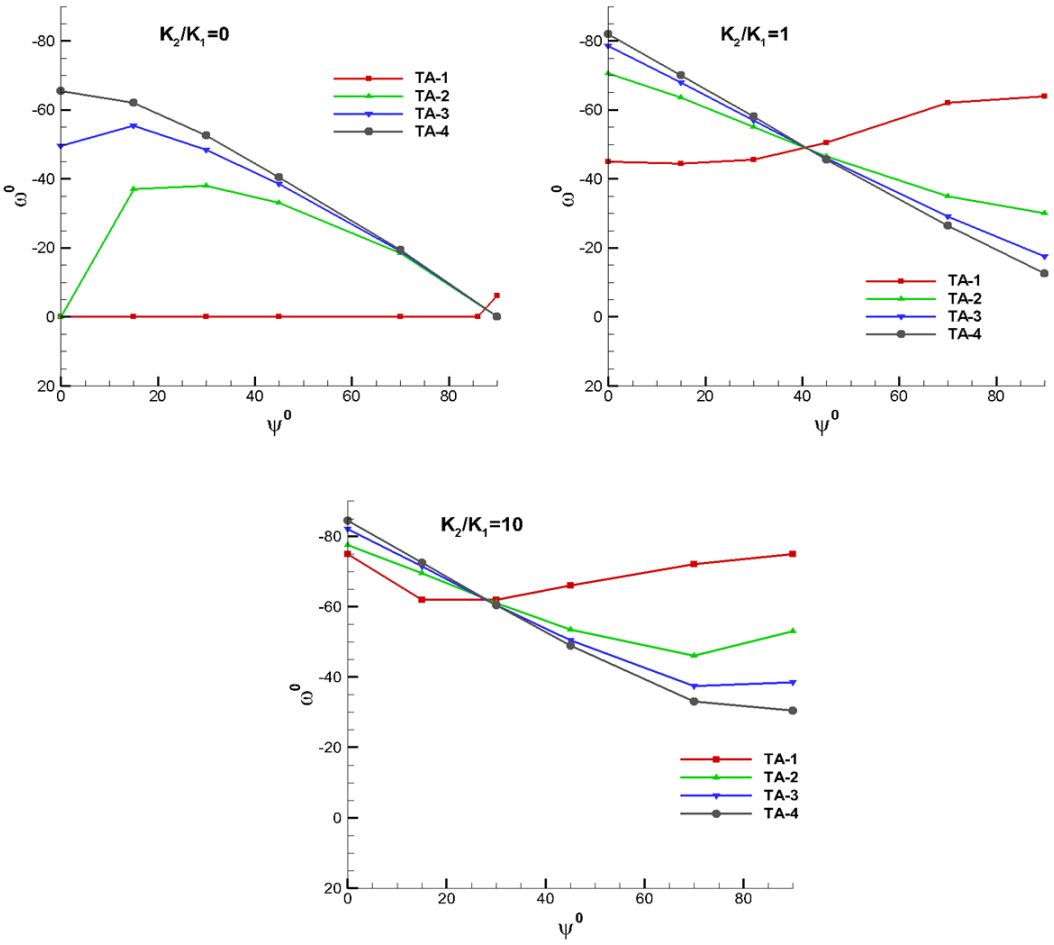

Figure 0-36. Shows the effect of loading condition (K_{II}/K_I), the orientation of bedding planes/fibers (ψ) and the degree of fracture toughness anisotropy (TA) on fracture extension angle (ω) in Rock-A.

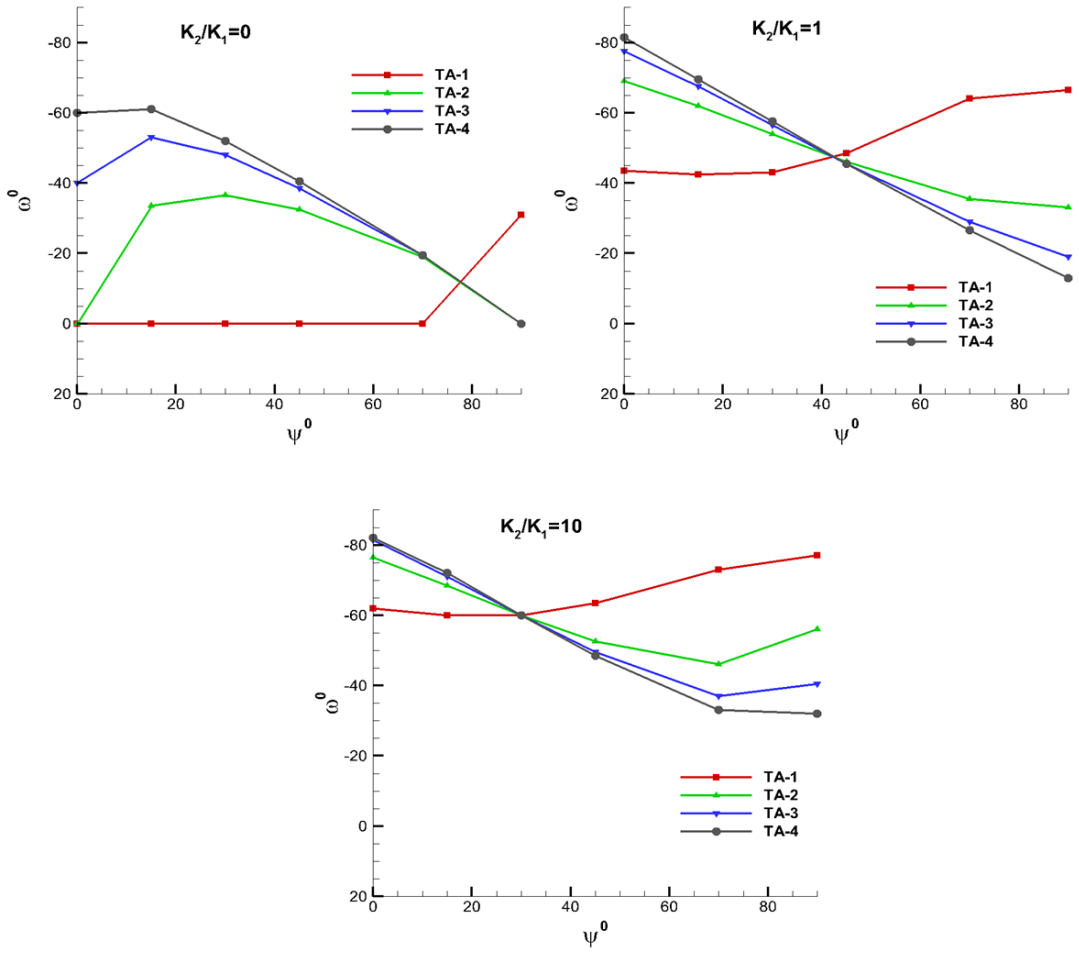

Figure 0-37. Shows the effect of loading condition (K_{II} / K_I), the orientation of bedding planes/fibers (ψ) and the degree of fracture toughness anisotropy (TA) on fracture extension angle (ω) in Rock-E.

Figure 6-4 shows fracture extension angle ω as a function of ψ for different loading conditions in Rock-E, which is a hypothetical transversely isotropic rock with strong degree of anisotropy 6. The elastic properties of the rock are given in Table 6-2. The results indicate that the behavior of ω as a function ψ is similar to Rock-A. Due to high degree of anisotropy in Rock-E, we see that the fracture extension angle under pure mode-1 loading when TA=1 and ψ =90^0 is -31^0 compared

to only -6.2^0 degree in Rock-A. We also notice strong dependency between fracture extension angle ω and ψ under mixed mode and mode-2 dominated loading when TA=1, similar to Rock-A.

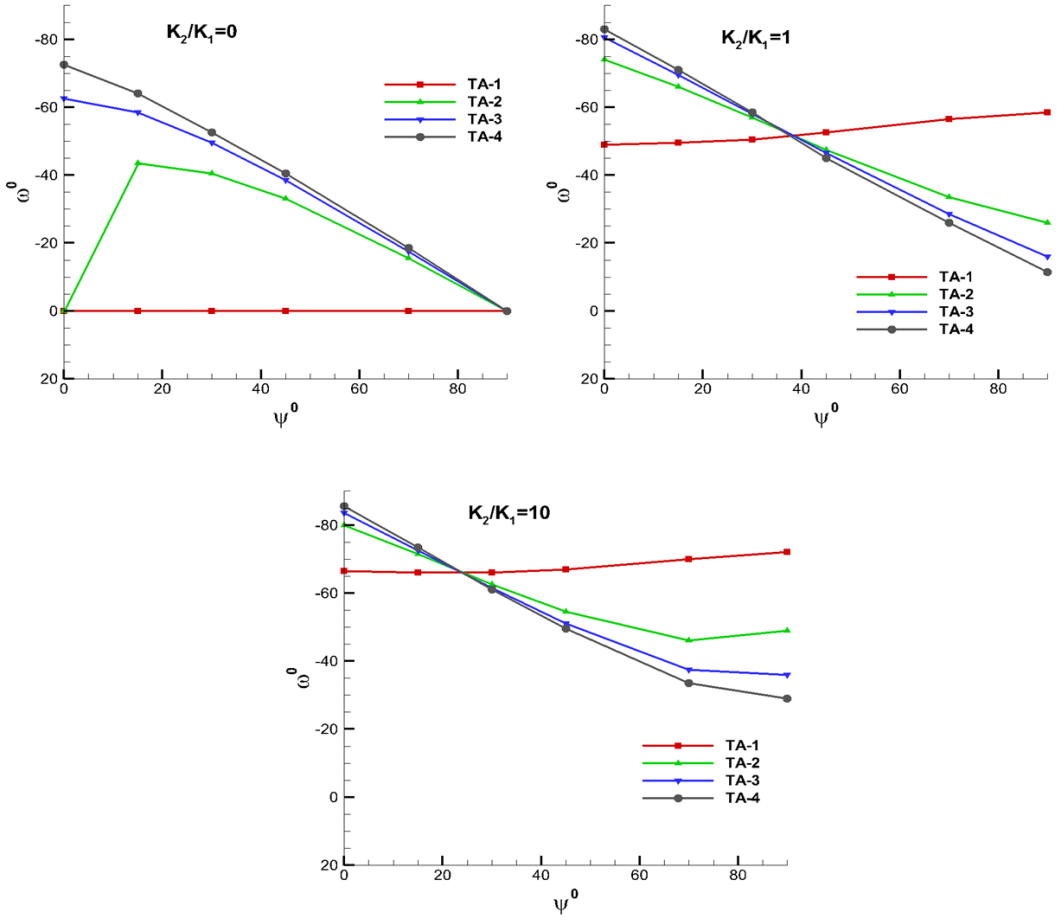

Figure 0-38. Shows the effect of loading condition (K_{II}/K_I), the orientation of bedding planes/fibers (ψ) and the degree of fracture toughness anisotropy (TA) on fracture extension angle (ω) in Rock-B.

Figure 6-5 shows fracture extension angle ω as a function of ψ under different loading conditions in Rock-B, which is a transversely isotropic belonging to Woodford shale with degree of anisotropy 1.88. The elastic properties of this rock are given in Table 6-3. In this moderately anisotropic rock, we found that fracture observe co-linear propagation for all ψ when fracture toughness is uniform, TA=1. Also, it appears that under mixed mode and mode-2 dominated

loading, the influence of ψ on fracture extension angle is not significant when TA=1 unlike in Rock-A and Rock-E. The general trend of curves showing the variation for ω as a function of ψ for different TA is same are previous rocks.

Overall these results indicate that strong material anisotropy can contribute to non-planar fracture propagation even when fracture toughness is uniform if the fracture is oriented along the bedding planes (however, this behavior might be unlikely as most strongly anisotropic rocks also have high degree of strength anisotropy based on experimental evidence). Also, the effect of material strength anisotropy on fracture extension angle is much stronger than the effect of material elastic anisotropy.

6.3 Effect of Rock Anisotropy on Fracture Propagation Path

To study the effect of material elastic and strength anisotropy on fracture propagation path, we consider propagation of a fluid driven fracture. The problem is considered in two cases, where in the first case, a small initial fracture (i.e. perforation) is taken in the direction of maximum principal stress (σ_H) that is Y-axis (Figure 6-1) and in the second case, an initial fracture inclined with maximum principal stress is considered. The difference between σ_H (along Y-axis) and minimum principal stress σ_h (along X-axis) is taken as 1 MPa. The initial fracture length is 0.5 m and the rock is transversely isotropic argillaceous shale (Rock-A) with elastic properties given in Table 6-1. It is assumed that the bedding planes/fibers that define the direction of maximum Young's modulus (E_1) are perfectly bonded and do not act as planes of weakness.

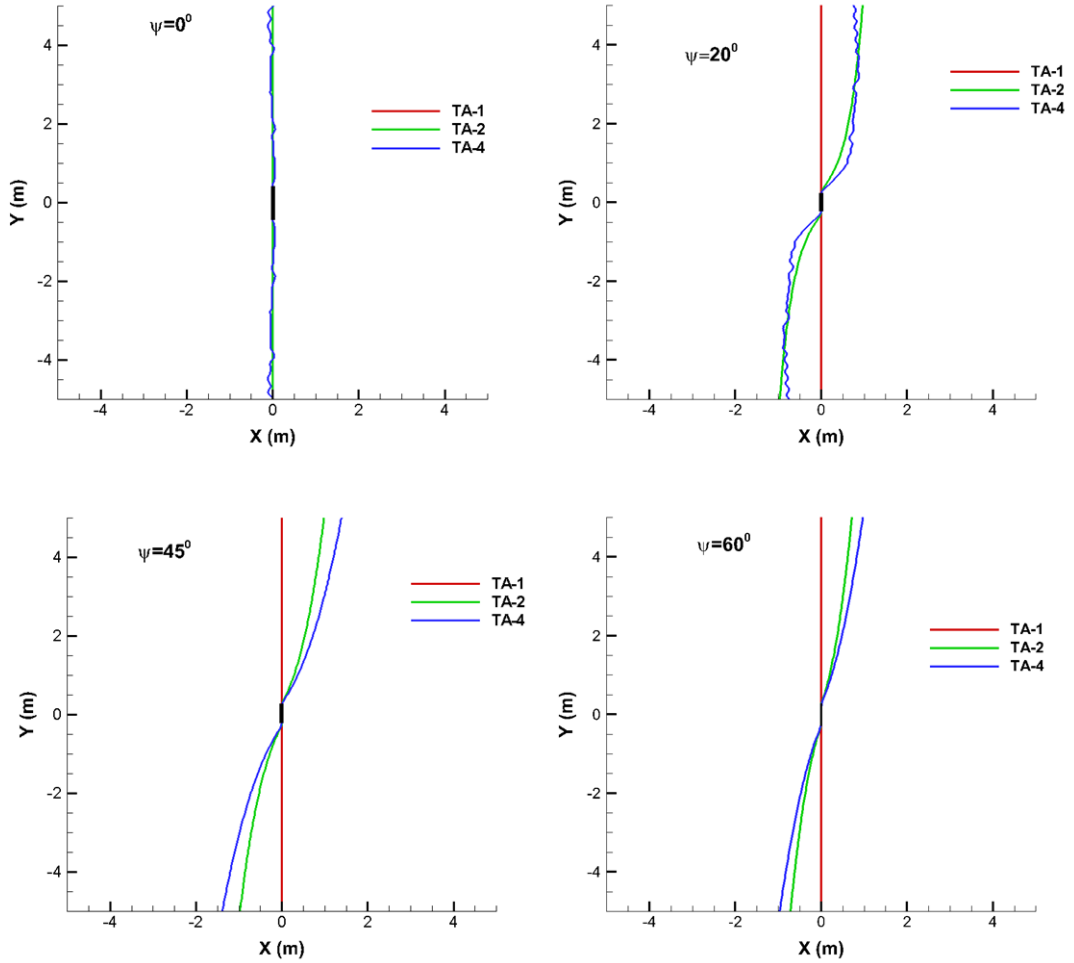

Figure 0-39. Propagation of a fluid driven fracture from small initial perforation oriented in the direction of σ_H (or *y*-axis) in Rock-A. When fracture toughness is uniform (TA=1) ψ appears to have no effect on fracture propagation path. In the presence of fracture toughness anisotropy, the fracture initially opened towards the direction of bedding planes/fibers and later re-orient towards the direction of σ_H.

Considering an initial perforation in the direction of σ_H (i.e. γ=90^0 from Figure 6-1), the fracture geometries obtained after injecting slick water (1 cP) at the rate 2.65e-4 m^2/s into the perforation are shown in Figure 6-6 for different values of ψ. The results indicate that when ψ =0^0 (i.e. initial fracture is perpendicular to bedding), fracture growth occurs in the direction of σ_H for all TA. When TA is high, the fracture path is tortuous. This is due to the combined effect of high degree

of fracture toughness anisotropy and far-field differential stress on fracture propagation and it should not be confused with the numerical error in fracture path that often occurs at high differential stresses (see Stone and Babuska, 1997). As we can see from Figure 6-2b, that when $\psi = 0^0$, high TA shifts the location of maximum value of $\sigma^*_{\omega\omega}$ farther away from azimuth of fracture tip which will lead to a kinked fracture. In the next step, the kinked fracture tries to align with far-field maximum principal stress. As this cycle repeats, the final fracture path although aligned with the direction of maximum principal stress when looking at larger scale is tortuous. When $\psi = 20^0$, in the case of uniform fracture toughness (i.e. TA=1), the fracture observed co-linear propagation. In the presence of fracture toughness anisotropy, the fracture initially opened towards the direction of fibers/bedding planes, however eventually turned towards the direction of maximum principal stress. After fracture re-orientation fracture followed tortuous path when TA=4, similar to the case $\psi = 0^0$. Similar results are observed for the cases $\psi = 45^0$& 60^0, where fracture initially opened towards the bedding planes and gradually re-orienting towards the direction of maximum principal stress. Also, for the cases $\psi = 45^0$& 60^0, fracture path is smooth for all TA. This indicates that tortuous fracture path will result in the cases where the rock fracture toughness anisotropy is high and the angle between bedding planes and maximum principal stress is large. Overall the results indicate that in anisotropic rock with uniform fracture toughness, fracture propagation is co-linear and is independent of angle between bedding planes and fracture axis (i.e. ψ). However, in the presence of fracture toughness anisotropy, fracture path is dependent on degree of fracture toughness anisotropy and ψ . In these cases, fracture initially appears to propagate towards the direction of bedding plane and later tends to re-orient towards the direction the maximum principal stress.

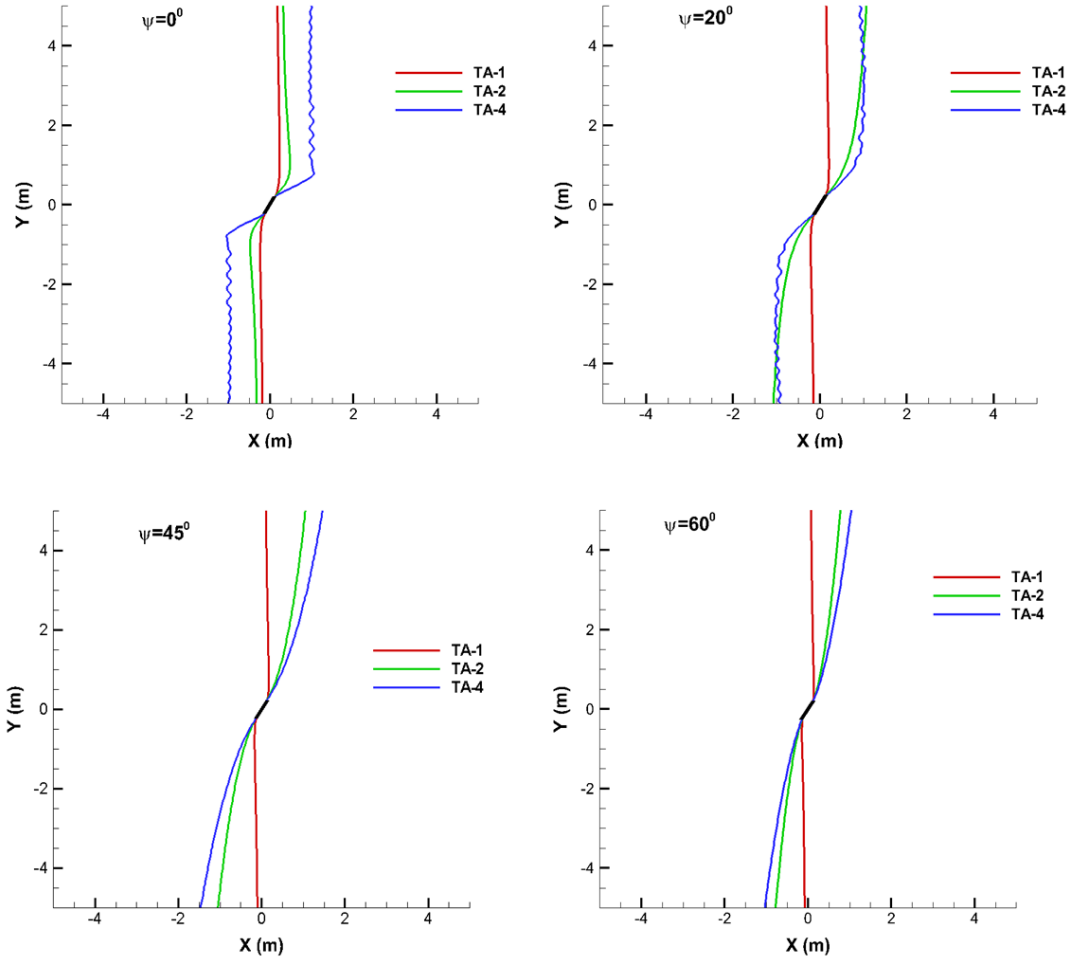

Figure 0-40. Propagation of a fluid driven fracture from small initial perforation that is inclined with the direction of σ_H (or *y*-axis) in Rock-A. When fracture toughness is uniform (TA=1) ψ appears to have no effect on fracture propagation path. In the presence of fracture toughness anisotropy, the fracture initially opened towards the direction of bedding planes/fibers and later re-orient towards the direction of σ_H.

These numerical results are supported by recent experiments (Luo et al. 2018) on Longmaxi shale which is a weak transversely anisotropy rock with degree of anisotropy 1.3, however with strong degree of fracture toughness anisotropy of around 2.5. Fracture propagation under pure mode-1 loading is considered using 3-point bending test on a notched specimen for different values of ψ. The results indicated that for both the cases $\psi = 0^0$ and $\psi = 90^0$, fracture observed co-linear

propagation. On the other hand, when ψ =60^0 the fracture initially extended through the bedding plane, however, is later observed to re-oriented towards the direction of maximum principal stress. Based on these experimental results we conclude that maximum tangential stress criterion can adequately describe the fracture path in anisotropic bodies.

In this example extension of an initial fracture that is inclined with respect to far-field σ_H is considered. As in previous example the initial size of the fracture is 0.5 m and the differential stress is 1 MPa. The inclination angle of fracture with respect to X-axis (γ) is 60^0. This example is chosen to illustrate the behavior of an inclined natural fracture that is subjected to fluid injection in complex fracture network problems. The fracture geometries for various ψ after injecting slick water at a constant rate of 2.5e-4 m^2/s is shown in Figure 6-7. The results indicate that when ψ =0^0, high TA causes the fracture to propagate towards the direction of fibers for longer distance before taking a sharp turn towards the direction of maximum principal stress (similar behavior is observed during the propagation of a fracture emanating from a perforation near the wellbore that is oriented towards the direction of fibers/bedding planes; see chapter 7). For all other ψ, fracture turning towards maximum principal stress appears to be more gradual. For the cases where angle between the direction of fibers and maximum principal stress is high, fracture path is tortuous for high TA similar to the previous example. Overall the results indicate that in the absence of fracture toughness anisotropy, fracture wings emanating from the initial fracture quickly re-oriented towards the direction of maximum principal stress. High fracture toughness anisotropy allows the fracture wings to propagate towards the direction of fibers/bedding planes for longer distance before they eventually reorient towards maximum principal stress.

7 Effect of Rock Anisotropy on Fracture Propagation near the Wellbore

In this chapter we use the 2D plane strain numerical model based on displacement discontinuity method (DDM) and fictitious stress method (FSM) to simulate fracture propagation from a wellbore in isotropic and anisotropic rocks. The FSM is employed to model wellbores, while DDM is used to model fractures. The DDM and FSM for anisotropic material are verified using the analytical solution for tangential stresses around a hole in an infinite orthotropic body that is subjected to far-filed stresses. For numerical simulations, we consider a transversely isotropic rock with bedding planes defining the plane of isotropy. Unless stated otherwise, the wellbore axis is assumed to lie parallel to the direction of minimum in-situ principal stress with vertical stress being the maximum in-situ principal stress. Fracture propagation is considered from a wellbore with perforations that are phased at 180 degrees and oriented at various angles with respect to the preferred planes of fracture initiation. Fracture growth in vertical direction and re-orientation due to the perforation misalignment are discussed. We also considered a case where "bedding" planes are inclined with respect to the horizontal plane. The results for near wellbore fracture geometry, aperture distribution and fluid injection pressures are reported for anisotropic rock and compared with isotropic case.

7.1 Numerical Model

Let us consider an infinite orthotropic body with 1-2-3 as material's axes of elastic symmetry containing a cavity '*c*' and a fracture '*f*' as shown in the Figure 7-1. A body that possesses three axis of elastic symmetry is known as orthotropic body with nine independent elastic constants. If one of the three planes formed by the axes of elastic symmetry (i.e., 1-2, 1-3, and 2-3) is a plane

of isotropy, the body is said to be transversely isotropic with five independent elastic constants (Lekhnitskii, 1963). If the boundary of the cavity '*c*' is discretized into *M* line segments and fractures '*f*' into *N* line segments, then the total normal (σ_n^i) and shear (σ_s^i) stresses acting on the surface of each segment can be expressed as in Eq. 7.1 (Crouch and Starfield, 1983),

$$\begin{aligned}\sigma_n^i &= \sum_{j=1}^{M}(A_{ns}^{ij}P_s^j + A_{nn}^{ij}P_n^j) + \sum_{j=M+1}^{M+N}(A_{ns}^{ij}D_s^j + A_{nn}^{ij}D_n^j) + \sigma_{no}^{\infty},\\ \sigma_s^i &= \sum_{j=1}^{M}(A_{ss}^{ij}P_s^j + A_{sn}^{ij}P_n^j) + \sum_{j=M+1}^{M+N}(A_{ss}^{ij}D_s^j + A_{sn}^{ij}D_n^j) + \sigma_{so}^{\infty} \quad (i=1, M+N),\end{aligned} \tag{7.1}$$

where the terms P_n, P_s represent fictitious stresses acting on the surface of the cavity '*c*' and σ_{no}^{∞}, σ_{so}^{∞} are far-field normal and shear stresses respectively. The terms D_n, D_s represent displacement discontinuities of fracture elements and A_{ns}^{ij}, etc., are boundary stress influence coefficients which give normal/shear stress at the midpoint of i^{th} segment due to the unit fictitious stress or displacement discontinuity at j^{th} segment. The linear combination of the influences of the fictitious stresses and the displacement discontinuities gives stresses on any given cavity/fracture segment or at any point in the rock. The displacement discontinuities (DDs) on fracture segments represent fracture opening (D_n, normal DD) and sliding (D_s, shear DD). Although the DDM can also be used to model cavities (such as wellbore), provisions must be made to prevent rigid body motion (Crouch and Starfield, 1983), and calculation of tangential stresses on cavity edges is relatively straightforward with FSM.

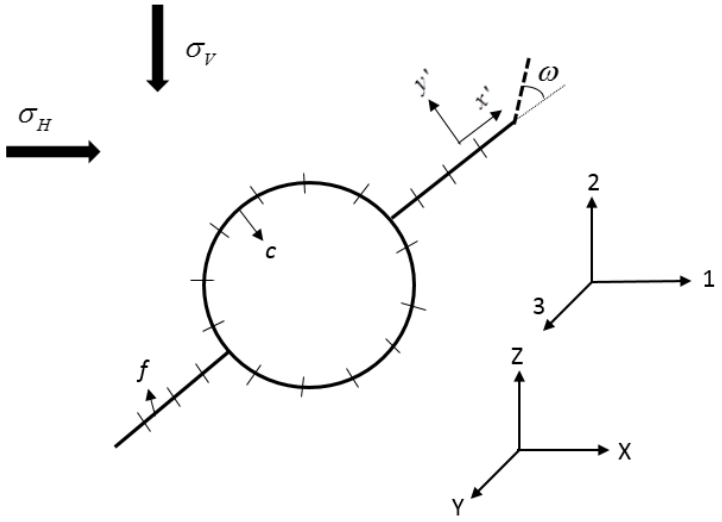

Figure 0-41. Discretization of cavity '*c*' and fracture '*f*' for boundary element method. *x*'-*y*' is fracture tip coordinate system. ω is fracture tip extension angle. 1-2-3 are the directions of material elastic symmetry. σ_V is principal vertical stress and σ_H is maximum principal horizontal stress.

A series of assumptions are made in the modeling process to simplify the analysis of fracture propagation in anisotropic rock. Some are based on experimental evidence while some are based on theoretical considerations in the pertinent literature. It is assumed that the initial far-field stress state is given and might have been affected by material anisotropy. As a result, the variations of the far-field principal stress directions are not studied. Based on experimental evidence (Ke et al., 2008; Chandler et al., 2016), the fracture toughness $(K_{IC}(\omega))$ of an anisotropic rock is taken maximum ($K_{IC,Max}$) in the plane perpendicular to the bedding and minimum ($K_{IC,Min}$) in the plane parallel to the bedding. The fracture toughness for any arbitrary plane β is expressed as an elliptical function given by Eq. 7.12 and fracture extension angle is obtained using Eq. 6.13. The Young's modulus of a transversely isotropic rock is taken maximum in the direction of the fabric

or bedding planes and is a minimum in the direction perpendicular to it. Finally, it is assumed that the bedding planes are perfectly bonded and are not plane of weakness.

Assuming that the hydraulic fracture propagation is dominated by mode-1 fracture deformation, the fracture extension criterion is:

$$K_I = K_{IC}(\omega) \tag{7.9}$$

As previously stated, the fracture toughness $(K_{IC}(\omega))$ of an anisotropic material is maximum ($K_{IC,Max}$) in the plane perpendicular to the bedding and minimum ($K_{IC,Min}$) in the plane parallel to the bedding. Assuming $\beta = 0$ in the direction of bedding planes, the fracture toughness for any arbitrary plane β is given by the following elliptical expression (Dai and Xia, 2008),

$$K_{IC}(\beta) = K_{IC\max}\sin^2(\beta) + K_{IC\min}\cos^2(\beta) \tag{7.12}$$

The fluid flow inside fractures is approximated as flow between two parallel plates for Newtonian and incompressible fluid:

$$q = -\frac{w^3 H}{12\mu}\frac{\partial p}{\partial x} \tag{7.13}$$

where q is the volumetric flow rate, H is the fracture height, μ is the fluid viscosity and w is the fracture aperture. Substituting Eq. 7-13 in the continuity Eq 7.14 and assuming constant height throughout the fracture length gives lubrication Eq 7.15.

$$\frac{\partial q}{\partial x} + \frac{\partial wH}{\partial t} + q_L = 0 \tag{7.14}$$

$$\frac{\partial w}{\partial t} = \frac{\partial}{\partial x}\left(\frac{w^3}{12\mu}\frac{\partial p}{\partial x}\right) \tag{7.15}$$

Owing to the ultra-low permeability of shale rocks, fluid leaf-off rate q_L is neglected in these calculations.

The partial differential Eq 7.15 is solved using the finite difference scheme with a 1D mesh that coincides with the DDM mesh shown in the Figure 7-1. The pressure and aperture are evaluated at the mid-point of each element. The wellbore is treated as a single element in the finite difference method, where frictional pressure losses are ignored. Therefore, the pressure at the inlet of a fracture is equal to the pressure inside the wellbore. Injection rate is prescribed at the center of the wellbore element as in Eq 7.16, which must be equal to the sum of flow rates into N fractures connected to the wellbore as in Eq 7.17.

$$q(0,t) = Q_o \tag{7.16}$$

$$\sum_{i=1}^{N} q_i = Q_o \tag{7.17}$$

In the case of a single bi-wing symmetrical fracture propagating from a wellbore, the flow rate into each fracture wing should be equal to $Q_o/2$. However, when multiple fractures are propagating from different clusters, flow rate into each fracture will be different and comes out as a part of the solution. Initial fractures of small size (equal to perforation length) are assumed in the direction of perforations with zero aperture as initial condition:

$$w(x,0) = 0 \tag{7.18}$$

Fracture aperture vanishes at fracture tips (Eq. 7.19) and assuming that the fluid front coincides with the fracture front (i.e., zero fluid-lag), a no flow boundary condition (Eq 7.20) is implemented at the fracture tips:

$$w(l,t) = 0 \tag{7.19}$$

7.2 Numerical Examples

Let us consider a wellbore in a transversely isotropic rock with the plane of isotropy parallel to the plane 1-3 as shown in Figure 7-2. The elastic constants E_1 = 40 GPa, E_2 = 10 GPa ν_{13} = 0.15 and

ν_{12} = 0.85. These values do not belong to any specific formation, however, they fall within the range observed in various mudstones (Suarez-Rivera et al., 2011). In order to eliminate the possibility of having shear stresses in the tangent plane of wellbore wall, the wellbore is taken parallel to the direction of minimum in-situ principal stress (Y-axis) where vertical (Z-axis) stress is the maximum principal stress as discussed previously. Additionally, the coordinate system 1-2-3 representing the rock's directions of elastic symmetry and is used to define rock properties. For sensitivity analysis only the value of E_2 is modified based on the degree of anisotropy (E_1/E_2).

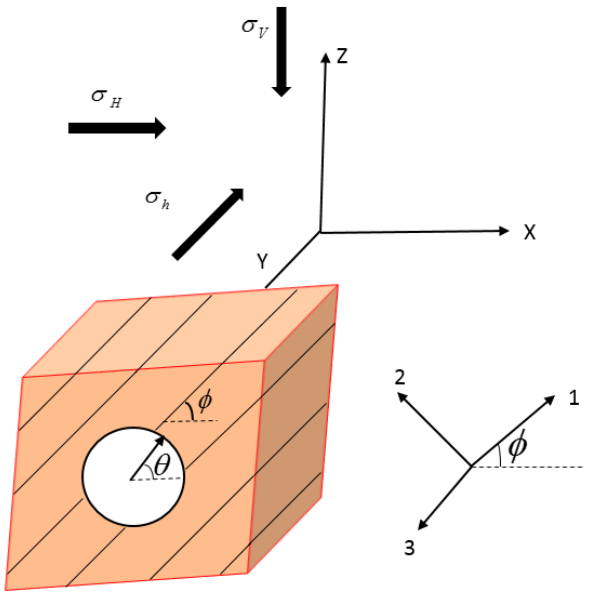

Figure 0-42. Cross-section of a wellbore in a transversely isotropic rock and far-field in-situ stresses aligned with coordinate axes X-Y-Z where $\sigma_V > \sigma_H > \sigma_h$. Bedding planes (black lines) are defined using the coordinate system 1-2-3 which also represents the directions of material elastic symmetry.

Let ϕ denote the angle of inclination of the bedding planes with respect to the horizontal plane X-Y, measured anticlockwise from the positive X-axis. Therefore, for a horizontal bedding, $\phi = 0^0$ (σ_V acts perpendicular to E_1) and for a vertical bedding, $\phi = 90^0$ (σ_V acts parallel to E_1). For isotropic body, the Young's modulus parallel to bedding planes E_1, Poisson ratio ν_{13} and fracture

toughness $K_{IC,Max}$ is used. The minimum fracture toughness of the anisotropic rock is obtained from the degree of fracture toughness anisotropy ($K_{IC,Max} / K_{IC,Min}$). The tensile strength is set to 7 MPa for both isotropic and anisotropic rocks. Perforations are created radially around the wellbore wall with 180 degrees phasing. The perforation angle θ is measured from positive X-axis in anticlockwise direction (see Figure 7-2). The particular problem of fracture growth near a wellbore is analyzed in plane strain in the plane X-Z, assuming that fracture extension in the direction of wellbore axis during the initial stage of propagation is greater than the fracture wing that is growing outwards from the wellbore radially.

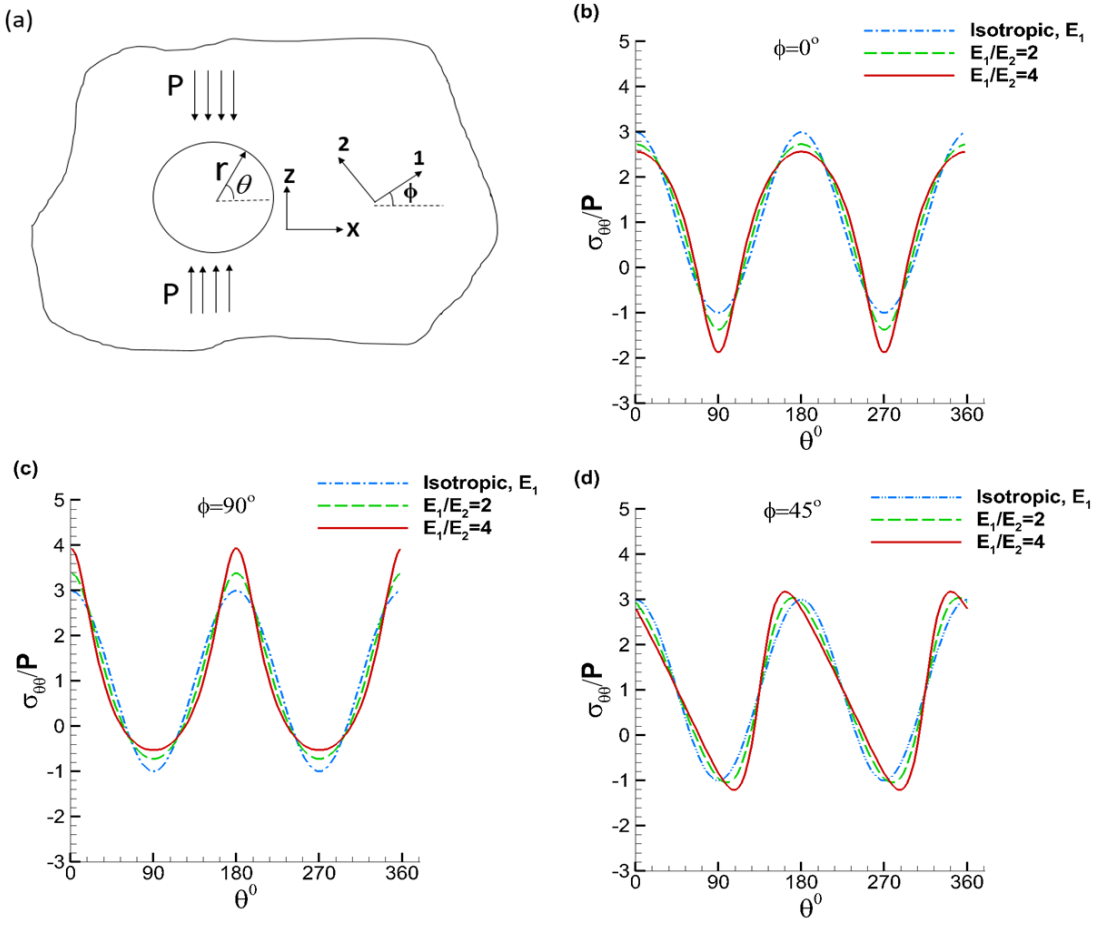

Figure 0-43. Normalized tangential stresses ($\sigma_{\theta\theta}$) at the wellbore wall in a transversely isotropic rock that is subjected to far-field uniaxial compressive stress P. (a) Z-X plane

view of Figure 4 with far-field stress P acting along Z-axis, (b) for bedding plane orientation ϕ =0^0, (c) ϕ =90^0, (d) and ϕ =45^0.

7.2.1 Effect of Anisotropy on Fracture Initiation Pressure and Location

In this section we will analyze the effect of rock anisotropy on fracture failure pressure and location by studying the stress concentration around a wellbore in anisotropic body and comparing the results with isotropic case. For isotropic case the material properties E_1 and v_{12} from previous section are used. The wellbore in an infinite rock mass is subjected to uniaxial far-field compressive stress P. This simple case of stress loading serves to clearly illustrate the behavior of stress distribution around the wellbore. Moreover, the result for this problem in isotropic rock is well known and are used here to make comparison with anisotropic case. The conclusions drawn here can be extended to more general case of stress state where wellbore is subjected to three different far-field principal stresses. Assuming the uniaxial compressive stress P is acting along the Z-axis (see Figure 7-3a), we evaluate the tangential stresses ($\sigma_{\theta\theta}$) around the wellbore wall under the assumption of plane strain in the X-Z plane for 3 possible scenarios of bedding plane orientation, ϕ with respect to the horizontal plane X-Y.

Figure 7-3 shows comparison of normalized tangential stresses ($\sigma_{\theta\theta}/P$) obtained from FSM at the wellbore wall in isotropic and anisotropic rocks. We notice when the rock is isotropic, the tangential stress distribution around the wellbore is symmetrical about the direction of applied stress P. Also at θ =90^0, the stress concentration is tensile and is equal to the magnitude of far-field applied stress P. At θ =0^0, the stress concentration is compressive with 3 times the magnitude of far-filed applied stress P. But in the case of an anisotropic body with E_1/E_2=2 and ϕ =0^0 (Figure 7-3b), the tangential stress concentration at θ =90^0 is more tensile (1.2P) compared to the isotropic

case (P). For a strongly anisotropic body with E_1/E_2=4 and ϕ =0^0, the tensile tangential stress concentration is at θ =90^0 is nearly 2P or twice that for the isotropic case (P). As a result, the wellbore pressure required to initiate tensile fractures from the wellbore would be less in anisotropic body for ϕ =0^0 compared to isotropic body that is subjected to same far-field stress conditions provided that they have same tensile strength. On the other hand, in anisotropic body for ϕ =0^0, the compressive tangential stress concentration at θ =0^0 decreased compared to isotropic body. This would affect the compressive failure condition of a wellbore, which can be analyzed using Mohr's coulomb failure criterion. However, we restrict our attention to tensile failure of wellbore in this paper.

In anisotropic body, for ϕ =90^0 (Figure 7-3c), the tangential stress concentration at θ =90^0 is less tensile compared to isotropic body. The tensile stress concentration at θ =90^0 further decreases with increase in the degree of material anisotropy. Therefore, in this scenario, we can expect higher wellbore pressure to initiate tensile fractures in anisotropic body compared to isotropic body. Although the magnitude of stress concentration around a wellbore in anisotropic body (for ϕ =0^0 & 90^0) is different from that in isotropic rock, the variation of $\sigma_{\theta\theta}$ is the same as the isotropic case, i.e., it is symmetrical about the axis of far-field stress, P.

A more interesting scenario is when bedding planes are inclined with respect to the direction of far-field principal stress P. For ϕ =45^0 (Figure 7-3d), the stress concentration at θ =90^0 is slightly more tensile (1.05P) in anisotropic body with E_1/E_2=2 than in isotropic body (P). When E_1/E_2=4, the tensile stress concentration at θ =90^0 has increased to 1.2P, but still less than the magnitude observed for ϕ =0^0 (2P). Interestingly, in this scenario, the locations of maximum tensile and compressive stress concentrations around the wellbore wall are shifted from the azimuth of far-

field principal stresses. For anisotropic body with E_1/E_2=2, the maximum tensile hoop stress is observed at θ =100^0, which is a 10^0 shift from the azimuth of applied stress P. In a material with much stronger anisotropy (E_1/E_2=4), the location has shifted further from the azimuth of P (θ =90^0) to θ =108^0. Therefore, induced tensile fractures in this scenario could follow complex trajectories as they try to align with the direction of maximum principal stress *P*. These conclusions hold true for a general case of stress state with three different far-field principal stresses, when the wellbore is aligned with one of the two principal horizontal stresses and maximum principal stress is acting in the vertical direction. It should be noted that in the case of rock with tensile strength anisotropy, the rock tensile strength along with the tangential stress distribution around the wellbore wall will influence the location of induced tensile fracture.

7.2.2 Effect of Anisotropy on Fracture Trace near Wellbore

For the stress state considered in Figure 7-2, the tensile fracture failure location for different rock types can be found from the tangential stress distribution plots shown in Figure 7-3. Tensile failure of a wellbore occurs when the tensile hoop stress around the wellbore wall reaches tensile strength of the rock. The plane of tensile fracture failure and propagation is called the preferred propagation plane. Perforations that are not aligned with preferred planes of fracture propagation can result in complex fracture growth near the wellbore. To illustrate this, we consider examples of fracture propagation from a wellbore for the cases of low and high perforation misalignment angles. The perforations are oriented radially outwards from the wellbore wall and their initial length is 25% of the wellbore radius. By using small size perforations we will be able to include the effect of wellbore deformation on fracture propagation. As previously discussed, the perforations are phased at 180 degrees; therefore, the two fracture wings emanating from the wellbore will be symmetrical. The wellbore configurations and the stress state is shown in the Figure 7-2. Under

the assumption of plain strain in X-Z plane, fracture propagation from wellbore is simulated in isotropic rock and anisotropic rock for two possible orientations of bedding planes with respect to the principal stresses. These two selected orientations correspond to a vertical transversely isotropic rock (VTI) and a tilted transversely isotropic rock (TTI). The material properties are given in previous section are used. The degree of material anisotropy is 4. In addition, to study the effect of fracture toughness anisotropy on fracture propagation, we consider a case of anisotropic rock with fracture toughness anisotropy (TA). For all the examples considered below, we assume 12 MPa difference between the vertical principal stress (σ_V =82 MPa) and the maximum horizontal principal stress (σ_H =70 MPa). In all numerical examples, slick water (of viscosity 0.001 Pa.s) is injected into the wellbore at a constant rate of 0.0002 m^2/s until each fracture wing propagating from the wellbore achieves a length equal to 6 times the radius of the wellbore. The results obtained for fracture geometry, aperture distribution and injection pressure are compared for isotropic and anisotropic rocks.

7.2.3 Perforations Oriented in Preferred Direction (horizontal bedding planes)

This example discusses fracture propagation from a wellbore when perforations are created along the preferred planes of fracture propagation. For anisotropic rock with bedding orientation of ϕ =0^0 (i.e., VTI), and for isotropic rock the tensile failure can be expected at θ =90^0 and θ =270^0 according to Figure 7-3b.

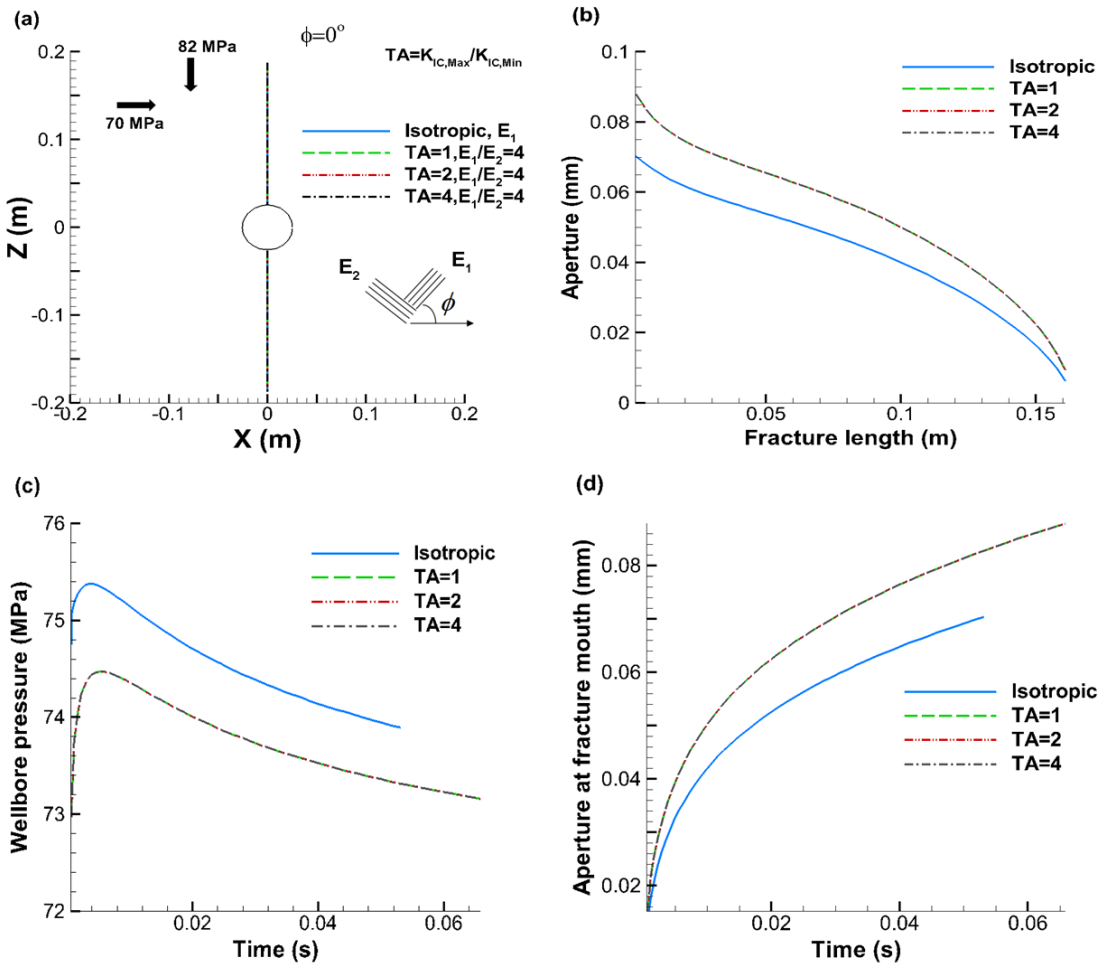

Figure 0-44. (a) Fracture trace from wellbore in both isotropic and anisotropic rocks, bedding plane orientation $\phi = 0^0$ indicates horizontal bedding, and TA is degree of fracture toughness anisotropy (b) Fracture aperture distribution from injection point to tip along one of the symmetrical wings, (c) wellbore pressure vs time, (d) aperture at fracture mouth (i.e., fracture inlet) vs time.

With perforations created at these locations, fracture trace, aperture distribution along the fracture and injection pressure are compared between isotropic and anisotropic rocks in Figure 7-4. Fracture trajectory from Figure 7-4a indicates that the assumed rock anisotropy condition has no impact on the fracture path. Planar fracture growth is observed in both isotropic and anisotropic rocks. The applied degree of fracture toughness anisotropy is not sufficient to cause fracture turning towards the plane of least fracture toughness. Note that for similar configuration, non-

planar fracture propagation is possible if the degree of material anisotropy is less than 0.5 even under uniform fracture toughness condition (Ye and Ayari, 1994 and see Chapter 6). Fracture aperture distribution in one of the symmetrical wings from fracture mouth to the tip (Figure 7-4b) indicates significant increase in fracture opening in anisotropic rock. Wellbore pressure (Figure 7-4c) tends to reach a peak value during the early stage of stimulation and decreases thereafter as the fracture length grows larger. Higher fracture opening at the injection location results in lower injection pressures for the assumed anisotropic condition compared to isotropic case. At the fracture mouth (Figure 7-4d), the aperture is gradually increasing with time in both isotropic and anisotropic rocks, which is similar to the behavior of single KGD fracture (Geertsma and De Klerk, 1969). Since the fracture path is in the plane of maximum fracture toughness, the fracture aperture and wellbore pressure were not affected by TA.

7.2.4 Perforations Oriented in Preferred Direction (Inclined bedding planes)

When the directions of elastic symmetry in an anisotropic material are not aligned with the far-field principal stresses, the locations of maximum tensile hoop stress around the wellbore shifts from the azimuth of maximum principal stress according to the Figure 7-3d. In such cases, perforations oriented in the preferred planes can result in non-planar fracture propagation due to fracture reorientation towards maximum principal stress. Non-planar fracture propagation is also possible even when the perforations are created at the azimuth of maximum principal stress due to asymmetrical stress distribution around the wellbore wall about the center line X=0 (see Figure 7-3d). To illustrate this we consider a case where the bedding planes in a transversely isotropic body are oriented at an angle 45 degrees with respect to the horizontal plane X-Y. For this configuration, and for E_1/E_2=4, the failure locations are observed at $\theta = 112^0$ and $\theta = 292^0$ from the Figure 7-5. Note that the failure locations observed in this case are not far from values ($\theta = 108^0$ and 288^0)

observed in the case of uniaxial stress state for the same rock. To study the effect of far-field stress magnitudes on failure locations, another stress state of 30 MPa differential stress is considered. Figure 7-5 shows failure locations are at θ =109^0 and θ =289^0 for this stress state. This suggests that the effect of far-field stress contrast on failure locations around a wellbore is not as significant as degree of rock anisotropy in a rock with dipping layers.

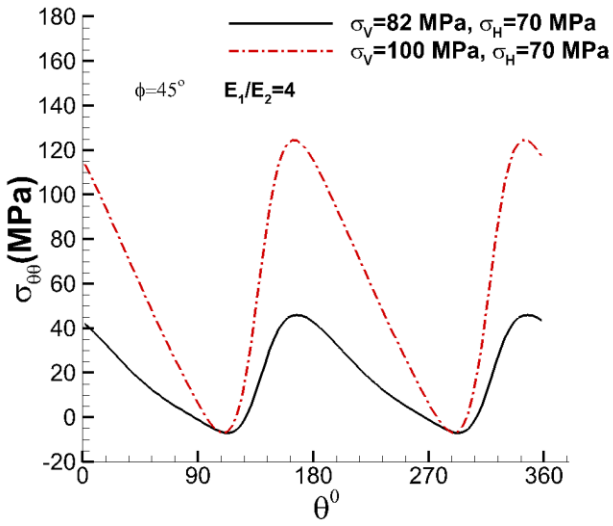

Figure 0-45. Tangential stresses ($\sigma_{\theta\theta}$) around wellbore wall at failure pressure for the two different stress states in a transversely isotropic rock. The bedding dip (ϕ) is 45^0.

Fracture propagation from a wellbore is simulated for 2 cases of perforation orientations, where in one case perforations are located at failure locations (θ =112^0 and 292^0) and in the other case, perforations are located at the azimuth of maximum principal stress (θ =90^0 and 270^0). Fracture geometry and aperture distribution along the fracture are compared between the two cases in Figure 7-6.

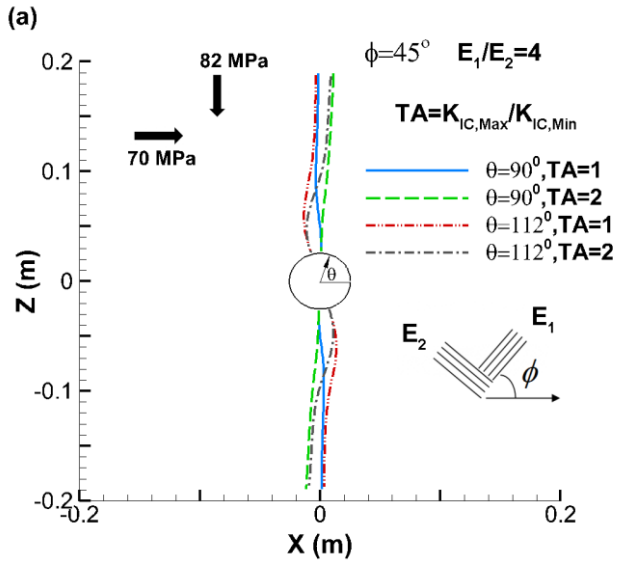

Figure 0-46. Fracture trace for perforation orientations (θ =112^0 and 292^0) and (θ =90^0 and 270^0) in a transversely isotropic rock with bedding plane dip ϕ =45^0.

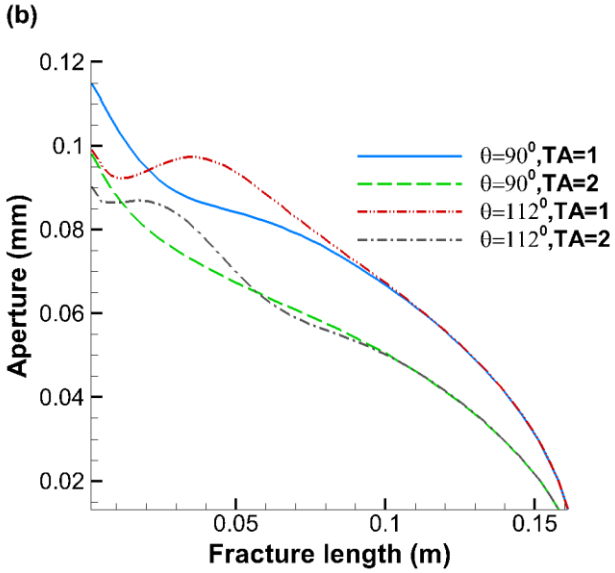

Figure 0-47. Aperture distribution along one of the symmetrical wings from fracture mouth to tip.

The results indicate non-planar fracture propagation when perforations are oriented in failure planes. Close observation shows a slightly non-planar fracture path even when the perforations are aligned in the direction of maximum principal stress. Since the locations of maximum tangential

tensile stress are at θ =112^0 and 292^0 for this configuration (see Figure 7-5), the fractures created in the direction of the vertical principal stress experience a slight attraction towards the locations of tensile stress concentration around the wellbore wall resulting in slight non-planarity. In both cases, the presence of fracture toughness anisotropy (i.e. TA=2) caused slight deviation of fractures towards the plane of least fracture toughness (i.e., towards the bedding planes) before the fractures aligned with maximum principal stress. The aperture distribution (Figure 7-6b) along the fracture indicates slight complexity near the wellbore due to the curved fracture path and reduction in aperture due to higher compressive normal stresses acting on the fracture surface near the wellbore when perforations are oriented in the preferred initiation plane. The apertures along the fracture length are slightly higher in this example compared to the previous one (Figure 7-4b) due to fractures opening against lower Young's modulus. Overall, the results indicate that in cases where the directions of elastic symmetry are not aligned with the principal stresses, it is still favorable to orient the perforations in the direction of the in-plane maximum principal stress although the locations of maximum tensile hoop stress are shifted from the azimuth of maximum principal stress.

7.2.5 Perforations with Lower Misalignment Angle

In this example we consider fracture propagation from wellbore with perforations that are not aligned with preferred directions of fracture initiation. The bedding planes of transversely isotropic body are taken parallel (ϕ =0^0) to the horizontal plane X-Y (see Figure 7-2).

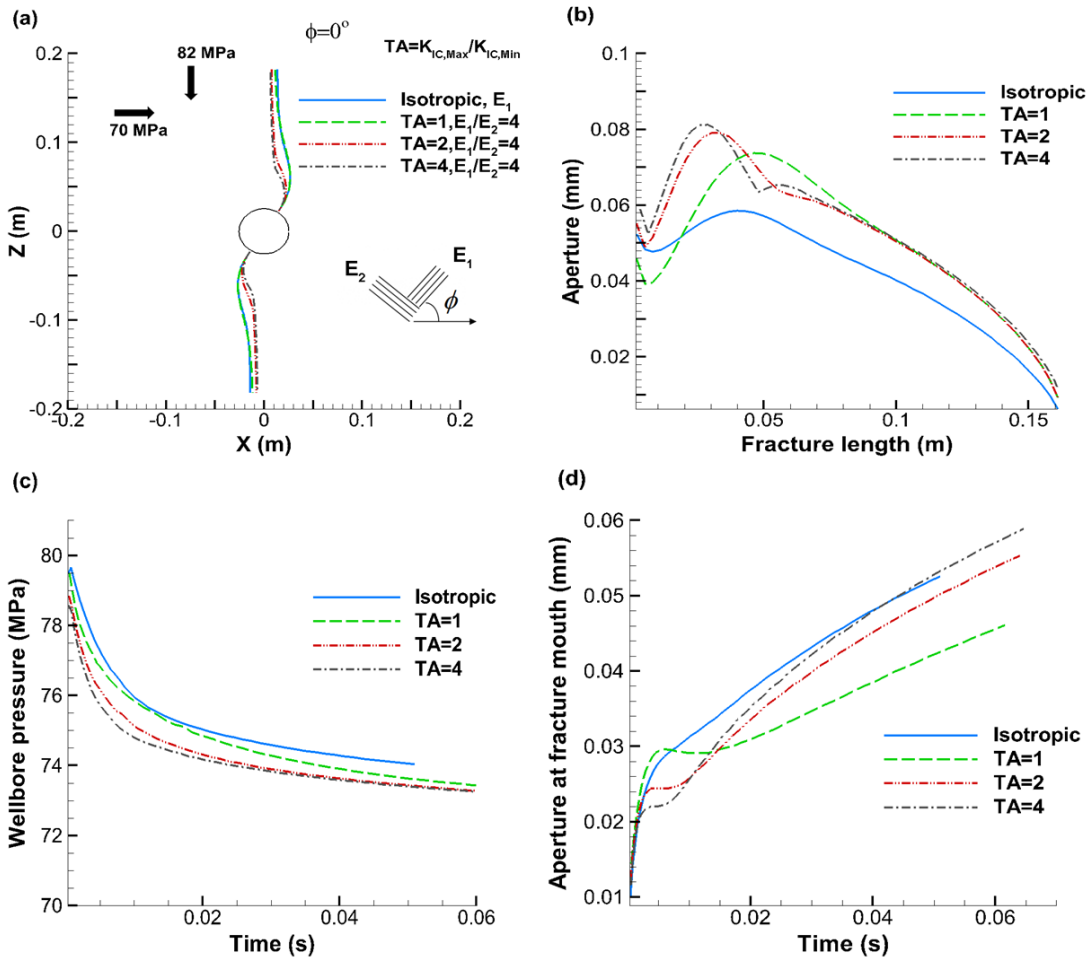

Figure 0-48. (a) Fracture trace, (b) aperture distribution along one of the wings from fracture mouth to tip, (c) wellbore pressure vs time, and (d) aperture at the fracture mouth as function of time in a transversely isotropic rock for case of low perforation misalignment angle.

The perforations are located at θ =60^0 and θ =240^0. As mentioned previously, for this bedding plane orientation, the preferred locations of fracture initiation are θ =90^0 and 270^0 for both isotropic and anisotropic rocks (Figure 7-3b). Therefore, the perforation misalignment angle, which is the difference between the preferred fracture initiation angle and the perforation angle is 30 degrees in this example. The computed fracture geometry, aperture distribution and injection pressure at the wellbore are plotted in Figure 7-7 for isotropic and anisotropic cases.

The results (Figure 7-7a) indicates rock anisotropy has negligible effect on fracture propagation path when the fracture toughness is uniform in the rock. Also, in anisotropic rock with fracture toughness anisotropy (i.e. TA= 2& 4), the turning radius of fractures towards the direction of maximum principal stress is decreased and fractures appear to align with the centerline of the wellbore (X=0). Aperture distribution (Figure 7-7b) indicates, fracture apertures very near to the wellbore region in anisotropic rock are lower compared to isotropic case. Fracture toughness anisotropy appears to diminish this effect as we see an increase in aperture at fracture mouth in anisotropic rock with TA= 2& 4. In the region away from the wellbore, fracture apertures are higher in anisotropic rock. However, aperture at fracture mouth is critical since it plays a significant role in establishing the commutation between the fractures and wellbore. Aperture at fracture mouth vs. time plot (Figure 7-7d) indicates significant drop in aperture at fracture mouth in the anisotropic rock during fracture reorientation towards the principal vertical stress, which is not seen in isotropic case. Maximum drop in aperture at fracture mouth during reorientation has occurred in anisotropic rock with fracture toughness anisotropy due to sharp fracture turning (see Figure 7-7a). As the fractures extend in the direction of principal vertical stress, aperture at fracture mouth tends to increase with time. Therefore, proppant can be placed inside fractures after sufficient rise in aperture at fracture mouth in anisotropic rock. Pressure at the wellbore (Figure 7-7c) in this case does not indicate appreciable difference between isotropic and anisotropic rocks. Similar to the previous examples, the injection pressures observed during fracture propagation are decreasing with time as fracture aperture at injection location and length increases with time. However, the injection pressures observed in this case are higher compared to the case where perforations are placed along preferred failure plane (Figure 7-7c) since the fractures need to open against higher normal compressive stresses.

7.2.6 Perforations with Higher Misalignment Angle

In this example the perforations are located at $\theta = 10^0$ and 190^0 which is close to the azimuth of minimum in plane principal stress. The stress state and bedding planes orientation ($\phi = 0^0$) are same as in previous example. Therefore, the perforation misalignment angle in this example is 80^0. Figure 7-8 shows comparison of fracture trace, fracture apertures and injection pressures at the wellbore for isotropic and anisotropic rocks.

Fracture trajectory plot (Figure 7-8a) indicates, fractures propagated longer distance in the plane of perforation before turning towards the direction of principal vertical stress when compared to the case of low perforation misalignment angle (Figure 7-7a). Also, there is no considerable difference between the fracture paths in isotropic rock and anisotropic rock with uniform toughness similar to the previous examples. In anisotropic rock with fracture toughness anisotropy (i.e. TA= 2& 4), perforations are oriented closer to the plane of least fracture toughness (i.e. bedding planes). In this scenario, it appears that the distance traveled by the fractures in the plane of perforation (or towards the plane of least fracture toughness) before making a sharp turn towards the principal vertical stress increases with increase in the degree of fracture toughness anisotropy. In comparison, fracture turning is more gradual in isotropic rock and in anisotropic rock with uniform fracture toughness.

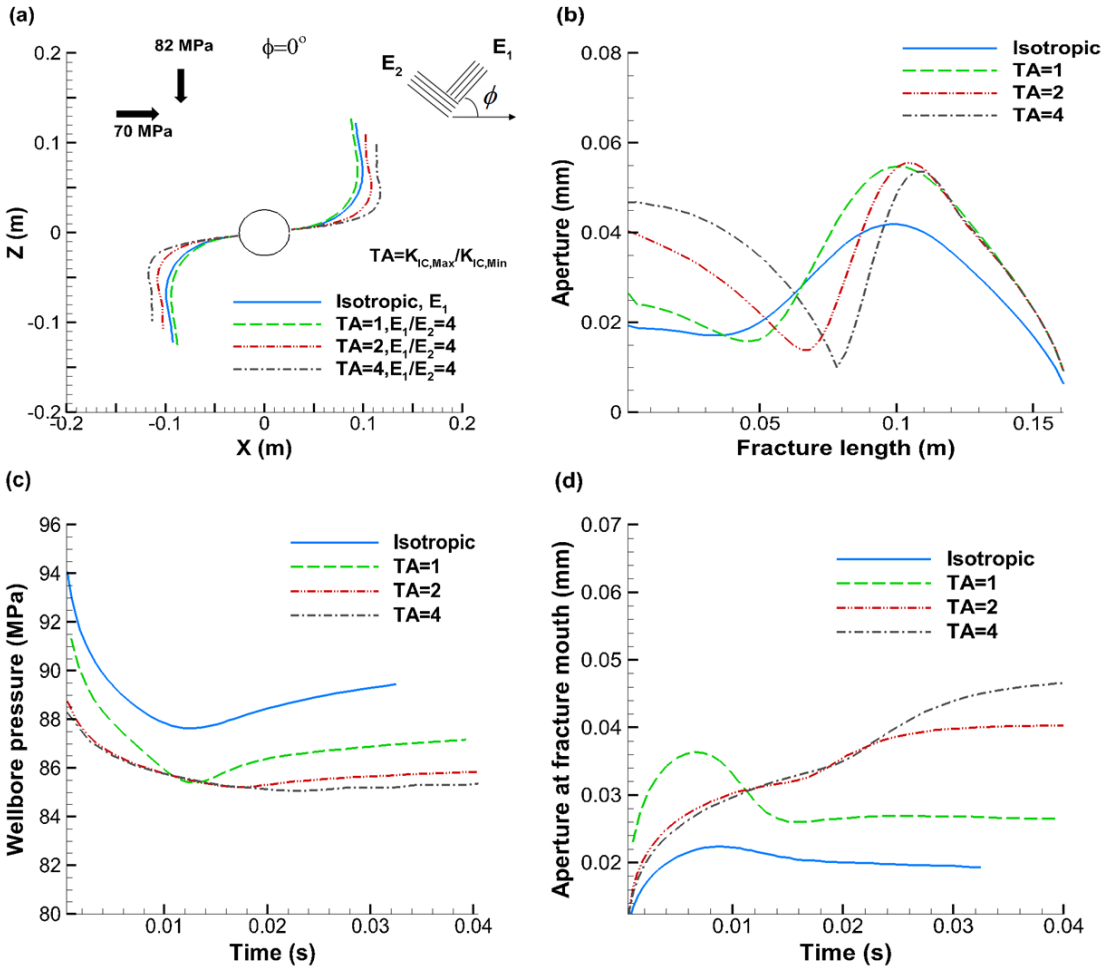

Figure 0-49. (a) Fracture trace, (b) aperture distribution along one of the wings from fracture mouth to tip, (c) wellbore pressure vs time, (d) aperture at fracture mouth as function of time in a transversely isotropic rock with high perforation misalignment angle.

Fracture aperture distribution (Figure 7-8b) in isotropic rock indicates apertures are lowest near the region of wellbore and gradually increases along the region that is extended in the direction of principal vertical stress. This is due to very high normal compressive stresses acting on the fracture surface closer to the wellbore as the perforations are oriented almost perpendicular to in-plane maximum principal stress (σ_V). In anisotropic rock, fracture opening is higher in the near wellbore region compared to isotropic rock, but decreases below the value observed in isotropic rock near the region of fracture turning. This effect is exacerbated in anisotropic rock with the increase in

fracture toughness anisotropy, which resulted in choking point near the location of fracture turning. As the perforations are oriented towards the direction of maximum Young's modulus (E_1), initially the fracture opens against lower Young's modulus in anisotropic rock; hence, higher opening is observed in the near wellbore region. The choking effect near the location of fracture turning is the result of drastic change in material properties (especially for sharp fracture turning), as the fracture turns towards the direction of E_2 and opens against E_1 (which is 4 times E_2). Similar to the case of lower perforation misalignment angle (Figure 7-7d), apertures at fracture mouth in anisotropic rock dropped during the period of fracture reorientation (Figure 7-8d). However, apertures at fracture mouth are not regained after fracture reorientation contrary to previous examples. Instead, they tend to reach a constant value (although apertures continue to decrease, the rate of aperture drop reduced considerably with time). Despite appreciable increase in aperture at fracture mouth in anisotropic rock with fracture toughness anisotropy, choking point (Figure 7-8b) created at the location of fracture turning can hinder the placement of proppant inside fractures. Injection pressures at wellbore (Figure 7-8c) initially decreased with time, which is associated with increase in aperture at fracture mouth. During and after fracture reorientation, the injection pressure tends to increase in response to keep the fracture near wellbore region from closing due to high normal compressive stresses acting on fracture surface, which is in agreement with the numerical results for isotropic rock in Zhang and Jeffery (2011). The pressure at wellbore in anisotropic rocks is lower compared to isotropic rock but, higher than the values observed in the case of lower perforation misalignment (Figure 7-7c).

8 Height Correction Factor for Anisotropic Displacement Discontinuity Method

Consider a fracture in an orthotropic body such that its height H is parallel to axis Z and length L is parallel to axis Y, and is subjected to constant internal net pressure P as shown in Figure 8-1. X-Y-Z also represents directions of the three far-field principal stresses. The axes of the rock's elastic symmetry 1-2-3 are such that they are parallel to the axes X-Z-Y respectively as shown in Figure 8-1a. If, L>>H, the plane XZ is considered to be in the state of plane strain, and all physical quantities are independent of Y. Similarly, if H>>L, the plane XY is considered to be in the state of plane strain, and all physical quantities are independent of Z. Therefore, fracture propagation models based on plane strain assumption are restricted to these two limiting conditions. However, in reality, a typical hydraulic fracture may have any value for the ratio, L/H. Moreover, in problems pertaining to layered media, typically, fracture growth predominantly occurs in the direction of length as the height is contained by high stress barriers above and below the payzone. This suggests that the problem is truly 3D in nature, however, 3D models come at significantly high computational cost. Without losing the computational advantage offered by 2D DDM, Olson (2004), proposed the so called 3D correction factor "G" that incorporates the effect of fracture height into 2D solution, and the resulting enhanced 2D DDM is more suitable to model large scale multiple hydraulic fracture propagation where fracture height can be treated as a fixed value. In this section, the 3D correction factor developed for isotropic plane strain DDM is extended to anisotropic case. Sensitivity analysis is conducted to study the dependence of 3D correction factor for anisotropic DDM on material constants.

The 3D correction factor for isotropic body was developed based on the premise that in the limiting case *L>>h* (for the configuration shown in Figure 8-1), when corrected using the G factor, the numerically obtained induced stresses normal to the fracture surface (σ_{XX}) along the line passing through the fracture center should approach the (σ_{XX}) obtained from XZ plane strain analytical solution. Since the induced stress component perpendicular to the fracture surface is the one that primarily affects the interaction between multiple parallel fractures, the G factor is derived based on it.

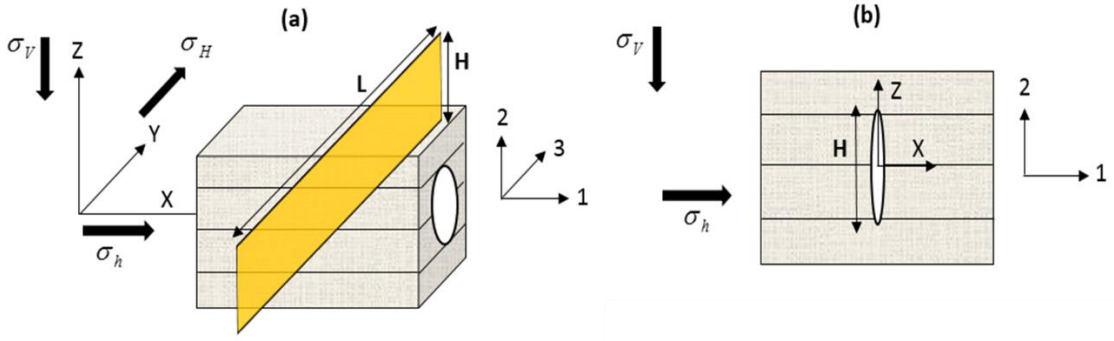

Figure 0-50. a) Illustrative figure of orthotropic body containing a rectangular fracture of length L and height H, where, L/H>>1. The three axes of elastic symmetry 1-2-3 coincides with the three far-field principal stress directions also, the global coordinate axes X-Y-Z, b) Z-X plane of Figure 3a. The fracture is subjected to constant internal net pressure P.

8.1 Development

If we consider a uniformly pressurized fracture in an orthotropic body (see Figure 8-1) and if plane XZ is in the state of plane strain, the analytical solution for induced normal stress components in the directions X and Z along the line Z=0 is given as (Azhdari et.al, 2000),

$$\sigma_{xx(z=0)} = 2\,\mathrm{Real}\left[\frac{\sigma\mu_2}{2(\mu_1-\mu_2)}\left(1-\frac{\mu_1 x}{\sqrt{(\mu_1 x)^2-(H/2)^2}}\right)+\frac{\sigma\mu_1}{2(\mu_2-\mu_1)}\left(1-\frac{\mu_2 x}{\sqrt{(\mu_2 x)^2-(H/2)^2}}\right)\right] \qquad (8.1)$$

$$\sigma_{zz(z=0)} = 2\ \text{Real}\left[\frac{\sigma\mu_2\mu_1^2}{2(\mu_1-\mu_2)}\left(1-\frac{\mu_1 x}{\sqrt{(\mu_1 x)^2-(H/2)^2}}\right)+\frac{\sigma\mu_1\mu_2^2}{2(\mu_2-\mu_1)}\left(1-\frac{\mu_2 x}{\sqrt{(\mu_2 x)^2-(H/2)^2}}\right)\right] \quad (8.2)$$

The terms μ_1 and μ_2 are the complex roots of the following characteristic equation,

$$a_{11}\mu^4 - 2a_{16}\mu^3 + (2a_{12}+a_{66})\mu^2 - 2a_{26}\mu + a_{22} = 0 \quad (8.3)$$

The material constants a_{ij} are related to engineering constants as,

$$a_{11}=\frac{1}{E_X}, a_{22}=\frac{1}{E_Z}, a_{33}=\frac{1}{E_Y}, a_{12}=\frac{\nu_{ZX}}{E_Z}, a_{13}=\frac{\nu_{YX}}{E_Y}, a_{23}=\frac{\nu_{ZY}}{E_Z}, a_{66}=\frac{1}{G_{XZ}} \quad (8.4)$$

For plane strain problems, the constants a_{ij} in Eq. 8.4 should be replaced with b_{ij} in Eq. 8.5,

$$b_{ij} = a_{ij} - \frac{a_{i3}a_{j3}}{a_{33}} \quad (8.5)$$

Eq. 8.5 is obtained by equating the strain components in Z direction to zero in stress-strain relations for orthotropic material. Finally, for the condition of plane XZ in the state of plane strain, the induced stress component in Y-direction (i.e. parallel to fracture length) can be expressed as,

$$\sigma_{yy(z=0)} = -\left(a_{13}\sigma_{xx(z=0)} + a_{23}\sigma_{zz(z=0)}\right)/a_{33} \quad (8.6)$$

If a fracture is discretized along its length (a plane cut normal to the fracture height) into N constant displacement discontinuity elements, the normal and shear stresses at each element center can be represented as,

$$\begin{aligned}\sigma_n^i &= \sum_{j=1}^{N} G^{ij}A_{ns}^{ij}D_s^j + \sum_{j=1}^{N} G^{ij}A_{nn}^{ij}D_n^j \\ \sigma_s^i &= \sum_{j=1}^{N} G^{ij}A_{ss}^{ij}D_s^j + \sum_{j=1}^{N} G^{ij}A_{sn}^{ij}D_n^j \\ (i&=1,N)\end{aligned} \quad (8.7)$$

where A_{ns}^{ij}, etc., are the influence coefficients that gives normal/shear stress on element i due to unit normal/shear displacement discontinuity acting on element j in an orthotropic rock. The Eq.

8.7 is conventional DD formulation for stress vectors with a correction factor G introduced to account for the fact that the fracture height, H, might not be the largest fracture dimension.

Consider the two limiting cases where $H \to \infty$ and $H \to 0$ for the configuration depicted in Figure 8-1. One can argue that the corresponding G factor (in Eq. 8.7) for these two limiting cases must be 1 and 0 respectively. This is because, when $H \to \infty$, the Eq. 8.7 should revert back to original DDM formulation, as a result G factor must be 1. On the other hand, when $H \to 0$, the induced stresses around the fracture must reach zero; thus G factor must be zero in this case.

Following the approach of Olson (2004), if we write the analytical expression for σ_{XX} from Eq. 8.1 in the following form by replacing X with d_{ij} (representing the distance between the displacement discontinuity elements i and j),

$$G^{ij} = 2\,\text{Real}\left[\frac{P\mu_2}{2(\mu_1-\mu_2)}\left(\frac{(\mu_1 d_{ij})^{\beta}}{\sqrt{(\mu_1 X)^2-(H/\alpha)^2}}-1\right)+\frac{P\mu_1}{2(\mu_2-\mu_1)}\left(\frac{(\mu_2 d_{ij})^{\beta}}{\sqrt{(\mu_2 X)^2-(H/\alpha)^2}}-1\right)\right] \qquad (8.8)$$

the limiting conditions of G described above are satisfied. Moreover, as we are trying to match the numerical solution with analytical solution for the component σ_{XX}, Eq. 8.1 is obvious choice for constructing the G factor. For instance, if the distance (d_{ij}) between the elements i and j is extremely large compared to the fracture height (H), the G^{ij} goes to zero and the influence of element j on element i is nullified in Eq. 8.7. Similarly, if fracture height is extremely large compared to the distance between the elements i and j, G^{ij} goes to 1; therefore the influence of element j on element i is unaltered from original DD formulation. For all other intermediate values of d_{ij}/H, G^{ij} is between 0 and 1 and therefore reduces the strength of influence coefficients between the elements i and j by a factor.

The constants alpha and beta are curve fitting constants and they are found by trial and error to give the best fit between the analytical solution of σ_{xx} from Eq. 8.1 and the numerical DDM solution of σ_{xx} with G factor from Eq. 8.7 for the problem depicted in Figure 8-1, when L/H>>1. The original values of alpha and beta (i.e. 2 and 1 respectively from Eq. 8.1) can be used as initial guesses.

For an orthotropic material with properties given in Table 8-1 (Young's modulus values are displayed on figures and shear modulus G_{xz} is obtained using Eq. 8.9), Figure 8-2a shows that α =1.25 and β =0.98 yield the best fit between the normalized solutions of σ_{xx} from DDM with G^{ij} (Eq. 8.7) and analytical formula (Eq. 8.1). Although the best values for α and β are obtained by matching only the σ_{xx} component, comparison of σ_{yy} (i.e. in the direction of fracture length) component between analytical (Eq. 8.6) and numerical (Eq. 8.7) solutions indicate a higher deviation (see Figure 8-2b) similar to isotropic case, however is within the acceptable range. Overlaid numerical solutions of induced σ_{xx} and σ_{yy} components in Figure 8-2 that are obtained without using 3D correction factor G indicates gross overestimation of stresses around a fracture, when L/H>>1.

$$G_{XZ} = \frac{E_X E_Z}{E_X (1+2\nu_{XZ}) + E_Z} \tag{8.9}$$

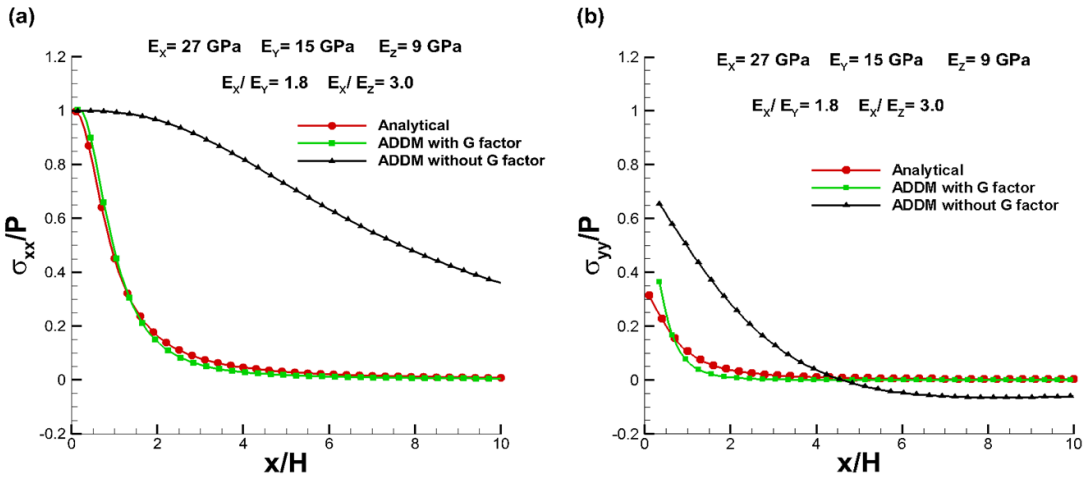

Figure 0-51. a) Comparison between analytical and numerical solutions of induced stress (compressive stresses are positive) components in X and, (b) Y-directions around the fracture in a homogeneous elastic orthotropic body shown in Figure 1. Analytical solution corresponds to the limiting case of a fracture with finite height H and infinite length. Numerical solution corresponds to a fracture of height H and length L, where L/H>>1.

Table 0-8. Elastic constants for orthotropic body in the coordinate system XYZ.

Elastic constants	Value
ν_{YX}	0.25
ν_{ZY}	0.10
ν_{ZX}	0.08

8.2 Sensitivity

Unlike isotropic case (Olson, 2004), the 3D correction factor G for anisotropic DDM is not purely geometric, since Eq. 8.8 includes material constants. This is because of the directional dependence of material properties in an anisotropic body. This also means that the G factor for anisotropic body not only adjust the DDM solution for finite fracture height, but also considers the effect of material properties in the direction of fracture height. As a result, it is expected that the fitting

parameters α and β of G from Eq. 8.8 to have some dependency on material properties. A sensitivity analysis is conducted by only varying the elastic parameters E_X, E_Y, E_Z, and G_{xz} while keeping the other elastic constants same as in the Table 8-1 to study the effect of material properties on curve fitting constants α and β. The results from Figure 8-3 indicate that the empirically derived constants α =1.25 and β =0.98 are very stable for a wide range of Young's modulus values, while the Poisson's ratio values are kept constant in an orthotropic body. On the other hand for a transversely isotropic rock with completely different set of properties given in Table 8-2, the best values of α and β are found to be 1.15 and 0.97 respectively from Figure 8-4. Nevertheless, the G factor for anisotropic DDM can be readily recalibrated (i.e. finding new values of α and β) for any specific set of orthotropic (or transversely isotropic) rock properties.

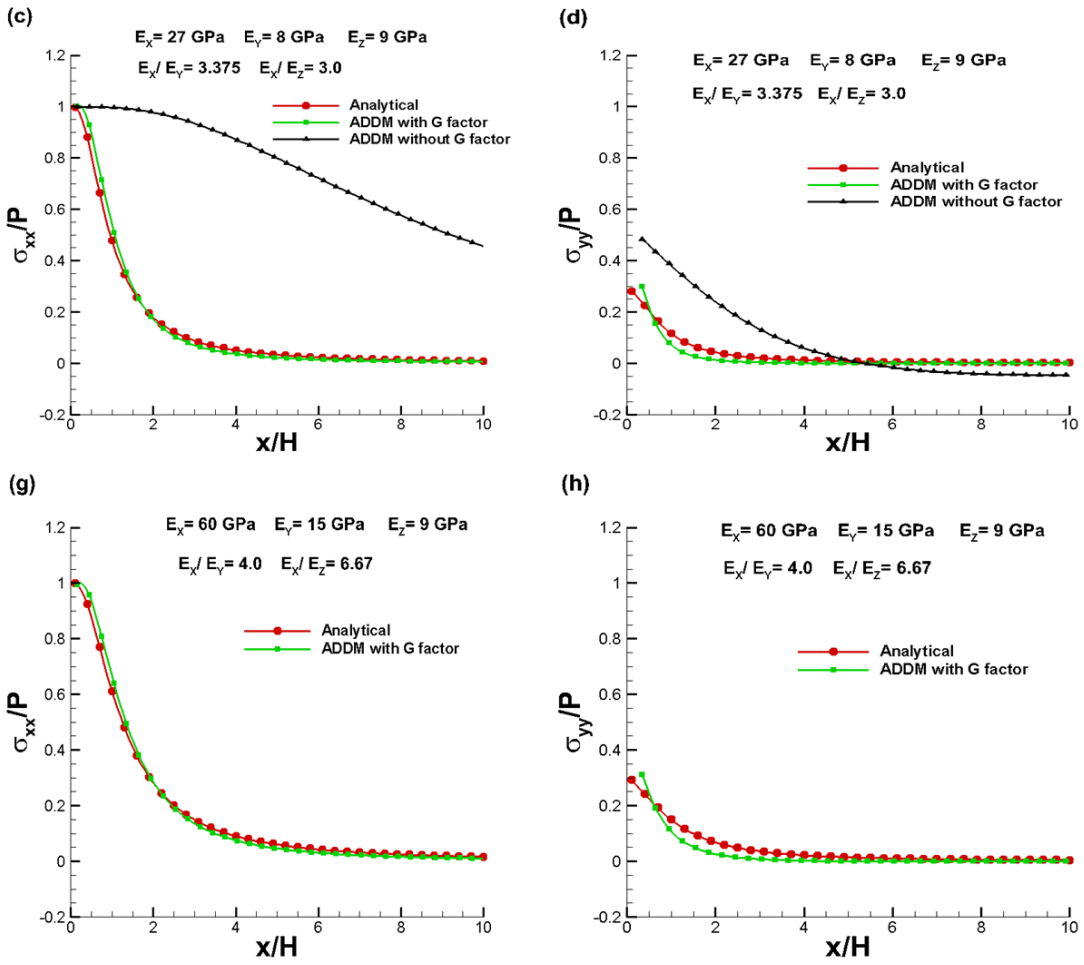

Figure 0-52. (c-h) Study of sensitivity of fitting parameters α and β to rock properties. Analytical solutions correspond to the limiting case of fracture with finite height H and infinite length. Numerical solutions correspond to a fracture of height H and length L where L/H>>1.

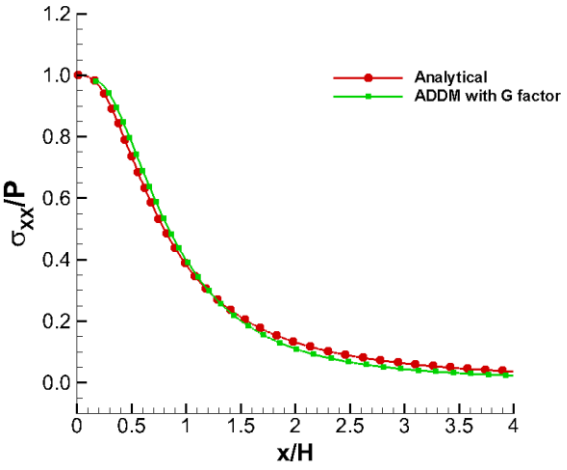

Figure 0-53. Normalized induced stress component σ_{xx} from numerical solution (Eq. 7) matched with analytical solution (Eq. 1) with curve fitting parameters α and β, 1.15 and 0.97 respectively. The material properties of the transversely isotropic rock are given in Table 8-2.

Table 0-9. Elastic constants of a transversely isotropic rock (Figure 1) in the coordinate system XYZ

E_X (GPa)	E_Y (GPa)	E_Z (GPa)	ν_{XY}	ν_{XZ}	G_{XZ} (GPa)
19.6	19.6	10.4	0.166	0.25	5.0

9 Effect of Anisotropy on Hydraulic Fracture Propagation at Field Scale

In the previous chapter, the effect of rock anisotropy on fracture opening and induced stresses is discussed using a single uniformly pressurized plane strain fracture. In this chapter, we will consider numerical simulations of propagation of simultaneous hydraulic fractures from a horizontal wellbore at field scale using enhanced 2D DDM based model and the effect of rock anisotropy on fracture geometry and opening is discussed. Figure 9-1 shows cross-sectional view of a fracture and anisotropic rock configuration. '*f*' is a vertical fracture with height 'H' parallel to axis Z, which is also the direction of principal vertical stress. The length 'L' of the fracture '*f*' is taken parallel to the axis X, which is also the direction of maximum principal horizontal stress. The minimum principal horizontal stress is in the direction of axis Y and the plane XY is a horizontal plane. It is also assumed that the height of the fracture '*f*' is contained to payzone thickness 'H' due to high stress barriers acting above and below it. Therefore, fracture propagation occurs only along the lateral direction. Axes 1, 2 and 3 indicate the axes of rock's elastic symmetry. For a vertical transversely isotropic rock (VTI) the horizontal plane 1-3 is isotropic.

The configuration of multiple vertical fractures from top view (i.e. XY plane view) is shown in Figure 9-2. In multi-stage hydraulic fracturing, multiple horizontal wells (typically 2 to 4) are stimulated in multiple stages (ranging 10-15) sequentially or simultaneously from toe to heel (Waters et al. 2009). A fracturing stage typically consists of 4 to 7 clusters of perforations that are evenly spaced. Traditionally, in all fracture models a single fracture per cluster is assumed. Based on this assumption, Figure 9-2 shows two fracturing stages that are created sequentially (i.e. Stage-2 follows Stage-1) from toe to heel with each stage containing three hydraulic fractures that emerged from three perforation clusters. Following the rock and fracture configuration depicted in

Figures 9-1& 9-2, we will consider single and multi-stage hydraulic fracturing numerical examples to study the effect of rock anisotropy on resultant fracture lengths and apertures.

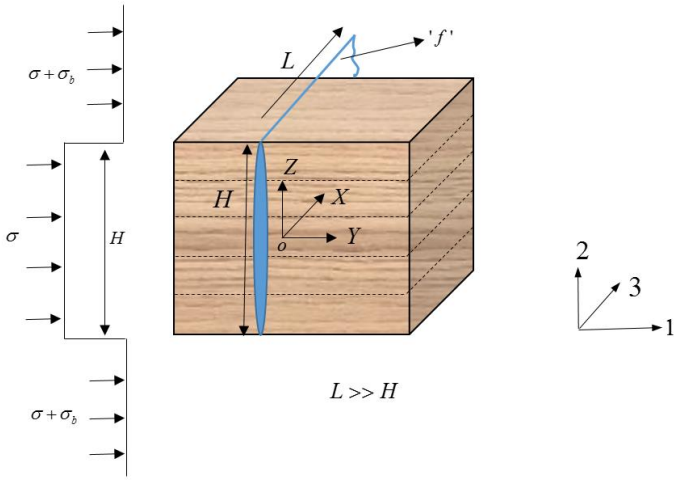

Figure 0-54. Geometry of a vertical fracture '*f*' in an anisotropic rock. Fracture height H is contained. 1, 2 and 3 are the three axes of rock's elastic symmetry. If the horizontal plane 1-3 is isotropic, the rock is called vertical transversely isotropic rock.

For all the examples consider below, the injection fluid is taken as slick water with viscosity 1 cP. The injection rate for each stage is 50 bpm and injection time for each stage is 17 min. We assume that the rock is impermeable and the effect of fluid leak-off is ignored. All fractures have a constant height of 30 m, whose effect in the solution of displacement discontinuity method is considered using a correction factor (see Chapter 8). The stress contrast in the horizontal plane is taken as 1 MPa to encourage complex fracture growth. Unless otherwise mentioned, in all examples (both isotropic and anisotropic) fracture toughness is taken as 2 MPa.m$^{0.5}$ and perforation friction is ignored.

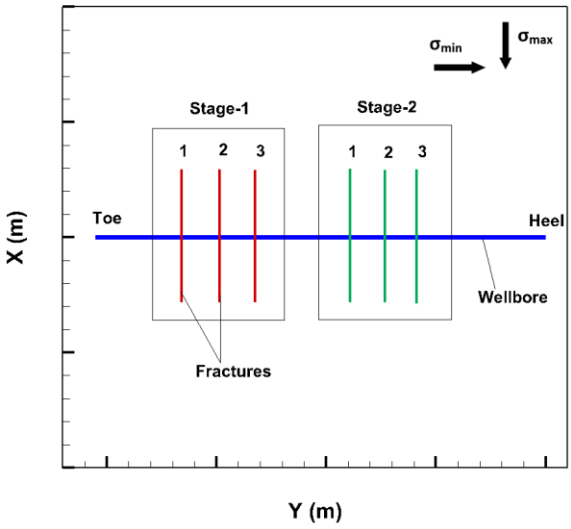

Figure 0-55. Layout of a single lateral with two stages created sequentially from toe to heel. Each stage contains multiple perforation clusters, where a single fracture is emerged from each cluster.

Table 0-10. Properties of Rock-A

E_1 (GPa)	E_3 (GPa)	E_2 (GPa)	ν_{13}	ν_{12}	G_{12} (GPa)	K_{IC} (Mpa.m$^{1/2}$)
40	40	10	0.15	0.185	7.45	2.0

9.1 Numerical Examples

9.1.1 Example-1 Single Stage Hydraulic Fracture Simulation in Rock-A

The first example investigates the effect of rock anisotropy on single stage hydraulic fracturing. Two different vertical transversely isotropic rocks are considered. The first one is Argillaceous shale (which is referred hereon as Rock-A) with high degree of anisotropy 4 (see Table 9-1), and the second one is Woodford shale (which is referred hereon as Rock-B) with moderate degree of anisotropy 1.88 (see Table 9-2). To highlight the effects of rock anisotropy on the results, isotropic

results are also presented for comparison. Isotropic results are obtained using the Young's modulus and Poisson's ratio of the isotropic plane in VTI rock (i.e. E_1 and ν_{13} according to Figure 9-1).

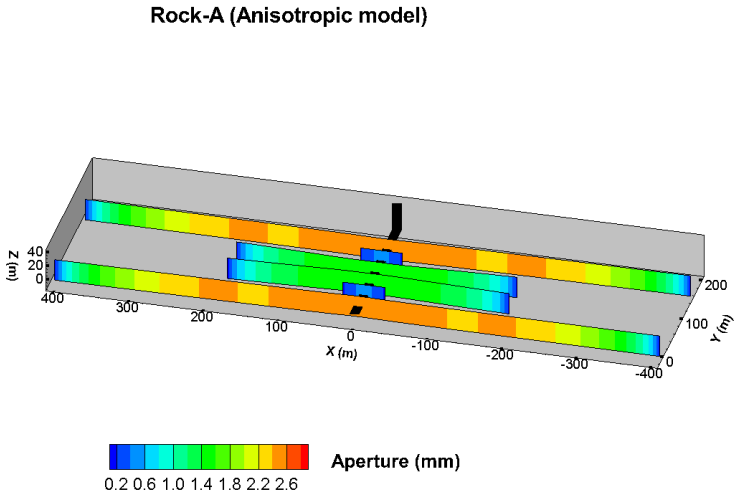

Figure 0-56. Fracture geometry and aperture distribution obtained after injection 17 min of slick water injection into six perforation clusters spaced 30 m in Rock-A using anisotropic model.

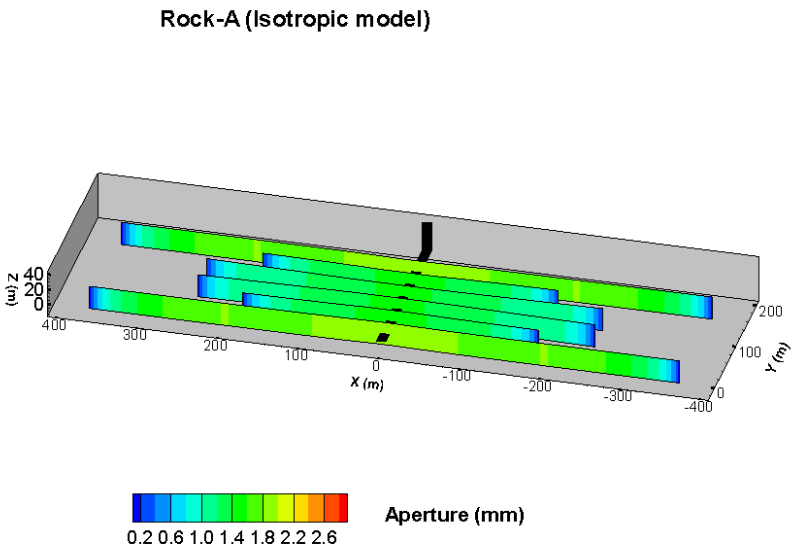

Figure 0-57. Fracture geometry and aperture distribution obtained after injection 17 min of slick water injection into six perforation clusters spaced 30 m in Rock-A using isotropic model.

The fracturing stage contains 6 perforation clusters with even spacing of 30 m (i.e. the ratio of spacing to fracture height is 1). Assuming an initial fracture of length 2 m from each perforation cluster, the numerical results after 17 min of fluid injection are shown in Figures 9-3& 9-4 for Rock-A from anisotropic and isotropic models.

At the first glance, one can see that the isotropic model overestimated lengths of all 4 inner fractures and underestimated the apertures of 2 outermost fractures. Both isotropic and anisotropic models predicted early termination of fractures adjacent to the dominant outer ones. However, in anisotropic model this effect is much more pronounced. Based on the analysis of induced stresses around a single static plane strain fracture from the previous chapter, we note that in VTI rock, the induced stresses normal to the surface of a vertical fracture increases in magnitude and areal extent

with increase in degree of anisotropy compared to isotropic case. As a result, the 30 m spacing between the clusters is insufficient in Rock-A to avoid early termination of inner fractures due to stress shadow effect. Also, note that based on the analysis of a single static plane strain fracture from the previous chapter, a vertical fracture in a VTI rock would observe much higher opening compared to isotropic case. However, in the case of closely spaced multiple fractures, only outer fractures observed increase in fracture apertures. The increased effect of stress shadow between the fractures in anisotropic rock suppressed both lateral growth and opening of inner fractures as seen from Figure 9-3.

Table 0-11. Properties of Rock-B

E_1 (GPa)	E_3 (GPa)	E_2 (GPa)	ν_{13}	ν_{12}	G_{12} (GPa)	K_{IC} (Mpa.$m^{1/2}$)
19.6	19.6	10.4	0.166	0.25	5.0	2.0

9.1.2 Example-2 Single Stage Hydraulic Fracture Simulation in Rock-B

In this example we consider fracture propagation in Rock-B which is moderately anisotropic compared to Rock-A, while keeping the remaining input parameters same as in Example-1. The results obtained using isotropic and anisotropic models are presented in Figures 9-5& 9-6. One can see that even in the case of a moderately anisotropic rock, the effect of rock anisotropy on fracture propagation is evident. The anisotropic model predicts much smaller lengths and apertures for inner fractures due to increase in stress shadow effect between the fractures. Another interesting aspect of these results is that the predicted lengths of inner fractures adjacent to the dominant outermost fractures by isotropic model for Rock-B are much lower compared to isotropic model

results for Rock-A. From previous chapter, we note that the induced stresses normal to fracture surface are independent of elastic properties in isotropic rock for the case of single static uniformly pressured plane strain fracture. Although this is generally the case for a single fracture in isotropic rock, however, in the case of multiple fractures, relative opening of each fracture is important since the flow partition into fractures is proportional to the cube of fracture opening at the inlet (based on cubic law). The lower Young's modulus of Rock-B (which is about 50% of Rock-A's isotropic Young's modulus) facilitated higher opening of outer fractures, allowing them to take the most fluid and resulting in early termination of inner fractures adjacent it. This analysis suggests the strong coupling nature of simultaneously propagating multiple fractures where a simple predictive relationships between fracture lengths and rock elastic properties cannot be defined.

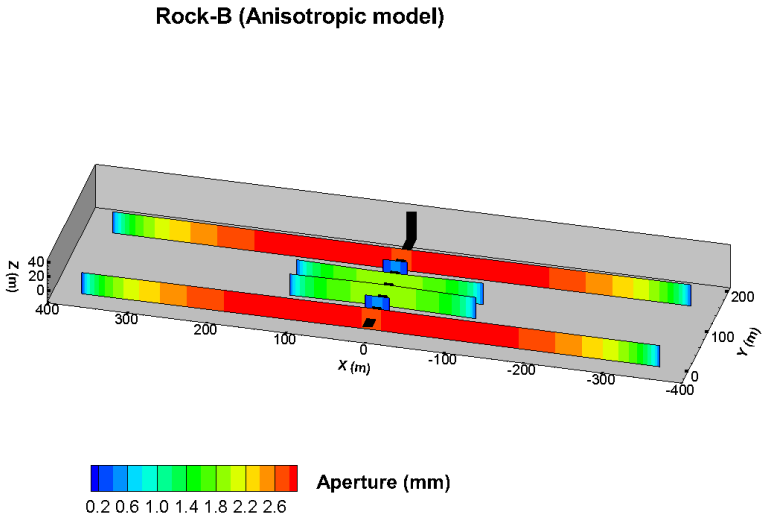

Figure 0-58. Fracture geometry and aperture distribution obtained after injection 17 min of slick water injection into six perforation clusters spaced 30 m in Rock-B using anisotropic model.

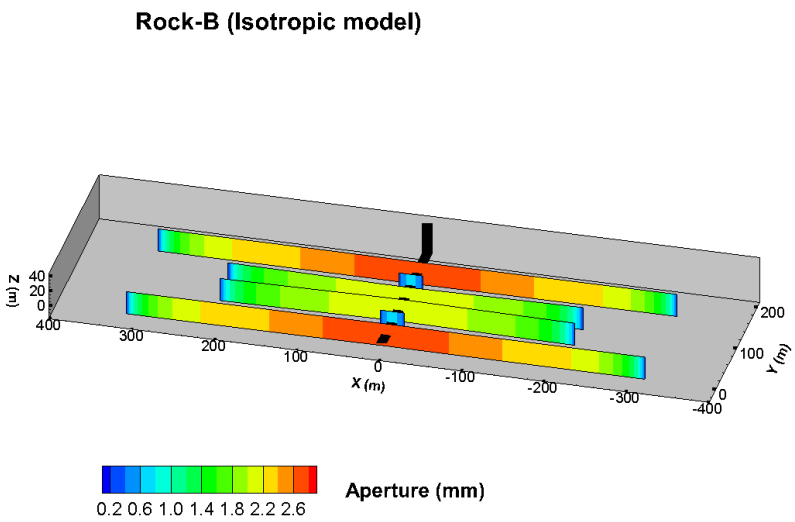

Figure 0-59. Fracture geometry and aperture distribution obtained after injection 17 min of slick water injection into six perforation clusters spaced 30 m in Rock-B using isotropic model.

Table 0-12. Properties of Rock-C.

E_1 (GPa)	E_3 (GPa)	E_2 (GPa)	ν_{13}	ν_{12}	ν_{23}	G_{13} (GPa)	G_{12} (GPa)	G_{23} (GPa)	K_{IC} (Mpa.$m^{1/2}$)
19.6	11.85	10.4	0.16	0.25	0.25	6.56	5.0	5.0	2.0

9.1.3 Example-3 Single Stage Hydraulic Fracture Simulation in Rock-C

In the previous examples, propagation of multiple hydraulic fractures is considered in vertical transversely isotropic rocks. Although most of the laboratory experiments on core size shale samples characterize shale as transversely isotropic, in general, rock masses can possess additional degree of anisotropy due to the presence of natural fractures sets or rock stratification. For example, an isotropic rock mass containing three orthogonal sets of natural fractures can be treated as orthotropic rock when deformation is viewed at large scale. If a rock has dense network of

natural fractures with well-defined orientation as indicated in Figure 9-7, modeling every natural fracture explicitly is impractical due to unreasonable computation time. Rather it is much easier and computationally efficient to treat such rocks as anisotropic. This is illustrated in this example by considering a vertical transversely isotropic rock (Rock-B) with evenly distributed vertical natural fractures (indicated by black lines in the plane XY) that are oriented at an angle ψ with respect to minimum principal horizontal stress direction (i.e. Y-axis) as indicated in Figure 9-7. Assuming the directions parallel and perpendicular to the natural fractures as the directions of the axes of elastic symmetry 1 and 2 in the plane XY, and *d* is the spacing between the natural fractures, the new elastic constants in the plane 1-2 are given as (Goodman, 1976),

$$\begin{aligned} E_1 &= E_1 \\ E_3 &= \frac{E_1}{1 + E_1 / dK_n} \\ G_{13} &= \frac{G_{13}}{1 + G_{13} / dK_s} \\ \nu_{13} &= \nu_{13} \end{aligned} \tag{9.1}$$

where K_n and K_s are natural fractures normal and shear stiffness respectively. Taking the elastic constants of Rock-B given in Table 9-2 and K_n, K_s as 30 GPa/m, and the spacing between natural fractures *d* as 1 m, the induced degree of anisotropy due to the presence of natural fractures in the plane 1-3 (E_1/E_3) is 1.65 using Eq. 9.1. Note that plane 1-3 is isotropic before including the effect of natural fractures. Therefore, a transversely isotropic rock (Rock-B) with natural fractures gives an equivalent anisotropic rock that is orthotropic and will be referred as Rock-C hereon. The complete list of nine independent elastic constants of Rock-C is given in Table 9-3.

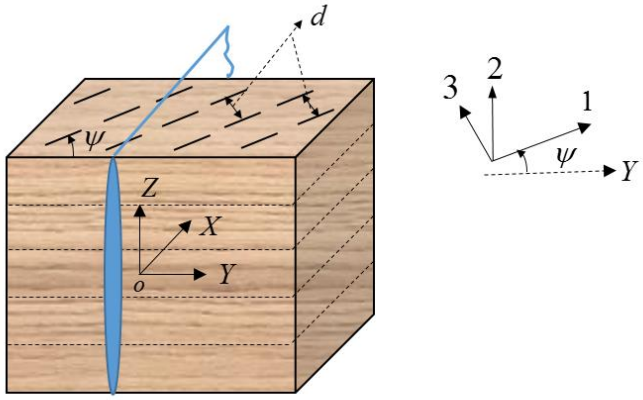

Figure 0-60. Cross section of a vertical transversely isotropic rock with vertical natural fracture sets (indicated by black lines) with spacing d and orientating at an angle ψ with respect to the direction of minimum principal horizontal stress (i.e. axis Y).

Figure 9-8 shows computed fracture geometry and apertures for Rock-C using anisotropic model while keeping the other input parameters same as previous examples. This result belongs to the case where the orientation of natural fractures is parallel to minimum principal horizontal stress or Y-axis (i.e. $\psi = 0^0$). It can be seen that the predicted lengths and apertures of all four inner fractures are much smaller than those observed for Rock-B. The presence of anisotropy in the horizontal plane XY further enhanced the stress shadow effect between the fractures which negatively impacted the growth of inner fractures while creating dominant outer fractures with much higher fracture opening compared to those observed in Rock-B (see Figures 9-5& 9-6).

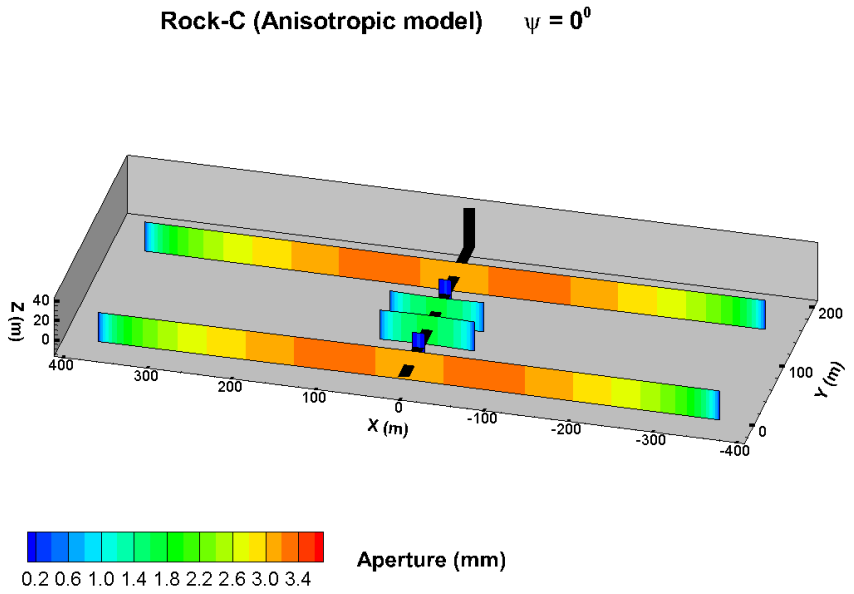

Figure 0-61. Fracture geometry and aperture distribution obtained after injection 17 min of slick water injection into six perforation clusters spaced 30 m in Rock-C with ψ =0^0. The presence of rock anisotropy in the horizontal plane further enhanced the interaction between the fractures affecting the lateral growth of inner fractures negatively.

To study the effect of the orientation of the axes of elastic symmetry with respect to the direction of fracture propagation, we considered a case where ψ =45^0 and the computed results are presented in Figure 9-9. The results indicate early termination of all four inner fractures and growth of two dominant outer fractures with very high apertures. We noted from the stress analysis of a single pressurized plane strain fracture that the induced stresses normal to the fracture surface will gradually decline as the direction of maximum Young's modulus is rotated from its direction perpendicular to the fracture surface (see Chapter 2). The observed results from Figure 9-9 are contrary to this where all inner fracture growth is highly suppressed. This is because, as the direction of maximum Young's modulus is rotated from its direction perpendicular to the fracture

surface, the fractures will open against lower Young's modulus. As noted in Example-2, the lower Young's modulus creates high fracture opening in outermost fractures allowing them to take most fluid while leaving the inner fractures unstimulated.

The last variation of this example is a case where the rock possess fracture toughness anisotropy. As discussed previously (see Chapter 7), we assume that minimum fracture toughness of the rock is observed in the direction parallel to the natural fractures (i.e. direction 1 in Figure 9-7) and maximum fracture toughness of the rock is observed in the direction perpendicular to the natural fractures (i.e. direction 2). For any arbitrary direction, the fracture toughness is obtained using an elliptical expression shown in Eq 7.12 from Chapter 7. Taking the maximum value of fracture toughness as 2 MPa.m$^{0.5}$ and minimum value of fracture toughness as 1 MPa.m$^{0.5}$ (i.e. the degree of fracture toughness anisotropy is 2), the computed results for Rock-C with ψ =45^0 are presented in Figure 9-10.

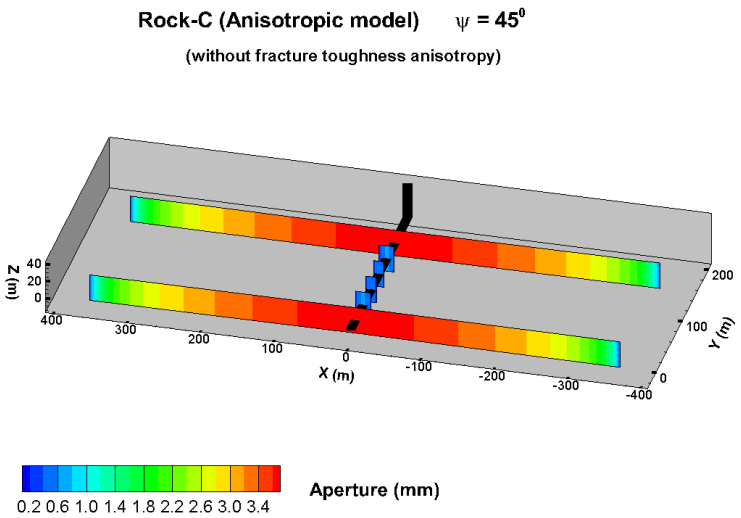

Figure 0-62. Fracture geometry and aperture distribution obtained after injection 17 min of slick water injection into six perforation clusters spaced 30 m in Rock-C with ψ =45^0. In

this case, the fractures opened against the direction of much lower Young's modulus which created higher fracture opening in outermost fractures that allowed them to take most fluid while leaving the inner ones unstimulated.

Two different observations can be made from this result. The first one is that the lengths of the inner most fractures are greatly improved compared to the previous two cases and the second one is asymmetrical lateral growth of inner fractures. The improvement in the lateral growth of inner fractures can be attributed to decrease in rock's resistance for fracture propagation (due to fracture toughness anisotropy) and decrease in stress shadow effect between the fractures as the fractures are no longer perpendicular to the direction of maximum Young's modulus since $\psi = 45^0$. The asymmetry in lateral growth of inner fractures can be attributed to rotation of stress shadow towards the direction of maximum Young's modulus (see Figure 3-2) due to which the growth of fractures in the direction of maximum Young's modulus is suppressed to an extent. In this example, the degree of rock anisotropy in the horizontal plane XY is just 1.65. For much higher degree of anisotropy in the horizontal plane, a greater asymmetry in the fracture lengths can be expected. We can also notice some tilt in the direction of fracture growth in the XY plane (note that the amount of tilt appears in Figure 9-10 is exaggerated due to distorted scale in the XY plane). This is due to fact that the fractures trying to orient towards the direction of least fracture toughness (which is at 45^0 with respect to Y-axis).

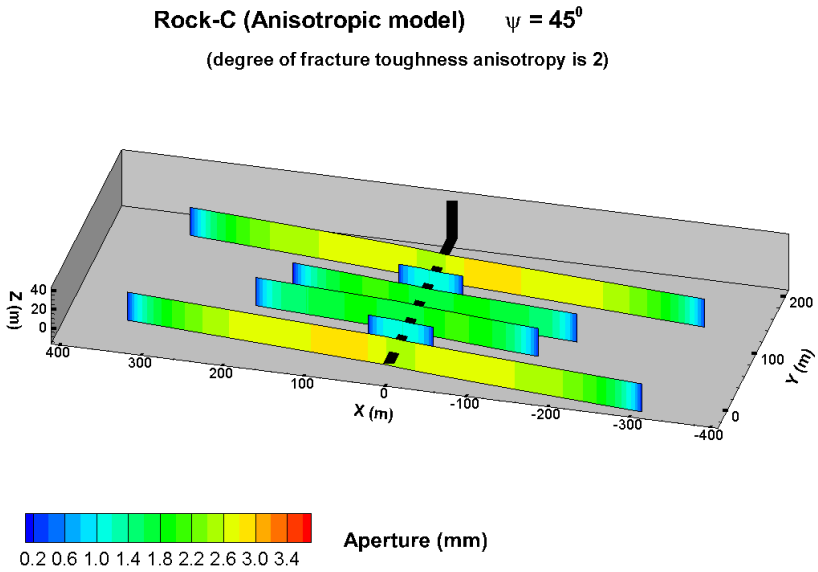

Figure 0-63. Fracture geometry and aperture distribution obtained after injection 17 min of slick water injection into six perforation clusters spaced 30 m in Rock-C with ψ =45^0. The rock has fracture toughness anisotropy of degree 2 in XY plane. Note that the amount of fracture tilt appears in the figure is exaggerated due to distorted scale in the XY plane.

Nevertheless, even in the presence of fracture toughness anisotropy, all fractures still appear to propagate towards the direction of maximum principal horizontal stress (i.e. along X-axis) although the stress contrast is just 1 MPa. This result is consistent with the results of near wellbore fracture propagation (Sesetty and Ghassemi, 2018), where far-field stress directions are observed to have dominant control on fracture paths compared to fracture toughness anisotropy.

9.1.4 Example-4 Multi-Stage Hydraulic Fracture Simulation in Rock-B

In this example we will consider numerical simulation of multi-stage hydraulic fracturing of a single lateral well. The well and fracture layout is shown in Figure 9-2. The well is stimulated in three stages working from toe to heel with each stage consisting of six perforation clusters. Each

stage has a span of 200 m along the lateral with 40 m spacing between perforation clusters. The spacing between outermost fractures of two subsequent stages is also 40 m (this is usually referred as stage spacing). Each fracturing stage is stimulated for 17 min by injecting slick water at 50 bpm. In field, prior to the stimulation of later stages, previous stages are either propped or kept pressurized by preventing fluid flow-back to avoid closure of created fracture network. Due to gradual leaf-off of fluid into formation and stress shadowing from the current stage fractures, the previous stage fractures will experience some fracture closure. In numerical simulations, this behavior can be simplified by assigning a specified amount of closure to previous stage fractures. The induced stresses due to the retained apertures of fractures from previous stages on the current stage fractures is explicitly calculated at every time step. This approximation considers closure of fractures from previous stages and their stress shadowing effect on current stage fractures without involving high computational effort that would be required if all fractures from all stages (previous and current) are solved as a coupled system. In this example, all previous stages fractures are assumed to hold only 70% for their total widths (note that the fracture apertures displayed in the results are total values obtained at the end of injection into each stage).

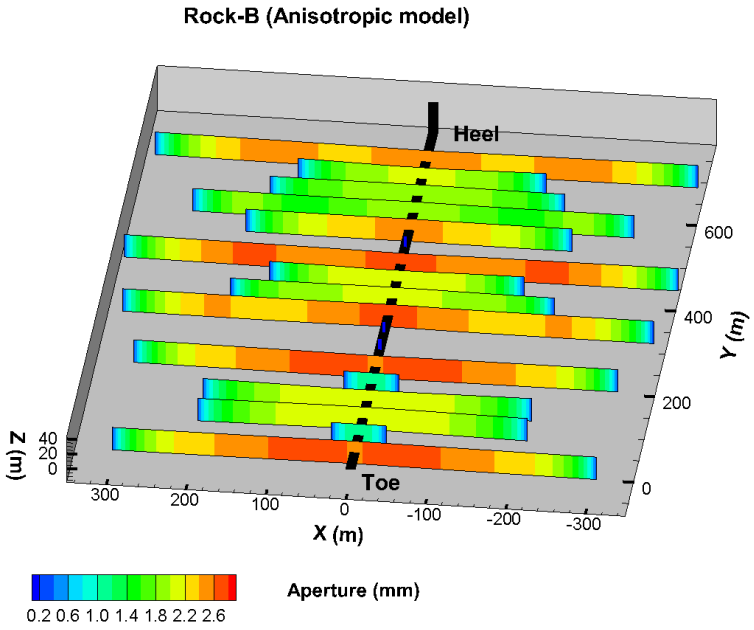

Figure 0-64. Fracture geometry and aperture distribution obtained after injection 17 min of slick water injection into each of the three stages in Rock-B using anisotropic model.

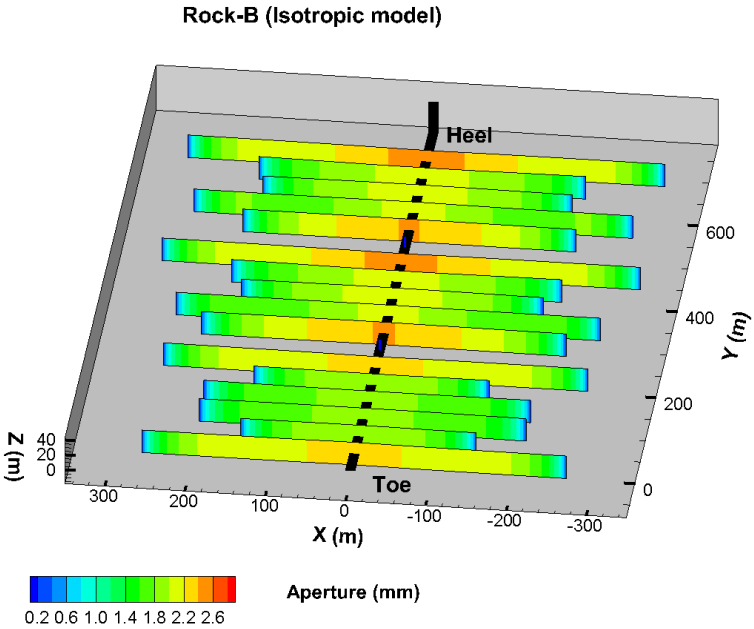

Figure 0-65. Fracture geometry and aperture distribution obtained after injection 17 min of slick water injection into each of the three stages in Rock-B using isotropic model.

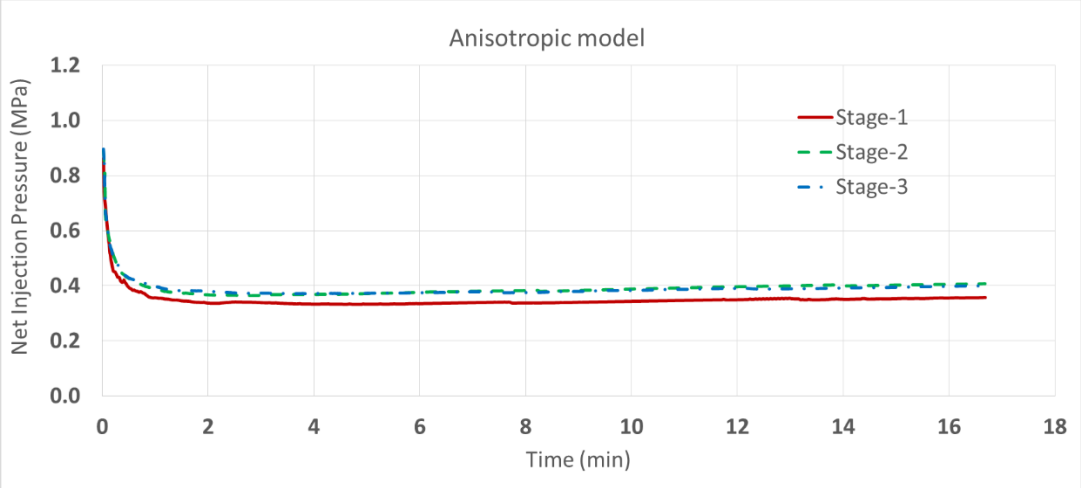

Figure 0-66. Comparison of injection pressure profiles for all 3 stages for Rock-B obtained from anisotropic model.

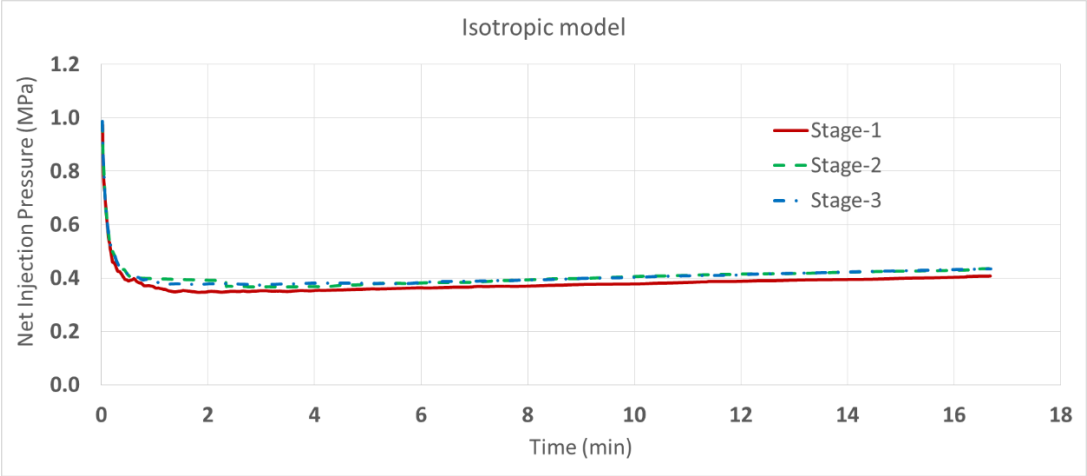

Figure 0-67. Comparison of injection pressure profiles for all 3 stages for Rock-B obtained from isotropic model.

The numerical results for Rock-B from isotropic and anisotropic models are shown in Figures 9-11& 9-12. In Stage-1, which was created at the toe of the well, all the six clusters were stimulated in both isotropic and anisotropic models. However, in Stages 2& 3, only 5 clusters were stimulated in isotropic model. Anisotropic model shows stimulation of only 4 clusters from Stage-2 and 5 clusters from Stage-3. This is due to stress shadow effect from previous stage fractures. Moreover, the outermost fracture on the heel side of Stages 2& 3 appear to achieve largest length among all

fractures especially in anisotropic model. This phenomenon is generally referred as “heel bias” and has been well reported in micro-seismic data from field operations (Waters et al. 2009). The increased stress shadow effect due to rock anisotropy exerted significant negative influence on lateral growth of inner fractures in all three stages, thereby allowing the outer most fractures (on the heel side) to achieve the largest lengths. One can also see that the predicted fracture lengths and apertures in each stage is markedly different between isotropic and anisotropic models even for a rock with degree of anisotropy just 1.88.

The net injection pressure at the wellbore during all three fracturing stages from isotropic and anisotropic models is given in Figures 9-13& 9-14. The injection pressure initially observed drop and later approached an almost constant value (a slight upwards trend can be noticed due to height containment and fractures attaining PKN geometry) in all stages. Appreciable increase in injection pressures in subsequent stages (i.e. Stages 2& 3) is not observed in both isotropic and anisotropic models. There is a misconception that subsequent stage fractures observe higher injection pressures compared to previous stage fractures as the new fractures are created in the presence of stress shadow. This could be true for the case of a single fracture created in the presence of high stress shadow. However, when multiple clusters are present spanning a large area, the injected fluid can migrate into clusters that are least affected by the stress shadow, thereby acting as a pressure relief mechanism while leaving the clusters most affected by stress shadow unstimulated (see Figures 9-11& 9-12). This phenomenon is also mentioned in (Waters et al., 2009) where increasing trend of injection pressures was not observed when stimulating a lateral from toe to heel in a field operation.

Table 0-13. Perforation properties.

n (number of perforations per cluster)	D (diameter of perforation, inch)	C Perforation coefficient
15	0.4	0.5

9.1.5 Example-5 Effect of Perforation Friction

Previous examples demonstrated the effect of rock properties on simultaneous propagation of multiple hydraulic fractures in the absence of perforation friction. When perforation friction is not accounted, the injection pressure in the wellbore and fluid pressure inside the fractures at their inlet will be very close and the flow partition into each fracture will be primarily controlled by fracture opening at the inlet (which is affected by stress shadow). The fractures with relatively higher opening will take the most fluid while leaving the remaining clusters unstimulated. By introducing perforation friction, the flow partition between the clusters can be equalized by overcoming the effect of stress shadow. This example demonstrates the effect of perforation friction on hydraulic fracture propagation. The Example-1 is repeated with the perforation parameters given in Table 9-4 and the computed result using anisotropic model is given in Figure 9-15.

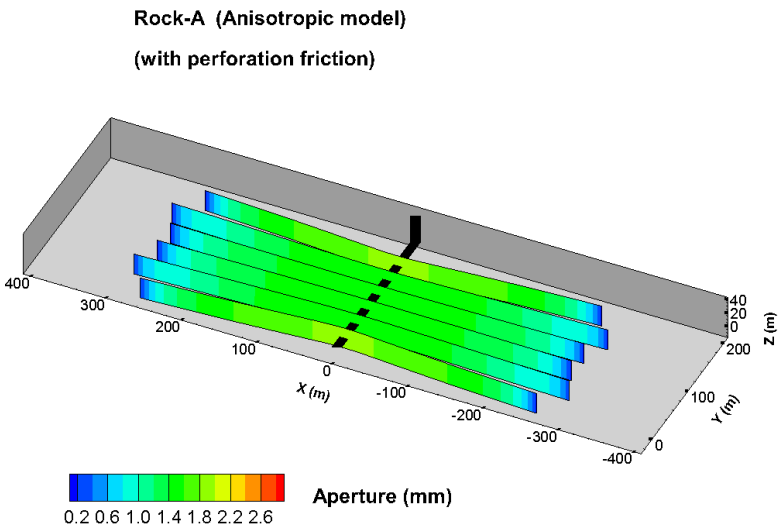

Figure 0-68. Fracture geometry and aperture distribution obtained after injection 17 min of slick water injection into six perforation clusters spaced 30 m in Rock-A considering perforation friction.

One can see equal fracture growth from all perforation clusters in this case. By introducing perforation friction the net injection pressure in the wellbore is kept at higher value than the net pressure inside the fractures as indicated in Figure 9-16. The difference between these values is perforation friction. Since the pressure drop at each cluster inlet is proportional to the square of the flow rate into that cluster (according to Eq.), as the flow rate into a cluster dominates, its pressure drop increases, thereby forcing to the fluid into other clusters that are taking less fluid. The method of optimizing flow partition between the clusters has been demonstrated before (Cheng et al. 2016) and is referred as "Limited Entry Technique". Although this technique should work in theory, however, in practice the perforation friction deteriorates with time due to perforation erosion from injection rates higher than the rated values and abrasive proppant (Crump and Conway, 1988) and affects fracture propagation. To demonstrate this, we repeated the above

example with perforation erosion where perforation friction deteriorates with time and the computed results are shown in Figures 9-13& 9-14. The perforation properties given in Table 9-4 are altered with time as follows

$D = 0.4$ inch, C=0.5 : 0-200 sec
$D = 0.6$ inch, C=0.7 : 201-500 sec
$D = 0.8$ inch, C=0.9 : 501-1000 sec

We note that the inner fractures still observed appreciable growth, however is less than the case where perforations are not eroded (see Figure 9-11). Also, in these example we assumed that all 15 perforations (Table 9-4) in a clusters are in communication with injection fluid. However, in practice some clusters can have poor perforation connectivity where all 15 perforations may not be in communication with the fluid. This can alter the flow partition between the clusters considerably and should be accounted.

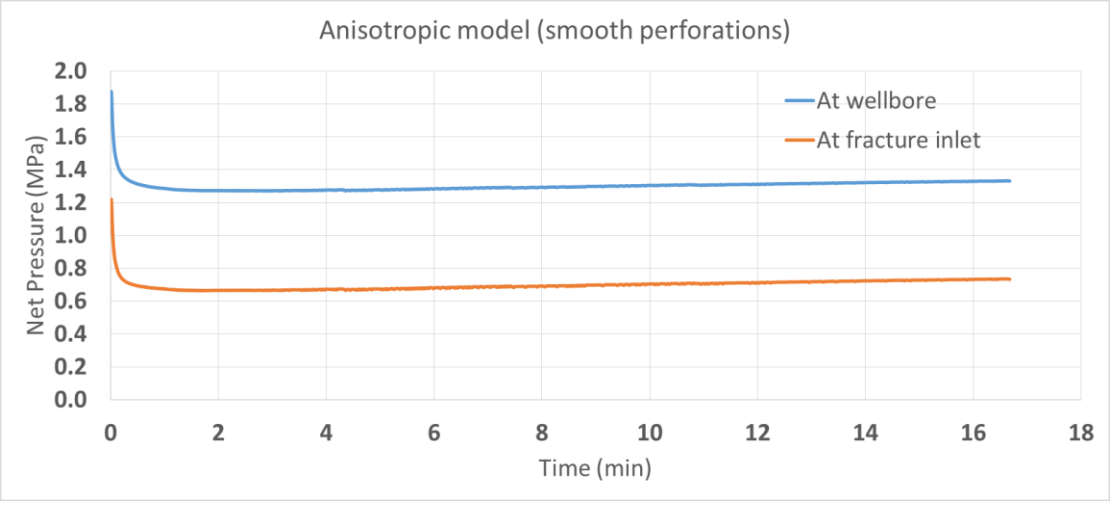

Figure 0-69. Net injection pressure at wellbore and maximum net pressure inside fractures at inlet for the numerical simulation shown in Figure 9-11. The difference between these two values gives perforation friction.

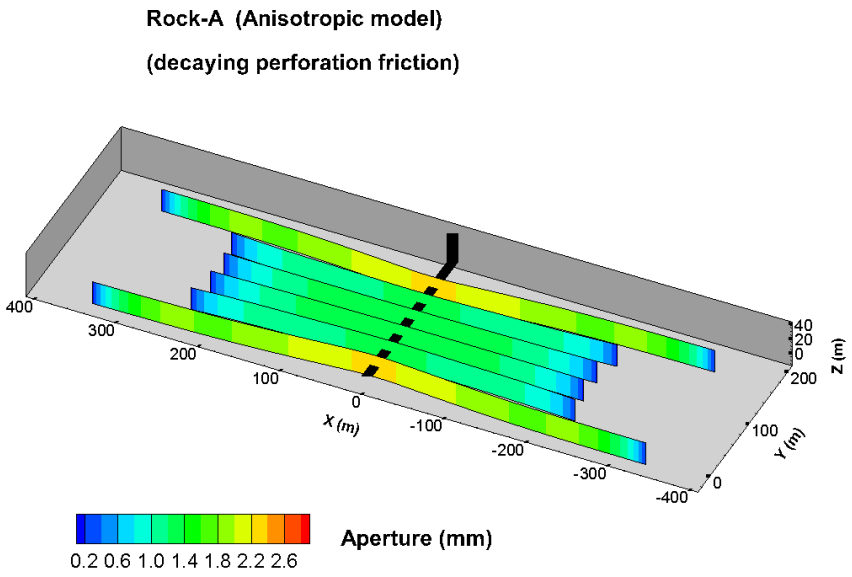

Figure 0-70. Fracture geometry and aperture distribution obtained after injection 17 min of slick water injection into six perforation clusters spaced 30 m in Rock-A for the case with deteriorating perforation friction.

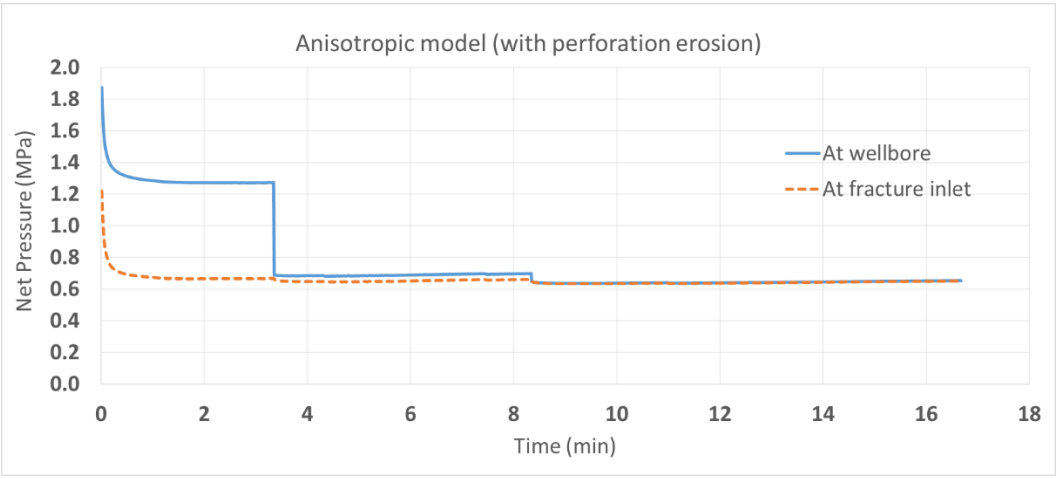

Figure 0-71. Net injection pressure at wellbore and maximum net pressure inside fractures at inlet for the numerical simulation shown in Figure 12. The difference between these two values gives perforation friction. After some time, the perforation friction drops to zero due to erosion.

9.2 Summary

In this chapter numerical examples illustrating simultaneous and sequential multiple hydraulic fracture propagation at field scale considering both rock modulus anisotropy and strength anisotropy are presented. A 2D DDM based fracture propagation model is employed for numerical simulations. All fractures are assumed to have a fixed height and the effect of fracture height in the solution of 2D DDM is accounted using a correction factor.

Analysis of field-scale fracture propagation shows the importance of rock anisotropy on interaction between simultaneously propagating multiple parallel fractures. One might consider rock anisotropy to be advantageous since the opening of a vertical fracture is enhanced with increase in degree of anisotropy in a VTI body as discussed in Chapter 7, however, the increase in induced normal stresses perpendicular to the fracture surface (see Figure 3-2) will negatively impact the fracture growth when fractures are closely spaced (which is critical to maximize stimulated reservoir volume). One of the shortcomings of 2D models is the assumption of infinite fracture height. However, the correction factor developed herein (see Chapter 8) can remedy this aspect to a large extent. On the other hand, semi-analytical planar 3D height growth models (see Chapter 9) do not account for the interaction between multiple fractures and are limited only to planar fractures. The fixed height plane strain numerical models such as 2D DDM with height correction factor are computationally efficient and can assess field scale non-planar fracture propagation and complex fracture networks while capturing the main features of the problem. For example, comparison between the 2D DDM and 3D results of fracture opening and length for the problem of a single planar fracture propagating between two symmetrical stress barriers indicates very close match for two different values of fracture toughness corresponding to viscous and toughness

regimes (see Chapter 3). The results of zipper fracturing from isotropic 2D DDM (Sesetty and Ghassemi, 2015) compares well with fully 3D isotropic DDM model (Kumar and Ghassemi, 2016). Also, the injection pressures and fracture trace (non-planar) from 2D DDM (Sesetty and Ghassemi, 2017a) is in very good agreement with laboratory results of Kear et al. (2013). In situations where fracture height growth cannot be ignored, and consideration of out of zone issues are needed, a complete 3D model is essential. Such models have been developed but even DD-based models come with additional computational costs and with the present computational resources they are not suitable for field-scale simulations. On the other hand 2D DDM simulations can be performed in reasonable time. The examples demonstrated in this chapter shows fractures where their lengths reach up to 800 m. The typically computation time for simulating a single stage with 6 clusters at field scale is around 3 hours on a desktop.

Field scale multi-cluster multi-stage fracturing simulations indicate the strongly coupled nature of the problem. The results are very sensitive to cluster spacing, rock stiffness, modulus anisotropy, fracture toughness, fracture toughness anisotropy and perforation parameters. These results indicated that rock modulus anisotropy enhances stress shadow effect between the fractures and therefore for spacing consideration between perforation clusters, the rock anisotropy must be accounted for optimal fracture growth from all perforation clusters. It is also interesting to note than even with low differential stress (1 MPa), fractures in all the stages have well defined azimuths pointing almost towards the direction of maximum principal stress (i.e. axis X). The rotation of these fractures was unlikely due to moderate net pressure buildup (see Figures 9-13& 9-14) that decreases with time and is not significant to cause stress reversal near the fractures. Also, when injecting fluid into multiple clusters, the fluid can always migrate into a fracture, which has least resistance (i.e. fracture which is least affected by stress shadowing of other fractures) to

opening thereby creating dominant fractures. Note that coalescence between fractures is possible under low differential stress conditions provided the spacing between the fractures is very low and the injection fluid is forced into the clusters by artificially elevating the injection pressures using perforation friction to overcome stress shadow between the fractures.

Overall, including rock anisotropy in fracture propagation models can be beneficial as they provide better understating of micro-seismic cloud patterns observed during multi-stage fracture stimulation process and facilitate optimization of completion strategies to achieve maximum stimulated reservoir volume.

10 Planar Height Growth Model for Anisotropic Rock

Fracture propagation models that consider all aspects (length, height growth, non-planarity and poroelasticity) in 3D (Kumar and Ghassemi, 2016& 2018) increase computational cost and could even become prohibitive to model multiple fractures at field-scale. Hence P3D (Planar-3D) models have been developed to reduce computational costs while addressing the shortcoming of early 2D models such as KGD and PKN. Both of these models are used to describe evolution of length and apertures of a vertical fracture while assuming a fixed fracture height.

In order to study the effect of material elastic anisotropy on hydraulic fracture height growth, in this work, the P3D model is extended to orthotropic rock for the case of a single fracture. Then, the single fracture P3D model is extended to the case of multiple fractures using the anisotropic 2D DDM to simulate interaction between the fractures. The DD approach includes the new 3D correction factor (see chapter 8) derived to improve the accuracy of induced stress calculations. The model is used to simulate and analyze hydraulic fracturing in anisotropic rock. Results for a single fracture P3D and 2D DDM in isotropic body are compared with 3D model results to assess the model accuracy. Then, simulations of large-scale simultaneous propagation of multiple fractures are carried out to compare fracture interactions in anisotropic and isotropic formations.

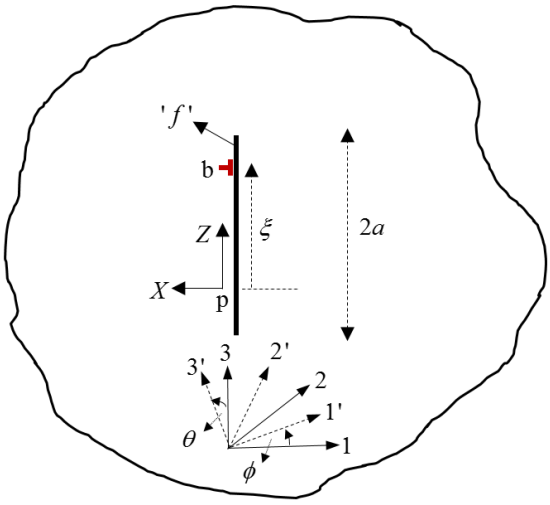

Figure 0-1. Infinite orthotropic body with line segment '*f*' of length 2a parallel to Z-axis and extends to infinity in the direction of Y-axis. 1-2-3 are the material's axes of elastic symmetry. X-Y-Z and 1-2-3 are in the same plane.

Consider an infinite elastic homogeneous orthotropic body with three principal axes of elastic symmetry in the directions 1, 2 and 3 as indicated in Figure 10-1. It is assumed that: (i) line segment '*f*' has length 2a in the direction of Z-axis and extends to infinity in the direction of Y-axis (i.e. perpendicular to the plane X-Z), (ii) as a result, the plane strain condition applies in the plane X-Z. Noting that the coordinate systems 1-2-3 and X-Y-Z lie in same planes, the induced stress in the X-direction at any point p (z, 0) along the line segment due to a single edge dislocation vector b (indicated by red color in Figure 10-1) on the line segment at a distance ξ from point p (z, 0) is given as (Azhdari et al., 1999; Obata et al., 1989),

$$\sigma_{xx} = 2\text{Real}\,[\mu_1^2\phi(z_1) + \mu_2^2\psi(z_2)]$$

where

$$\phi(z_1) = \frac{1}{2\pi i b_{11}} \frac{\mu_1 b_z - b_x}{\hat{\mu}_1} \frac{1}{z-\xi} \tag{10.1}$$

$$\psi(z_2) = \frac{1}{2\pi i b_{11}} \frac{\mu_1 b_z - b_x}{\hat{\mu}_2} \frac{1}{z-\xi}$$

$$\left\{ \begin{matrix} \hat{\mu}_1 = (\mu_1 - \mu_2)(\mu_1 - \mu_3)(\mu_1 - \mu_4) \\ \hat{\mu}_2 = (\mu_2 - \mu_1)(\mu_2 - \mu_3)(\mu_2 - \mu_4) \end{matrix} \right\}$$

In the above equation, b_x and b_z are edge dislocations in the directions X and Z respectively. μ_1, etc., are complex roots of the characteristic equation (Eq. 10.2) that always occur as conjugates (i.e. $\mu_3 = \bar{\mu}_1$ and $\mu_4 = \bar{\mu}_2$). For consistency with the reference material, μ_1 and μ_2 always indicate complex roots of characteristic equation (Eq. 10.2) with positive imaginary parts.

$$b_{11}\mu^4 - 2b_{16}\mu^3 + (2b_{12} + b_{66})\mu^2 - 2b_{26}\mu + b_{22} = 0 \tag{10.2}$$

$$b_{ij} = a_{ij} - \frac{a_{i3}a_{j3}}{a_{33}}$$

where a_{ij} are material constants in the new coordinate system 1'-2'-3' with $\phi = 0^0$ and $\theta = 90^0$ (ϕ is rotation angle of coordinate system 1-2-3 about axis 3, and θ is rotation angle of coordinate system 1-2-3 about axis 2). Their relationship with engineering constants is given in Appendix C.

The solution given in Eq. 1 can be generalized for continuous distribution of dislocations (of different magnitudes) along the entire length of 2a using principal of superposition, and the resultant induced stress in the X-direction at a point (z,0) on the line segment '*f*' is (Azhdari et al., 1999; Crouch and Starfield, 1983),

$$\sigma_{XX}(z,0) = 2\text{Real}\left(\frac{1}{2\pi i b_{11}} \int_{-a}^{a} \frac{1}{z-\xi} \left[\frac{\mu_1 b_z(\xi) - b_x(\xi)}{\hat{\mu}_1} + \frac{\mu_2 b_z(\xi) - b_x(\xi)}{\hat{\mu}_2} \right] d\xi \right) \tag{10.3}$$

where $b_x(\xi)$ and $b_z(\xi)$ are dislocation density functions in X and Z directions respectively and they are related to fracture opening ($w(\xi)$) and fracture ride ($r(\xi)$) as

$$\begin{aligned} b_x(\xi) &= -w'(\xi) \\ b_z(\xi) &= -r'(\xi) \end{aligned} \tag{10.4}$$

When $b_z(\xi)$ is zero (which is the case when crack is free of shear stresses and when the crack axes X-Y-Z coincides with the material axes 1-2-3), and noting that induced normal stresses on crack face $\sigma_{xx}(z,0)$ is equal to the net pressure inside the crack $p(z)$, the Eq. 10.3 is simplified to Eq. 10.5. (The complex situations that arise when material axes 1-2-3 are not aligned with fracture axes X-Y-Z are discussed later)

$$p(z) = \frac{\hat{\mu}_1 + \hat{\mu}_2}{\hat{\mu}_1 \hat{\mu}_2} 2\text{Real}\left(\frac{1}{2\pi i b_{11}} \int_{-a}^{a} \frac{w'(\xi)}{z-\xi} d\xi \right) \tag{10.5}$$

The equivalent expression for isotropic body is given as (Spence and Sharp, 1985) in Eq. 10.6.

$$p(z) = \frac{G}{(1-\nu)2\pi} \int_{-a}^{a} \frac{w'(\xi)}{z-\xi} d\xi \tag{10.6}$$

where G is shear modulus and ν is Poisson's ratio.

Noting the symmetry in pressure and aperture profiles about the center of the crack the Eq. 10.5 can be further simplified to Eq. 10.7.

$$p(z) = \frac{2\Delta_1}{b_{11}\Delta_0 \pi} \int_{0}^{a} \frac{\xi w'(\xi)}{\xi^2 - z^2} d\xi \tag{10.7}$$

which is inverted using Hilbert transform (see Spence and Sharp, 1985) to give $w'(z)$ as in Eq. 10.8.

$$\frac{\Delta_1}{b_{11}\Delta_0} w'(z) = \frac{z}{\sqrt{a^2 - z^2}} \frac{2}{\pi} \int_{0}^{a} \frac{\sqrt{a^2 - \xi^2}\, p(\xi)}{\xi^2 - z^2} d\xi + \frac{C'}{x\sqrt{a^2 - z^2}} \tag{10.8}$$

where C' is a constant which is taken as zero to bound w' at z=0. Finally, integrating the above equation with respect to z (see Spence and Sharp, 1985) with the boundary condition $w(a)$ =0 gives an integral equation that relates fracture aperture with pressure distribution inside a line fracture of length 2a in an orthotropic rock body.

$$\frac{\Delta_1}{b_{11}\Delta_0} w(z) = \frac{1}{\pi}\int_0^a \ln\left|\frac{\sqrt{a^2 - z^2} + \sqrt{a^2 - \xi^2}}{\sqrt{a^2 - z^2} + \sqrt{a^2 - \xi^2}}\right| p(\xi) d\xi \qquad (10.9)$$

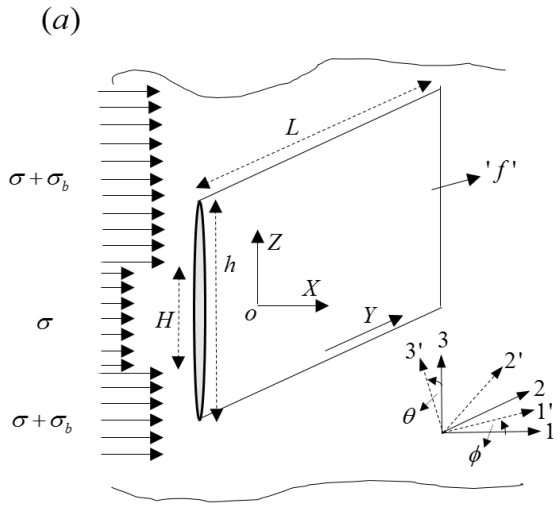

Figure 0-2. Geometry of a symmetrical planar fracture '*f*' with length *L* and height *h* such that *L*/*h*>>1. *H* is the thickness of payzone.

10.1 Formulation of a Single Fracture P3D Model

10.1.1 Fracture Aperture

Consider an infinite orthotropic formation subjected to far-field compressive stress of magnitude σ in the X-direction over a thickness *H* (payzone) as indicated in Figure 10-2. The payzone is bounded by two symmetrical higher stress zones that extends to infinity, where far-field stress

magnitude in X-direction is $\sigma+\sigma_b$. Also, the maximum principal stress is always parallel to Z-axis. If we consider a symmetrical fracture '*f*' with geometry shown in Figure 10-2, that extends into the higher stress zones and has a total height '*h*' that is much greater than its length *L*, it is appropriate to use plane strain condition in the plane X-Z. Moreover, we assume that fracture '*f*' is free of far-field shear stresses and the axes of elastic symmetry coincides with the fracture axes X-Y-Z. Under these conditions and choosing origin '*o*' at the center of payzone *H* (i.e. midpoint of fracture height *h*), one can use Eq. 10.9 to perform piece wise integration over the entire height *h* to obtain fracture aperture distribution for a given constant net pressure P inside the fracture. The resultant equation that relates fracture aperture, net pressure and height is given as,

$$w(z)=\frac{b_{11}\Delta_0}{2\Delta_1}(P-\sigma_b)\sqrt{h^2-4z^2}+\frac{\Delta_0 b_{11}\sigma_b}{\Delta_1\pi}\left\{\begin{array}{l}\sqrt{h^2-4z^2}\arcsin\left(\frac{H}{h}\right)-z\ln\left|\frac{H\sqrt{h^2-4z^2}+2z\sqrt{h^2-H^2}}{H\sqrt{h^2-4z^2}-2z\sqrt{h^2-H^2}}\right| \\ +\frac{H}{2}\ln\left|\frac{\sqrt{h^2-4z^2}+\sqrt{h^2-H^2}}{\sqrt{h^2-4z^2}-\sqrt{h^2-H^2}}\right|\end{array}\right\} \qquad (10.10)$$

The equivalent expression for isotropic body is (Adachi et al., 2010)

$$w(z)=\frac{2(1-\nu^2)}{E}(P-\sigma_b)\sqrt{h^2-4z^2}+\frac{4(1-\nu^2)\sigma_b}{E\pi}\left\{\begin{array}{l}\sqrt{h^2-4z^2}\arcsin\left(\frac{H}{h}\right)-z\ln\left|\frac{H\sqrt{h^2-4z^2}+2z\sqrt{h^2-H^2}}{H\sqrt{h^2-4z^2}-2z\sqrt{h^2-H^2}}\right| \\ +\frac{H}{2}\ln\left|\frac{\sqrt{h^2-4z^2}+\sqrt{h^2-H^2}}{\sqrt{h^2-4z^2}-\sqrt{h^2-H^2}}\right|\end{array}\right\} \qquad (10.11)$$

where *z* is measured from the midpoint of payzone thickness *H*. The above equations can be used to calculate aperture profile in the plane X-Z (i.e. along fracture height) for a symmetrical fracture with three stress layers in isotropic or orthotropic bodies. In below sections Eq. 10.10/10.11 is used to develop P3D using a criterion that describes fracture height growth into the layers of higher stress.

10.1.2 Fracture Height

Equilibrium fracture height growth model is developed based on the assumption that fluid pressure variation along the fracture height is negligible. In other words, viscous dissipation in the direction of fracture height is zero, therefore fracture growth is completely controlled by fracture toughness. The assumption of negligible viscous dissipation in the direction of fracture height is valid only when the rate of growth of fracture height is very small compared to rate of growth of fracture in the lateral direction. Therefore, equilibrium fracture height growth modeling only applies in situations where fracture height growth is restricted, such in the case of formation payzone surround by high stress barriers. Consider a vertical fracture in an orthotropic body as shown in Figure 10-2. Assuming plane strain condition in the plane X-Z, the mode-1 stress intensity factor due to distributed net pressure $p(\xi)$ along the entire fracture height 2h is given as (Barnett and Asaro, 1972),

$$K_I = \frac{1}{\sqrt{a\pi}} \int_{-a}^{a} \sqrt{\frac{a+\xi}{a-\xi}}\, p(\xi) d\xi \tag{10.12}$$

As stated above, fracture height growth is assumed to occur in toughness dominated regime, therefore the mode-1 stress intensity factor (K_I) at fracture tips in the plane X-Z (see Figure 10-2) is always at equilibrium with fracture toughness of the rock (K_{IC}). For a symmetrical fracture 'f' (Figure 10-2) in three stress layer formation, using the bounding conditions given in Eq. 10.13 and performing piece wise integration of Eq. 10.12 gives Eq. 10.14.

$$P(\xi) = \begin{pmatrix} P - \sigma_b, & \text{H/2}<\xi<\text{h/2} \\ P, & \text{-H/2}<\xi<\text{h/2} \\ P - \sigma_b, & \text{-H/2}<\xi<\text{-h/2} \end{pmatrix} \tag{10.13}$$

$$2\arcsin\left(\frac{H}{h}\right)-\left(1-\frac{P}{\sigma_b}\right)\pi=\sqrt{\frac{2\pi}{H}}\frac{K_{IC}}{\sigma_b}\sqrt{\frac{H}{h}} \tag{10.14}$$

The above equation can be used to evaluate fracture height *h*, given the net pressure *P* inside the fracture, payzone thickness *H*, fracture toughness K_{IC} and excess confining stress in bounding layers σ_b. Note that equilibrium fracture height equation derived for anisotropic body (Eq. 10.14) is independent of material properties and is identical to isotropic case (Simonson et al., 1976). This is because the mode-1 (K_I) and mode-2 (K_{II}) stress intensity factors in anisotropic body are independent of material properties (Sih et al., 1965) when the conditions of plane strain/stress exists and the loading on the fracture surface is self-balanced (i.e. net load on fracture is zero) as in the case of pressurized fractures (or hydraulic fractures). Note that in situations where viscous dissipation cannot be ignored in the direction of fracture height (such as in the cases of extremely low fracture toughness or inadequate fracture containment), Eq. 10.14 gives erroneous estimation for fracture height. As a remedy, Dontsov and Pierce (2015) proposed a correction term called apparent fracture toughness that can be added to the fracture toughness of the rock (K_{IC}) to improve the accuracy of fracture height calculated from Eq. 10.14, however, the correction term is limited to a single plane strain fracture.

The analytical expressions for fracture width and fracture height given in Eqs. 10.10/10.11& 10.14 respectively for a plane strain fracture in a formation with multi-stress layers is used to develop a P3D model. Take a fracture with geometry depicted in Figure 10-2 and discretize it into small grids with each grid having its own height as shown in Figure 10-3. Assuming that X-Z plane strain condition holds for every grid, the height and aperture distribution along each grid segment can be related to the pressure inside that grid according to Eq. 10.10/10.11& 10.14 respectively. In order to account for viscous dissipation in the fracture lateral direction, fluid flow inside fracture is formulated as shown below.

(*b*)

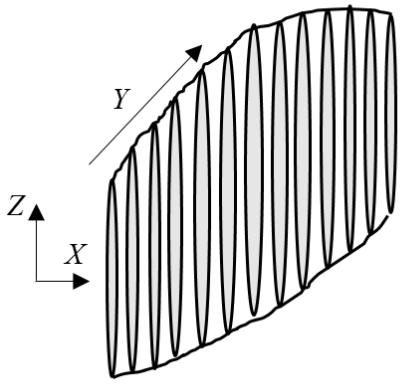

Figure 0-3. A planar fracture having non-uniform height can be approximated by number of small segment grids each having its own height.

10.1.3 Fluid Flow

Assuming fracture as two smooth parallel plates, the fluid flux in the fracture in lateral direction is given by

$$q = -\frac{w^3}{12\mu}\frac{\partial p}{\partial s} \tag{10.15}$$

where q is volumetric flow rate in the direction s per unit thickness of plate, μ is dynamic viscosity of the injection fluid, dp/ds is pressure gradient, and w is separation between parallel plates.

As indicated before, pressure gradient is taken zero in the direction of fracture height; therefore, fluid flow approximation becomes one dimensional (i.e. along the fracture length). Eqs. 10.10& 10.11 indicate that fracture aperture varies along height, as a result, the expression for flow rate given in Eq. 10.15 is replaced with an expression for average volumetric flow rate per unit payzone thickness inside fractures as (Dontsov and Peirce, 2015; Adachi et al., 2010),

$$\bar{q} = -\frac{1}{12\mu H}\frac{\partial p}{\partial y}\int_{-h/2}^{h/2} w(z,y)^3 dz \tag{10.16}$$

The integral term in the above equation accounts for variation of fracture aperture along fracture height, which can be evaluated numerically for a given pressure and height using Eqs 10.10/10.11. Finally, the continuity equation inside fracture (excluding leak-off) is given as

$$\frac{\partial \bar{w}}{\partial t} + \frac{\partial \bar{q}}{\partial y} = \frac{Q_0}{H} \tag{10.17}$$

where $\partial \bar{w} / \partial t$ indicates storage (i.e. change in average aperture over a small change in time). The average aperture $\bar{w}$ is defined as in Eq. 10.18 to account for variation of fracture aperture along fracture height and Q_0 is volumetric injection rate of source which is prescribed.

$$\bar{w} = \frac{1}{H} \int_{-h/2}^{h/2} w(z, y) dz \tag{10.18}$$

Using the following initial and boundary conditions, the partial differential equation (Eq. 10.17) is approximated using finite difference method.

$$w(z, y)_{t=0} = 0 \tag{10.19}$$

Eq. 10.19 indicates that initial fracture apertures are zero

$$\frac{\partial p}{\partial y} \int_{-h/2}^{h/2} w(z, L)^3 dz = 0 \tag{10.20}$$

Eq. 10.20 indicates no flow boundary condition at fracture tips assuming zero fluid-lag.

10.1.4 Fracture Length

Based on linear elastic fracture mechanics, fracture propagation in the plane XY (see Figure 10-2) takes place when mode-1 stress intensity factor reaches fracture toughness (Eq. 10.21) in isotropic (Erdogan and Sih, 1962) and anisotropic (Wu, 1967) bodies assuming that stresses near fracture

tips due to skew symmetric loading is negligible. It is also shown (Sih et al., 1965) that the order of stress singularity near fracture tips in anisotropic bodies is $r^{-1/2}$ (where r is distance from fracture tip) as in isotropic material. Also, the fracture aperture varies in the order $r^{1/2}$ near fracture tip in anisotropic body similar to isotropic case (therefore, fracture propagating in toughness regime takes square root asymptote near fracture tip in anisotropic body similar to isotropic case). The fracture tip displacement discontinuities are related with stress intensity factors according to Eq. 10.22 and Eq. 10.23 in isotropic (Yan, 2004) and anisotropic (Chang and Liao, 2014) bodies respectively.

$$K_I = K_{IC} \tag{10.21}$$

$$K_I = -\frac{\sqrt{2\pi}GD_n}{4(1-\upsilon)\sqrt{r}}, \quad K_{II} = -\frac{\sqrt{2\pi}GD_s}{4(1-\upsilon)\sqrt{r}} \tag{10.22}$$

$$D_s = 2\sqrt{\frac{2r}{\pi}}\left(H_{11}K_I + H_{12}K_{II}\right), \quad D_n = 2\sqrt{\frac{2r}{\pi}}\left(H_{21}K_I + H_{22}K_{II}\right) \tag{10.23}$$

where G is shear modulus, v is Poisson's ratio and r is the half length of the fracture tip element. The terms H_{ij} are related to material constants (see section 4.10.1). Note that mode-1 and mode-2 stress intensity factors are exclusively related to normal and shear displacement discontinuities respectively in isotropic body. Whereas, in the case of anisotropic body, mode-1 and mode-2 stress intensity factors are related to both normal and shear displacement discontinuities.

Although the above equations for stress intensity factor calculation are formulated strictly for using with fracture tip displacement discontinuities that are provided by the displacement discontinuity method, we assume that they are valid when the normal displacement discontinuity (D_n) is replaced with maximum aperture of fracture tip element evaluated using Eq. 10.10/10.11 Since P3D is only a planar model, the fracture ride (D_s) cannot be captured and is assumed zero.

Finally, in both isotropic and orthotropic rocks, toughness asymptote (Eq. 10.21) is used at the fracture tips (Sesetty and Ghassemi, 2018b) irrespective of fracture propagation regime. According to Sesetty and Ghassemi (2017a) toughness asymptote can provide sufficiently accurate results for fracturing input parameters typically used in unconventional reservoirs.

10.1.5 Solution Method

For every fracture grid (see Figure 10-3), there are three unknowns which are pressure, aperture and height. Eq. 10.14 provides relation between fracture height and pressure for every grid. The continuity equation for every grid can also be expressed in terms of fracture height and pressure since fracture apertures are related to pressure and height. Therefore, the continuity equation (Eq. 10.17) together with equilibrium height equation (Eq. 10.14) provides the necessary set of two equations for each grid that can be solved (using a non-linear solver) for the unknowns fracture height and pressure. This is achieved by first assuming initial guess values of fracture height and pressure for each grid and small time interval Δt. New estimates for fracture height and pressure are obtained using newton iteration until converged solution is obtained (i.e. solution fracture height and pressure satisfy Eqs. 10.14& 10.17 simultaneously).

Once fracture height and pressure for each grid is determined, the aperture profile for the entire fracture can be obtained using Eq. 10.10/10.11 Note that the equilibrium height equation is valid only when fracture height *h* is greater than payzone thickness *H*. Therefore, during the newton iteration process of solving the Eqs. 10.14& 10.17, if fracture height *h* is observed to be less than payzone thickness *H* for any grid, Eq. 10.14 for that grid is removed from the system of equations and fracture height *h* for that grid is made equal to payzone thickness *H*.

To check for fracture propagation condition, K_I is evaluated from Eqs. 10.22/10.23 using maximum aperture at fracture tips. For any fracture tip, if the difference between K_I and K_{IC} is

within the prescribed tolerance limit (1 percent in this work), a new grid is added to that fracture tip and the problem is moved to the next time step. On the other hand, if fracture propagation condition is not satisfied at least at one of the fracture tips, a new Δt is used to solve Eq. 10.14& 10.17. This is repeated until fracture propagation condition is met at least at one of the fracture tips. Notice that this is a way of implementing square root tip asymptote at fracture tips and requires solving equations (Eq. 10.14 and 10.17) multiples times which is time consuming. To speed up the process, in this work, we adopted the bisection method that typically takes 3-4 iterations to find Δt for a tolerance limit of 1 percent.

10.2 Comparison of P3D Model with 3D Model

Propagation of a single planar hydraulic fracture is considered using the P3D and 2D DDM models and the results are compared with a 3D modeling result from the literature (Dontsov and Peirce, 2015). The input parameters used for simulation are given in Table 10-1. These values are from a lab scale hydraulic fracture experiment (Jeffery and Bunger, 2009). The payzone thickness (*H*) is 0.05 m and the excess confining stress (σ_b) in the two symmetrical bounding layers above and below the payzone is 4.3 MPa. Since the 2D DDM model cannot simulate fracture height growth, a fixed fracture height equal to payzone thickness is assumed throughout the simulation. The propagation of hydraulic fracture is considered in two cases. The first case has high fracture toughness (0.94 MPa.m$^{1/2}$) and the second one has low fracture toughness (0.16 MPa.m$^{1/2}$). Figure 10-3a shows comparison of the maximum fracture aperture from the center of the fracture to its tip at time 604 sec for high fracture toughness case. The results indicate that the P3D model overestimates fracture length and underestimates width compared to 3D simulation. The fracture length and aperture profile obtained by 2D DDM (with the 3D correction factor G) are much closer to 3D results. Also, the P3D model indicates no growth into bounding layers according to Figure

10-3b. The 3D model indicates slight growth (around 6 mm on both sides) of fracture into the bounding layers. For the case of low fracture toughness, the estimation of fracture length and maximum fracture aperture profile by both P3D and 2D DDM (with the 3D correction factor) models is close to the 3D model (Figure 10-3c). Moreover, P3D model in this case gives a better estimation of fracture height growth according to Figure 10-3d. Overall, these results indicate that when fracture toughness is high, the P3D model poorly estimates all characteristics of a hydraulic fracture (such as fracture length, aperture and height). This could be due to the lack of mechanical interaction between the fracture elements as we assume fracture aperture and height of each grid is exclusively related to the pressure in that grid. This will result in erroneous estimation of mode-1 stress intensity factor using Eq. 10.22/10.23 which controls lateral fracture propagation. On the other hand, the 2D DDM model with height correction gives better estimation of fracture length and aperture in both high and low fracture toughness cases even though it assumes a constant fracture height.

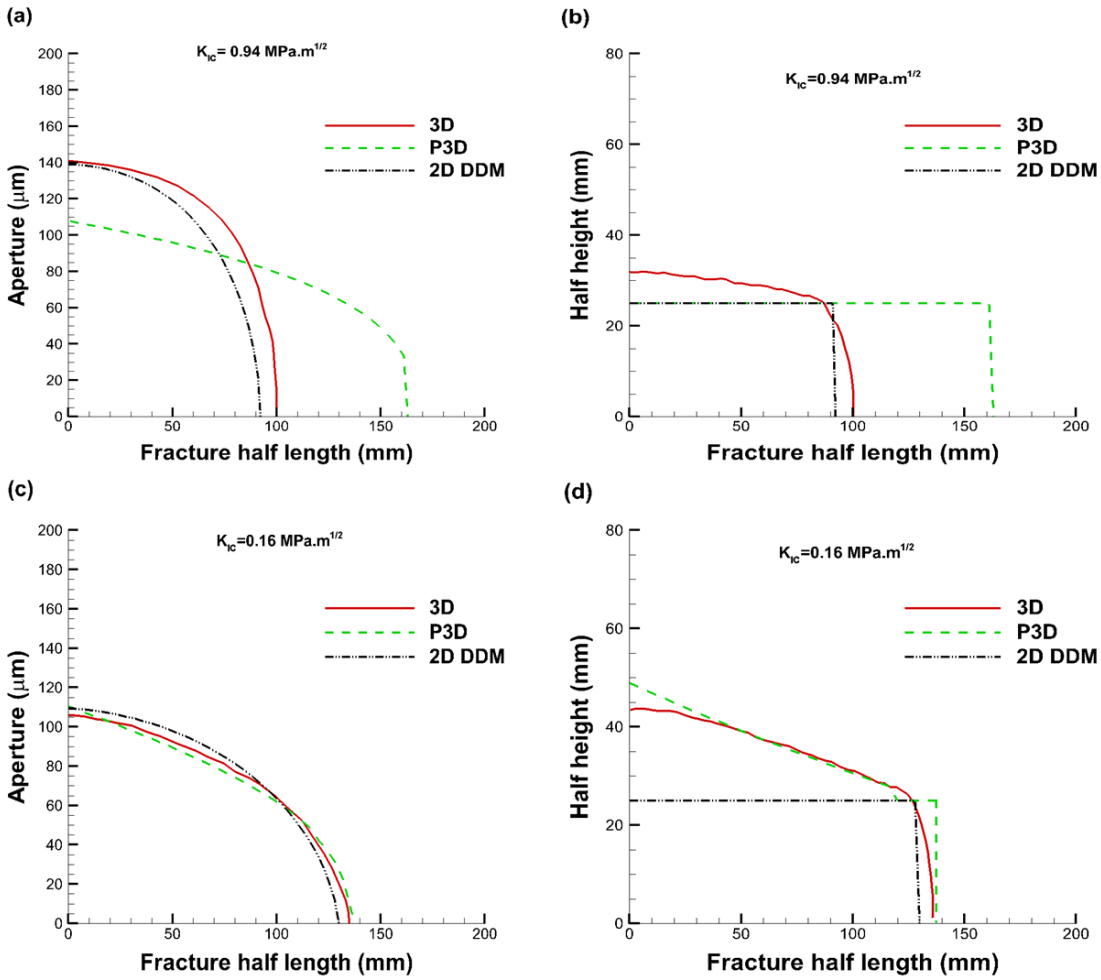

Figure 0-4. Comparison of results from 3D, P3D and 2D DDM models for a planar fracture propagation in isotropic body for the case of high fracture toughness (a) maximum aperture, (b) fracture half height from fracture center to its tip, and low fracture toughness (c) maximum aperture, (d) fracture half-height from fracture center to tis tip.

Table 0-1. Input parameters used for P3D and 2D DDM validation

E (GPa)	ν	μ (cP)	H (m)	Q_0 (mm^3/s)	σ_b (MPa)
3.3	0.4	30200	0.05	1.7	4.3

10.3 Effect of Rock Anisotropy on Fracture Aperture, Length and Height

The P3D model developed in this work is used to simulate single planar hydraulic fracture propagation in an anisotropic rock. To highlight the effects of rock anisotropy on fracture parameters, the anisotropic results are compared with those obtained from isotropic P3D model. The elastic and strength properties of anisotropic rock (Rock-A) are given in Table 6-1. Rock-A is a vertical transversely isotropic rock (VTI) with degree of anisotropy 4 (ratio of the bedding plane parallel and bedding plane perpendicular Young's moduli, E_1/E_3). These elastic constants are close to those of the argillaceous shale from Suarez-Rivera et al. (2011). For isotropic P3D model, we use Young's modulus parallel to the bedding planes (E_1) and Poisson's ratio v_{12} (fracture toughness anisotropy is not considered in this study, therefore both isotropic and anisotropic rock have same K_{IC} (see Sesetty and Ghassemi, (2016) for fracture toughness anisotropy effect on fracture propagation). Slick water (1 cP) is injected at 10 bpm for 300 sec into a small perforation of initial length 3 ft. Other input parameters are given in Table 10-2.

Figure 10-5 compares the fracture aperture distribution, half-length, half-height and net injection pressure between anisotropic and isotropic rocks. The results indicate higher fracture aperture in anisotropic rock compared to isotropic case. On the other hand, isotropic model predicts higher height growth into the bounding layers (for σ_b =1 MPa) compared to anisotropic model. This is because of lower net injection pressures obtained during the propagation of the fracture in anisotropic rock. Since fracture height growth is directly proportional to net pressures inside the fracture according to Eq. 10.14, lower net pressures inside the fractures in anisotropic rock resulted in lesser height growth compared to isotropic case. Significant difference in fracture length is not observed between isotropic and anisotropic rocks. Overall, these results indicate that simplifying a VTI rock as isotropic rock will result in underestimation of fracture apertures and overestimation

of fracture height (note that these results are applicable only for VTI rocks with vertical fracture that has dominant growth in horizontal direction and is free of shear stresses).

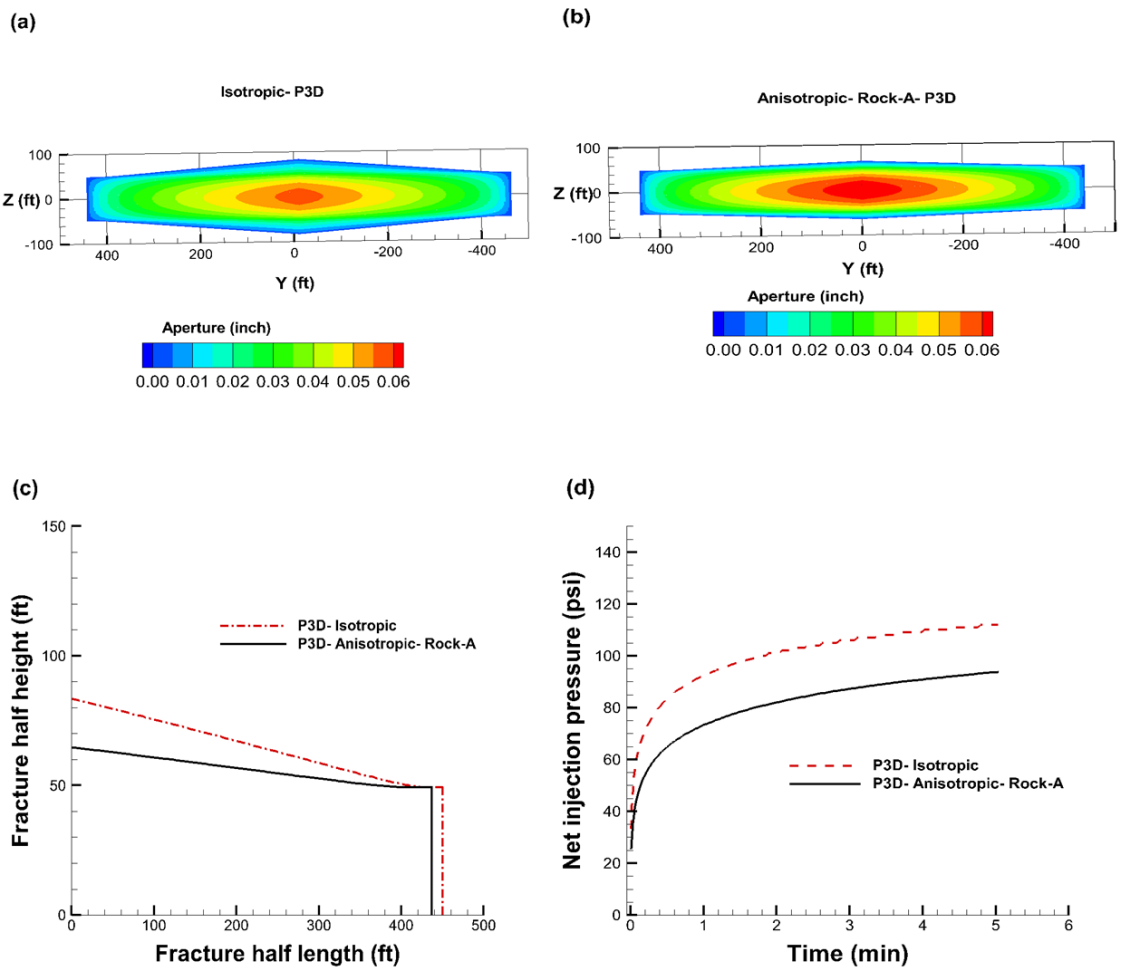

Figure 0-5. Comparison of (a, b) fracture aperture distribution, (c) fracture half-height and (d) net injection pressures between isotropic and anisotropic P3D models for a single planar fracture.

Table 0-2. Simulation input parameters.

Q_0 (bpm)	μ (cP)	H (ft)	σ_b (MPa)
10	1	100	1

10.4 Extension of P3D Model for Multiple Fractures in Anisotropic Rock

The analytical expression for fracture aperture in the P3D model is developed based on the assumption of single plane strain fracture in an infinite body. When multiple fractures are present, the Eqs. 10.10& 10.11 need to be modified to account for interaction between the fractures. We extend the P3D model to the case of multiple hydraulic fractures based on the following assumptions, (i) fractures are always free of shear loading and do not exert shear stresses on adjacent fractures, (ii) therefore, interaction between multiple fractures is only due to induced normal stresses, (iii) and plane strain condition applies in the plane XZ. Under these assumptions, Eqs. 10.10& 10.11 can be used for simulating growth of multiple parallel fractures by replacing far-field stress, σ, with total stress (the sum of the far-field stress and induced normal stress). Since fractures are assumed to be free of shear loading in the P3D model, induced shear by neighboring fractures is not considered. As a result, the model is limited to planar hydraulic fracture propagation. We will show that this assumption can be justified when considering propagation of parallel hydraulic fractures from multiple clusters even when far-field horizontal stress contrast is as low as 1 MPa if spacing between the clusters is sufficiently large. Note that because the 2D DDM model does not have these limitations, it can handle simultaneous propagation of multiple non-planar hydraulic fractures.

To simulate simultaneous propagation of parallel hydraulic fractures from multiple perforation clusters using P3D model, at the end of every time step, the solution of pressure inside fractures, fracture length and height are used to solve 2D DDM (with 3D correction factor G) to evaluate displacement discontinuities, which are then used to calculate induced normal stresses in the rock next to every fracture element. In the next time step, these induced normal stresses are added to

far-field stress. This way of externally calculating induced stresses using a 2D DDM after every time step mimics interaction between multiple fractures. In addition, an expression that describes flow partition into each perforation cluster needs to be included in the system of coupled fracture deformation and fluid flow equations. Ignoring the wellbore friction, Eq. 10.28 (Elbel et al., 1992) is used to calculate frictional pressure drop in perforations (i.e. P_{perf}). Flow balance equation (Eq. 10.29) and perforation friction equation (Eq. 10.28) for each cluster provides N+1 additional equations to solve for injection pressure and flow rates (q_i) into N clusters.

$$P_{perf} = \frac{0.237\rho q_i^{\,2}}{n^2 D^4 C^2} \tag{10.28}$$

$$\sum_{i=1}^{N} q_i = Q_o \tag{10.29}$$

10.5 Evaluation of Induced Stresses near P3D Fracture Using Displacement Discontinuity Method

As discussed previously, we use 2D DDM with 3D correction factor to evaluate induced stresses on adjacent fracture elements after every time step to mimic interaction between fractures. To assess the accuracy of this technique, we consider an example of a single P3D fracture propagating in isotropic and anisotropic rocks. In order to facilitate direct comparison of numerically evaluated induced normal stresses with analytical solution (Eq. 10.27), the confining stress in bounding layers is assumed to be very large, so that fracture height growth is negligible (therefore, *h*=*H*). The thickness of the payzone is 100 ft. Slick water is injected at 10 bpm for 180 sec into a small perforation of length 3 ft. As the fracture grows, induced stresses in the direction normal to the fracture surface are calculated using 2D DDM with 3D correction factor at two different locations.

The first location is at a distance (X) of $h/2$ from the injection point along the line Z=0 and the second location is at a distance h from the injection point along the line Z=0. The numerically obtained induced stresses at these locations are normalized with net pressure at injection point (P_{injp}).

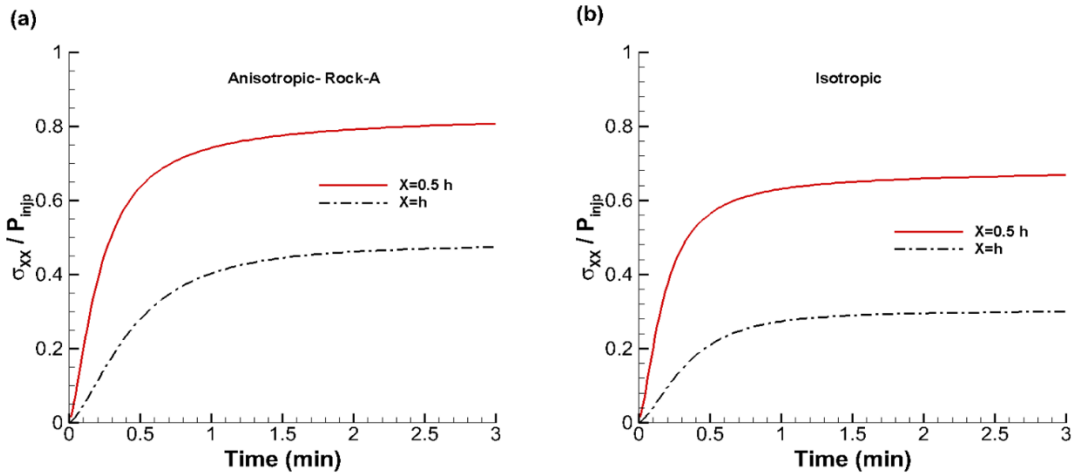

Figure 0-6. (a) Induced stress component perpendicular to fracture surface at a distance from injection point along the line Z=0 (fracture geometry in Figure 2a) normalized with net injection pressure P_{injp}, (a) in anisotropic rock, (b) isotropic rock.

Figure 10-6 indicates that as fracture grows in length (while height being constant due to high confining stresses in bounding layers), the normalized induced stress at X/h=0.5 and X/h=1 reaches 0.8 P_{injp} 0.47 P_{injp} respectively . These values are very close to analytical solution given in Figure 3-4. Similarly, in isotropic body, numerically evaluated induced stress at X/h=0.5 and X/h=1 are approaching 0.67 P_{injp} and 0.3 P_{injp} respectively which is also close to analytical solution according to Figure 3-4. These results indicate that, by using a proper correction factor, the 2D DDM can be used to predict induced stresses around P3D fracture accurately in both isotropic and anisotropic rocks.

Table 0-3. Perforation properties.

n (number of perforations per cluster)	D (diameter of perforation, inch)	C Perforation coefficient
80	0.6	0.9

10.6 Simultaneous Propagation of Multiple Fractures

To illustrate the effect of stress shadow on simultaneous growth of multiple parallel fractures, the P3D and 2D DDM models are used to simulate large scale fracture propagation in anisotropic rock, and the results are compared with isotropic case.

A single fracturing stage, span 260 ft of the wellbore is considered with five perforation clusters that are spaced 60 ft apart. The thickness of the payzone (*H*) is 100 ft and the difference between maximum and minimum principal horizontal stress is 1 MPa. Perforation properties are given in Table 10-3. Higher number of perforations and large perforation diameter is selected intentionally to eliminate the effect of perforation friction on flow partition into each cluster. As a result, the flow partition into each cluster (which is a part of the solution) is completely controlled by stress shadow between the fractures. In order to allow comparison of P3D results with the results obtained from fixed height 2D DDM model, very high excess confining stress (σ_b) of magnitude 4 MPa is used to restrict the fracture height growth into the bounding layers above and below the payzone in P3D model. Rock elastic and strength properties are given in Table 6-1. For isotropic P3D model, we use Young's modulus parallel to the bedding planes (E_1) and Poisson's ratio ν_{12}. Assuming an initial fracture of length 3 ft in the direction of maximum principal horizontal stress from each perforation cluster, slick water (1 cP) is injected at rate of 50 bpm for 250 sec into the wellbore to enter the clusters. The resultant fracture geometry and aperture distribution obtained

from P3D and 2D DDM models in isotropic and anisotropic rock (Rock-A) are displayed in Figure 10-7.

Fracture geometry from both P3D and 2D DDM models show early termination of fractures from clusters in the immediate vicinity of the outer fractures in both isotropic and anisotropic rocks. This indicates significant interaction between the parallel hydraulic fractures at the spacing considered in this example (which is 60 percent of the payzone thickness). Moreover, the centermost fracture in anisotropic rock has lower apertures and lesser growth compared to the centermost fracture in isotropic rock. This effect is more visible in the results from 2D DDM model (Figure 10-7d). This is due to increase in stress shadow effect between the fractures in anisotropic rock as discussed previously (see Figures 3-2& 3-4). Facture aperture distribution in anisotropic rock is more uniform compared to isotropic case where there is a significant variation from fracture centers to their tips. Fracture aperture prediction from 2D DDM method is very close to P3D result. Also, the results (both 2D DDM and P3D) indicate very little difference in fracture lengths of the outermost clusters in isotropic and anisotropic rocks. However, overall the P3D model predicts much longer fractures compared to ones obtained from 2D DDM model. This is probably due to the lack of interaction between fracture elements that makes implementing toughness asymptote (Eq. 10.21) at the fracture tips less accurate in the P3D model. Although a 3D solution for this problem (in both isotropic and anisotropic rocks) is not readily available, the analysis of a single planar fracture in isotropic body presented above indicates that when height growth is limited, 2D DDM gives better prediction of fracture lengths compared to P3D model. Nevertheless, the results from both P3D and 2D DDM models show much stronger interaction between fractures in anisotropic rock compared to isotropic case when fracture spacing is about 60 percent of payzone thickness (note that in this example both P3D and 2D DDM models have same fracture height

which is equal to payzone thickness (100 ft.) as height growth is restricted by using very large excess confining stress in bounding layers).

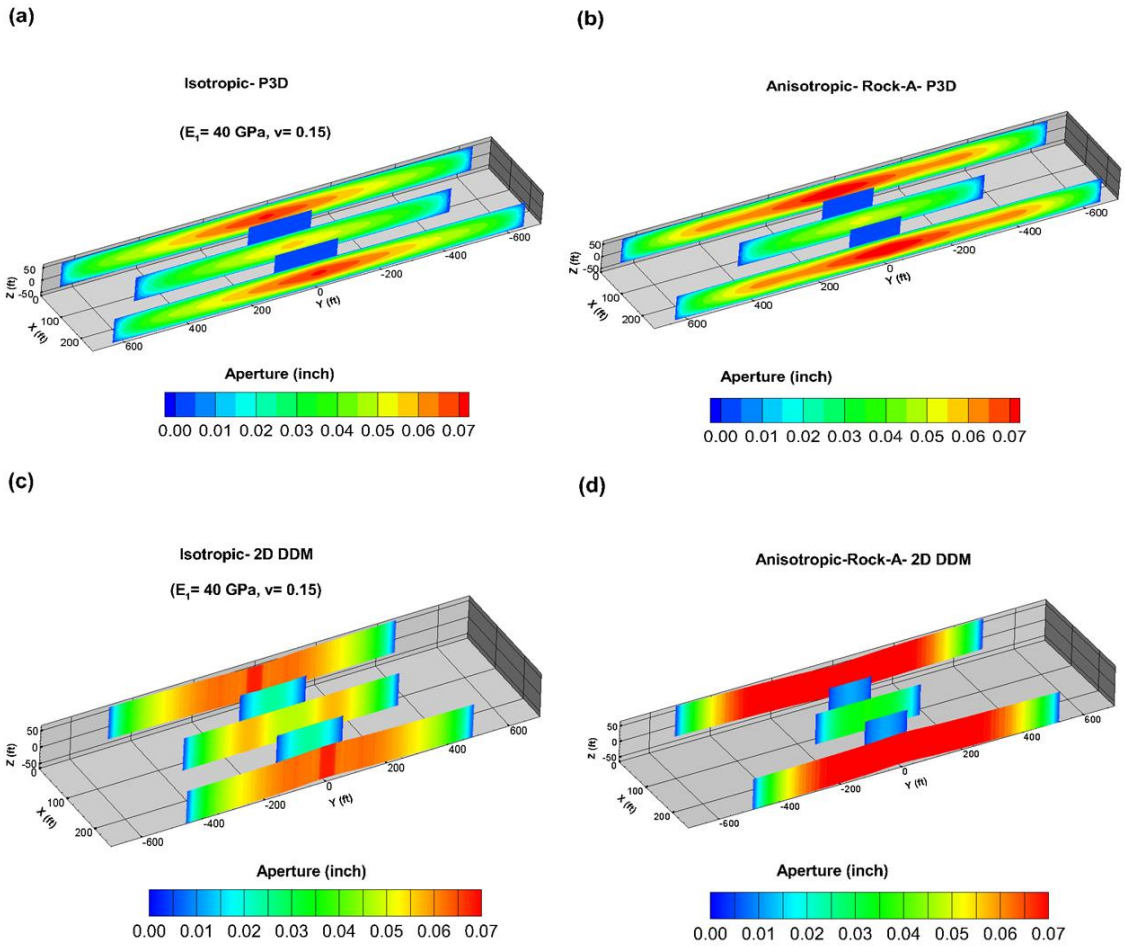

Figure 0-7. Comparison of fracture geometry and aperture distribution obtained from simultaneous propagation of fractures from multiple clusters using P3D and 2D DDM models in, (a-c-e) isotropic rock and (b-d-f) anisotropic rock (Rock-A).

As mentioned previously, the P3D model for multiple fractures is simplified by assuming that fracture planes are always free of shear stresses. As a result, fractures propagate in their own plane. For the current cluster spacing of 60% of payzone height, the fracture trace obtained from the 2D DDM model in the plane XY shown in Figures 10-7e and 10-7f indicate nearly planar fractures

even when contrast between far- field horizontal principal stresses is as low as 1 MPa (this is due to the fact that the system as a whole tends to minimize the energy required for fracture propagation so when multiple clusters are available, the fractures can avoid curving as long as a path of least resistance for another fracture in a different cluster is available-see Tarasov and Ghassemi, 2014). Moreover, for the current spacing, ignoring induced shear stresses due to interaction between the fractures appears to have little effect on fracture apertures since the fracture apertures obtained from P3D and 2D DDM models are close.

Figure 10-8 shows comparison of fracture geometry obtained in isotropic and anisotropic rock (Rock-B) with properties given in Table 6-3. All other input parameters used in the simulation are same as previous example. In the isotropic formation, close to uniform fracture growth is observed from outer and centermost clusters. Similar to previous example, aperture distribution is more uniform in fractures in anisotropic rock. The important observation from this example is that, even when the degree of anisotropy is low (i.e., 1.88), the inner fractures feel strong interaction from the dominant outer fractures in anisotropic rock. As a result, fracture growth from centermost cluster is more restricted in anisotropic rock compared to isotropic case.

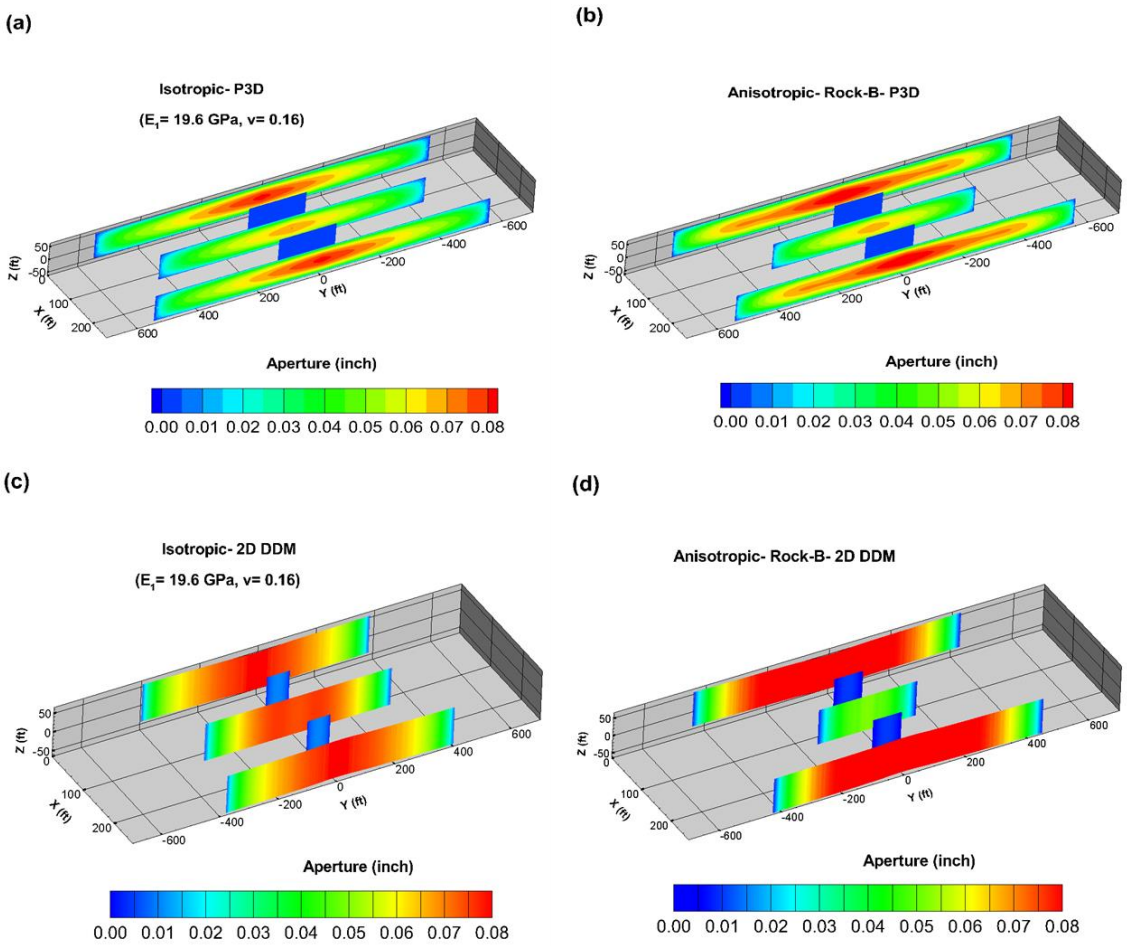

Figure 0-8. Comparison of fracture geometry and aperture distribution obtained from simultaneous propagation of fractures from multiple clusters using P3D and 2D DDM models in, (a-c-e) isotropic rock and (b-d-f) anisotropic rock (Rock-B).

In the previous examples, we restricted height growth in P3D model to study the effect of rock elastic properties on interaction mechanisms and allow comparison of results with 2D DDM model. To study the effect of elastic anisotropy on height growth, the excess confining stress in the bounding layers (σ_b) is reduced from 4 MPa (previous examples) to 1 MPa.

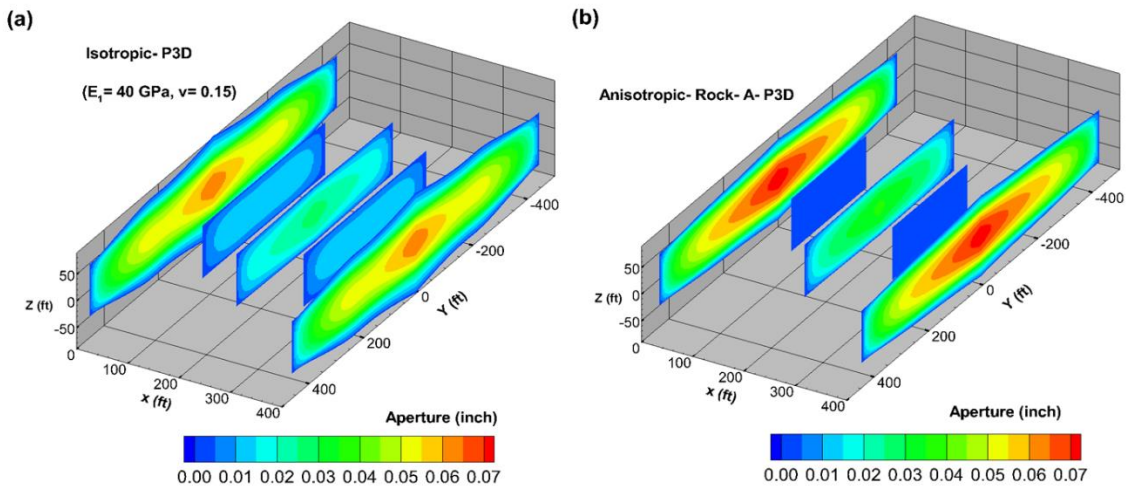

Figure 0-9. Comparison of fracture geometry and aperture distribution obtained from simultaneous propagation of fractures from multiple clusters using P3D model in, (a) isotropic rock and (b) anisotropic rock (Rock-A) with 90 ft cluster spacing and 1 MPa excess confining stress in the bounding layers (σ_b).

Figure 10-9 shows the resultant fracture geometry and aperture distribution in isotropic and anisotropic rock (Rock-A) after injecting slick water for 250 sec at 50 bpm into 5 perforation clusters spaced at 90 ft (i.e., fracture spacing equal to payzone thickness). Rock elastic and strength properties are given in Table 6-1. In this case, the outermost fractures in anisotropic rock observed higher opening compared to isotropic case. Also, the outermost fractures in isotropic rock show significant growth in height (more than double the payzone thickness) near the location of fluid entry. Fracture height growth in anisotropic rock is lower compared to the isotropic case. Most importantly, the fractures adjacent to the outermost fractures in anisotropic rock have been terminated early even for the fracture spacing of 90 ft. Whereas, in isotropic rock, all fractures continued to propagate (at different rates) until the end of injection period (although the inner fractures show much less apertures). This further confirms our suggestion (Sesetty and Ghassemi 2018a) that cluster spacing needs in anisotropic rock are different than that of isotropic rock.

10.7 Complex Scenarios

10.7.1 Rock Mass with Orthogonal Sets of Natural Fractures

In the previous examples, hydraulic fracture propagation in a vertical transversely isotropic rocks is considered. Although most of the laboratory experiments on core size shale samples characterize shale as transversely isotropic, most rock masses can possess additional degree of anisotropy due to the presence of natural fractures or rock stratification. For example, an isotropic rock mass containing orthogonal sets of natural fractures can be treated as orthotropic rock when deformation is viewed at large scale. If a rock has dense network of natural fractures with well-defined orientation as indicated in Figure 10-10, modeling every natural fracture using DDM is impractical due to unreasonable computation time. Rather it is much easier and computationally efficient to treat such rocks as anisotropic. This is illustrated using an example by considering a vertical transversely isotropic rock (Rock-B) with evenly distributed vertical natural fractures (indicated by orange lines) that are oriented in the direction of minimum principal horizontal stress (X-axis) as indicated in Figure 10-10.

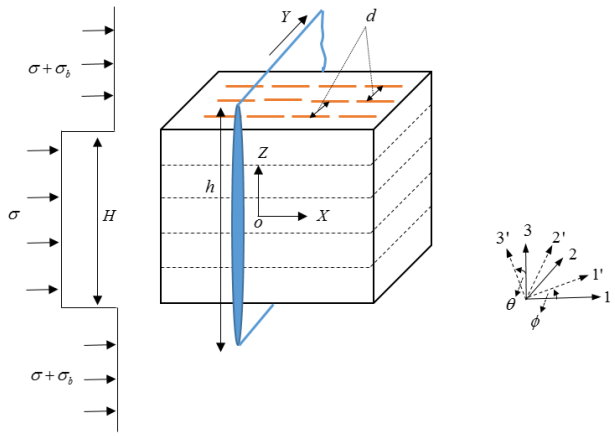

Figure 0-10. Cross section of a rock mass with bedding planes parallel to the plane X-Y and vertical natural fractures (indicated by orange lines) with spacing d in the direction of X-axis. 1-2-3 are the axes of elastic symmetry of the rock.

If natural fractures are aligned in the direction 1 and *d* is the spacing between the natural fractures, the new elastic constants in the plane 1-2 are given as (Goodman, 1976),

$$E_2 = \frac{E_1}{1 + E_1 / dK_n}$$
$$G_{12} = \frac{G_{12}}{1 + G_{12} / dK_s} \qquad (10.30)$$
$$\nu_{12} = \nu_{12}$$
$$E_1 = E_1$$

where K_n and K_s are natural fractures normal and shear stiffness respectively. Taking the elastic constants of Rock-B given in Table 6-3 and K_n, K_s as 30 GPa/m, and the distance between natural fractures *d* as 1 m, the induced degree of anisotropy due to the presence of natural fractures in the plane 1-2 (E_1/E_2) is 1.65 using Eq. 10.30. Note that plane 1-2 is isotropic before including the effect of natural fractures. Therefore, a transversely isotropic rock (Rock-B) with natural fractures gives an equivalent anisotropic rock which is orthotropic and will be called as Rock-C.

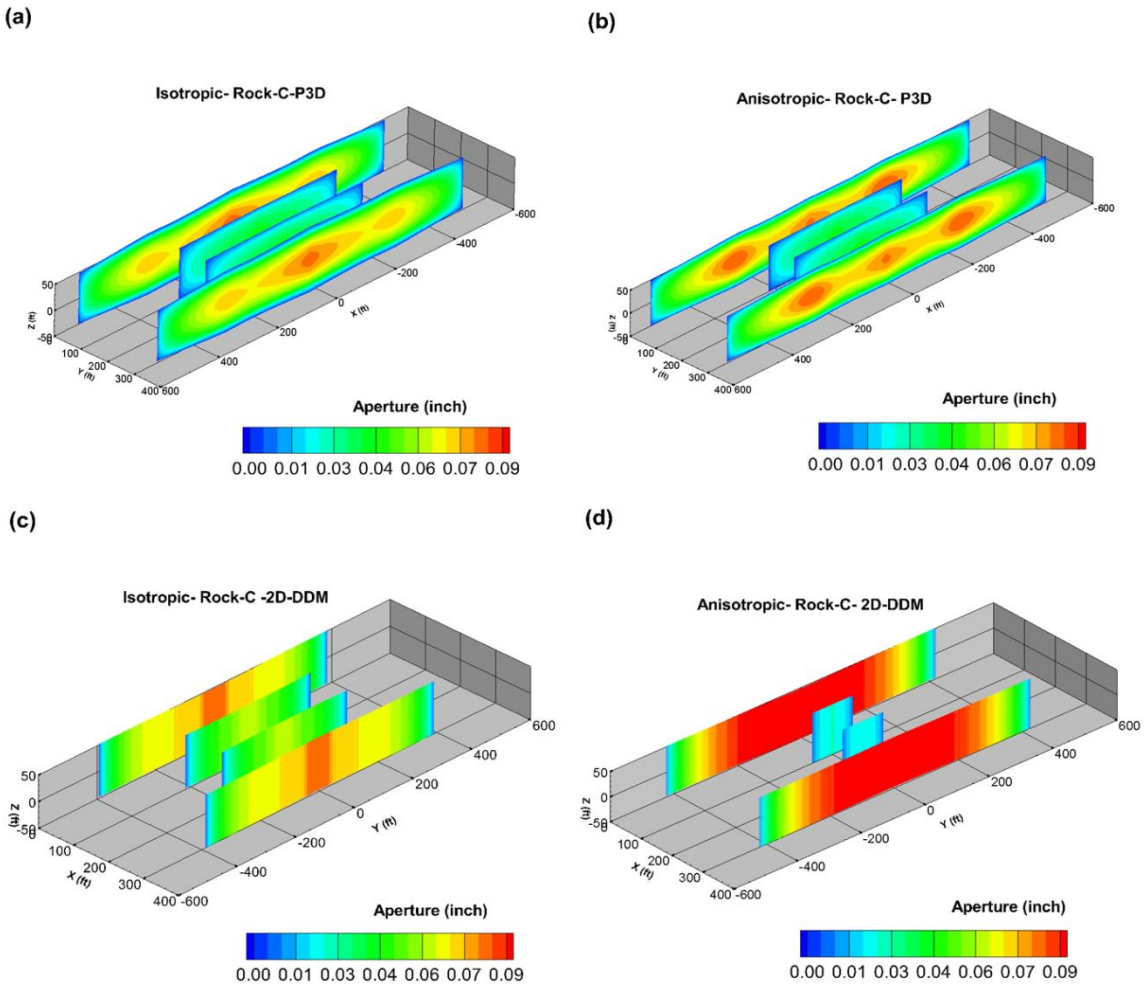

Figure 0-11. Comparison of fracture geometry and aperture distribution obtained from simultaneous propagation of fractures from multiple clusters using P3D and 2D DDM models in, (a-c-e) isotropic rock and (b-d-f) anisotropic rock (Rock-C).

The full list of nine independent elastic constants of Rock-C are given in Table 6-4.

The problem of Hydraulic fracture propagation in Rock-C is considered using the P3D model developed in this work. Note that hydraulic fractures and natural fractures do not interact directly, since natural fractures are not explicitly modeled in this problem. The effect of natural fractures on hydraulic fractures is considered by altering the material properties of the rock. The elastic constants of the Rock-C given in Table 6-4 are used. For isotropic approximation, E_1 and ν_{12} are used. The excess confining stress in the bounding layers is 1 MPa.

Four perforation clusters are considered with 125 ft spacing. Slick water is injected at a rate of 50 bpm for 250 sec into the wellbore where fluid is parted into clusters. Ignoring perforation friction and leak-off, the resultant fracture network at the end of injection period in isotropic and orthotropic rocks is shown in Figure 10-11. Results indicate that in orthotropic rock, the fractures from inner clusters tend to terminate earlier than in isotropic rock due to increase in stress shadow effect. Also, fracture outer fractures in orthotropic rock observed higher fracture apertures compared to isotropic case. It appears that the P3D model tend to overestimate fracture lengths as in previous examples, due to lack of interaction between the fracture elements.

10.7.2 Tilted Transversely Isotropic Rock

In an anisotropic body if all the axes of a fracture does not coincide with the material's axes of elastic symmetry, the fracture will experience shear displacement discontinuity even under pure mode-1 loading. Therefore, the anisotropic P3D model is developed based on the critical assumption that the fracture axes are always aligned with the material's axes of elastic symmetry. This assumption will allow to decouple fracture normal displacement discontinuity from shear displacement discontinuity (see Eq. 10.3). If we consider a fracture '*f*' in an infinite orthotropic body such that L/h>>1 as the one depicted in Figure 10-12, the closed form solution for fracture aperture $w(z)$ and ride $r(z)$ if the net pressure inside the fracture P is constant is given as,

$$w(z) = b_{11}\sqrt{h^2 - 4z^2}\left[\left(\beta_1\left(\alpha_2^2 + \beta_2^2\right) + \beta_2\left(\alpha_1^2 + \beta_1^2\right)\right)P + \left(\alpha_1\beta_2 + \alpha_2\beta_1\right)\sigma_{XZ}\right] \tag{10.31}$$

$$r(z) = b_{11}\sqrt{h^2 - 4z^2}\left[\left(\alpha_1\beta_2 + \alpha_2\beta_1\right)P + \left(\beta_1 + \beta_2\right)\sigma_{XZ}\right] \tag{10.32}$$

where α_1, α_2 and β_1, β_2 are real and imaginary parts of respectively of the two complex roots μ_1 and μ_2 of characteristic equation (Eq. C.6 in Appendix C), σ_{XZ} is shear loading on fracture surface. The rotation angle of material coordinate system 1-2-3 with respect to X-axis is angle θ degrees.

The coefficients b_{ij} of the characteristic equation are evaluated in the coordinate system 1'-2'-3' for ϕ=90^0.

From Eqs. 10.31& 10.32, we can see that in anisotropic body, fracture ride $r(z)$ is non-zero even when shear load (σ_{XZ}) on fracture is zero if,

$$\left(\alpha_1\beta_2 + \alpha_2\beta_1\right) \neq 0 \qquad (10.33)$$

Similarly, fracture aperture $w(z)$ is non-zero under pure mode-2 loading provided Eq. 10.33 is true.

The requirement in Eq. 10.33 is always satisfied when any of the three axes of a fracture (i.e. X-Y-Z) is not aligned with axes of elastic symmetry (i.e. 1-2-3) in an anisotropic body. Therefore if we consider a problem of vertical hydraulic fracture in a transversely isotropic rock with planes of isotropy inclined with respect to horizontal plane as in Figure 10-12, the hydraulic fracture will experience some ride and therefore the P3D analytical expression for fracture aperture in Eq. 10.1 can give erroneous solution since the assumption of zero fracture ride is violated. In order to assess the accuracy of P3D solution in such cases, we use closed form solution given in Eq. 10.31 for fracture aperture and compare it with the P3D result.

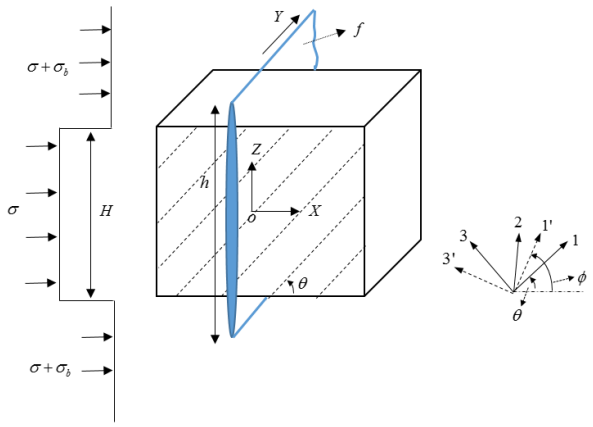

Figure 0-12. Cross section of a rock mass with bedding planes dipping at θ^0 with respect to the plane X-Y and vertical fracture '*f*' has height *h*, where L/*h*>>1. 1-2-3 are the axes of elastic symmetry of the rock.

Consider a transversely isotropic rock with bedding planes rotated by 30^0 (θ) counterclockwise with respect to the horizontal plane X-Y. If a vertical fracture '*f*' is taken such that L/*h*>>1, fracture apertures in the plane X-Z can be calculated using Eq. 10.31 for a constant net pressure P inside the fracture. Constants α_1, α_2 and β_1, β_2 are obtained in the coordinate system 1'-2'-3' with $\phi = 90^0$. The material constants in the coordinate system 1-2-3 are given in Table 6-1 (Rock-A). Similarly, we can use P3D model to calculate fracture apertures in the plane X-Z using Eq. 10.10.

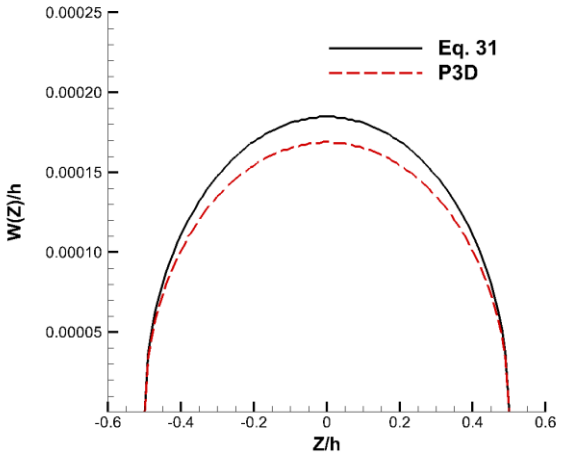

Figure 0-13. Comparison of fracture apertures obtained from Eq. 10.31 and P3D model for a vertical plane strain fracture in a transversely isotropic rock with bedding inclination angle $\theta=30^0$ (See Figure 10-12). The net pressure inside the fracture is 2 MPa and elastic constants are given in Table-6-1.

From Figure 10-13, comparison of P3D result with closed form solution from Eq. 10.31 indicates that the difference between the two solutions is not insignificant, however, the maximum error between the solutions which is 8.7% is within the acceptable range. Note that based on Eqs. 10.1& 10.31, the error between P3D and closed form solutions is not expected to change with fracture geometry and net pressure, however, is only sensitive to material elastic constants. Since the example rock (Rock-A) has a degree of anisotropy 4, which on the higher end side for a typical shale, we can expect that the error in fracture aperture approximation for anisotropic rocks where fractures are not aligned with material's axes of elastic symmetry using P3D typically falls in the same range as observed in Figure 10-13.

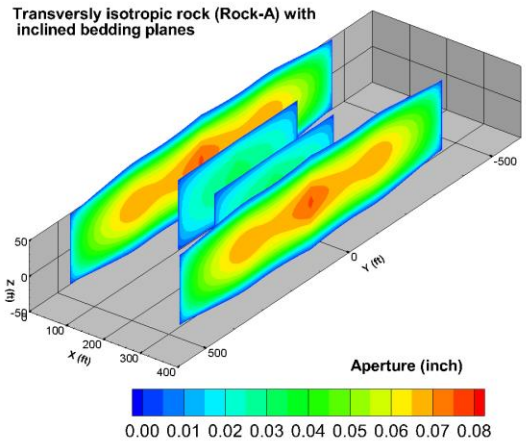

Figure 0-14. Fracture geometry and apertures from P3D model in a transversely isotropic rock with bedding inclination angle θ=30^0 (See Figure 10-12). Rock elastic constants are given in Table 6-1.

The equilibrium height expression in Eq. 10.14 is still valid irrespective of bedding plane inclination θ with respect to the fracture '*f*' in Figure 10-12, provided that the fracture '*f*' is free of shear loading. This is because the stress intensity factors (Eq. 10.12) at the tips of a plane strain fracture are independent of material elastic constants for self-equilibrium loading. Also, non-zero fracture ride (Eq. 10.32) does not produce mode-2 stress singularity near fracture tips as long as the fracture is free of shear loading (i.e. σ_{XZ} =0). Therefore, Eqs. 10.1& 10.14 can be used to model hydraulic fracture propagation in anisotropic body where material's axes of elastic symmetry are inclined with respect to fracture's axes by ignoring the error associated with evaluation of fracture apertures.

Figure 10-14 shows fracture apertures and geometry after injecting slick water at the rate of 50 bpm into four perforation clusters spaced 90 ft. As before, leak-off and perforation friction are ignored. The input properties of rock in the coordinate system 1-2-3 is given in Table 6-1 (Rock-A) and bedding planes are inclination angle θ is 30^0. Figure 10-14 indicates that fracture geometry

is symmetric about the line X=0, as in previous examples. However, according to Sesetty and Ghassemi (2016), when fractures in an anisotropic body are not aligned with material's axes of elastic symmetry, the induced compressive normal stresses in the direction perpendicular to the fracture surface tend to rotate towards the direction of maximum Young's modulus, due to which asymmetric fracture growth is observed when closely spaced multiple fractures are propagated simultaneously. Since in the example considered here, the direction of maximum Young's modulus E_1 is at an angle 30^0 counterclockwise from X-axis, the stress shadow rotation towards the direction of E_1 is expected to have some effect on fracture height growth. However, in P3D model the induced stresses are evaluated only at the midpoint of fracture height to account interaction between adjacent fractures; therefore, the effect of rock anisotropy on induced stress variation along fracture height cannot be captured. As a result, fracture height growth is not affected by stress shadow rotation in P3D model.

To study the effect of induced stress rotation in the plane X-Z on fracture height growth we use 2D DDM. Consider a transversely isotropic rock with bedding planes inclined at 30^0 from X-axis. Using the material constants from Table 6-1 (i.e. Rock-A), simultaneous growth of fractures from two perforation clusters is considered using 2D DDM assuming X-Z plane strain condition (since L>>*h*). Note that X-Z plane indicates fracture height growth. The problem is considered in three cases, where in the first case we assume that there are no stress barriers above and below the payzone. In the second case we take two symmetrical stress barriers bounding the payzone, and in the third case we consider asymmetric stress barrier. The thickness of the payzone (*H*) is 90 ft. Slick water is injected into two clusters spaced 30 ft apart along the line Z=0 at a rate 0.66 bpm/ft until at least one of the fracture wings reach half-height of 100 ft. The fracture geometry and aperture distribution at the end of injection for all three cases are shown in Figure 10-15.

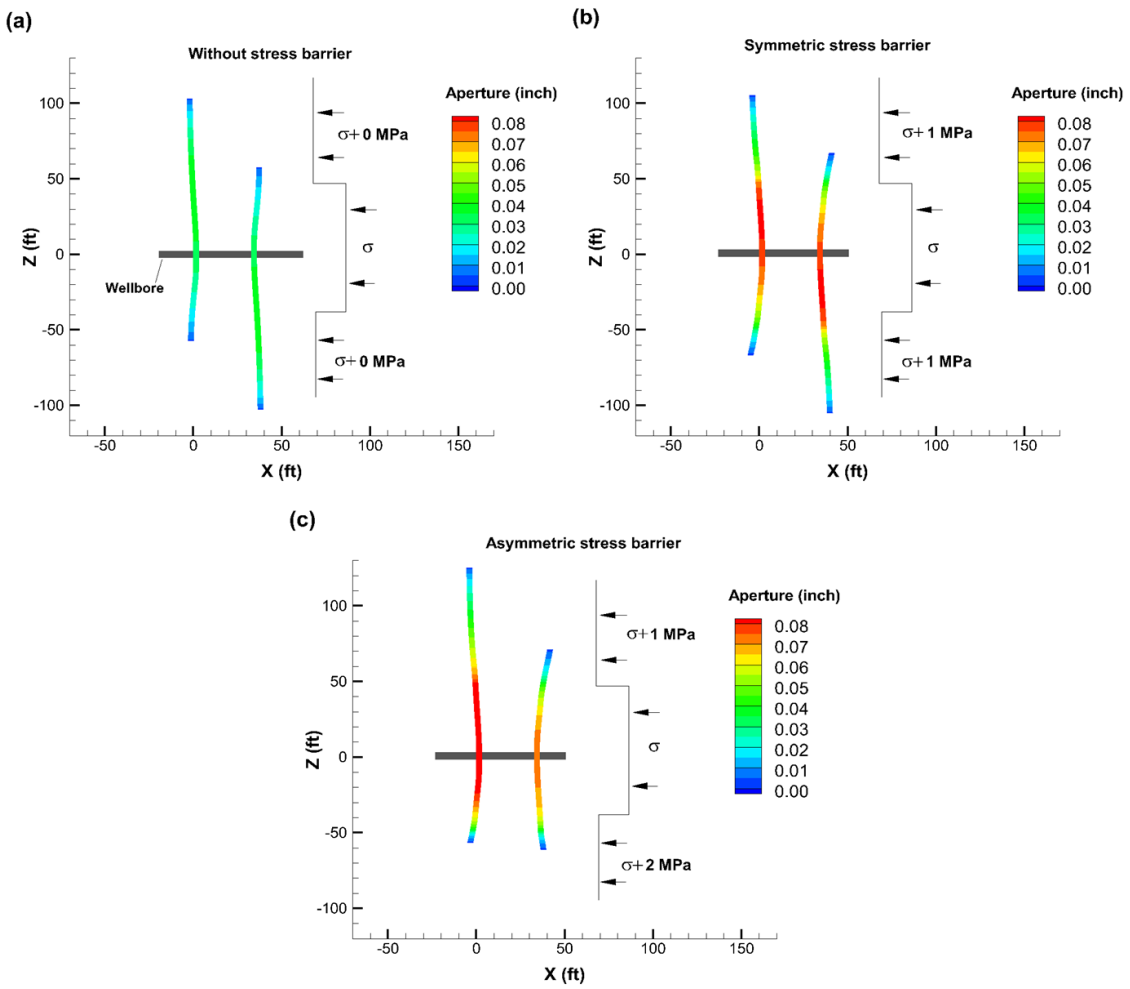

Figure 0-15. Comparison of height growth between fractures from two perforation clusters spaced 30 ft under different conditions of far-field horizontal confining stress. The rock is transversely isotropic with bedding inclination angle θ= 30^0 (see Figure 10-12). Rock elastic constants are given in Table 6-1.

Fracture geometry in the plane X-Z (i.e. fracture height growth) for the case with no stress barrier and the case with symmetrical stress barrier are similar from Figures 10-15a and 10-15b. The results indicate asymmetric fracture height growth that can be attributed to rotation of induced stress towards E_1 which is 30^0 counterclockwise from X-axis. Due to the rotation of stress shadow, the growth of bottom wing of left fracture and top wing of right fracture is restricted. An interesting result is observed when the stress barrier is asymmetric from Figure 10-15c. In this case, the left

and right fractures have completely different height, where the left fracture dominant in height growth. This is because the bottom wings of both left and right fractures are restricted due to higher stress barrier. Additionally, stress shadow rotation towards E_1 restricted the growth of top wing of right fracture. Therefore, in this case, the combined effect of asymmetric stress barrier and stress shadow rotation resulted in uneven fracture height growth. Note that the differences in apertures in all the three cases is due to difference in far-field confining stress.

These results indicate that material anisotropy can result in complex fracture geometries depending on the orientation of fractures with respect to material's axes of elastic symmetry. Although, plane strain models such as DDM or P3D can be used to approximate fracture apertures and geometry for simple rock and fracture configurations such as those discussed in the previous examples, for complex rock and fracture configurations, where fractures are orientated at any arbitrary angle with respect to rock's elastic axes of symmetry, a complete 3D model may be necessary to model accurate fracture geometries. Moreover, natural fractures, fracture toughness anisotropy can have significant effect of fracture propagation and complicates the problem further. Overall, the analysis of hydraulic fracture propagation in anisotropic rock shows that rock anisotropy has significant effect on fracture geometry and apertures. Not accounting rock anisotropy in completion optimization can result in undesirable results.

10.8 Summary

This work describes development and application of a new P3D model for hydraulic fracturing in orthotropic reservoirs. As 2D DDM model is based on the assumption that hydraulic fractures are perfectly contained, its results could be less accurate when this assumption is not satisfied. Analytical expression for fracture aperture and height growth have been developed for orthotropic body and used to study the effect of rock anisotropy on fracture height growth where hydraulic

fracture is not well contained. Also, a 2D DDM with 3D correction factor has been used to extend the single fracture P3D model to the case of simultaneously propagating multiple fractures.

Analysis of a single fracture propagating in an isotropic body with multi-stress layers indicate lower accuracy for P3D results when compared to 3D results when fracture toughness is high. In the case of low fracture toughness, the accuracy of P3D result becomes much better. This is because the fracture tip aperture (in the lateral direction), which is used to calculate mode-1 stress intensity factor cannot be solved accurately in P3D model due to the lack of interaction between fracture elements. Therefore, when fracture propagation is in the toughness dominated regime (as in the case of high fracture toughness), fracture growth in the lateral direction is affected due to error in stress intensity factor calculation. On the other hand, 2D DDM model yields results with sufficient accuracy in both high and low fracture toughness cases.

Modeling of propagation of uncontained single planar fracture in isotropic and vertical transversely isotropic rocks using P3D model indicates that fracture height growth in isotropic rock is significantly higher than that in anisotropic rock. Apertures of the fracture in VTI rock are higher than the isotropic case. Induced normal stresses perpendicular to the fracture surface around a single plane strain fracture is 69% higher in a VTI rock with the degree of anisotropy of 4. The effect of stress increase in anisotropic rock can be observed in large-scale simulations of multiple hydraulic fractures. When well contained fractures propagate from multiple clusters simultaneously, the fractures from the inner clusters experience a significant reduction in length in anisotropic rock compared to the isotropic case. This effect can be seen even when the degree of anisotropy is just 1.88. Also, in large-scale simulations, when fractures are very well contained, fracture aperture prediction by both 2D DDM and P3D models are close (especially for outermost

fractures), however fracture length prediction by P3D model is larger than results from 2D DDM model (due to lack of interaction between fracture elements as discussed previously).

Finally, it should be noted that models based on plane strain assumption have some limitations. In situations where rock and fracture configuration are complex, such as in the case of a multiple vertical fractures propagating in tilted transversely isotropic (TTI) rock, accurate predictions for fracture length and height are hard to obtain. For example, simulation of propagation of two simultaneous vertical hydraulic fractures in a TTI rock using 2D DDM indicated asymmetric fracture height growth due to rotation of stress shadow. However, such details are eluded in P3D model since it is incapable of considering variation of induced stresses in vertical direction. Therefore, one would need a complete 3D model to fully understand the effects of rock anisotropy on fracture propagation in complex rock and fracture configurations. Since a full 3D model that can simulate large-scale hydraulic fracture is not available yet, one can make the use of both 2D DDM and P3D model to look at different aspects of effect of rock anisotropy on possible outcomes for fracture geometry. Moreover, these model can assist in better understanding and interpreting of microseismic data. Overall, the numerical analysis presented in this work indicates that formation anisotropy has a significant impact on hydraulic fracture geometry, aperture variation, and height. Therefore, rock anisotropy needs to be considered during spacing optimization and proppant selection to maximize productivity from unconventional reservoirs.

11 Complex Fracture Networks

In this chapter we present a complex fracture model based on 2D DDM that is capable of simulating reservoir scale hydraulic/natural fracture interaction. The natural fractures are modeled using linear joint displacement discontinuity (DD) elements. Fluid flow inside the fractures is modeled using the lubrication equation and is fully coupled with fracture deformation. The non-linear system of fracture deformation and fluid flow equations are solved using globally convergent Newton-Raphson method. Based on LEFM, quasi static fracture propagation is considered where propagating fracture's mixed-mode equivalent stress intensity factor is always at equilibrium with fracture toughness of the rock. Special crack tip elements (Yan 2004) are used to calculate stress intensity factors accurately. Fracture crossing/arrest criterion (Gu and Weng 2010; Renshaw and Pollard 1995), is extended and implemented for cases where hydraulic fracture tip is not aligned with principal stresses. In this paper, the model is first used to present a detailed analysis of the interaction of a single hydraulic fracture with two inclined natural fractures to study the formation of wing fractures. Then, field scale numerical examples are considered using a randomly generated natural fracture network. The results for fracture network geometry, aperture distribution and slip profile are presented for low and high in-situ stress contrasts. The numerical model presented in this paper can act as a useful tool in understanding the behavior of complex fracture networks that can be integrated with MEQ to optimize completion design. Also, this numerically robust model can be used to validate simplified, less computational field scale models.

To quantify and explore the evolution of shear slip at field scale, numerical simulations are conducted using the newly developed complex fracture network model. Simulating hydraulic

fracture propagation in the presence of natural fracture pose a significant challenge. As hydraulic fracture approaches natural fracture it may either cross or arrest and deflect into natural fracture depending on the mechanical properties of rock and natural fracture, and stresses state ahead of the hydraulic fracture tip (Cook and Underwood 2001, Renshaw and Pollard 1995). Furthermore, fluid penetration into favorably oriented natural fractures that are intersected by hydraulic fracture can cause slippage of natural fractures if sufficient fluid pressure has built up. Since the constitutive equations involving natural fractures depend on their state (i.e., slipped/unslipped) which itself is a part of the solution requires this problem to be solved in an iterative manner. As a result, a numerical model that fully couples fracture mechanics with fluid flow and considers all aspects of fracture interaction described above at field scale can be quite challenging in terms of numerical stability and computation time.

The complex fracture model has following characteristics: (a) boundary element based displacement discontinuity method (Crouch and Starfield 1983) is used to model fracture deformation; (b) Newtonian fluid flow inside the fractures is governed by lubrication equation; (c) extended fracture crossing/arrest criterion (Gu and Weng 2010) based on stress field a head of hydraulic fracture tip is used; (d) fracture extension is based on maximum tangential stress hypothesis (Erdogan and Sih 1962) assuming rock as a brittle material; (c) hydraulic fracture tip extension is allowed only when mode-1 stress intensity reaches fracture toughness of the rock; (d) a diffusion based pressure dependent model is used to calculate fluid leak off into the matrix; (e) finally, the model can distinguish between open element (i.e., element supported solely by fluid) and closed element (i.e., element supported by both asperities and fluid) that are in slipped and unslipped condition.

For numerical simulations a randomly generated network of natural fractures is selected. Rock and natural fracture mechanical properties obtained from experiments are used as input for numerical model. Hydraulic fracture propagation in a network of random natural fractures is considered under low (145 psi) and high (1000 psi) in-situ horizontal stress anisotropic conditions. Numerical results show fracture geometry, state of all fractures (open/close/slipped/unslipped), shear slip magnitudes, fluid pressure distribution and fracture apertures distribution at the end of fluid injection.

11.1 Numerical Model

11.1.1 Fracture Deformation

The deformation of natural and hydraulic fractures is modeled using displacement discontinuity method (Crouch and Starfield 1983) where a thin crack is discretized into N constant line elements and the total normal (σ_n^i) and shear stresses (σ_s^i) acting on each element is expressed as,

$$\sigma_n^i = (\sigma_n^i)_0^\infty + \sum_{j=1}^{N} G^{ij} A_{ns}^{ij} D_s^j + \sum_{j=1}^{N} G^{ij} A_{nn}^{ij} D_n^j$$
$$\sigma_s^i = (\sigma_s^i)_0^\infty + \sum_{j=1}^{N} G^{ij} A_{ss}^{ij} D_s^j + \sum_{j=1}^{N} G^{ij} A_{sn}^{ij} D_n^j \qquad (11.1)$$
$$\{i = 1, N\}$$

In the above equation $(\sigma_n^i)_0^\infty$ and $(\sigma_n^i)_0^\infty$ are far-field normal and shear stresses acting on fracture elements. D_n is normal displacement discontinuity (DD) which indicates difference in normal displacement between two sides of a fracture element. Similarly, D_s is shear displacement discontinuity (DD) which indicates difference in shear displacement between two sides of a fracture element. The terms A_{ns}^{ij}, etc., gives normal/shear stress at *i*th element due to unit normal/shear DD at *j*th element. The parameter G^{ij} varies between 0 and 1 and considers the effect

of fracture height on fracture opening/sliding (see chapter 8). To be consistent with the sign convention used in the reference (Crouch and Starfield 1983), fracture opening is represented by a negative D_n. Therefore, fluid driven fracture elements with negative D_n are supported solely by fluid pressure (i.e., their effective stress is zero) as in shown Figure 11-1a, and are identified as mechanically opened elements. Whereas fracture elements with a positive D_n are called mechanically closed elements which are supported by both fluid and asperities (effective stress greater than zero) as shown in Figure 11-1b. Although positive D_n has no physical meaning for fracture elements (since fracture surface overlap is not possible mechanically), it is physically meaningful for natural fractures or joints since they have some thickness due to asperities. In this case, Eq. 11.1 can be modified for natural fractures by introducing linear spring elements:

$$P^i = \overset{i}{K}_n D_n^i + (\sigma_n^i)_0^\infty + \sum_{j=1}^{N} G^{ij} A_{ns}^j D_s^j + \sum_{j=1}^{N} G^{ij} A_{nn}^j D_n^j \qquad (11.2a)$$

$$-\overset{i}{K}_s D_s^i = (\sigma_s^i)_0^\infty + \sum_{j=1}^{N} G^{ij} A_{ss}^j D_s^j + \sum_{j=1}^{N} G^{ij} A_{sn}^j D_n^j \qquad (11.2b)$$

In the above equations, a positive D_n indicates the amount of closure experienced by the spring element/asperity. K_n and K_s represents normal and shear stiffness of natural fractures which are measured experimentally and P is fluid pressure. The term $\overset{i}{K}_n D_n^i$ indicates effective stress of the ith natural fracture element. Natural fractures that are under compressive stresses at depth experience some closure (Goodman 1976; Barton et al. 1985). Laboratory measurements suggest that the amount of closure experienced by a fracture due to compressive normal stresses acting on it is limited. In this paper, the maximum possible closure experienced by a natural fracture which is also equal to its thickness is taken as 0.1 mm. Although the relationship between fracture closure and normal stress is non-linear, the linear model used in this paper can sufficiently describe the behavior of joint closure under lower effective stress conditions (Sesetty and Ghassemi 2012).

During the solution processes the status of an *i*th element can change from close to open and vice versa, which is found based on the sign of D_n^i. Since open elements cannot support shear stresses, the total shear stress σ_s^i acting on any open element must be zero. A closed element can experience frictional sliding when total shear stress acting on it reaches yielding limit. Using simple Coulomb frictional law, the yield stress of a closed natural fracture element is expressed as:

$$\sigma_y^i = c + (\sigma_n^i - P^i)\tan\phi \tag{11.3}$$

Where, σ_y^i and σ_n^i are yield stress and total normal stress for the *i*th fracture element respectively, *c* is cohesion, P^i is fluid pressure inside *i*th fracture element and ϕ is friction angle. The condition for slip of an *i*th fracture element is:

$$\left|\sigma_s^i\right| = \sigma_y^i \tag{11.4}$$

Combining Eq. 11.1 and Eq. 11.3 gives the governing Eq. 11.5 for shear deformation of a slipping element:

$$c + (-\sigma_n^i - P^i)\tan\phi = (\sigma_s^i)_0^\infty + \sum_{j=1}^{N} G^{ij} A_{ss}^j D_s^j + \sum_{j=1}^{N} G^{ij} A_{sn}^j D_n^j \tag{11.5}$$

The state of a slipped element is changed back to stick state if Eq. 11.4 is no longer valid on that particular element. For such elements (i.e., elements that have previously undergone slip) shear deformation can be expressed as in Eq.11.6.

$$(\sigma_s^i)^{k-1} + \overset{i}{K}_s (D_s^i)^{k-1} = \overset{i}{K}_s D_s^i + (\sigma_s^i)_0^\infty + \sum_{j=1}^{N} G^{ij} A_{ss}^j D_s^j + \sum_{j=1}^{N} G^{ij} A_{sn}^j D_n^j \tag{11.6}$$

Where, *k* denotes time step number and the terms $(\sigma_s^i)^{k-1}, (D_s^i)^{k-1}$ indicate total shear stress and shear DD on the *i*th element during time step (*k*-1) respectively.

Therefore, hydraulic fracture elements (i.e., open elements) are governed by equation (1). Closed elements of natural fractures under stick condition (i.e., $\left|\sigma_s^i\right| < \sigma_y^i$) are modeled using Eq. 11.2 and Eq. 11.6. Under the condition of slip, Eq. 11.2b is replaced with Eq. 11.5 for closed elements. In order to reduce computational cost, Eqs. 11.1-11.6 exclude the elements of natural fractures that were not intersected by hydraulic fracture. Therefore, a hydraulic fracture cannot interact with surrounding natural fractures until they intersect. Such an approximation does not alter the solution if natural fractures have high stiffness or good frictional strength (Sesetty and Ghassemi 2017a).

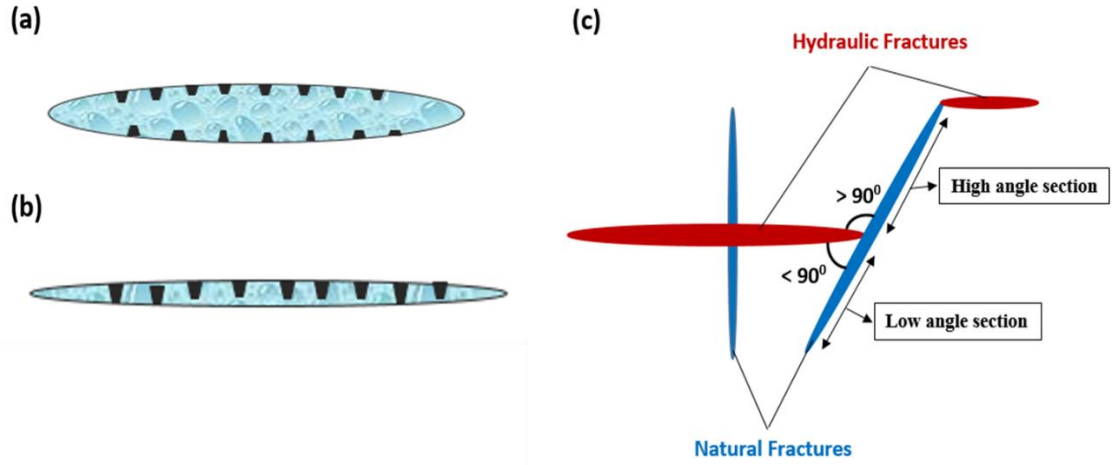

Figure 0-16. Natural fracture element (a) opened mechanically and supported solely by fluid, (b) mechanically closed element supported by fluid and asperities, (c) section of natural fracture making >90^0 with respect to hydraulic fracture is called high angle section, whereas, section making <90^0 is called low angle section.

11.1.2 Fluid Flow

Experimental evidence (Gale 1982) suggest that fluid flow inside hydraulic fractures and narrow channels of mechanically closed segments of natural fractures can be approximated using cubic law:

$$q = -\frac{w^3 h}{12\mu}\frac{\partial p}{\partial x} \tag{11.7}$$

Where q is volumetric flow rate, μ is dynamic viscosity of the injection fluid, and w, h are fracture total width and height, respectively.

Fracture total width w can be directly equated to the normal DD ($-D_n$) obtained from Eq. 11.1 for fracture elements created during propagation and are opened mechanically. These newly created fracture elements can experience complete closure (i.e. D_n=0) due to stress shadow effect. However, in order to continue fluid flow through them, these elements are assigned small residual aperture w_0. On the other hand, pre-existing fractures can be conductive even under high effective stresses as they retain residual apertures due to surface roughness. The closure experienced by natural fractures under compressive stresses can be reversed by decrease in effective stress due to increase in fluid pressure. Assuming V_{mc} as the maximum possible closure value for a natural fracture element and V_{mc}^t as the closure value during fluid injection at time t, the effective gain in natural fracture aperture during the time t, is $V_{mc} - V_{mc}^t$ (neglecting hysteresis). Also, shear slip causes dilation of natural fractures due to their surface roughness. The total dilation (limited to a maximum value of 0.05 mm) can be expressed in terms of shear slip (D_s) and dilation angle (ψ) which is experimentally measured. When effective stress acting on a natural fracture element reaches zero, the element begins to open mechanically. The total width w of a natural fracture element can be expressed as sum of the residual aperture (w_0), reversal in closure ($V_{mc} - V_{mc}^t$), shear dilation ($|D_s| \tan\psi$) and mechanical opening (w_m) as:

$$w = w_0 + (V_{mc} - V_{mc}^t) + w_m + |D_s| \tan\psi \tag{11.10}$$

Where, w_m is zero when the effective stress acting on a natural fracture element is greater than zero (i.e. closed elements) and V_{mc}^{t} is zero when effective stress is zero. Note that residual aperture is required to allow fluid flow through closed elements. Assuming very low values for residual aperture can lead to very high net pressures inside the fractures to compensate high frictional pressure losses (Zhang and Jeffrey 2009). In this work, we set w_0 to 0.05 mm.

The continuity Eq. 11.11 along with cubic law, Eq. 11.9 governs fluid flow inside the fractures:

$$\frac{\partial q}{\partial x}+\frac{\partial A}{\partial t}+q_L=0 \tag{11.11}$$

Where A is the cross-sectional area of the fracture and q_L is the fluid leak-off volume rate per unit length of the fracture which is ignored in this model. Substituting Eq. 11.9 in Eq. 11.11 and assuming that the fracture height is constant with time and along the length of all fractures, gives the lubrication Eq. 11.12 which is solved using finite difference approximation.

$$\frac{q_L}{h}+\frac{\partial w}{\partial t}=\frac{\partial}{\partial x}\left(\frac{w^3}{12\mu}\frac{\partial p}{\partial x}\right) \tag{11.12}$$

11.1.3 Fracture Propagation

Quasi-static fracture growth is considered where mixed-mode equivalent stress intensity factor for propagating fractures is always at equilibrium with fracture toughness of the rock as in Eq. 11.7 (Erdogan and Sih 1963). Therefore, tensile wing fractures can be initiated from natural fracture tips due to their slippage even if they are under mechanically closed state (i.e., K_I=0). The stress intensity factors are evaluated using fracture tip displacement discontinuities. Special square root elements are implemented at fracture tips to improve the accuracy of stress intensity factors.

$$K_{Eq}=\cos\frac{\theta}{2}\left(K_I\cos^2\frac{\theta}{2}-\frac{3}{2}K_{II}\sin\theta\right)=K_{IC} \tag{11.7}$$

Fracture tips that meet propagation condition Eq. 11.7 are extended in the direction θ (Stone and Babuska 1997), calculated from Eq. 11.8,

$$\theta(K_I, K_{II}) = \begin{cases} 0 & if\ K_{II} = 0 \\ 2\arctan\left(\dfrac{\dfrac{K_I}{K_{II}} - \mathrm{sgn}(K_{II})\sqrt{\left(\dfrac{K_I}{K_{II}}\right)^2 + 8}}{4} \right) & if\ K_{II} \neq 0 \end{cases} \tag{11.8}$$

11.1.4 Fracture Crossing and Arrest

The fracture crossing/arrest criterion used in this work is based on the stress field ahead of the hydraulic fracture tip approaching a natural fracture. This criterion, initially developed by Renshaw and pollard (1995) for orthogonal intersections, checks if both the no slip and tensile failure conditions on a natural fracture are satisfied due to the stress field ahead of the approaching fracture tip and if so, fracture crossing occurs. In the event that of one of the above two conditions is not met, the approaching fracture is assumed to terminate at the natural fracture. This criterion can be simply extended to non-orthogonal fracture intersections and situations where hydraulic fracture tip is not aligned with a far-field principal stresses (i.e., $K_{II} \neq 0$) as in Gu and Weng, (2010). Note that in this criterion, fracture crossing/arrest is decided before fracture intersection and is independent of the injection fluid properties (Weng et al. 2014). In the event of fracture arrest, fluid is allowed to flow into the natural fracture and the potential locations for new fracture initiation along the natural fracture can be found by analyzing the tangential stresses on its surface (Chuprakov et al. 2014; Cook and Underwood 2001; Zhang and Jeffery 2009). Although this can be easily implemented in this model as the stresses along the natural fracture surfaces are readily available, for simplicity we assume new fracture initiation from a natural fracture will always occur

at its tips if the propagation condition given in Eq. 11.7 is met. Square root elements are replaced with ordinary DD elements at the fracture tips that remain arrested after intersection.

11.1.5 Solution Procedure

Since a slight change in the fluid pressure inside fracture affects its deformation which in turn affects fluid pressures, this problem is strongly non-linear and coupled. Moreover, the effective stress changes on closed natural fracture elements can cause slip and eventually change their status from closed to open elements. As a result, the problem of hydraulic fracture propagation in a network of natural fractures is much more complex than simulating hydraulic fractures alone. Along with the unknown fracture widths and pressures, the status (i.e., open, close, stick and slip) of every natural fracture element must be obtained as a solution. At the beginning of each time step, the status of all natural fracture elements are fixed to close. Similarly, the status of all closed elements are fixed to stick. Using the trail status of all the natural fracture elements, the system of Eqs. 11.1, 11.2& 11.12 are solved for unknown values of fracture apertures and pressures for a time interval Δt. Natural fracture elements with negative D_n are changed to open elements and condition for slip on closed elements is checked using Eq. 11.4.With the updated status of all natural fracture elements, the system of Eqs. 11.1, 11.2, 11.5, 11.6& 11.12 are solved for the same time interval Δt. This process is repeated until the statuses of all fracture elements converge. Before advancing to the next time step, stress intensity factors are evaluated using fracture tip displacement discontinuities. Fracture tips that meet the propagation criterion Eq. 11.7 are extended by adding a new element in the direction evaluated from Eq. 11.8. (Although it is possible to add more number of elements at fracture tips after each time step to save computation time, it decreases the accuracy of fracture propagation path). If fracture propagation condition is not met at least at one of the fracture tips, the above procedure is repeated with different time interval Δt.

It is obvious from the above discussion that the two most computationally intensive steps are iterating over natural fracture element statuses and finding exact Δt to satisfy propagation condition since it requires the Eqs. 11.1, 11.2, 11.5, 11.6& 11.12 to be solved multiple times. Although root finding algorithms like bisection method used in this model reduces the number of iterations required to achieve satisfactory convergence on Eq. 11.7, it is still computationally burdensome. The numerical model developed in this paper, typically finds Δt in 3-4 iterations for simple fracture trajectories, however can take up to 20 iterations for complex fracture trajectories (typically encountered during the re-orientation of natural fracture wings).

Table 0-4. Experimentally determined Input parameters for numerical model (Zhi et al. 2018).

Parameter	Value	Units
Young's modulus	25.55 (3.70×10^6)	GPa (psi)
Poisson's ratio	0.287	
Tensile strength	9.39 (1362)	MPa (psi)
Normal stiffness of natural fractures	377 (1.39×10^6)	GPa/m (psi/inch)
Shear stiffness of natural fractures	300 (1.11×10^6)	GPa/m (psi/inch)
Cohesion	0 (0)	MPa (psi)
Coefficient of friction	0.752	

Table 0-5. Assumed Input parameters for numerical model.

Parameter	Value	Units
Minimum principal horizontal stress (σ_h)	40 (5800)	MPa (psi)
Hydraulic/Natural fracture height (all examples)	30 (100)	m (ft)
Injection fluid viscosity	1	cP
Fracture toughness	1.65 (1500)	$MPa.m^{0.5}$ ($psi.inch^{0.5}$)
Maximum closure value of natural fractures	0.1 (0.004)	mm (inch)
Residual aperture	0.05 (0.002)	mm (inch)
Dilation angle	2	degrees

11.2 Wing Fractures

The behavior of a hydraulic fracture approaching two natural fractures that are at equal distance from the injection point (0, 0) (shown by red circle) in Figure 11-2a is studied in this example. The natural fractures are discretized into constant elements of size 0.6 ft and same size elements are used for newly added fractures during propagation. The two natural fractures are initially in mechanically closed state under zero pore pressure, however, they are hydraulically conductive from residual opening. A constant fracture height of 100 ft is assumed for all fracture elements. The fracture height is in Z-direction; therefore X-Y plots show a top view of fracture networks. Experimentally (Zhi et al. 2018) obtained mechanical properties of rock and natural fracture listed

in Table 11-1 are used as input to the simulator. Input parameters that are not available from experiments are assumed and these are listed in Table 11-2. The horizontal in-situ stress contrast for this example is 725 psi (5 MPa). The orientation of natural fractures is taken as 27^0 w.r.t the X-axis so that the hydraulic fracture will arrest at the locations of fracture intersection based on the crossing/arrest criterion. Water is injected at 10 bpm for 110 sec into a small perforation having an initial length of 3 ft in the direction of Y-axis and with midpoint (0, 0). Neglecting fluid leak-off, the fracture geometry, aperture distribution, pressure distribution, shear displacements and status of all elements at the end of injection period are shown in Figure 11-2.

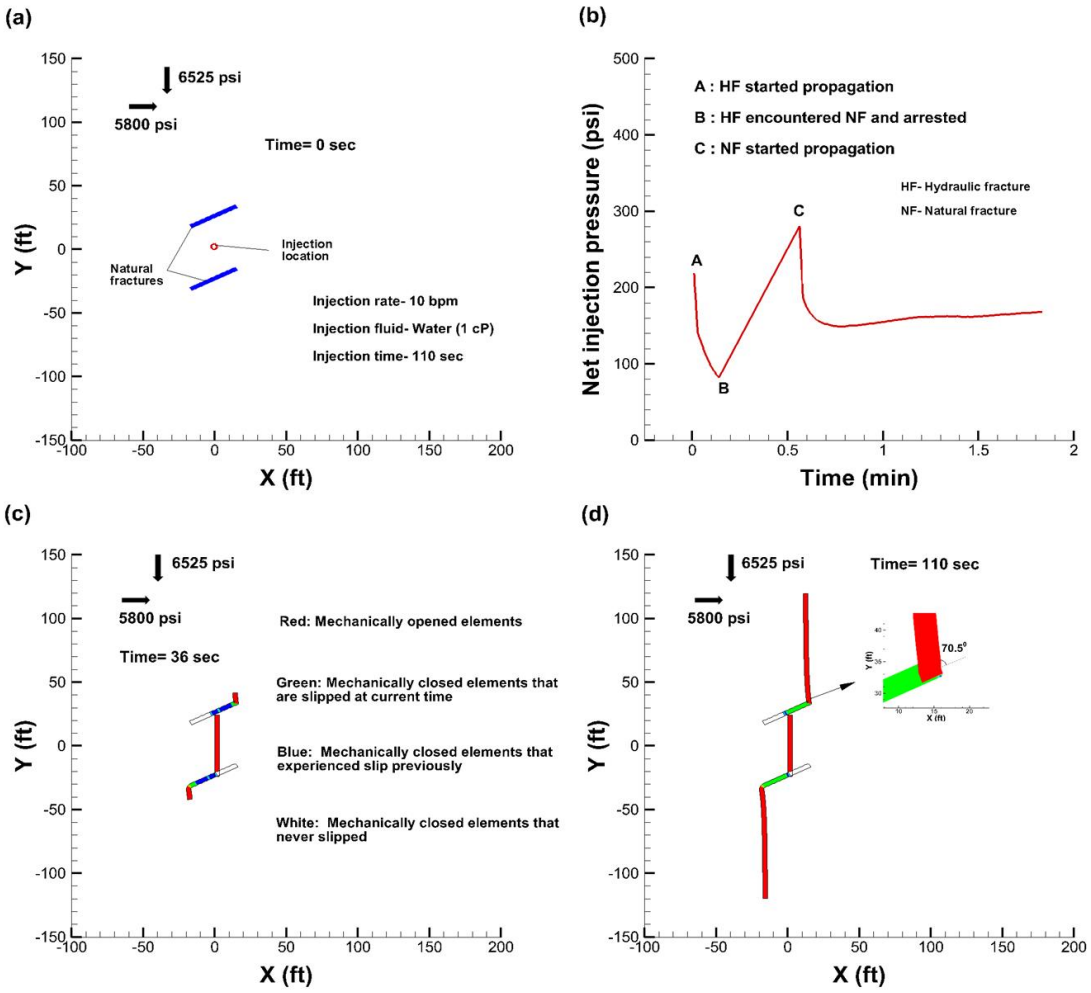

Figure 0-17. (a) location of natural fractures and injection point with input parameters, (b) net injection pressure profile vs time, (c) status of each fracture element at 36 sec, (d) status of each fracture element at 110 sec (inset showing propagation angle at natural fracture tip).

The net injection fluid pressure vs time plot from Figure 11-2b shows a decreasing trend from point A as the hydraulic fracture propagates in the direction of the maximum far-field principal stress. The hydraulic fracture arrest at the intersection with the two natural fractures is indicated by point B where the fluid pressure starts to rise. The rise in net injection pressure is continued until point C to about 280 psi, where one of the tips of both natural fractures meets the propagation condition, after which the net injection pressure starts to fall and stabilizes at around 170 psi

(although the net injection pressure appears to increase with time, the rate of increase is very small; this could be due to increase in compressive σ_{YY} on natural fracture elements with increase in main hydraulic fracture opening (see Figure 11-4b) or transition of fracture geometry to PKN (i.e. L>H)). The drop in injection pressure after natural fracture propagation is due to the re-orientation of the natural fracture wings towards the direction of local maximum principal stress. The magnitude of the net pressure increase required to initiate propagation from the natural fracture tips is a function of the contrast between the far-field principal stresses and the natural fractures orientation with respect to them. Fracture geometry and status of all fracture elements immediately after natural fractures started propagation is shown in Figure 11-2c. A four color system is used to represent the status of each fracture element. The color red represents mechanically open elements. Green color indicates a mechanically closed element that is currently undergoing slip whereas the color blue indicates a mechanically closed element that is currently in stick condition but experienced slip previously. White color elements are mechanically closed and never slipped. From Figure 11-2c, we can see that natural fractures propagation initiated from their tips only because of slippage. Figure 11-2c also indicates some of the natural fracture elements that slipped are going back to the stick state due to sudden drop in the injection pressure. Since the injection pressure (Figure 11-2b) never exceeded the normal stress acting on the natural fractures (6380 psi or 44 MPa), the natural fracture elements cannot mechanically open so that the mode-1 stress intensity factor (K_I) at the natural fracture tips must be zero. When $K_I=0$, the angle of fracture propagation is 70.5^0 anticlockwise from the axis of the fracture tip based on Eq. 11.8. This can be observed by taking a closer look at the natural fracture tip as in Figure 11-2d. Substituting $K_I=0$ and $\theta=70.5^0$ in Eq. 11-7 gives $K_{II} \approx 0.86\ K_{IC}$ which is the condition to initiate propagation from a natural fracture tip due to slippage while in a mechanically closed state.

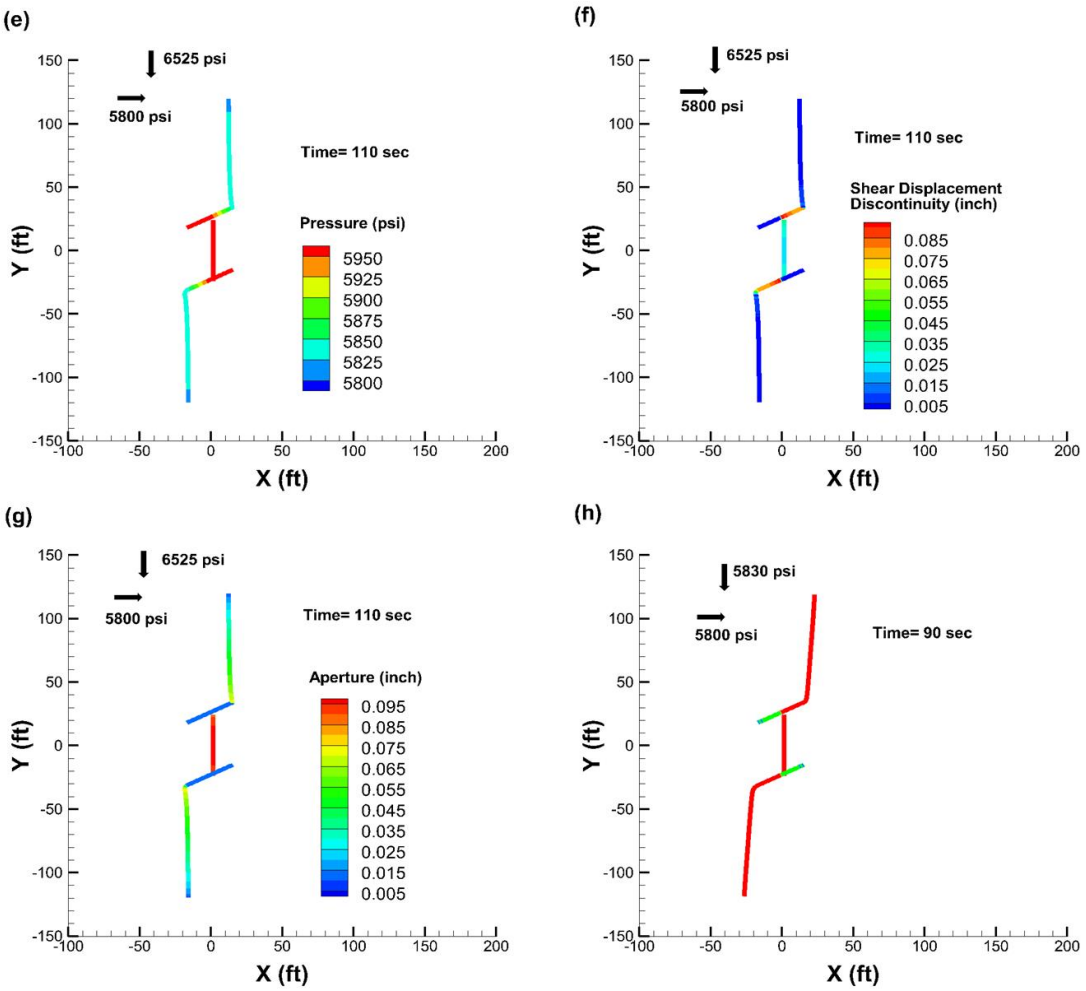

Figure 0-18. (e) pressure , (f) shear DD, (g) aperture distribution at 110 sec, (h) fracture geometry and element status for a case with very low in-situ horizontal stress contrast.

Figure 11-2d shows that at 110 sec, both natural fractures remained mechanically closed. Only the main hydraulic fracture and natural fracture wings which are now aligned with the maximum far-field principal stress are mechanically opened. Also notice that slippage occurred only on the high angle (see Figure 11-1c) sections of the natural fractures. The low angle (see Figure 11-1c) sections of natural fractures never experienced slip. This is despite the high fluid pressure (close to 6000 psi) buildup inside these sections of the natural fractures as indicated in Figure 11-3e. Figure 11-3f shows shear DD's of all fracture elements. The maximum shear DD has occurred along high angle sections of natural fractures. Although the main hydraulic fracture is aligned with the

maximum far-field principal stress, it has experienced shear deformation due to slippage of the natural fractures and the associated shear stress shadow. The natural fracture wings that are almost aligned with the maximum far-field principal stress did not experience considerable shear DD. The aperture distribution (Figure 11-3g) has a large variation along the fracture network; higher fracture apertures occur along those network segments that opened against the minimum principal stress (i.e. along the main hydraulic fracture and natural fracture wings). At the locations of fracture intersection there is a sudden drop in fracture apertures. Therefore, fluid from the main hydraulic fracture has to pass through extremely narrow channels in natural fractures to flow to their wings.

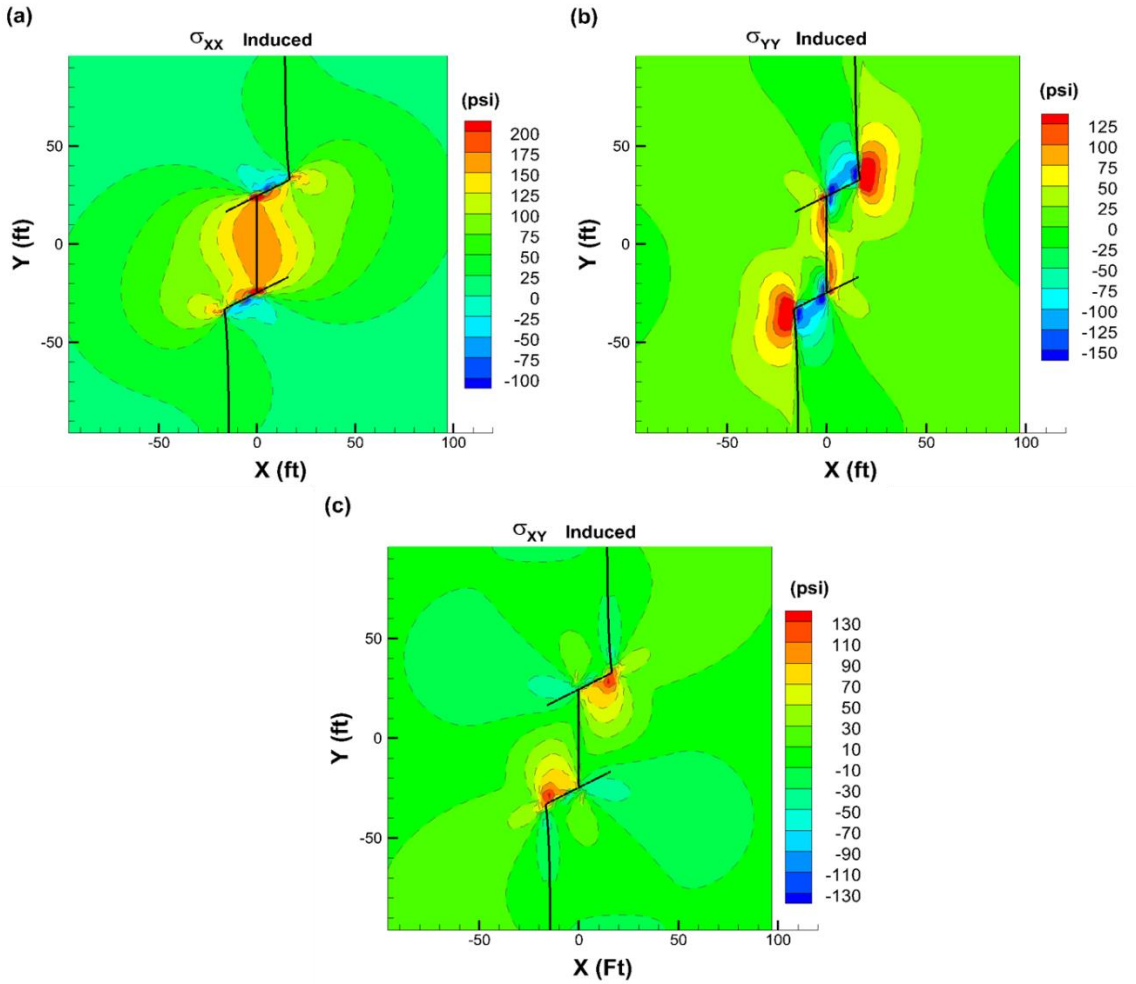

Figure 0-19. Distribution of induced stresses (compressive positive) in (a) X-direction, (b) Y-direction, (c) shear stresses

Figure 11-4 shows the induced normal and shear stress distributions around the fractures at 110 sec. An increase in compressive stresses up to 170 psi is evident near the surface of the main hydraulic fracture in the direction normal to it (Figure 11-4a). The induced compressive σ_{XX} along the line Y=0 drops to 125 psi at 20 ft from the fracture surface and to 30 psi at 100 ft from it. Tensile σ_{XX} stresses of up to 100 psi are induced near the high angle sections of both natural fractures due to their slippage. Induced (σ_{YY}) from Figure 11-4b indicate increased compressive stresses (up to 100 psi) on the low angle sections of the natural fractures. As a result, the low angle

sections of the natural fractures neither mechanically open nor slip. On the other hand, the high angle sections of the natural fractures experience a decrease in the compressive stresses acting on them due to the induced tensile stresses. This means mechanical slippage on high angle sections of the natural fractures can occur at a lower pressure. This is the reason for eventual slip (Figure 11-2d) of all high angle natural fracture elements even after the drop in injection pressure (Figure 11-2b) once they began to propagate. It is interesting to note that even under the scenario of a very low far-field principal horizontal stress contrast of 30 psi (0.2 MPa), the effect of induced σ_{YY} still exists on the low angle sections of natural fractures as propagation occurs only from the high angle sections as indicated by Figure 11-3h. Figure 11-4c shows the distribution of the induced shear stresses component (σ_{XY}); it has a high magnitude of 130 psi near the edges of the high angle sections of the natural fractures due to their slippage. It is interesting to note that the induced shear stresses are observed only on one side of natural fractures that is facing towards the main hydraulic fracture. The induced shear stresses have the potential to destabilize any surrounding natural fractures that are critically oriented. On the other hand the induced compressive normal stresses will have a stabilizing effect. As a result, the stability of natural fractures in the region of stress perturbation is a function of overall stress state (initial plus induced) and the pore pressure (Warpinski 2001).

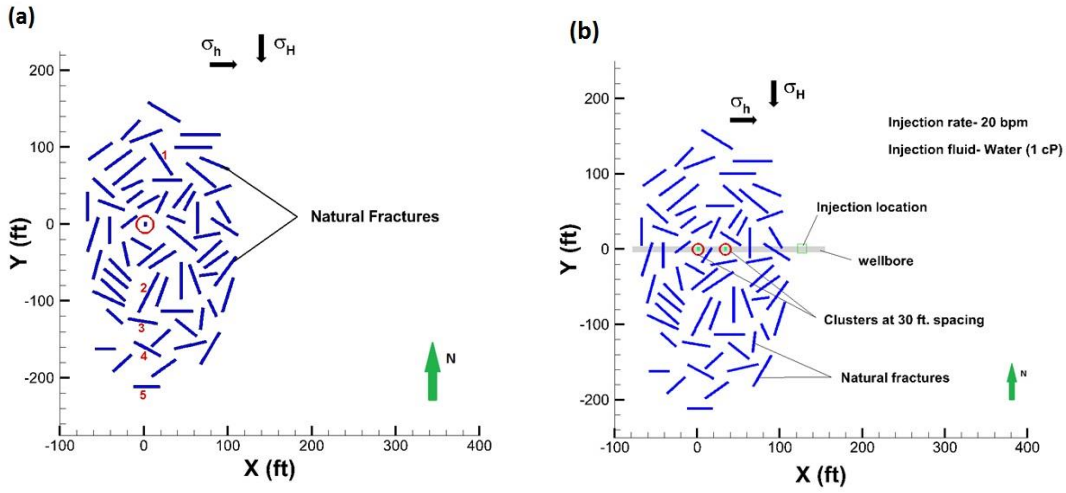

Figure 0-20. Randomly generated networks of natural fractures. Left picture is Network-1 and right picture is Network-2. Perforation locations are indicated by red circles. Far-field maximum in-situ stress is acting along north.

11.3 Complex Fracture Network Numerical Simulations

To numerically model hydraulic fracture growth in a naturally fractured rock, the experimentally obtained mechanical properties of rock and natural fracture listed in Table 11-1 are used as input. Input parameters that are not available from experiments are assumed and these are listed in Table 11-2. Figure 11-5a shows a randomly generated network of vetical natural fractures (blue lines). The length of these natural fractures are in the range of 20-60 ft. and their height is fixed at 100 ft. The perforation is located at (0, 0) and is indicated by red circle in Figure 11-5a.

11.3.1 Network-1 (Low In-situ Horizontal Stress Contrast)

As a first case we consider hydraulic fracture propagation from perforation location under low in-situ stress anisotropic condition. The in-situ horizontal stress anisotropy in this case is 145 psi with maximum principal horizontal stress acting along the direction of Y-axis (see Figure 15a). Slick

water (1 cP) is injected at a constant rate of 30 bpm for 160 sec and the resultant fracture network is shown in Figures (11-6)-(11-9). Figure 11-7 indicates the state of all the fractures at end of injection period. A three color scheme is used to represent the state of each fracture. Mechanically opened (i.e. asperities of fracture surfaces are not in contact) fracture segments are shown in red color. Blue color shows fracture segments that are mechanically closed (i.e. asperities of fracture surfaces are in contact) and unslipped. Green color shows fracture segments that are mechanically closed, however are slipped. We can make the following observations from Figures (11-6)-(11-9). All the natural fractures that are not intersected by hydraulic fracture remained in mechanically closed state at end of the stimulation (Figure 11-7). The combined effect of induced stresses around the fractures and pore pressure rise did not cause any slip on these isolated fractures. Most of the segments of natural fractures that are intersected by hydraulic fracture are still in mechanically closed state. This is due to the effect of stress shadow between the fracture wings. Fluid penetration (through native hydraulic aperture) and eventual increase in net pressure inside the natural fractures that are intersected by hydraulic fracture caused their slippage. The magnitude if shear slip along the segments of natural fracture that are mechanically closed is in the order of 0.005-0.09 inch (Figure 11-8). Due to shear slip induced fracture dilation, the fracture conductivity of slipped elements increased up to 2 md-ft (Figure 11-9).

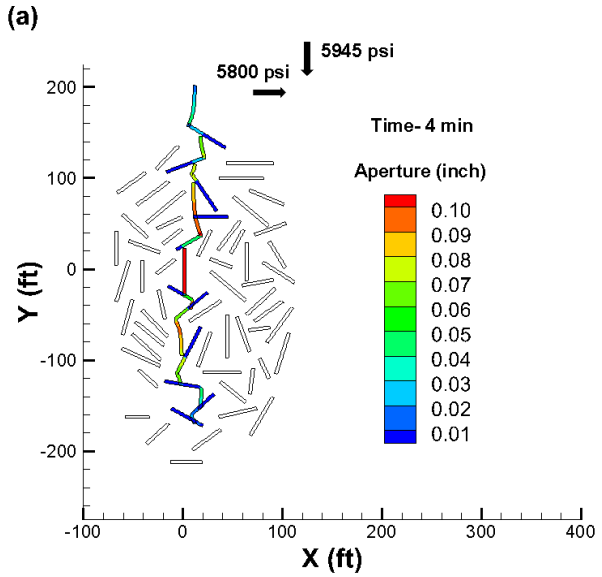

Figure 0-21. Aperture distribution in complex fracture network with in-situ horizontal stress anisotropy of 145 psi. Initial fracture network is shown in Figure 11-5a.

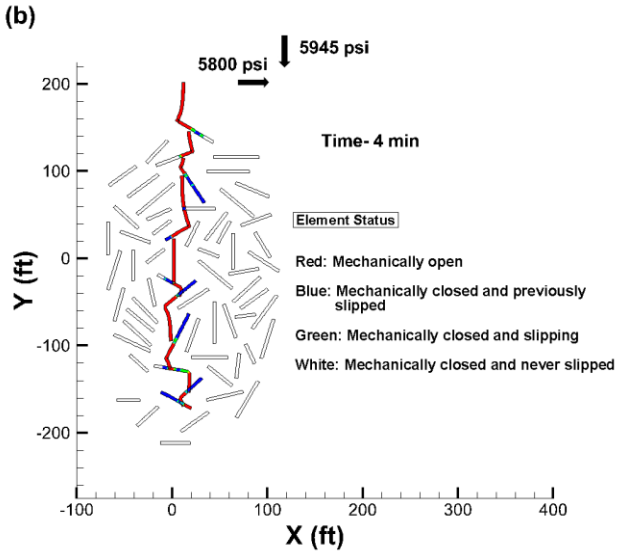

Figure 0-22. Status of all fracture elements

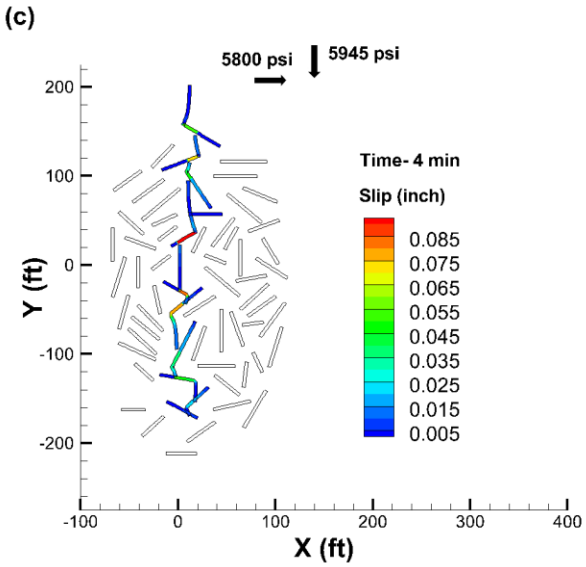

Figure 0-23. Slip distribution

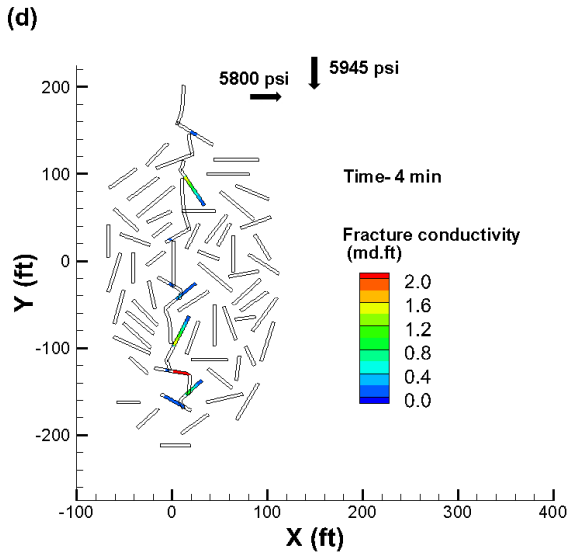

Figure 0-24. Fracture conductivities on natural fractures due to dilation

Fracture apertures (Figure 11-6) varied extremely in the final network where fracture opening along the segments that are under higher compressive stress is restricted. This can result in proppant screen-out issues. Fracture geometry is complex and asymmetric where propagation is dominated towards north.

11.3.2 Network-1 (High In-situ Horizontal Stress Contrast)

In this case we consider hydraulic fracture propagation under high in-situ horizontal stress anisotropy of 1000 psi. Slick water (1 cP) is injected at perforation location (see Figure 11-5a) at a constant rate of 30 bpm for 100 sec. Fracture network obtained at the end of stimulation is shown in Figures (11-10)-(11-13). The results indicate that fracture network outcome is dependent on stress anisotropy, as hydraulic fracture growth is dominated towards south in this case (contrary to the case of low stress anisotropy where fracture propagation is dominated towards north). Also, hydraulic fracture simply crossed natural fractures with low inclination angle. Natural fractures that are unconnected by hydraulic fracture are in mechanically closed and unslipped state (Figure 11-10). Only natural fractures that are at high inclination angle and connected by hydraulic fracture have experienced slip. The shear slip (Figure 11-12) experienced by mechanically closed segments of natural fractures in this case is higher (0.02-0.2 inch) in magnitude compared to the case of low stress anisotropy (0.005-0.09 inch). As a result, higher fracture conductivity is observed in mechanically closed and slipped elements (Figure 11-13). This is due to higher shear stresses acting on the inclined surfaces of natural fracture in the case of high stress anisotropy. Aperture distribution (Figure 11-11) in the fracture network indicates considerable variation similar to the case of low stress anisotropy. Aperture drop at fracture intersections can lead to screenout issues.

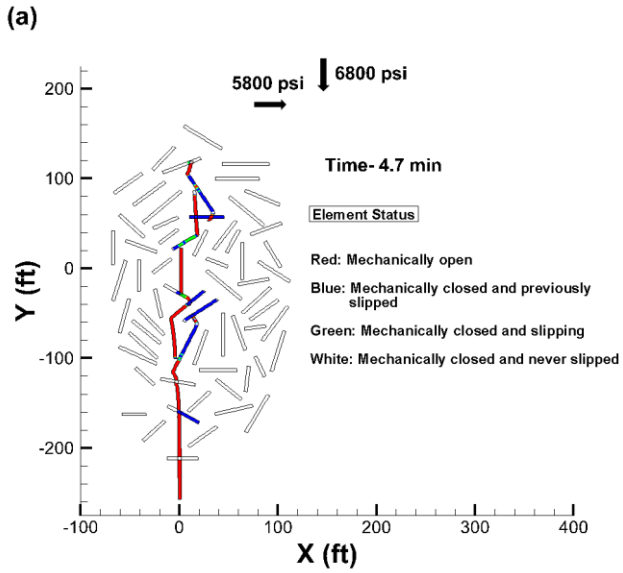

Figure 0-25. Element status in complex fracture network with in-situ horizontal stress anisotropy of 1000 psi. Initial fracture network is shown in Figure 11-5a.

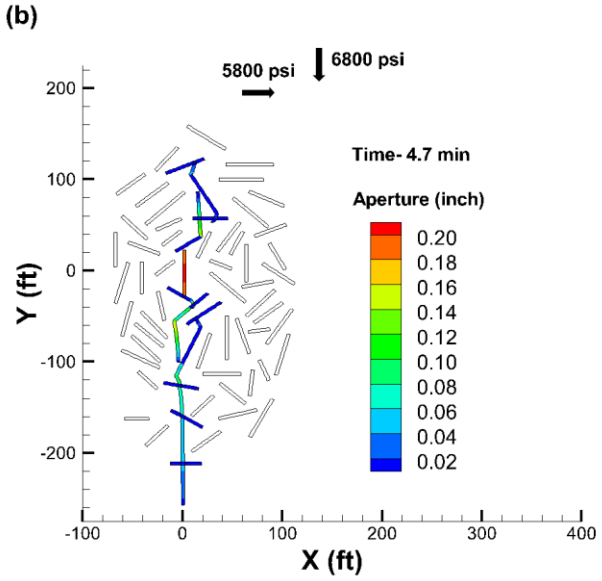

Figure 0-26. Aperture distribution

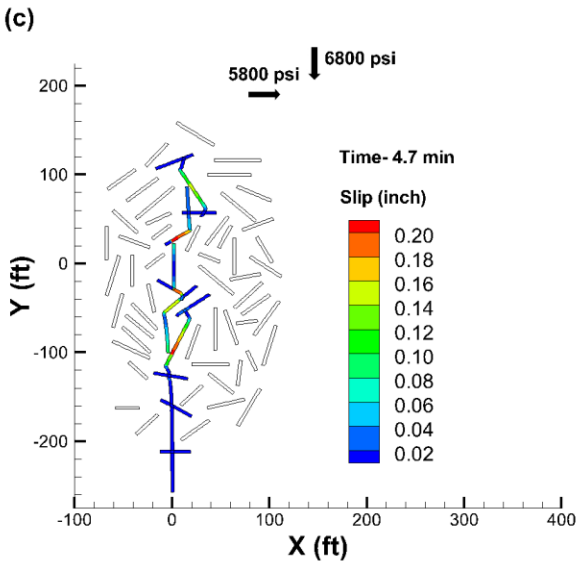

Figure 0-27. Slip distribution

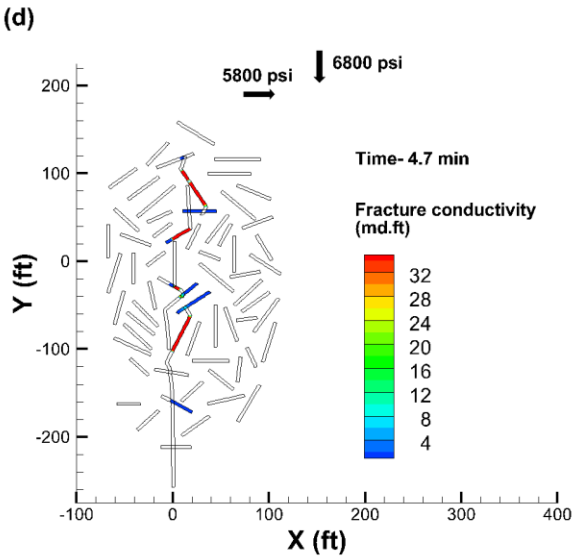

Figure 0-28. Fracture conductivities

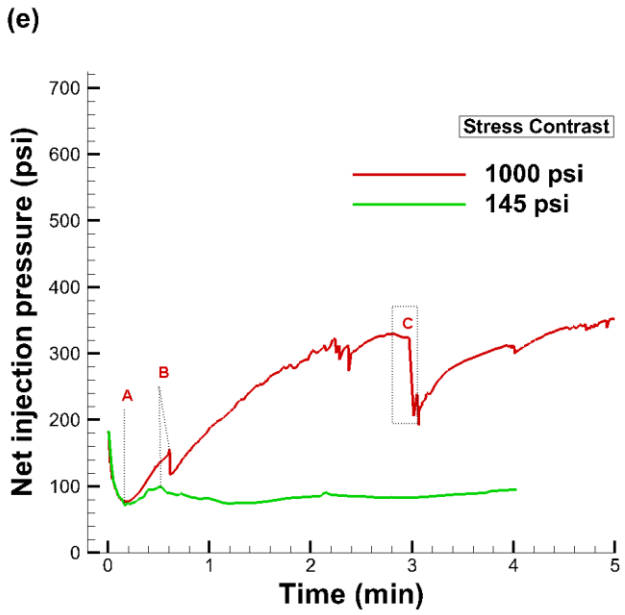

Figure 0-29. Comparison of net injection pressures at wellbore for network 11-5a for high and low in-situ stress contrast cases.

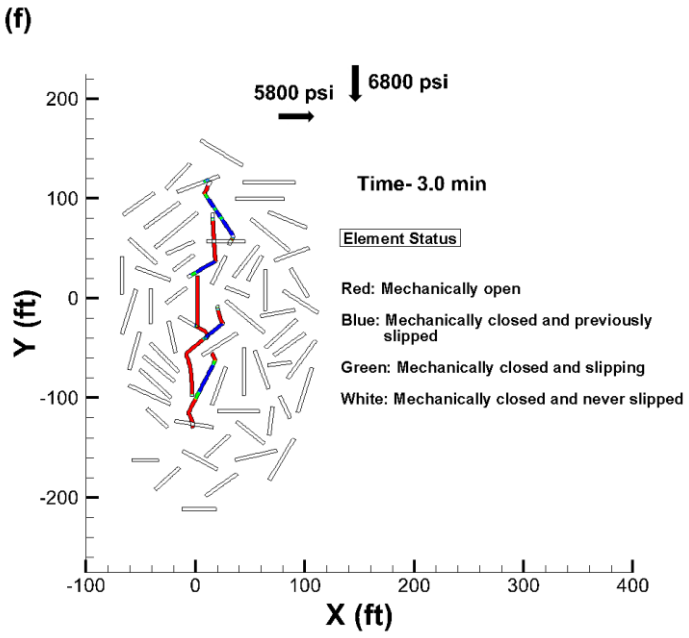

Figure 0-30. State of all fracture elements at time 3 min (stress anisotropy is 1000 psi).

11.3.3 Injection pressure response

Propagation of a planar hydraulic fracture typically produces smooth injection pressure profile. However, in the case of complex fracture networks, simultaneous propagation of multiple fracture tips and continuous change of stresses on natural fracture elements and their status results in a complex injection pressure profile. Figure 11-14 shows comparison of net injection pressure response with time for the cases of low and high in-situ stress contrast. The results indicates that net injection pressure drops initially when a planar hydraulic fracture is initiated and propagates in the direction of maximum principal stress. Injection pressure starts to rise (indicated by point A) after hydraulic fracture is arrested at the intersection with natural fractures (4 and 5) on both sides (i.e., north and south). According to Sesetty and Ghassemi (2018), the magnitude of injection pressure rise depends on the in-situ stress contrast and the orientation of natural fractures with respect to the in-situ principal stresses. The increase in injection pressure is continued until propagation is initiated from the tip of natural fracture 6 (indicated by point B). The instantaneous pressure drop at natural fracture propagation can be attributed to creation of new fracture elements in the direction of local maximum principal stress direction that do not require much pressure to open mechanically. In the case of low in-situ stress contrast, injection pressure continues to drop after this point and almost stabilized. On the other hand, injection pressure continues to increase during the propagation of natural fracture wings (from Fractures 4 and 6; see Figure 11-5a) in the case of high in-situ stress contrast. This is because the natural fractures are mechanically closed in this case and create a higher resistance to fluid flow from injection point through narrow sections of natural fractures to their tips. This increase in injection pressure is responsible for higher opening observed along the segments of hydraulic fracture that are oriented almost parallel to maximum principal stress when in-situ stress contrast is high compared to the case of low in-situ stress contrast. Injection pressure drop of up to 150 psi at around 3 min (indicated by point C in

Figure 11-14) is observed in the case of high stress contrast during the propagation of Fracture 8 after hydraulic fracture arrested on both sides of the network at Fractures 1 and 8. This is due to mechanical opening of high angle sections of natural fractures 5, 6 and 8, which provide the path of least resistance for the fluid to flow towards the south wing of the hydraulic fracture as indicated by Figure 11-15. This effect is temporary (as the Fracture 5 eventually closed according to Figure 11-10) and the injection pressure gradually increases to 350 psi and is almost maintained that level as the the hydraulic fracture propagates towards the south by crossing Fractures 9, 10 and 11. Note that the steep drops observed in injection pressure profile corresponds to the onset of propagation from natural fractures, whereas small disturbances observed are due to change of stresses on fracture elements as their status change between slip and stick.

11.3.4 Effect of fluid leak-off

To study the effect of fluid leak-off on fracture network outcome, the case of high in-situ stress contrast is repeated by including pressure dependent leak-off term in fluid flow equation. Using the input parameters given in Tables 11-1 and 11-2, and assuming the permeability of the matrix to be 0.5 md, the simulation results are shown in Figures (11-16)-(11-19). It is interesting to note that fluid leak-off has not affected the fracture network geometry considerably. Fracture apertures observed are slightly lower than the case with no leak-off due to continuous loss of pressure in fracture elements with the passage of time. Pressure loss in fracture elements due to leak-off has affected slippage (see Figure 11-17) of natural fractures, where slip is not observed on natural fractures 1, 7 and 10 (compare this with Figure 11-10) that were intersected by natural fractures. On the contrary, some unconnected natural fractures experience slip when fluid leak-off is included. From Figure 11-18, significant increase in pore pressure can be observed up to 40 ft from the surfaces of the connected fractures. The increases in pore pressure decreases the total (in-situ

plus induced) compressive normal stresses acting on natural fractures and causes slip. Finally, the net injection pressure profile with fluid leak-off (Figure 11-20) shows similar behavior to the case of no leak-off (Figure 11-14). The injection pressure drops over 200 psi during the propagation of Fracture 8 at around 10 min. Later, the injection pressure gradually increases and stabilizes at a value of about 300 psi as the hydraulic fracture continues to propagate towards the south by crossing Fractures 9, 10 and 11, similar to the case of no leak-off. Note that when fluid leak-off is included, steep drops in injection pressure also indicate hydraulic fracture tip contact with natural fracture (which enhances fluid leak-off) apart from initiation of propagation from natural fractures.

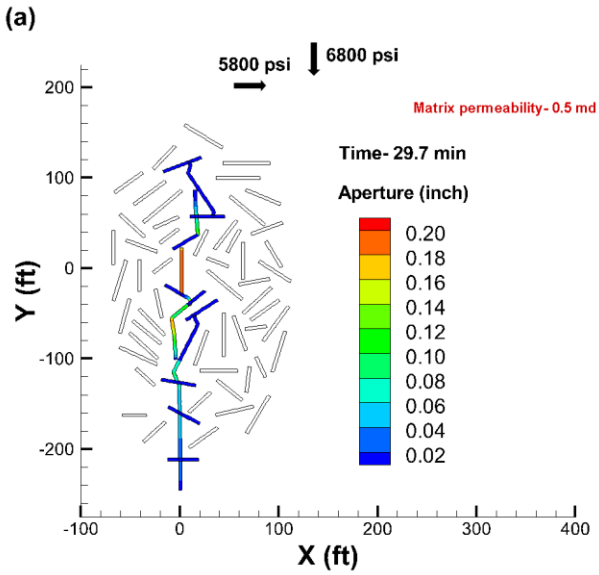

Figure 0-31. Aperture distribution in complex fracture network with in-situ horizontal stress anisotropy of 1000 psi. Initial fracture network is shown in Figure 11-5a. Matrix permeability is 0.5 md.

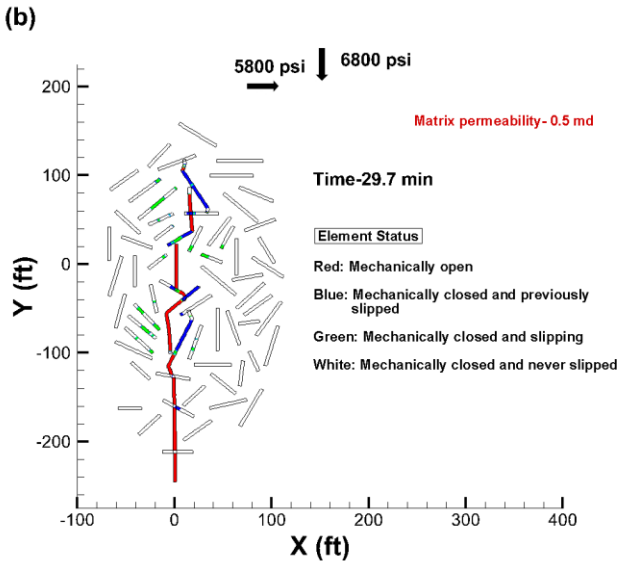

Figure 0-32. Element status in complex fracture network with in-situ horizontal stress anisotropy of 1000 psi. Initial fracture network is shown in Figure 11-5a. Matrix permeability is 0.5 md.

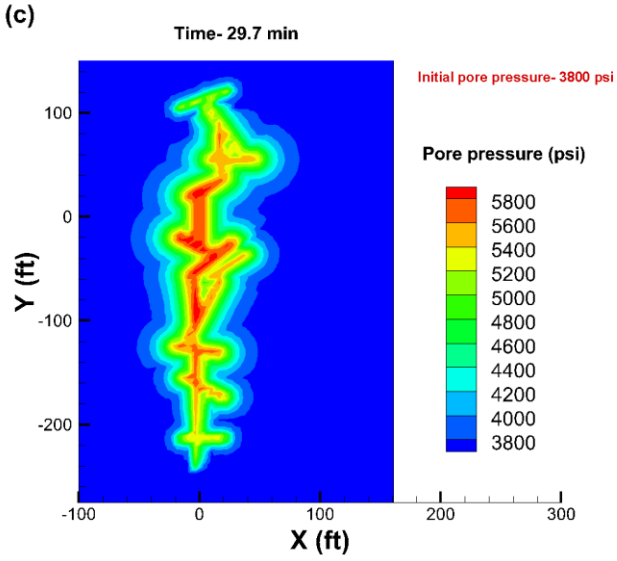

Figure 0-33. Pore pressure distribution in complex fracture network generation with in-situ horizontal stress anisotropy of 1000 psi. Initial fracture network is shown in Figure 11-5a. Matrix permeability is 0.5 md.

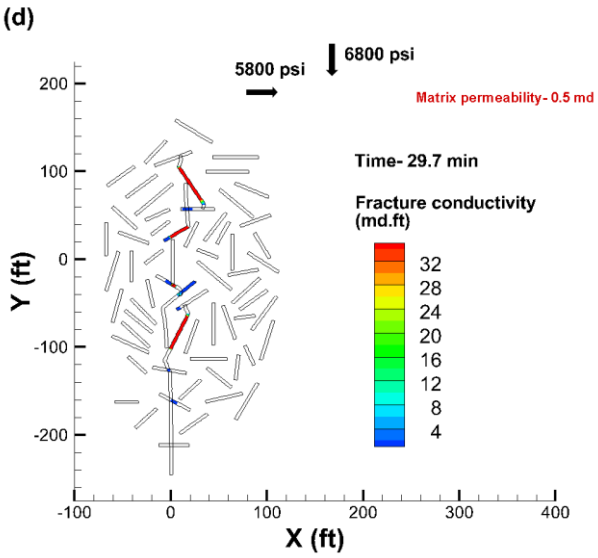

Figure 0-34. Fracture conductivities in complex fracture network generation with in-situ horizontal stress anisotropy of 1000 psi. Initial fracture network is shown in Figure 11-5a. Matrix permeability is 0.5 md.

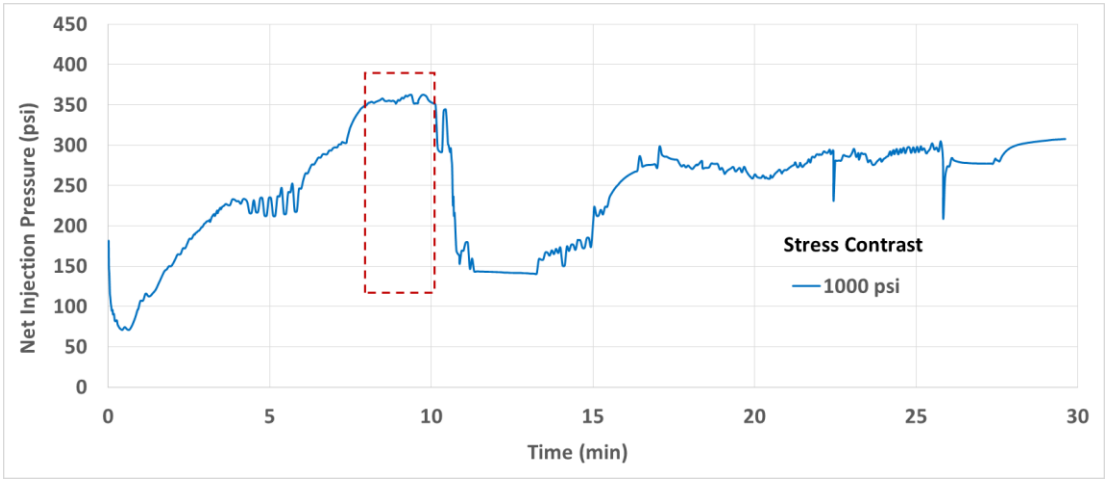

Figure 0-35. Comparison of net injection pressures at wellbore for network 11-5a for high and low in-situ stress contrast cases. Matrix permeability is 0.5 md.

11.3.5 Network-2

In this example we consider a randomly generated network of natural fractures as shown in Figure 11-5b. The natural fractures indicated by thick blue lines vary from 30-60 ft. in length. The height of all natural fractures is fixed at 100 ft. along the Z-axis. Two perforations of initial size 3 ft. and spacing 30 ft. are located along the line Y=0 at X=0 ft. and 30 ft. (note that the wellbore included in the Figure 11-5b is for illustration purpose only. It does not interact with fractures mechanically). Since isolated natural fractures do not enter the system of Eqs. (11.1-11.6), their slip is found by evaluating the stresses on them at every time step and applying the Mohr-Coulomb criterion. The effects of perforation and wellbore friction on fluid flow partition into each cluster is ignored in this paper. Therefore, the location of the fluid source along the wellbore does not impact the flow rate division into each cluster which is obtained as a part of the solution. Water is injected at a constant rate of 20 bpm into both clusters simultaneously until hydraulic fractures go beyond the boundaries of the natural fracture zone. Other input parameters used in simulator are given in Tables 11-1& 11-2. Assuming all natural fractures are initially mechanically closed with zero pore pressure, and neglecting leak-off and related pore pressure changes, the effect of far-field horizontal stress contrast on complex fracture network evolution is studied.

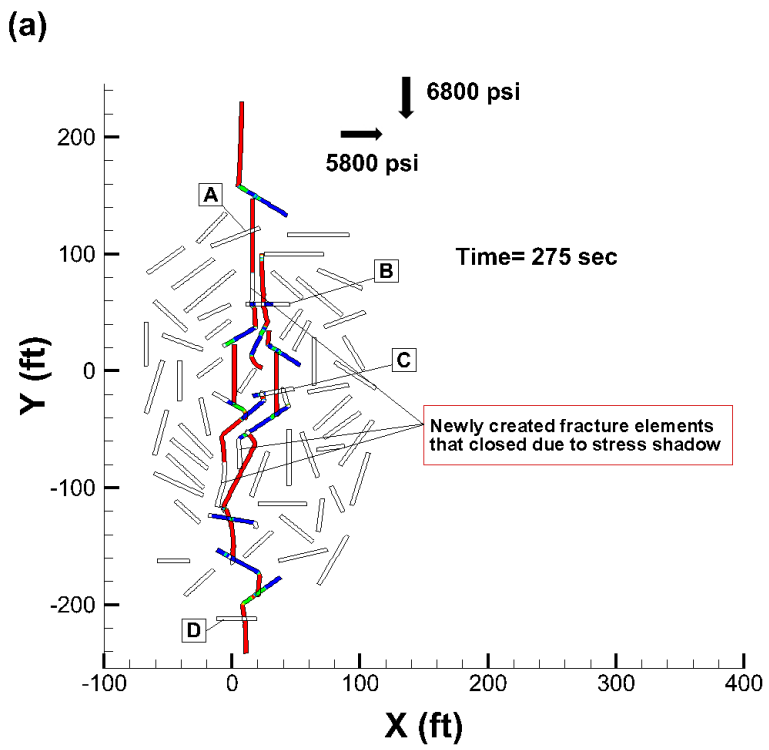

Figure 0-36. Element status in complex fracture network with in-situ horizontal stress anisotropy of 1000 psi. Initial fracture network is shown in Figure 11-5b.

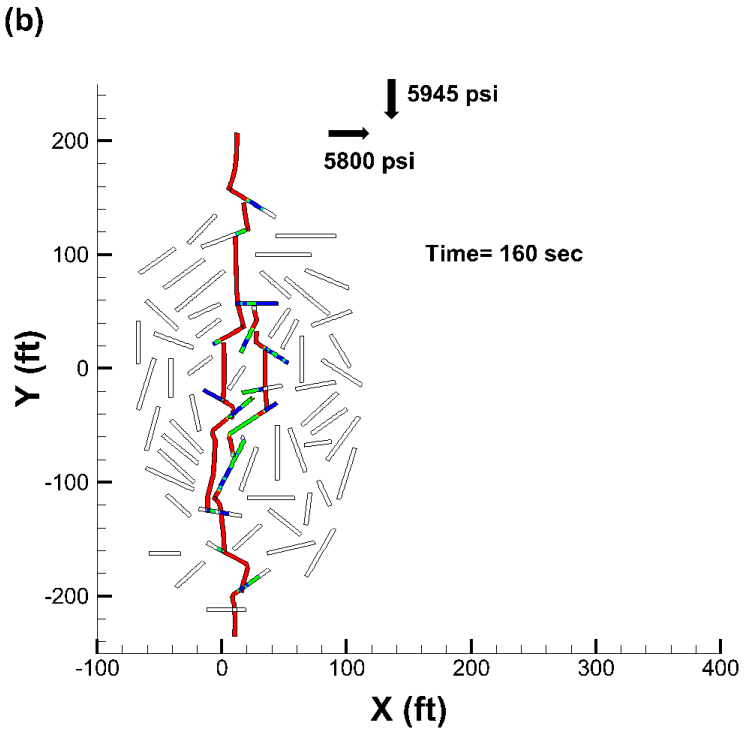

Figure 0-37. Element status in complex fracture network with in-situ horizontal stress anisotropy of 145 psi. Initial fracture network is shown in Figure 11-5b.

Figures 11-21& 11-22 show fracture networks obtained under high (1000 psi) and low (145 psi) in-situ stress contrast situations. In both cases hydraulic fractures from the two perforation clusters ultimately merged to form a single fracture propagating towards N-S (i.e., in the direction of maximum in-situ stress). When the in-situ stress contrast is low, the natural fractures have extended only from one of their tips. Whereas, under the condition of high in-situ stress contrast some natural fractures have experienced bi-wing propagation (i.e., fracture propagation occurred from both tips of natural fractures). This is due to higher shear stresses acting on the inclined natural fractures in this case causing sufficient slip to initiate natural fracture propagation from both tips. The indication is that in some cases a higher complexity may result under a high stress contrast in disagreement with conventional wisdom. Figures 11-21& 11-22 show several natural fracture elements are transitioning between slip and stick state. This can be mainly attributed to

pressure and stress changes in the network especially during natural fracture wings re-orientation. It can also be seen that natural fractures that are not favorably oriented (such as A, B, C, and D from Figure 11-21) and natural fracture segments under low inclination angle never opened or even slipped. Few fractures have experienced slip on their low angle sections, however, this is limited to very small magnitudes even when in-situ stress contrast is low according to Figures 11-23& 11-23. This is due to the effect of induced compressive normal stresses acting directly on the natural fracture surfaces that are at low angle. Stress redistribution around the fracture network did not cause slip along the isolated natural fractures (i.e., natural fractures that are not connected to main hydraulic fracture) in both cases (this is not the case, however, in the presence of pore pressure and leak-off as shown previously).

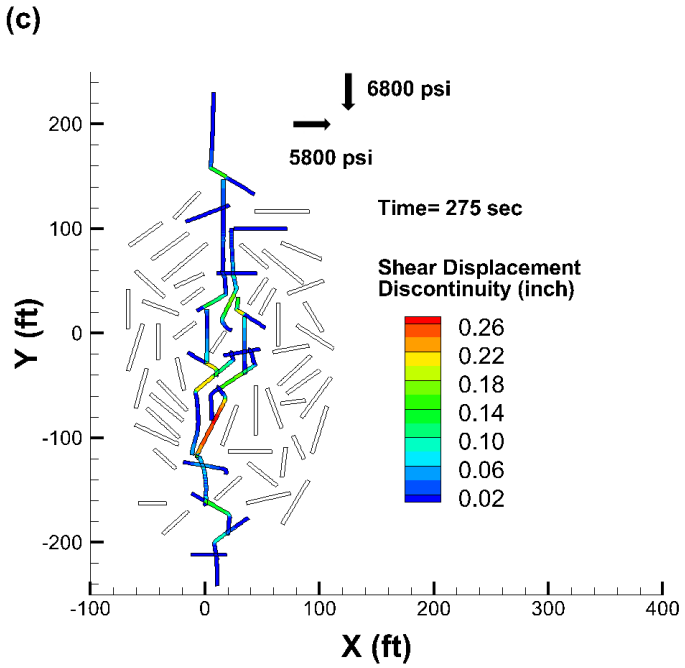

Figure 0-38. Shear displacement discontinuities for stress contrast of 1000 psi.

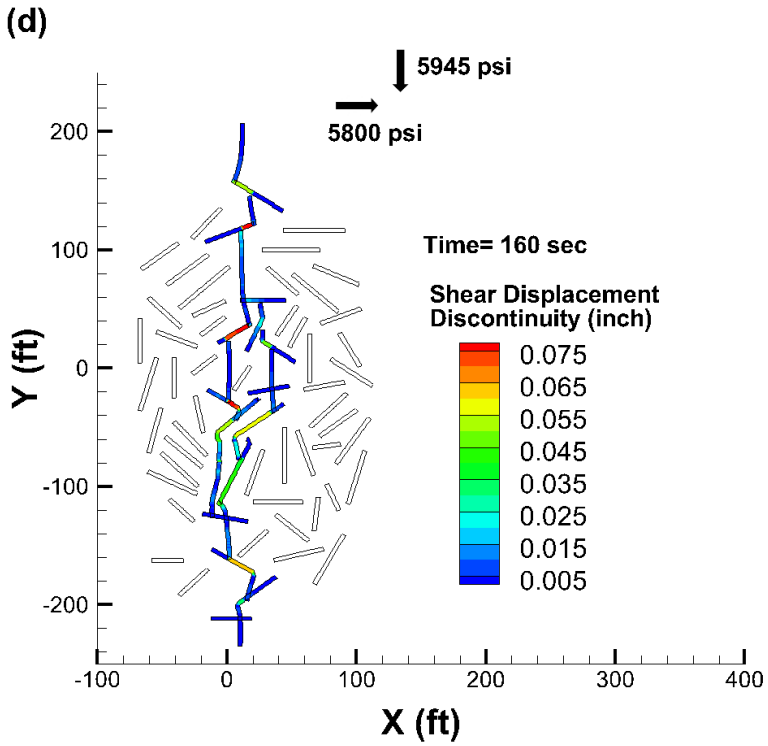

Figure 0-39. Shear displacement discontinuities for stress contrast of 145 psi.

Cumulative shear DD from Figure 11-23 &11-24 indicates almost threefold increase in shear DD magnitude along the inclined surfaces of natural fractures in the case of high in-situ stress contrast (1000 psi) compared to the case of low in-situ stress contrast (145 psi). Natural fractures that are almost perpendicular to the maximum in-situ stress and the natural fracture segments that are at low angle have experienced little to no shear deformation. Aperture profile from Figures 11-25& 11-26 indicate extreme variation along the network with sharp drops near the locations of fracture arrest in both cases. Higher magnitude of fracture apertures are observed in the network with high in-situ stress contrast. This can be attributed to higher net pressures of over 300 psi generated inside fractures in the network with high in-situ stress contrast compared with low in-situ stress contrast from Figures 11-27& 11-28.

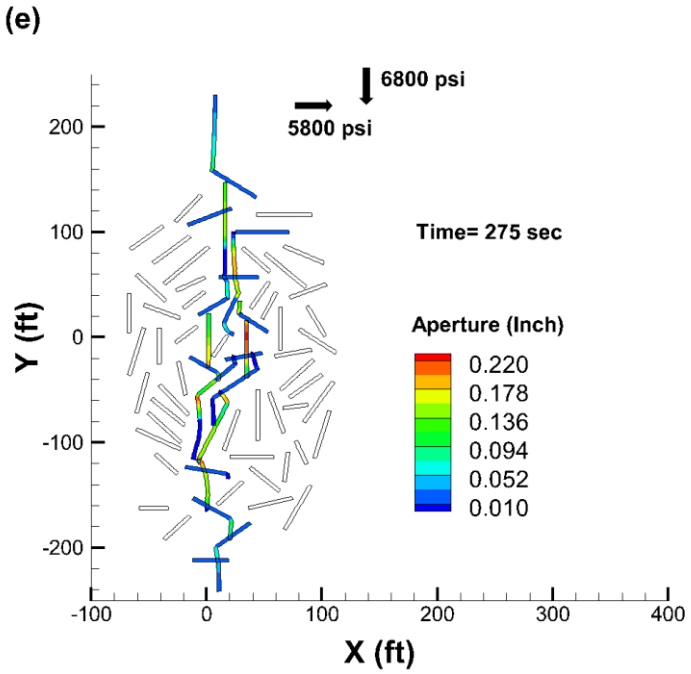

Figure 0-40. Aperture distribution for stress contrast of 1000 psi.

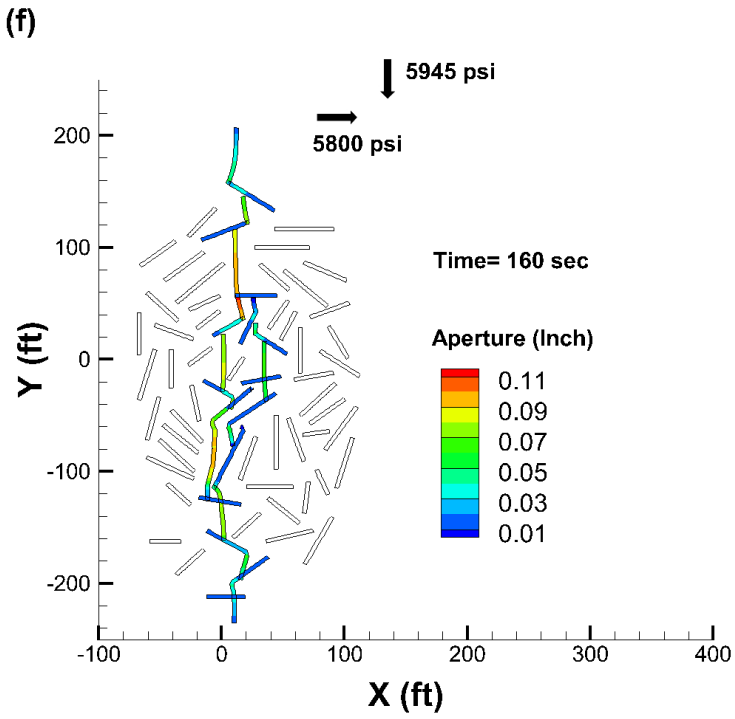

Figure 0-41. Aperture distribution for stress contrast of 145 psi.

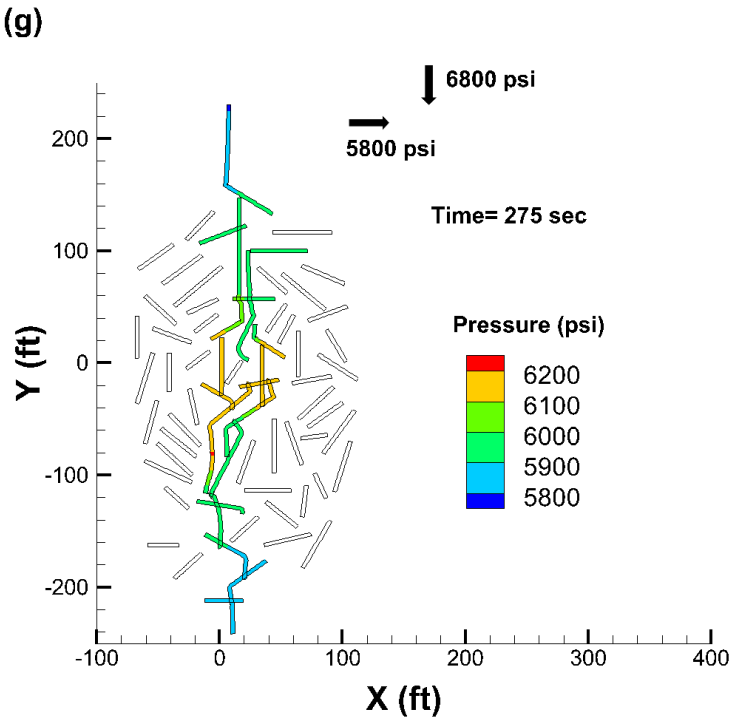

Figure 0-42. Pressure distribution for stress contrast of 1000 psi.

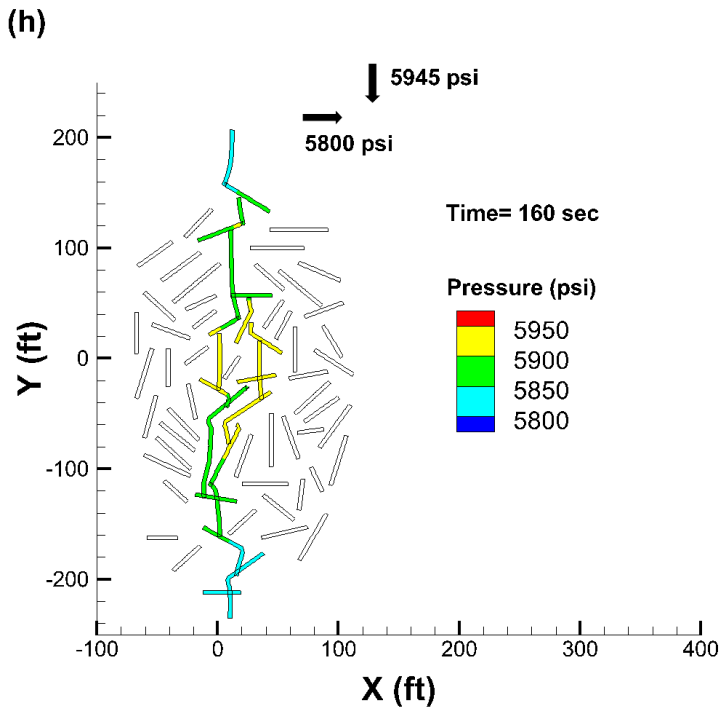

Figure 0-43. Pressure distribution for stress contrast of 145 psi.

While high angle sections of natural fractures experienced slip, most of them are under mechanically closed state in the case of high in-situ stress contrast. Also, some fracture elements that are created during propagation also experienced closure due to stress shadow effect as indicated in Figure 11-21. In these sections the fluid has to flow through the narrow hydraulic apertures assigned to them. On the other hand, high angle sections of natural fractures are mechanically opened when in-situ stress contrast is low, suggesting that the net pressures generated inside the fractures are sufficient to keep them open in this case.

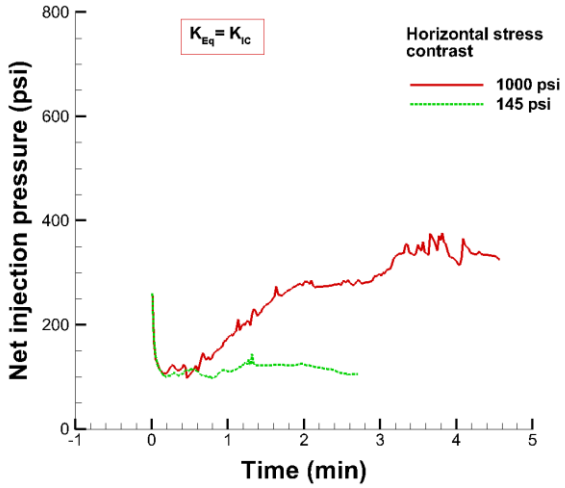

Figure 0-44. Comparison of net injection pressure at wellbore for high and low stress contrast cases.

Figure 11-29 shows a comparison of the net injection pressure obtained for the networks with low and high in-situ stress contrast. Injection pressure is characterized by initial decreasing trend in both cases similar to previous examples. Once the hydraulic fractures hit natural fractures, there is a pressure rise in the case of high in-situ stress contrast while the pressure profile for the low in-situ stress contrast remains nearly stable with few peaks which are due to the change in pressure requirements during fracture propagation and stress redistribution on fracture elements. The Injection pressure peaks appears to diminish with reduction in in-situ stress contrast. Under high

in-situ stress contrast, the net injection pressure gradually increases before stabilizing around 350 psi. Higher net injection pressures are necessary in this case to compensate for higher pressure losses in narrow sections of the mechanically closed natural fractures. On the other hand the net injection pressures does not rise substantially in the case of the low in-situ stress contrast (as in this case high angle natural fracture segments are opened mechanically) and stabilized around 100 psi.

11.4 Summary

Results obtained from a numerical model based on 2D DDM and LEFM indicate potentially complex behavior of hydraulic fractures in the presence of pre-existing natural fractures. Detailed analysis of the example of a hydraulic fracture propagating in between two natural fractures inclined to the in-situ stress served to illustrate the fundamental mechanisms involved in HF/NF interaction using a crossing criterion based on the stress field ahead of hydraulic fracture tip approaching a natural fracture.

Analysis of the stress distribution around the resulting simple fracture network has revealed the effect of induced stresses on the evolving network. Induced compressive stress (σ_{YY}) in the direction parallel to the hydraulic fracture surface due to its opening acts directly on the low angle sections of natural fractures restricting their propagation and in some cases even their ability to slip. On the other hand, induced tensile stress along the high angle sections of natural fractures facilitates slippage even at low pressures. Induced stresses around the fracture network do not cause slippage on isolated natural fractures that are not within the zone of influence of the induced stresses. For a network under high in-situ stress contrast, most natural fractures remain mechanically closed restricting flow only through the residual aperture. In the case of low in-situ stress contrast, most sections of natural fractures that are at high angle are opened. In both the low

and high stress contrast scenarios, fracture apertures show a high degree of variability along the network with the lowest aperture observed along low angle sections of the natural fractures and at fracture arrest sites. Severe restriction of the fracture opening along these segments can create difficulties for proppant transport. The numerical analysis presented in this paper captures the fundamental physics of HF/NF interaction by rigorous modeling of the natural fracture constitutive behavior and fracture mechanics involved in hydraulic fracturing. Yet, the model is relatively efficient in simulating large scale multi-cluster cases. It is a useful tool for not only gaining insights in the role of in-situ stress contrast and induced stresses on evolution of fracture networks but also for optimizing cluster spacing, and for better interpretation of micro-seismic signals. A key assumption made in this work is that the rock is isotropic. HF/NF interactions in anisotropic rock is and will be the subject of a future work.

12 Numerical Analysis of Fracture Swarms Observed in Field Studies

Coring adjacent to a hydraulically fractured horizontal well in Eagle Ford shale by Conoco-Phillips has revealed several closely spaced parallel hydraulic fractures (separated only by few inches) propagating in the direction perpendicular to the wellbore axis. The number of observed hydraulic fractures greatly exceed the number of clusters according to the recent paper titled "Sampling a Stimulated Rock Volume: An Eagle Ford Example". The observed behavior is contrary to the conventional practice of hydraulic fracture modeling where often a single fracture from each perforation cluster.

Hydraulic fractures segmentation can occur due to its interaction with bedding planes, natural fractures and faults. Field observations (Pollard et al., 1982; Baer, 1991) show vertical segmentation of hydraulic fracture at the bedding interfaces as the fracture grows in height. The resultant fracture is an echelon type fracture rather than a single continuous one. Similarly, presence of natural fractures can cause fracture offsets after hydraulic fracture intersection (Anderson, 1981; Warpinski and Teufel, 1987), which can lead to segmentation of hydraulic fracture as it grows laterally. Moreover, secondary fractures can initiate from weak flaws along the natural fractures if the injection pressure is sufficiently high (Zhang and Jeffrey, 2006). Other significant factors that contribute to multi-stranded hydraulic fracture propagation are rock heterogeneity (in both elastic and strength properties) (Stadulis, 1995), spatial variation of in-situ stress (Weijers et al., 2000) and mode-3 fracture splitting (Wu and Germanovich, 2009). Note that the results from Eagle ford field test indicates sparse distribution of natural fractures, suggesting that the complexity of hydraulic fracture propagation cannot be attributed to the the presence of natural fractures alone.

With mounting evidence gathered from hydraulic fracturing field tests from different sites, the single planar fracture models show to be less reliable for unconventional stimulation design. Presence of fracture swarms affect all aspects of hydraulic fracture design such as treatment pressures, fracture widths, and length and proppant distribution (Ciezobka et al., 2018). Therefore, it is imperative to understand the behavior of closely spaced multi-strand fracture propagation. In this chapter, the implications of fractures propagating as dense parallel strands (without considering the mechanisms of fracture branching) is discussed. For this, a 2D displacement discontinuity based hydraulic fracture propagation model is used to simulate fracture propagation from individual perforations in a single cluster near the wellbore. Factors (in-situ horizontal stress contrast, fracture toughness of medium, and perforation properties) affecting near wellbore fracture connectivity and fracture lateral growth are discussed. The effect of extremely small spacing between the fractures on fracture widths, injection pressure, net pressure inside the fractures and the ability of the fractures to grow overcoming stress shadow effect is studied. The results of multi-stranded fractures are compared with the results obtained using single planar fracture to highlight the differences. Although the analysis is performed for multiple fractures emanating from a cluster of perforations near the wellbore, these results in general should be applicable to fracture strands observed at far-field (see Figure 12-1) in understanding the effects of close spacing on fracture widths and net pressures. Fracture non-planarity, coalescence, coupling between fracture deformation/fluid flow and perforation friction, near tip processes are considered in great detail.

12.1 Model Description

Fracture deformation is modeled using 2D displacement discontinuity method (DDM). It is assumed that all fracture have constant height and the effect of finite fracture height on DDM solution is accounted using a 3D correction factor. Fluid flow inside fractures are approximated using lubrication equation neglecting fluid leak-off. Finally it is imperative to consider the role of perforation friction pressure drop on fracture propagation as high perforation pressure drop keeps the wellbore pressure high enough to initiate and force multiple fractures to propagate. The perforation friction drop is calculated using Eq. 10.28. Fracture propagation is approximated in small time steps, where at every time step, the fracture deformation equation, fluid flow equation, perforation friction and mass balance are solved simultaneously.

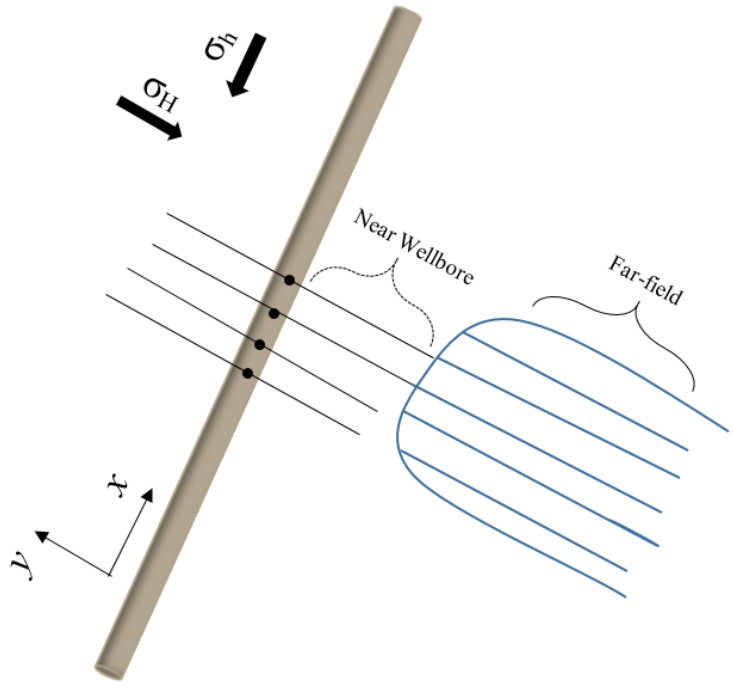

Figure 0-45. Fractures emanating from a cluster of perforations phased at 180^0 near the wellbore. Fracture segmentation far from wellbore causing fracture strands. Artwork re-created from (Weijers et al., 2000).

12.2 Numerical Experiment Setup

For numerical simulations, a horizontal wellbore with 20 perforations over an interval of 5 ft with 180^0 phasing is considered. Figure 12-1 shows placement of perforations on the wellbore and hydraulic fractures emanating from them. We assume 10 bi-wing fractures from 20 perforations in a cluster. For modeling purposes, small initial fractures of size 0.15 ft from each perforation on both sides of the wellbore are placed in the direction of maximum in-situ horizontal principal stress. Although fracture propagation near a wellbore can be affected by wellbore deformation (see chapter 7), in this study, the wellbore effect is ignored assuming that fractures quickly grow out from the zone of wellbore influence. The input parameters used in numerical simulations are listed in Table 12-1. The elastic properties (Young's modulus and Poisson's ratio) given are averaged values from static measurements (Jansen, 2014) for Eagle Ford shale. All fractures have a fixed height of 30 ft. For sensitivity analysis, some input parameters are modified in the later sections. For all the examples, the injection fluid is water (1 cP) and injection rate is 20 bpm. In the DD model, fractures are discretized into very fine line elements of size 0.06 ft, therefore requires about 17 elements to simulate fracture of size 1 ft and increases the computational time considerably, nevertheless it is required to capture the non-planar fracture growth accurately. Moreover, selecting elements that are larger than the spacing between the fractures induces high numerical errors in the solution.

Table 0-6. Input parameters used in numerical model.

Parameter	Value	Units
Minimum principal horizontal stress (σ_h)	5655	psi
Young's modulus	4.0	Mpsi
Poisson's ratio	0.27	
Hydraulic/Natural fracture height (all examples)	30	ft
Injection fluid viscosity (all examples)	1	cP
Injection rate (all examples)	20	bpm
Perforation diameter	0.4	inch
Coefficient of discharge	0.45	

12.3 Results

12.3.1 Effect of in-situ horizontal stress contrast

Figure 12-2 shows fracture geometry and aperture distribution for three different horizontal in-situ stress contrast conditions at the end of fluid injection (note that a common scale is not used due large variation observed in results between different cases). The fractures are numbered for identification. For low stress contrast value of 145 psi, of the 10 fractures, 3 factures on the left side (Frac-2, 3& 4) and 3 fractures on the right side (Frac-7, 8& 9) curved away from the center fractures (Frac-5& 6) connected at a distance about 2 ft from the wellbore to form single fractures.

The two center fractures appear to grow parallel to maximum principal stress without coalescing. Widths at fracture inlets are maximum for center fractures and lowest for outermost fractures (see Figure 12-3a; note that due to problem symmetry, result for only 5 fractures are displayed). The lower opening of outer fractures can be attributed to induced compressive stresses on the midsections of the fractures due to curving. We can also notice that near the location of fracture intersections, widths are greatly reduced.

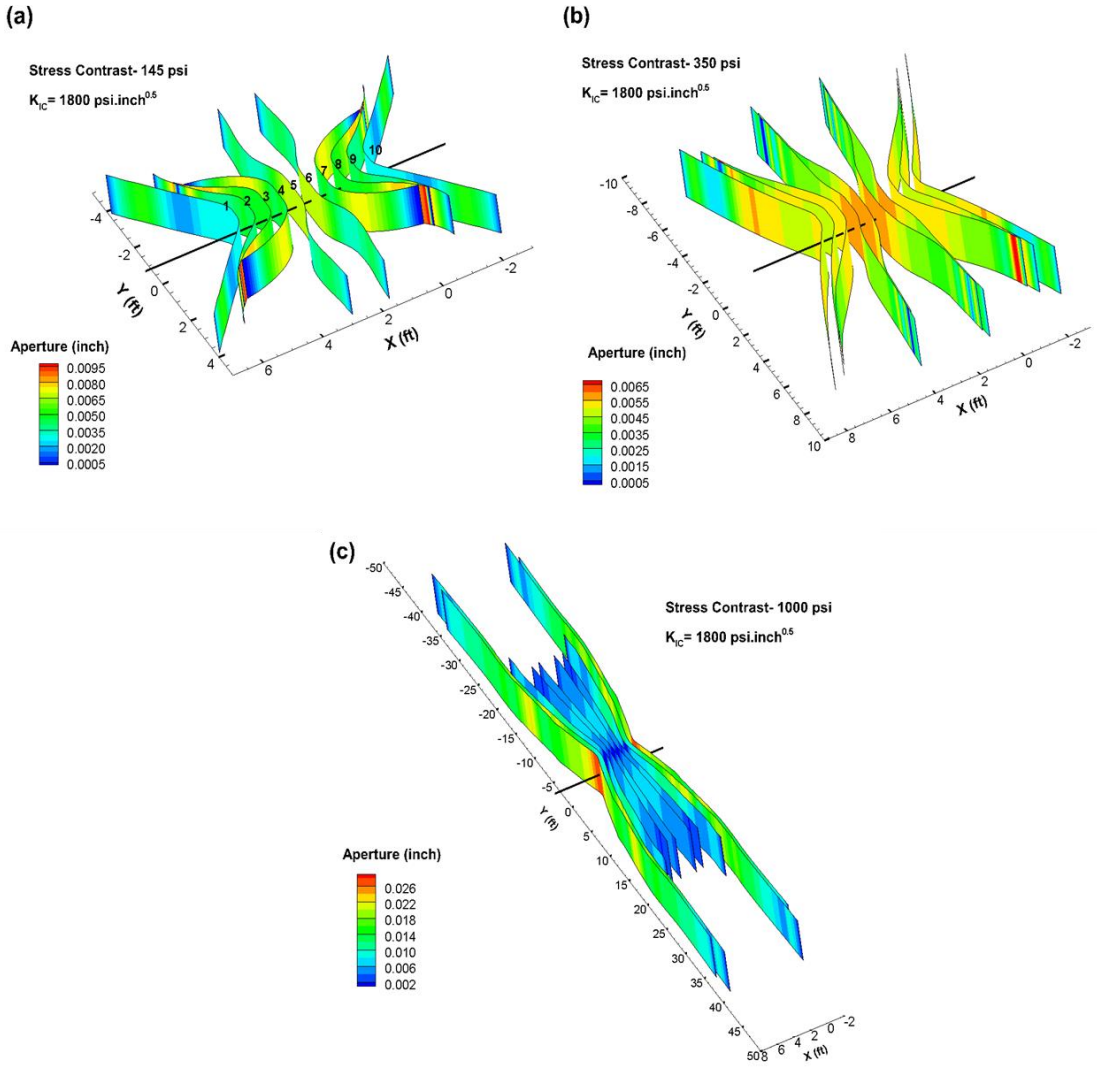

Figure 0-46. Fractures emanating from individual perforations from wellbore and their apertures for in-situ horizontal stress contrast of (a) 145 psi, (b) 350 psi and (c) 1000 psi. Fracture toughness, K_{IC} is 1800 psi.inch$^{0.5}$.

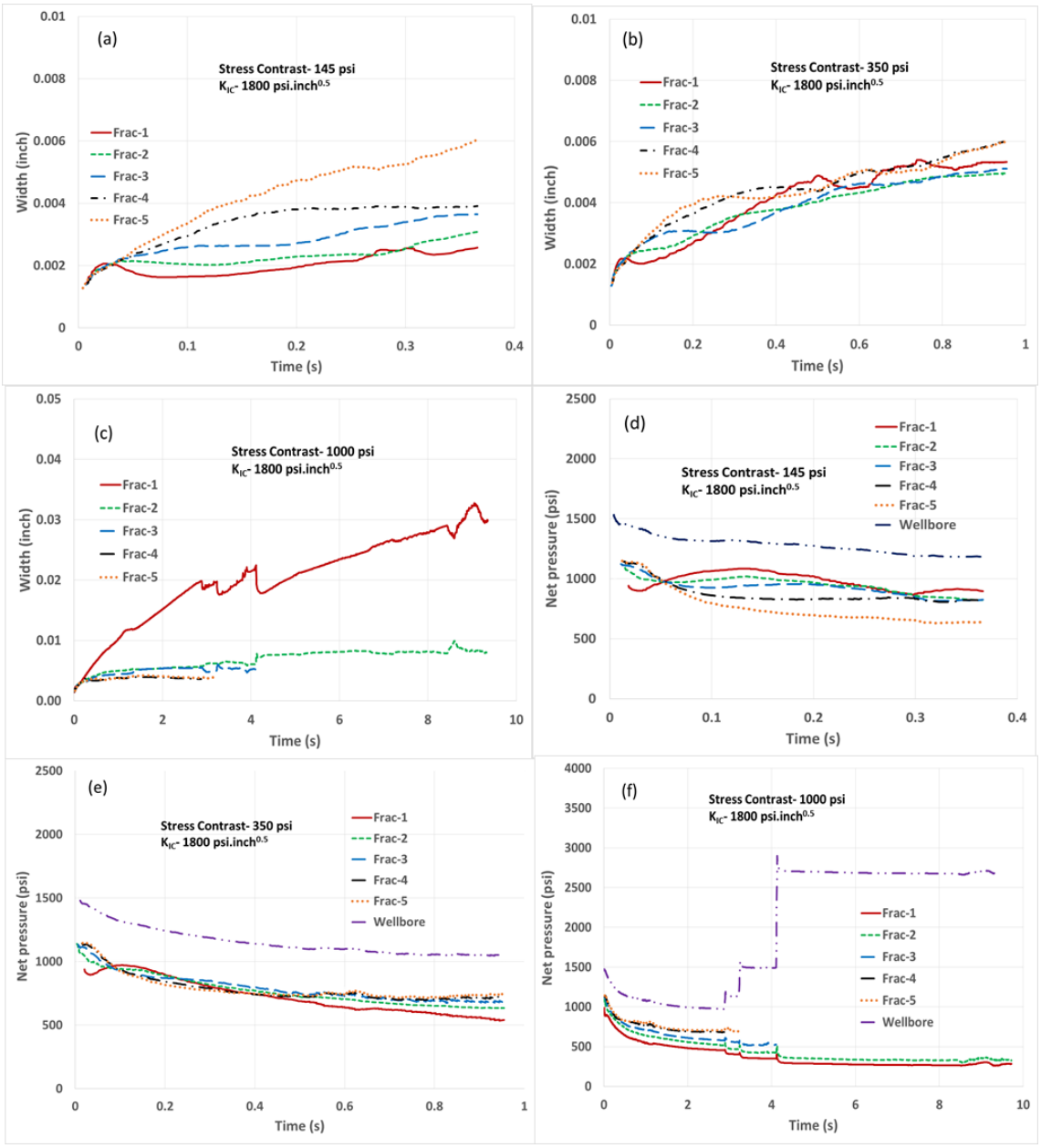

Figure 0-47. Width at the inlet of each fracture as a function of time for in-situ horizontal stress contrast of (a) 145 psi, (b), 350 psi and (c) 1000 psi, (d) net pressure at fracture inlet and wellbore as a function of time for in-situ horizontal stress contrast of 145 psi, (e) 350 psi, (d) 1000 psi. Fracture toughness, K_{IC} is 1800 psi.inch$^{0.5}$. Note that due to problem symmetry results for only 5 fractures are displayed.

For moderate stress contrast value of 350 psi, fractures appear to grow farther from wellbore before coalescence occurred (Figure 12-2b). Of the 10 fractures, the 8 inner fractures connected with

other fractures to form 4 fractures about 4 ft from the wellbore. Further coalescence among fractures is not observed. The inner most coalesced fractures appear to grow parallel to maximum principal stress. Similar to the case of low stress contrast, here widths at fracture inlets are maximum for center fractures (see Figure 12-3b) as the outer fractures curve away.

For the case of high stress contrast of 1000 psi, fracture connection near the wellbore is not observed (Figure 12-2c). As indicated before, the fracture height is 30 ft and spacing between adjacent fractures is 0.5 ft. This gives spacing ratio, *x*/H (*x* is spacing between fractures and H is fracture height) of 0.016, which is very small compared to the spacing ratio's used in conventional fracture models that range from 0.1-1. For the small spacing ratio considered, the inner fractures were able to achieve fracture half-lengths up to 20 ft before they terminated. Of the 10 fractures, only 4 fractures extended beyond 20 ft from the wellbore and continue to grow as doublets on both sides of the cluster. Even though the inner fractures (Frac-3 to Frac-8) achieved lengths up to 40 ft, their widths are extremely low (only about 0.005 inch) throughout the injection period (see Figure 12-3c). Although the aperture distribution is very uniform (according to Figure 12-2c) along the lengths of 4 dominant outer fractures (Frac-1, 2, 9& 10), at the fracture inlet, apertures are highest for the end fractures (i.e. Frac-1& 10) which is about 0.03 inch (see Figure 12-3c). At the inlet of inner fractures (Frac-2& 9), apertures are only about 0.008 inch.

Figures (12-3d)-(12-3f) show net pressure (pressure above minimum horizontal stress) at wellbore and fracture inlets as a function of time. The difference between wellbore pressure and fracture inlet pressure is pressure drop due to perforation friction. The results indicate significantly high net pressures inside simultaneously propagating multiple fractures (later we will compare these results with single fracture model). The magnitude of net pressures appear to be greatest for innermost fractures when fractures are propagating parallel to maximum stress according to Figure

12-3f for the case of high stress contrast of 1000 psi. This is due to very low widths observed for inner fractures (Figure 12-3c) which increases the resistance for fluid flow inside them. The peaks observed in net pressure plot (Figure 12-3f) in the period 3 to 4 sec corresponds to termination of fractures due to stress shadow effect. The termination of each fracture increases the available injection fluid for other fractures and also perforation friction which is reflected in the injection pressure rise. Note that in practice, the rise in injection pressure might re-open the closed fracture, however, this effect is not considered in the numerical model for simplicity. Based on Figure 12-3f, the order of fracture closure is Frac-4& 7; Frac-5& 6; Frac-3& 8. The results also indicate that the magnitude of the net pressure inside fracture is a strong function of the number of fractures propagating at a given time. As the inner fractures close, the net pressure inside outer fractures tend to drop. After the closure of 6 inner fractures (i.e. Frac-3 to Frac-8), the net pressure inside outer fractures dropped to about 370 psi and stabilized (Figure 12-3f).

12.3.2 Effect of fracture toughness

Figure 12-4 shows fracture geometries and aperture distribution obtained at the end of fluid injection for 3 different values for in-situ horizontal stress contrast when the fracture toughness of rock is reduced by 4 times (K_{IC}=450 psi.inch$^{0.5}$) compared to previous example (K_{IC}=1800 psi.inch$^{0.5}$). The other input parameters can be found in Table 12-1. In this case, connection between the fractures is not observed even for low stress contrast value of 145 psi (Figure 12-4a). The fractures appear to curve away from each other due to stress shadow effect, however, the degree of fracture curving depends on magnitude of stress contrast. For the case of stress contrast of 145 psi, aperture at the fracture inlet is greatest for innermost fractures (Frac-4, 5, 6& 7) similar to previous example (Figure 12-5a). For high (1000 psi) and moderate (350 psi) stress contrast values, highest opening at fracture inlet is observed for outer fractures as in these cases fracture

curving is not significant. Moreover, the lateral growth of inner fractures is significantly improved compared to the previous example (compare Figure 12-3c and 12-4c). For stress contrast of 1000 psi, the 6 inner fractures (Frac-3 to Frac-8) achieved about 70 ft length before they terminated, and similar to the previous example, the 4 outer fractures (Frac-1, 2, 9, & 10) propagate as doublets on both sides of the cluster after the termination of inner fractures. Aperture distribution at fracture inlet show that about 60 percent of the fracture opening is accounted by the end members (Frac-1& 10), while the rest of the fractures contribute only 40 percent of fracture opening at the inlet by the end of injection in case where stress contrast is 1000 psi (see Figure 12-5c).

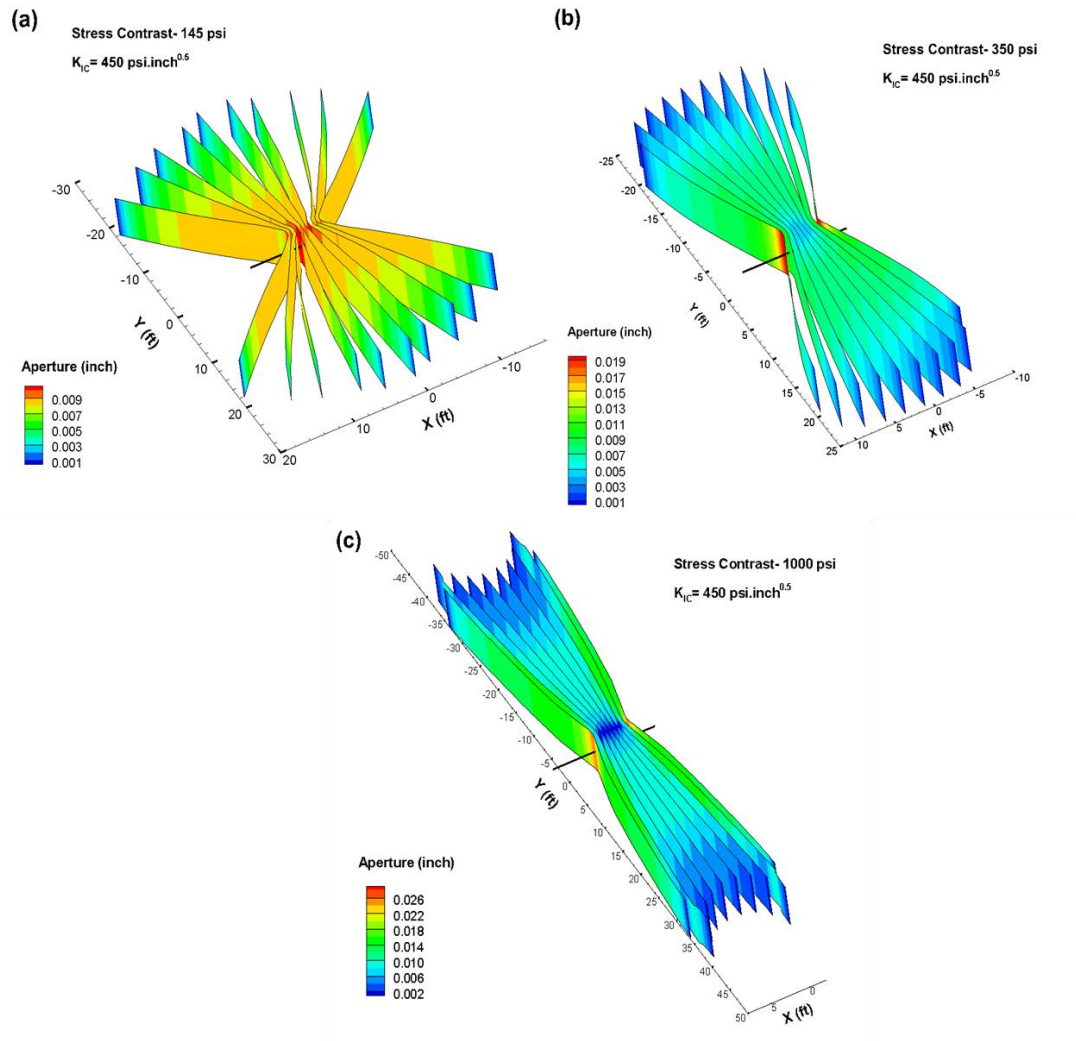

Figure 0-48. Fractures emanating from individual perforations from wellbore and their apertures for in-situ horizontal stress contrast of (a) 145 psi, (b) 350 psi and (c) 1000 psi. Fracture toughness, K_{IC} is 450 psi.inch$^{0.5}$.

The lack of connection between the fractures in this example is due to decrease in the extent of the region influenced by induced stresses at fracture tips. According to LEFM, the induced stress ($\Delta\sigma$) at a fracture tip due to mode-1 stress intensity factor is given by (see also Nolte, 1993)

$$\Delta\sigma = \frac{K_{IC}}{\sqrt{2\pi r}} \qquad (12.1)$$

Where *r* is distance from fracture tip. Eq. 12.1 shows direct proportionality between tip stresses and fracture toughness of the rock. As a result, when fracture toughness of the rock is reduced, the interaction between fracture tips is also reduced as observed in this example of closely spaced multiple fractures (Figure 12-4). On the other hand, the compressive stresses induced near the mid-sections of fractures pushed the fracture away causing them to curve.

We also observed that decrease in rock's fracture toughness improved growth of inner fractures. According to LEFM, fracture widths very near the tips can be expressed as

$$w(x)_{tip} \approx \frac{4K_{IC}(1-\nu^2)\sqrt{2x}}{\sqrt{\pi}E} \tag{12.2}$$

The above equation indicates that lower fracture toughness of the rock allows propagation of thin fractures as seen from the results shown in Figure 12-4. Alternatively, one can argue that in rock with low fracture toughness, the energy required to create new surface area would be less (based on the relation between Griffith energy and fracture toughness), therefore for a given energy input, fractures with larger length can be created. Conversely, high fracture toughness rock results in wide and short fractures.

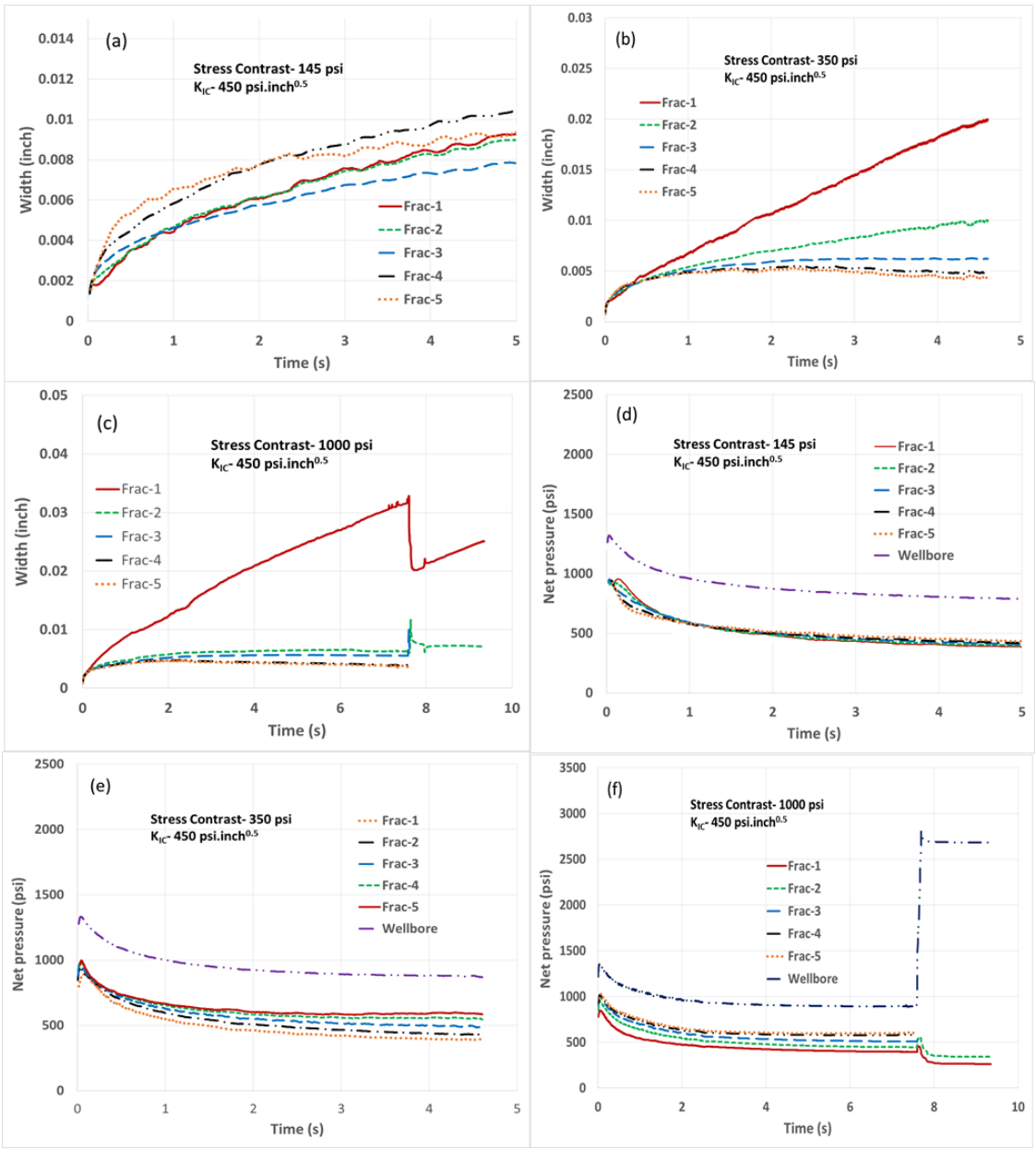

Figure 0-49. Width at the inlet of each fracture as a function of time for in-situ horizontal stress contrast of (a) 145 psi, (b), 350 psi and (c) 1000 psi, (d) net pressure at fracture inlet and wellbore as a function of time for in-situ horizontal stress contrast of 145 psi, (e) 350 psi, (d) 1000 psi. Fracture toughness, K_{IC} is 450 psi.inch$^{0.5}$. Note that due to problem symmetry results for only 5 fractures are displayed.

Figures (12-5d)-(12-5f) shows net pressure as a function of time at wellbore and fracture inlets for the 3 cases considered. Similar to previous example, we observe high net pressure inside the fractures. Net pressures appear to quickly drop from the initial peak and stabilizes as the fractures grow laterally. For the case of stress contrast of 1000 psi, maximum net pressures are observed at the inlet of innermost fractures (Frac-5& 6), where the value is about 600 psi. After 7 sec of injection, the inner fractures (Frac-3 to Frac-8) terminated almost at once, after which the net pressures inside outer fractures (Frac-1& 2; Frac-9& 10) dropped to about 260-350 psi and stabilized as they continue to grow.

12.4 Discussion

In this work propagation of closely spaced multiple hydraulic fractures with very small spacing ratio compared to those typically used in conventional fracture models is considered. Near wellbore fracture connectivity, fracture lateral growth, fracture widths and net pressures are investigated. The results indicate that propagation of closely spaced fractures (at the scale observed in recent field tests) is possible. The results do not indicate coalescence of near wellbore fractures to form a single dominant fracture as traditionally assumed in single fracture models. Moreover, fracture coalescence is suppressed by increase in far-field stress contrast and decrease in fracture toughness. In a rock with low fracture toughness, reduced interaction between the fracture tips prevented fracture coalescence even for case with low stress contrast. Also growth of inner fractures is enhanced in low fracture toughness rock. Aperture profile indicate that fracture opening at the inlet is mostly dominated by exterior fractures except for the case where stress contrast is very low. When fracture curving is negligible (as in the case of high stress contrast), the end fractures (Frac-1& 10) account for up to 60 percent of total widths at fracture inlets for the spacing considered in these examples. The effect of stress shadow suppressed opening of inner

fractures and eventually led to their termination. The results also indicate that fracture propagation under very tight spacing generate significant net pressures in the fractures to keep the fractures open overcoming the stress shadow effect. For the case of stress contrast of 1000 psi and K_{IC}=1800 psi.inch$^{0.5}$, it can be seen from Figure 12-3f that when 10 fractures propagate simultaneously, the net pressure inside the fractures vary from 700 psi in the centermost fractures (Frac-5& 6) to 500 psi in the outermost fractures (Frac-1& 10). A simple analytical expression that relates the net pressure (P_n) required to propagate multiple parallel fractures with the net pressure (P_s) required for single fracture is given as (Palmer and Veatch, 1990)

$$P_n \approx P_s\sqrt{n} \tag{12.4}$$

Where n is number of parallel propagating fractures. The above equation is obtained based on the assumption that all n fractures have equal widths and equal net pressure. The numerical results for net pressure for the case of high stress contrast of 1000 psi and K_{IC}=1800 psi.inch$^{0.5}$ from Figure 12-3f show an average net pressure (average of all 10 fractures) of about 600 psi at 2 sec into injection while 10 parallel fractures are propagating simultaneously. At 7 sec the number of propagating fractures are only 4 and the average net pressure is dropped to about 300 psi. The corresponding values for net pressures at these times obtained from a single fracture model (using the same input parameters) can be found in Figure 12-6a; they are 160 psi and 140 psi respectively. Now according to Eq. 12.3, using n as 10 and P_s as 160 psi, we get P_n as 500 psi which is somewhat close the prediction (600 psi) by numerical model for 10 fractures. For n=4 and P_s =140 psi, Eq. 12.3 predicts P_n as 280 psi which is consistent with result (300 psi) obtained from numerical model for multiple fractures. Similarly for the case of 1000 psi stress contrast and K_{IC}=450 psi.inch$^{0.5}$, we seen an average net pressure of 510 psi when 10 fractures are propagating simultaneously at 7 sec from Figure 12-5f. The corresponding value obtained from single fracture model is 150 psi.

Using n as 10 and P_s as 145 psi we obtained P_n as 475 psi, which is again close to the numerical result (510 psi). This analysis suggest that it might be possible to infer the number of parallel fractures propagating simultaneously based on net pressure data by comparing single fracture model predictions with field data. However, the pressure indicated at wellbore also include friction losses and in some cases their contribution could be far greater that the net pressure increase inside the fractures (see wellbore pressure in Figures 12-3f& 12-5f). This behavior has also been reported in field studies (Crump and Conway, 1988) where friction pressure losses (due to perforations or near wellbore tortuosity) account for significant increase in injection pressures. Therefore, misinterpreting friction losses as net pressure increase due to multiple fractures could lead to overestimation of number of fractures.

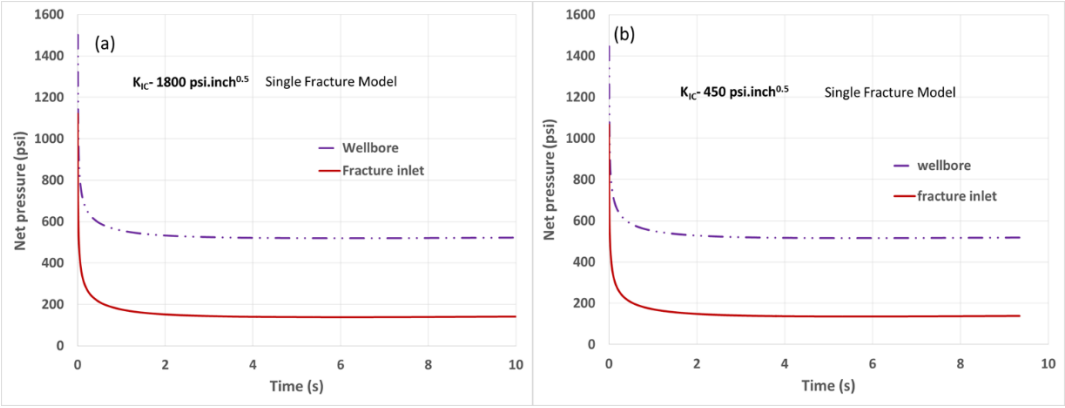

Figure 0-50. Net pressure at fracture inlet and wellbore obtained using single fracture model for (a) fracture toughness, K_{IC}= 1800 psi.inch$^{0.5}$, (b) 450 psi.inch$^{0.5}$. Other input parameters can be found in Table 1.

The numerical results indicate that higher injection pressure is needed for multiple closely spaced fractures to grow simultaneously by overcoming the negative effect of stress shadow. In these numerical simulations higher injection pressure at wellbore is achieved using perforation friction. If the injection pressure at wellbore and fluid pressure at fracture inlet are very close, the flow partition into each fracture will be primarily controlled by fracture opening at the inlet (which is

affected by stress shadow). The fractures with relatively higher opening will take the most fluid while leaving the remaining unstimulated. By elevating the wellbore pressure to a much higher value than fracture inlet pressures, fluid can be forced into the inner fractures with lower widths, therefore ensuring their growth. Figure 12-7 shows fracture geometry and apertures at the end of fluid injection for the case where perforation friction is reduced by increasing the diameter of perforations from 0.4 inch to 0.6 inch and coefficient of discharge from 0.45 to 0.9. The stress contrast for this example is 1000 psi and K_{IC} is 1800 psi.inch$^{0.5}$. The other input parameters can be found in Table 12-1. The results indicate growth of only 4 outer fractures (Frac-1, 2, 9& 10) while the rest terminated near the wellbore. In this case the effect of stress shadow on fracture propagation is prevalent causing the early termination of inner fractures due to lower injection pressure (in this case wellbore is kept at about only 100 psi above the fracture inlet pressures. For the cases with high friction losses, this value is almost 500 psi; compare Figures 12-3f, 12-5f and 12-7b) at wellbore as seen from the Figure 12-7b. Another important factor that can affect lateral growth of fractures is fracture height. In this study we assume a constant fracture height of 30 ft which results in spacing ratio of 0.015. For much higher fracture height the spacing ratio gets even smaller. As the induced normal stresses in the direction perpendicular to the fracture surface are inversely proportional to the spacing ratio (see Figure 3-4), very low values of spacing ratio can inhibit growth of inner fractures. On the other hand segmentation of fracture in vertical direction (which has been observed in field studies) increases the spacing ratio and can enhance propagation of inner fractures in a closely spaced fracture strand.

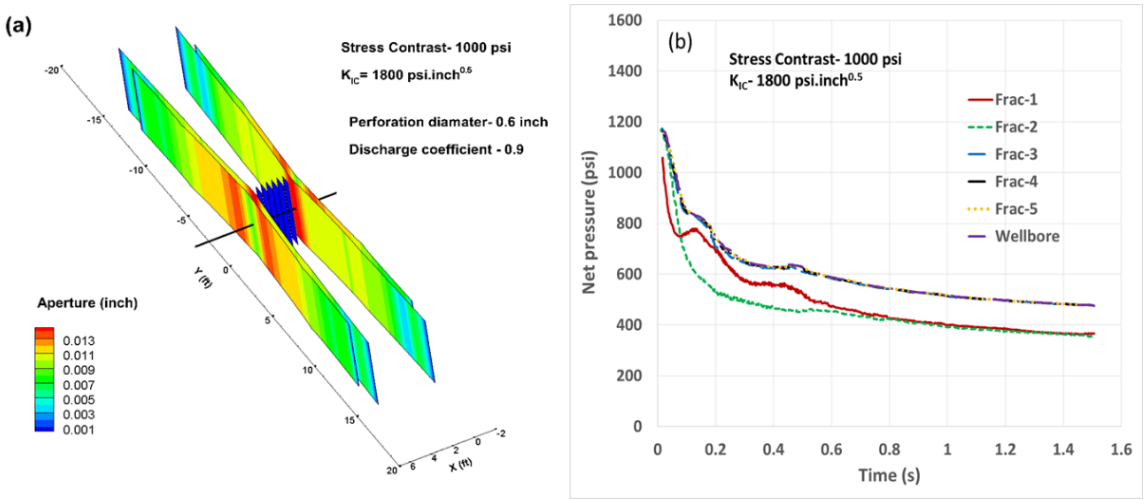

Figure 0-51. (a) Fracture geometry and apertures obtained using low perforation friction. Perforation diameter is 0.6 inch and discharge coefficient is 0.9, (b) the corresponding net pressure at fracture inlets and wellbore.

To understand the implications of treating a multiple fracture strand as a single fracture in numerical modeling for hydraulic fracture design analysis, we consider propagation of a single planar fracture with the input parameters given in Table 12-1. Figure 12-8 shows width at fracture inlet as a function of time for two different values of fracture toughness considered previously. The result from single fracture model (solid red line) is compared with the result from multiple fracture model (dashed green line), which indicates the sum of fracture widths at inlets for all the 10 fractures that are almost parallel (see Figures 12-3c& 12-5c) for the case of 1000 psi stress contrast. The step like decrease in the results of multiple fractures correspond to the closure of inner fractures. Results show that treating 10 parallel fractures as a single fracture grossly underestimates fracture widths (note that the error appears to decrease with closure of inner fractures). As discussed previously, propagation of multiple fractures result in net pressure increase inside the fractures. This increased injection pressure can be accounted in single fracture model by increasing the fracture toughness of the rock according to (Notle, 1993). Figure 12-9

shows comparison of net pressure and width at fracture inlet obtained from single fracture model with the corresponding values from multiple fracture model after matching injection pressure of single fracture model by increasing fracture toughness of the rock from 450 psi.inch$^{0.5}$ to 12600 psi.inch$^{0.5}$. It can be seen from the Figure 12-9 that injection pressure matching substantially reduced the difference between the results of single fracture and multiple fracture models. However, one should note that the prediction of fracture widths by single fracture model can only account for the total widths and it does not reflect the values of fracture widths observed by individual fractures in a strand which can be substantially lower than the total widths. Therefore, the standard single fracture models result in erroneous estimation of fracture widths which can impact proppant transport analysis.

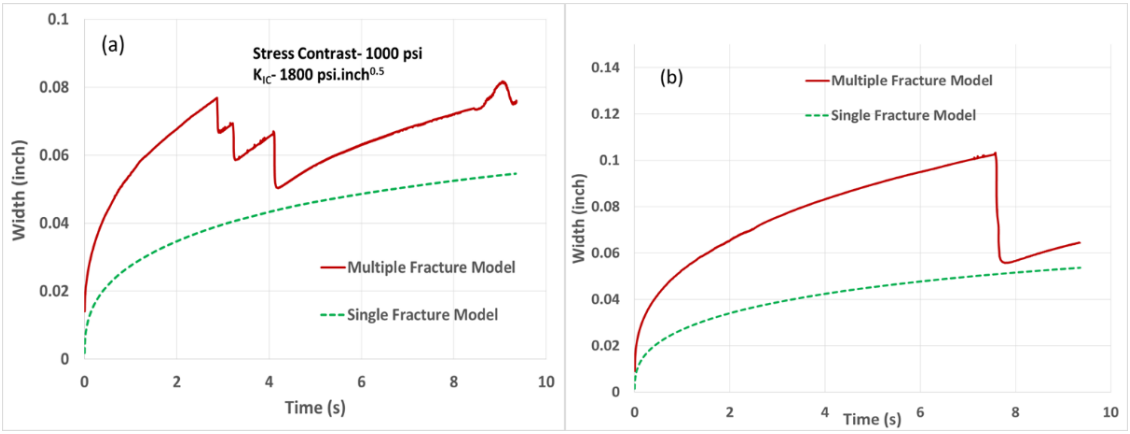

Figure 0-52. Comparison of total widths of all 10 fractures at their inlets with the result obtained using single fracture model for (a) fracture toughness K_{IC}, is 1800 psi.inch$^{0.5}$ and (b) K_{IC}, is 450 psi.inch$^{0.5}$. Stress contrast is 1000 psi. Note that the step like decrease in total width obtained from multiple fracture model corresponds to closure of inner fractures (see Figure 2c and 4c).

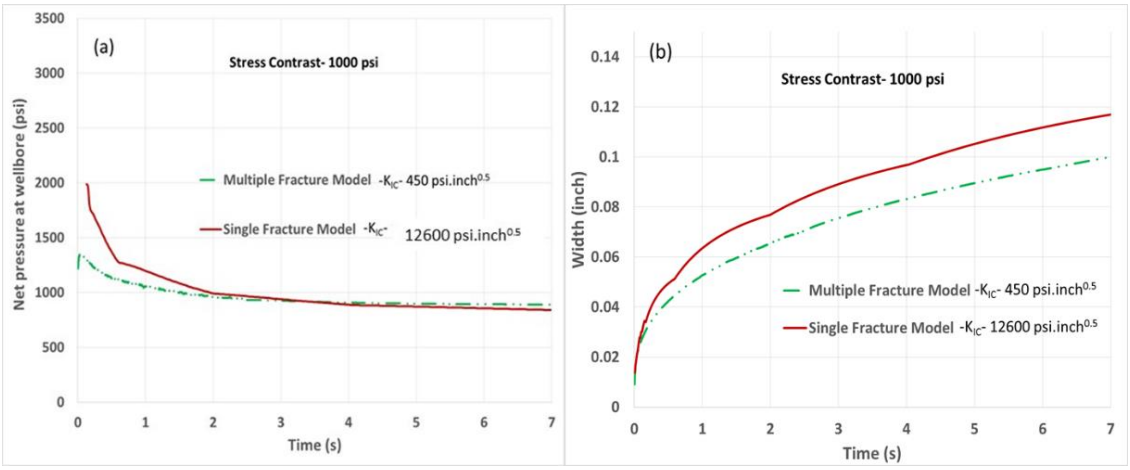

Figure 0-53. (a) Matching net pressure obtained from multiple fracture model (see Figure 5f) using single fracture model by altering fracture toughness. (b) Comparison of total widths of all 10 fractures at their inlets with the result obtained using single fracture model after net pressure matching. For multiple fracture model K_{IC}, is 450 psi.inch$^{0.5}$ and stress contrast is 1000 psi. For single fracture model K_{IC}, is 12600 psi.inch$^{0.5}$.

12.5 Summary

Numerical modeling of multiple hydraulic fracture propagation from a cluster of perforations does not indicate coalescence of fractures to form a single dominant fracture. Higher in-situ stress contrast and lower fracture toughness of rock appear to inhibit coalescence of closely spaced fractures. Propagation of multiple fractures at the spacing scales observed in recent field studies require significantly higher net pressures inside fractures to keep them open compared to a single fracture. The increase in net pressure inside the fractures is directly proportional to number of simultaneously propagating fractures. Also, it appears that an average increase in net pressure required to propagate multiple fractures can be related to net pressure for a single fracture, which might allow one to infer the number of fractures propagating simultaneously. Calibration of single fracture model using injection pressure matching can remedy error in estimation of total widths of fracture strands, however, the aperture distribution of individual strand cannot be obtained which is a critical parameter for proppant transport.

References

1. Aadnoy, B. S., 1987, Modelling of the stability of highly inclined boreholes in anisotropic rock formations: In Offshore Europe, SPE.
2. Abass, H. H., S. Hedayati, and D. L. Meadows, 1996, Nonplanar fracture propagation from a horizontal wellbore: experimental study: SPE Production & Facilities, 11, 133-137.
3. Adachi, J. I., Detournay, E., & Peirce, A. P. (2010). Analysis of the classical pseudo-3D model for hydraulic fracture with equilibrium height growth across stress barriers. International Journal of Rock Mechanics and Mining Sciences, 47(4), 625-639.
4. Adachi, J. I., and E. Detournay. 2002. Self-similar solution of a plane strain fracture driven by a power-law fluid. Int. J. Numer. Anal.Methods Geomech., 26:579–604.
5. Anderson, G.D., 1981. Effects of friction on hydraulic fracture growth near unbonded interfaces in rocks. Society of Petroleum Engineers Journal, 21(01), pp.21-29.
6. Azhdari, A. and Nemat-Nasser, S., 1996. Energy-release rate and crack kinking in anisotropic brittle solids. Journal of the Mechanics and Physics of Solids, 44(6), pp.929-952.
7. Azhdari, A., Obata, M. and Nemat-Nasser, S., 2000. Alternative solution methods for crack problems in plane anisotropic elasticity, with examples. International journal of solids and structures, 37(44), pp.6433-6478.
8. Barenblatt, G.I., 1962. The mathematical theory of equilibrium cracks in brittle fracture. In Advances in applied mechanics (Vol. 7, pp. 55-129). Elsevier.
9. Baer, G., 1991. Mechanisms of dike propagation in layered rocks and in massive, porous sedimentary rocks. Journal of Geophysical Research: Solid Earth, 96(B7), pp.11911-11929.

10. Batugin, S. A., and R. K. Nirenburg, 1972., Approximate relation between the elastic constants of anisotropic rocks and the anisotropy parameters: Journal of Mining Science, 8, 5-9.

11. Bakulin, A., M. Woodward, D. Nichols, K. Osypov, and Olga Zdraveva, 2010., Building tilted transversely isotropic depth models using localized anisotropic tomography with well information: Geophysics, 75, no. 4, D27-D36.

12. Beuth, J. L., M. A. Gregory, and C. T. Herakovich, 1986, Crack growth in unidirectional graphite-epoxy under biaxial loading: Experimental mechanics, 26, 245-253.

13. Brady, B. H. G., and J. W. Bray, 1978., The boundary element method for elastic analysis of tabular orebody extraction, assuming complete plane strain: International Journal of Rock Mechanics and Mining Sciences & Geomechanics Abstracts, 15, 29-37.

14. Blanton, T. L. (1982, January). An experimental study of interaction between hydraulically induced and pre-existing fractures. In SPE unconventional gas recovery symposium.

15. Barton, N., Bandis, S., & Bakhtar, K. (1985, June). Strength, deformation and conductivity coupling of rock joints. In International Journal of Rock Mechanics and Mining Sciences & Geomechanics Abstracts (Vol. 22, No. 3, pp. 121-140).

16. Bombolakis, E. G. (1973). Study of the brittle fracture process under uniaxial compression. Tectonophysics, 18(3-4), 231-248.

17. Barnett, D. M., & Asaro, R. J. (1972). The fracture mechanics of slit-like cracks in anisotropic elastic media. Journal of the Mechanics and Physics of Solids, 20(6), 353-366.

18. Bunger, A. P, E. Detournay, D.I. Garagash, R, and A.P. Peirce. 2007. Numerical Simulation of Hydraulic Fracturing in the Viscosity-Dominated Regime. SPE 106115, *SPE*

Hydraulic Fracturing Technology Conference, College Station, Texas, USA, 29–31 January.

19. Ciezobka, J., Courtier, J. and Wicker, J., 2018, September. Hydraulic Fracturing Test Site (HFTS)–Project Overview and Summary of Results. In Unconventional Resources Technology Conference, Houston, Texas, 23-25 July 2018 (pp. 1331-1339).
20. Crump, J.B. and Conway, M.W., 1988. Effects of perforation-entry friction on bottomhole treating analysis. Journal of petroleum technology, 40(08), pp.1-041.
21. Chandler, M. R., P. G. Meredith, N. Brantut, and B. R. Crawford, 2016, Fracture toughness anisotropy in shale: Journal of Geophysical Research: Solid Earth, 121, 1706-1729.
22. Chang, J. H., and G. J. Liao, 2014, Nonhomogenized displacement discontinuity method for calculation of stress intensity factors for cracks in anisotropic FGMs: Journal of Engineering Mechanics, 140, 04014093.
23. Cherny, S., D. Chirkov, V. Lapin, A. Muranov, D. Bannikov, M. Miller, D. Willberg, O. Medvedev, and O. Alekseenko, 2009, Two-dimensional modeling of the near-wellbore fracture tortuosity effect: International Journal of Rock Mechanics and Mining Sciences, 46, 992-1000.
24. Cooke, M. L., & Underwood, C. A. (2001). Fracture termination and step-over at bedding interfaces due to frictional slip and interface opening. Journal of Structural Geology, 23(2-3), 223-238.
25. Chuprakov, D., Melchaeva, O., & Prioul, R. (2014). Injection-sensitive mechanics of hydraulic fracture interaction with discontinuities. Rock mechanics and rock engineering, 47(5), 1625-1640.

26. Cheng, Q., & Ghassemi, A. (2017, August). Numerical Modeling of Fluid Flow, Heat Transfer and Induced Mircoseismicity in Three Dimensional Fracture Networks. In 51st US Rock Mechanics/Geomechanics Symposium.

27. Carbonell, R.S., J. Desroches, and E. Detournay. 1999. A comparison between a semi-analytical and a numerical solution of a two dimensional hydraulic fracture. Int. J. Solids Structures, 36 (31–32):4869–4888.

28. Chertov, M., 2012, Closed-form solution for vertical fracture width in anisotropic elastic formations: International Journal of Rock Mechanics and Mining Sciences, 53, 70-75.

29. Crouch, S.L., and A.M. Starfield, 1983, Boundary element methods in solid mechanics: George Allen & Unwin.

30. Cheng, C., Bunger, A.P. and Peirce, A.P., 2016, February. Optimal perforation location and limited entry design for promoting simultaneous growth of multiple hydraulic fractures. In SPE Hydraulic Fracturing Technology Conference. Society of Petroleum Engineers.

31. Daneshy, A. A. (2003). Off-balance growth: a new concept in hydraulic fracturing. Journal of petroleum technology, 55(04), 78-85.

32. Daneshy, A. A. (1974, January). Hydraulic fracture propagation in the presence of planes of weakness. In SPE European Spring Meeting.

33. Daneshy, A. A. (2016, July). Mechanics of Natural Fracture Activation by Hydraulic Fracturing". HFJ, Volume 3, No. 3.

34. Dahi-Taleghani, A., & Olson, J. E. (2011). Numerical modeling of multistranded-hydraulic-fracture propagation: Accounting for the interaction between induced and natural fractures. SPE journal, 16(03), 575-581.

35. Dai, F., and K. Xia, 2008, Dynamic tensile strength and fracture toughness of anisotropic rocks: Proceedings of the 11th international congress and exposition of the society for experimental mechanics, 2-5.

36. Desroches, J., E. Detournay, B. Lenoach, P. Papanastasiou, J.R.A. Pearson, M. Thiercelin, and A.H-D. Cheng. 1994. The crack tip region in hydraulic fracturing. Proc. Roy. Soc. London, Ser. A, 447:39–48.

37. Dewhurst, D.N., A.F. Siggins. 2006. Impact of fabric, microcracks and stress field on shale anisotropy. J. Geophys. Int. 165, 135-148.

38. Detournay, E. and Peirce, A., 2014. On the moving boundary conditions for a hydraulic fracture. International Journal of Engineering Science, 84, pp.147-155.

39. Dontsov, E. V., and A. P. Peirce, 2015, An enhanced pseudo-3D model for hydraulic fracturing accounting for viscous height growth, non-local elasticity, and lateral toughness: Engineering Fracture Mechanics, 142, 116-139.

40. Dontsov, E. V., A.P. Peirce. 2016. Implementing a universal tip asymptotic solution into an implicit level set algorithm (ILSA) for multiple parallel hydraulic fractures. Presented at 50th US Rock Mechanics/Geomechanics Symposium, Houston, Texas, USA, 26-29 June.

41. El Rabaa, W., 1989, Experimental study of hydraulic fracture geometry initiated from horizontal wells: In SPE Annual Technical Conference and Exhibition.

42. Erdogan, F., and G. C. Sih. 1963. On the crack extension in plates under plane loading and transverse shear. Journal of basic engineering 85, no. 4 : 519-525.

43. Fu, P., S.M. Johnson, Y. Hao, and C.R. Carrigan, 2011. Fully Coupled Geomechanics and Discrete Flow Network Modeling of Hydraulic Fracturing for Geothermal Applications.

Thirty-Sixth Workshop on Geothermal Reservoir Engineering, Stanford University, Stanford, California, January 31 - February 2.

44. Gao, Q., and A. Ghassemi, 2017, Pore pressure and stress distributions around a hydraulic fracture in heterogeneous rock: Rock Mechanics and Rock Engineering, 50 3157-3173.

45. Gdoutos, E.E., Zacharopoulos, D.A. and Meletis, E.I., 1989. Mixed-mode crack growth in anisotropic media. Engineering fracture mechanics, 34(2), pp.337-346.

46. Garagash, D. I., 2006. Propagation of plane-strain hydraulic fracture with a fluid lag: Early-time solution. Int. J. Solids Structures, 43:5811–5835.

47. Garagash, G.I., and E. Detournay. 2000. The tip region of a fluid-driven fracture in an elastic medium. ASME J. Appl. Mech., 67:183–192.

48. Geertsma, J., and F. De Klerk, 1969, A rapid method of predicting width and extent of hydraulically induced fractures: Journal of Petroleum Technology, 21, 1-571.

49. Goodman, R. E. 1976. Methods of geological engineering. St. Paul: West.

50. Gu, H., & Weng, X. (2010, January). Criterion for fractures crossing frictional interfaces at non-orthogonal angles. In 44th US rock mechanics symposium and 5th US-Canada rock mechanics symposium.

51. Gale, J. E. (1982, January). The effects of fracture type (induced versus natural) on the stress-fracture closure-fracture permeability relationships. In The 23rd US Symposium on Rock Mechanics (USRMS).

52. Gale, J.F., Elliott, S.J. and Laubach, S.E., 2018, September. Hydraulic Fractures in Core from Stimulated Reservoirs: Core Fracture Description of HFTS Slant Core, Midland Basin, West Texas. In Unconventional Resources Technology Conference, Houston, Texas, 23-25 July 2018 (pp. 1340-1357).

53. Ghassemi, A., 1997. Three-dimensional poroelastic hydraulic fracture simulation using the displacement discontinuity method.

54. Ghassemi, A. (2017). Three-Dimensional Modeling of Fracture Clusters in Geothermal Reservoirs (No. DE-FG36-08GO18196; OU-RM-DOE--17-F1). Univ. of Oklahoma, Norman, OK (United States).

55. Gordeliy, E., S. Abbas, and R. Prioul, 2016, Modeling of near-wellbore fracture reorientation using a fluid-coupled 2D XFEM algorithm: In 50th US Rock Mechanics/Geomechanics Symposium, American Rock Mechanics Association.

56. Gregory, M. A., and C. T. Herakovich, 1986, Predicting crack growth direction in unidirectional composites: Journal of composite materials, 20, 67-85.

57. Green, A. E., and G. I. Taylor, 1945, Stress systems in aeolotropic plates, III: Proceedings of the Royal Society of London A: Mathematical, Physical and Engineering Sciences, 184, 181-195.

58. Huang, K., Z. Zhang, and A. Ghassemi, 2013, Modeling three-dimensional hydraulic fracture propagation using virtual multidimensional internal bonds: International Journal for Numerical and Analytical Methods in Geomechanics, 37, 2021-2038.

59. Horii, H., & Nemat-Nasser, S. (1986). Brittle failure in compression: splitting faulting and brittle-ductile transition. Phil. Trans. R. Soc. Lond. A, 319(1549), 337-374.

60. Hoek, E., & Bieniawski, Z. T. (1965). Brittle fracture propagation in rock under compression. International Journal of Fracture Mechanics, 1(3), 137-155.

61. Jung, R. (2013). EGS—Goodbye or Back to the Future 95. In Effective and sustainable hydraulic fracturing. InTech.

62. Jacobs, T., 2014, The shale evolution: Zipper fracture takes hold: Journal of Petroleum Technology, 66, 60-67.

63. Jeffrey, R. G., & Bunger, A. (2009). A detailed comparison of experimental and numerical data on hydraulic fracture height growth through stress contrasts. SPE Journal, 14(03), 413-422.

64. Jeffrey, R.G., Enever, J.R., Phillips, R., Ferguson, T., Davidson, S.C. and Bride, J., 1993. Small-scale hydraulic fracturing and mineback experiments in coal seams.

65. Jeffrey, R.G., Vandamme, L. and Roegiers, J.C., 1987, January. Mechanical interactions in branched or subparallel hydraulic fractures. In Low Permeability Reservoirs Symposium. Society of Petroleum Engineers.

66. Jansen, T.A., 2014. The effect of rock properties on hydraulic fracture conductivity in the Eagle Ford and Fayetteville Shales.

67. Kresse, O., Weng, X., Gu, H., & Wu, R. (2013). Numerical modeling of hydraulic fractures interaction in complex naturally fractured formations. Rock mechanics and rock engineering, 46(3), 555-568.

68. Kamali, A., and A. Ghassemi, 2017, Reservoir stimulation in naturally fractured poroelastic rocks: In 51st US Rock Mechanics/Geomechanics Symposium, American Rock Mechanics Association.

69. Ke, C.-C., C.-S. Chen, and C.-H. Tu, 2008, Determination of fracture toughness of anisotropic rocks by boundary element method: Rock Mechanics and Rock Engineering, 41, 509-538.

70. Koshelev, V., & Ghassemi, A. (2003). Numerical modeling of stress distribution and crack trajectory near a fault or a natural fracture. In Soil and Rock America 2003; 30th US Rock Mechanics Symposium

71. Kamali, A., & Ghassemi, A. (2016, June). On the reservoir stimulation mechanisms in fractured reservoirs. In 50th US Rock Mechanics/Geomechanics Symposium

72. Kear, J., J. White, A. P. Bunger, R. Jeffrey, and M.-A. Hessami, 2013, Three dimensional forms of closely-spaced hydraulic fractures: Effective and Sustainable Hydraulic Fracturing, InTech.

73. Kimençe, B., and M. E. Ergüven, 2005, Influence functions of the displacement discontinuity method for anisotropic bodies: Computational Mechanics, 36, 484-494.

74. Kumar, D., & Ghassemi, A. (2018). Three-Dimensional Poroelastic Modeling of Multiple Hydraulic Fracture Propagation from Horizontal Wells. International Journal of Rock Mechanics and Mining Sciences, 105, 192-209.

75. Kumar, D., and Ghassemi, A. 2017. 3D geo-mechanical analysis of refracturing of horizontal wells. Unconventional Resources Technology Conference, Austin, TX, USA, pp.1-13.

76. Kumar, D., and A. Ghassemi, 2016, A three-dimensional analysis of simultaneous and sequential fracturing of horizontal wells: Journal of Petroleum Science and Engineering, 146, 1006-1025.

77. Lekhnitskii, S., 1963. Theory of elasticity of an anisotropic elastic body: Holden-Day Inc.

78. Laubie, H.H., 2013. Linear elastic fracture mechanics in anisotropic solids: Application to fluid-driven crack propagation (Doctoral dissertation, Massachusetts Institute of Technology).

79. Lecampion. B, J. Desroches, 2015. Simultaneous initiation and growth of multiple radial hydraulic fractures from a horizontal wellbore, *Journal of the Mechanics and Physics of Solids*, 82,235-258.

80. Lister, J. R., and R.C. Kerr. 1991. Fluid-mechanical models of crack propagation and their application to magma transport in dykes. J. Geophys. Res., pages 10,049–10,077.

81. Lister. J. R., Buoyancy-driven fluid fracture. 1990. The effects of material toughness and of low-viscosity precursors. J. Fluid Mech., 210:263–280.

82. McLennan, J. D., J.-C. Roegiers, and M. J. Economides, 1989, Extended reach and horizontal wells, in M. J. Economides and K. G. Nolte, eds., Reservoir Stimulation, second edn, Prentice Hall, Englewood Cliffs, chapter 19, 1-27.

83. McClure, M.W., 2012. *Modeling and characterization of hydraulic stimulation and induced seismicity in geothermal and shale gas reservoirs* (Doctoral dissertation, Stanford University).

84. Min, K. S., Zhang, Z., & Ghassemi, A. (2010, January). Numerical analysis of multiple fracture propagation in heterogeneous rock. In 44th US Rock Mechanics Symposium and 5th US-Canada Rock Mechanics Symposium.

85. Nolte, K. G., and M. J. Economides, 2000. Reservoir Stimulation. Chichester, NY: John Wiley & Sons.

86. Nolte, K.G., 1993. Discussion of examination of a cored hydraulic fracture in a deep gas well. SPE Production and Facilities (Society of Petroleum Engineers. 8(3).

87. Nordgren, R.P., 1972. Propagation of a vertical hydraulic fracture. Society of Petroleum Engineers Journal, 12(04), pp.306-314.

88. Nemat-Nasser, S., & Horii, H. (1984). Rock failure in compression. International Journal of Engineering Science, 22(8-10), 999-1011.

89. Olson, J. E., 2004, Predicting fracture swarms - the influence of subcritical crack growth and the crack-tip process zone on joint spacing in rock: Geological Society, London, Special Publications, 231, 73-88.

90. Ong, S.H., J.-C. Roegiers, 1993, Influence of anisotropies in borehole stability: International Journal of Rock Mechanics and Mining Sciences & Geomechanics Abstracts, 30, 1069-1075.

91. Peirce, A. and Detournay, E., 2009. An Eulerian moving front algorithm with weak-form tip asymptotics for modeling hydraulically driven fractures. Communications in Numerical Methods in Engineering, 25(2), pp.185-200.

92. Palmer, I.D. and Veatch Jr, R.W., 1990. Abnormally high fracturing pressures in step-rate tests. SPE Production Engineering, 5(03), pp.315-323.

93. Pollard, D.D., Segall, P. and Delaney, P.T., 1982. Formation and interpretation of dilatant echelon cracks. Geological Society of America Bulletin, 93(12), pp.1291-1303.

94. Palmer, I.D. and Carroll Jr, H.B., 1983. Three-dimensional hydraulic fracture propagation in the presence of stress variations. Society of Petroleum Engineers Journal, 23(06), pp.870-87.

95. Rice, J.R., 1968. Mathematical analysis in the mechanics of fracture. Fracture: an advanced treatise, 2, pp.191-311.

96. Renshaw, C. E., & Pollard, D. D. (1995, April). An experimentally verified criterion for propagation across unbounded frictional interfaces in brittle, linear elastic materials. In

International journal of rock mechanics and mining sciences & geomechanics abstracts (Vol. 32, No. 3, pp. 237-249).

97. Riahi, A., & Damjanac, B. (2013). Numerical study of interaction between hydraulic fracture and discrete fracture network. In Effective and Sustainable Hydraulic Fracturing. InTech.

98. Raterman, K.T., Farrell, H.E., Mora, O.S., Janssen, A.L., Gomez, G.A., Busetti, S., McEwen, J., Davidson, M., Friehauf, K., Rutherford, J. and Reid, R., 2017, September. Sampling a stimulated rock volume: an eagle ford example. In Unconventional Resources Technology Conference, Austin, Texas, 24-26 July 2017 (pp. 937-954).

99. Rizzo, F. J., and D. J. Shippy, 1970, A method for stress determination in plane anisotropic elastic bodies: Journal of Composite Materials, 4, 36-61.

100. Sesetty, V., and A. Ghassemi, 2015, A numerical study of sequential and simultaneous hydraulic fracturing in single and multi-lateral horizontal wells: Journal of Petroleum Science and Engineering, 132, 65-76.

101. Sesetty, V., and A. Ghassemi, 2016, Numerical modeling of hydraulic fracture propagation from horizontal wells in anisotropic shale: 50th US Rock Mechanics/Geomechanics Symposium, American Rock Mechanics Association.

102. Sesetty, V., and A. Ghassemi, 2017a, Simulation of hydraulic fracture clusters considering viscosity and toughness dominated propagation: 51st US Rock Mechanics/Geomechanics Symposium, American Rock Mechanics Association.

103. Sesetty, V., and A. Ghassemi, 2017b, Complex fracture network model for stimulation of unconventional reservoirs: 51st US Rock Mechanics/Geomechanics Symposium, American Rock Mechanics Association.

104. Suarez-Rivera, R., C. Deenadayalu, M. Chertov, R. N. Hartanto, P. Gathogo, and R. Kunjir, 2011, Improving horizontal completions on heterogeneous tight-shales: In Canadian Unconventional Resources Conference, SPE.

105. Sierra, R., Tran, M. H., Abousleiman, Y. N., & Slatt, R. M. (2010, January). Woodford shale mechanical properties and the impacts of lithofacies. In 44th US rock mechanics symposium and 5th US-Canada rock mechanics symposium. American Rock Mechanics Association.

106. Simonson, E.R., Abou-Sayed, A.S. and Clifton, R.J., 1978. Containment of massive hydraulic fractures. Society of Petroleum Engineers Journal, 18(01), pp.27-32.

107. Safari, R., & Ghassemi, A. (2016). Three-dimensional poroelastic modeling of injection induced permeability enhancement and microseismicity. International Journal of Rock Mechanics and Mining Sciences, 84, 47-58.

108. Sih, G. C., P. C. Paris, and G. R. Irwin, 1965, On cracks in rectilinearly anisotropic bodies: International Journal of Fracture, 1, 189-203.

109. Sih, G. C., E. P. Chen, S. L. Huang, and E. J. McQuillen, 1975, Material characterization on the fracture of filament-reinforced composites: Journal of composite materials, 9, 167-186.

110. Sih, George C. "Strain-energy-density factor applied to mixed mode crack problems." *International Journal of fracture* 10, no. 3 (1974): 305-321.

111. Saouma, V.E., Ayari, M.L. and Leavell, D.A., 1987. Mixed mode crack propagation in homogeneous anisotropic solids. Engineering Fracture Mechanics, 27(2), pp.171-184.

112. Spence, D. A., and P. W. Sharp. 1985. Self-similar solution for elastohydrodynamic cavity flow. Proc. Roy. Soc. London, 400:289-313

113. Spence, D.A., and D.L. Turcotte. 1985. Magma-driven propagation crack. J. Geophys. Res., 90:575–580.

114. Stone, T. J., & Babuška, I. (1998). A numerical method with a posteriori error estimation for determining the path taken by a propagating crack. Computer Methods in applied mechanics and engineering, 160(3-4), 245-271.

115. Stadulis, J.M., 1995, January. Development of a completion design to control screenouts caused by multiple near-wellbore fractures. In Low Permeability Reservoirs Symposium. Society of Petroleum Engineers.

116. Teufel, L. W., and J. A. Clark, 1984, Hydraulic fracture propagation in layered rock: Experimental studies of fracture containment: SPE Journal, 24.

117. Tsai, S. W., and E. M. Wu, 1971, A general theory of strength for anisotropic materials: Journal of composite materials, 5, 58-80.

118. Tarasovs, S., and Ghassemi, A. (2014). Self-similarity and scaling of thermal shock fractures. Physical Review E 90 (1), 012403-1-6.

119. Vahid, S., and A. Ghassemi, 2011, Hydraulic fracture initiation from a wellbore in transversely isotropic rock: In 45th US Rock Mechanics/Geomechanics Symposium. American Rock Mechanics Association.

120. Vachaparampil, A., L. Hu, X. Zhou, A. Ghassemi, I. Gill, and Y. Chitrala. 2016. Geomechanical Anisotropy of Utica Shale from Static and Dynamic Measurements.

121. Van Ketterij, R. B., and C. J. De Pater, 1999, Impact of perforations on hydraulic fracture tortuosity: SPE production & facilities, 14, 117-130.

122. Vandamme, L. and Curran, J.H., 1989. A three-dimensional hydraulic fracturing simulator. International Journal for Numerical Methods in Engineering, 28(4), pp.909-927.

123. Waters, G. A., B. K. Dean, R. C. Downie, K. J. Kerrihard, L. Austbo, and B. McPherson, 2009, Simultaneous hydraulic fracturing of adjacent horizontal wells in the Woodford Shale: SPE hydraulic fracturing technology conference.

124. Warpinski, N. R., R. A. Schmidt, and D. A. Northrop, 1982, In-situ stresses: the predominant influence on hydraulic fracture containment: Journal of Petroleum Technology, 34, 653-664.

125. Warpinski, N.R. and Teufel, L.W., 1987. Influence of geologic discontinuities on hydraulic fracture propagation (includes associated papers 17011 and 17074). Journal of Petroleum Technology, 39(02), pp.209-220.

126. Warpinski, N.R., Lorenz, J.C., Branagan, P.T., Myal, F.R. and Gall, B.L., 1993. Examination of a Cored Hydraulic Fracture in a Deep Gas Well (includes associated papers 26302 and 26946). SPE Production & Facilities, 8(03), pp.150-158.

127. Weng, X., 1993, Fracture initiation and propagation from deviated wellbores: SPE annual technical conference and exhibition.

128. Wang, X., & Ghassemi, A. (2011). A three-dimensional stochastic fracture network model for geothermal reservoir stimulation. In Thirty-Sixth Workshop on Geothermal Reservoir Engineering (in press), Stanford University, Stanford, California.

129. Weijers, L., Wright, C.A., Sugiyama, H., Sato, K. and Zhigang, L., 2000, January. Simultaneous propagation of multiple hydraulic fractures-evidence, impact and modeling

implications. In International Oil and Gas Conference and Exhibition in China. Society of Petroleum Engineers.

130. Willis-Richards, J., Watanabe, K., & Takahashi, H. (1996). Progress toward a stochastic rock mechanics model of engineered geothermal systems. Journal of Geophysical Research: Solid Earth, 101(B8), 17481-17496.

131. Weng, X., Sesetty, V., & Kresse, O. (2015, November). Investigation of shear-induced permeability in unconventional reservoirs. In 49th US Rock Mechanics/Geomechanics Symposium.

132. Weng, X., Kresse, O., Cohen, C. E., Wu, R., & Gu, H. (2011, January). Modeling of hydraulic fracture network propagation in a naturally fractured formation. In SPE Hydraulic Fracturing Technology Conference. Society of Petroleum Engineers.

133. Waters, G. A., Dean, B. K., Downie, R. C., Kerrihard, K. J., Austbo, L., & McPherson, B. (2009, January). Simultaneous hydraulic fracturing of adjacent horizontal wells in the Woodford Shale. In SPE hydraulic fracturing technology conference. Society of Petroleum Engineers.

134. Wu, E. M., 1963, Application of fracture mechanics to orthotropic plates: No. TAAM-R-248. Illinois Univ at Urbana-Champaign.

135. Wu, R., Germanovich, L.N. and Hurt, R.S., 2009, January. Experimental and theoretical study of mixed-mode I+ III crack propagation and segmentation. In 43rd US Rock Mechanics Symposium & 4th US-Canada Rock Mechanics Symposium. American Rock Mechanics Association.

136. Wu, K., 2014. *Numerical modeling of complex hydraulic fracture development in unconventional reservoirs* (Doctoral dissertation).

137. Yan, X., 2004, A special crack tip displacement discontinuity element: Mechanics Research Communications, 31, 651-659.

138. Ye, Z., Sesetty, V., & Ghassemi, A. (2018, January). Experimental and Numerical Investigation of Shear Stimulation and Permeability Evolution in Shales. In SPE Hydraulic Fracturing Technology Conference and Exhibition.

139. Zhang, X., R. G. Jeffrey, A. P. Bunger, and M. Thiercelin, 2011, Initiation and growth of a hydraulic fracture from a circular wellbore: International Journal of Rock Mechanics and Mining Sciences, 48, 984-995.

140. Zhang, X., Jeffrey, R. G., & Thiercelin, M. (2009). Mechanics of fluid-driven fracture growth in naturally fractured reservoirs with simple network geometries. Journal of Geophysical Research: Solid Earth, 114(B12).

141. Zhiming, Y., and M. L. Ayari, 1994, Prediction of crack propagation in anisotropic solids: Engineering fracture mechanics, 49, 797-808.

142. Zheltov, Yu. P., and Khristianovitch, S. A., 1995. On the mechanism of hydraulic fracture of an oil-bearing stratum, Izvestiya AN SSSR, OTN, No. 5, 3-41.

143. Zhang, X., & Jeffrey, R. G. (2006). The role of friction and secondary flaws on deflection and re-initiation of hydraulic fractures at orthogonal pre-existing fractures. Geophysical Journal International, 166(3), 1454-1465.

144. Zhou, J., Huang, H., McLennan, J., Meakin, P., & Deo, M. (2017). A dual-lattice discrete element model to understand hydraulic fracturing in a naturally fractured system. HFJ, Volume 4, No. 2.

Appendix A

The material constants c_{ij} for plane strain condition (see Eq. 2.18) are given as

$$
\begin{aligned}
c_{11} &= s_{26}^2 s_{33} - 2s_{23}s_{26}s_{36} + s_{23}^2 s_{66} + s_{22}(s_{36}^2 - s_{33}s_{66})/K_0 \\
c_{12} &= -s_{16}s_{26}s_{33} + s_{16}s_{23}s_{36} + s_{13}s_{26}s_{36} - s_{12}s_{36}^2 - s_{13}s_{23}s_{66} + s_{12}s_{33}s_{66}/K_0 \\
c_{16} &= -s_{13}s_{23}s_{26} + s_{12}s_{26}s_{33} + s_{16}(s_{23}^2 - s_{22}s_{33}) + s_{13}s_{22}s_{36} - s_{12}s_{23}s_{36}/-K_o \\
c_{21} &= c_{12} \\
c_{22} &= s_{16}^2 s_{33} - 2s_{13}s_{16}s_{36} + s_{13}^2 s_{66} + s_{11}(s_{36}^2 - s_{33}s_{66})/K_0 \\
c_{26} &= s_{13}^2 s_{26} + s_{12}s_{16}s_{33} - s_{11}s_{26}s_{33} + s_{11}s_{23}s_{36} - s_{13}(s_{16}s_{23} + s_{12}s_{36})/-K_0 \\
c_{16} &= -s_{13}s_{23}s_{26} + s_{12}s_{26}s_{33} + s_{16}(s_{23}^2 - s_{22}s_{33}) + s_{13}s_{22}s_{36} - s_{12}s_{23}s_{36}/-K_0 \\
c_{66} &= s_{13}^2 s_{22} - 2s_{12}s_{13}s_{33} + s_{12}^2 s_{33} + s_{11}(s_{23}^2 - s_{22}s_{33})/K_0
\end{aligned}
\tag{A.1}
$$

$$
K_0 = \begin{bmatrix}
s_{11}s_{26}^2 s_{33} + s_{16}^2(-s_{23}^2 + s_{22}s_{33}) - 2s_{11}s_{23}s_{26}s_{36} - s_{12}^2 s_{36}^2 + s_{11}s_{22}s_{36}^2 + \\
2s_{16}(s_{13}s_{23}s_{26} - s_{12}s_{26}s_{33} - s_{13}s_{22}s_{36} + s_{12}s_{23}s_{36}) + s_{11}s_{23}^2 s_{66} + s_{12}^2 s_{33}s_{66} \\
-s_{11}s_{22}s_{33}s_{66} + s_{13}^2(-s_{26}^2 + s_{22}s_{66}) + 2s_{12}s_{13}(s_{26}s_{36} - s_{23}s_{66})
\end{bmatrix}
$$

For the case of plane stress, the material constants c_{ij} are

$$
\begin{aligned}
c_{11} &= \frac{s_{26}^2 - s_{22}s_{66}}{s_{16}^2 s_{22} - 2s_{12}s_{16}s_{26} + s_{11}s_{26}^2 + s_{12}^2 s_{66} - s_{11}s_{22}s_{66}} \\
c_{12} &= \frac{-s_{16}s_{26} + s_{12}s_{66}}{s_{16}^2 s_{22} - 2s_{12}s_{16}s_{26} + s_{12}^2 s_{66} + s_{11}(s_{26}^2 - s_{22}s_{66})} \\
c_{16} &= \frac{s_{16}s_{22} - s_{12}s_{26}}{s_{16}^2 s_{22} - 2s_{12}s_{16}s_{26} + s_{11}s_{26}^2 + s_{12}^2 s_{66} - s_{11}s_{22}s_{66}} \\
c_{21} &= c_{12} \\
c_{22} &= \frac{s_{16}^2 - s_{11}s_{66}}{s_{16}^2 s_{22} - 2s_{12}s_{16}s_{26} + s_{11}s_{26}^2 + s_{12}^2 s_{66} - s_{11}s_{22}s_{66}} \\
c_{26} &= \frac{-s_{12}s_{16} + s_{11}s_{26}}{s_{16}^2 s_{22} - 2s_{12}s_{16}s_{26} + s_{12}^2 s_{66} + s_{11}(s_{26}^2 - s_{22}s_{66})} \\
c_{16} &= c_{16} \\
c_{26} &= c_{26}
\end{aligned}
\tag{A.2}
$$

$$c_{11} = \frac{s_{12}^2 - s_{11}s_{22}}{s_{16}^2 s_{22} - 2s_{12}s_{16}s_{26} + s_{11}s_{26}^2 + s_{12}^2 s_{66} - s_{11}s_{22}s_{66}}$$

Appendix B

The fundamental solution for stresses and displacements in an orthotropic material for the problem of concentrated line force can be expressed as

$$
\begin{aligned}
u_x &= P_x v_{11} + P_y v_{12} \\
u_y &= P_x v_{21} + P_y v_{22} \\
\sigma_{xx} &= P_x w_{11} + P_y w_{12} \\
\sigma_{yy} &= P_x w_{21} + P_y w_{22} \\
\sigma_{xy} &= P_x w_{31} + P_y w_{32}
\end{aligned}
\tag{B.1}
$$

where *x*, *y* and *z* are the three axes of elastic symmetry of the orthotropic material. P_x and P_y are concentrated line force components in directions *x* and *y* respectively.

The influence functions v_{ij} and w_{ij} in the coordinate system *xyz* are defined as below (Rizzo and Shippy, 1970)

$$v_{11} = k(\gamma_1 A_2^2 \ln r_1 - \gamma_2 A_1^2 \ln r_2)$$

$$v_{12} = v_{21} = -kA_1 A_2 (\theta_1 - \theta_2)$$

$$v_{22} = -k\left(\frac{1}{\gamma_1} A_1^2 \ln r_1 - \frac{1}{\gamma_2} A_2^2 \ln r_2\right)$$

$$w_{11} = kx\left(\frac{A_1}{\gamma_2 r_2^2} - \frac{A_2}{\gamma_1 r_1^2}\right) \tag{B.2}$$

$$w_{12} = ky\left(\frac{A_2}{\gamma_2^3 r_2^2} - \frac{A_1}{\gamma_1^3 r_1^2}\right)$$

$$w_{21} = kx\left(\frac{\gamma_1 A_2}{r_1^2} - \frac{\gamma_2 A_1}{r_2^2}\right)$$

$$w_{22} = ky\left(\frac{A_1}{\gamma_1 r_1^2} - \frac{A_2}{\gamma_2 r_2^2}\right)$$

$$w_{31} = ky\left(\frac{A_1}{\gamma_2 r_2^2} - \frac{A_2}{\gamma_1 r_1^2}\right)$$

$$w_{32} = kx\left(\frac{A_1}{\gamma_1 r_1^2} - \frac{A_2}{\gamma_2 r_2^2}\right)$$

where

$$A_i = s_{12} - \gamma_i^2 s_{22}$$
$$r_i = \sqrt{x^2 + y_i^2}$$
$$y_i = \frac{y}{\gamma_i}$$
$$k = \frac{1}{2\pi(\gamma_1^2 - \gamma_2^2)s_{22}}$$
$$\theta_i = \arctan\left(\frac{y_i}{x}\right)$$

γ_1^2 and γ_2^2 are the two roots of the below quadratic equation in γ^2

$$c_{11}c_{66}\gamma^4 + [c_{12}(c_{12} + 2c_{66}) - c_{11}c_{22}]\gamma^2 + c_{22}c_{66} = 0$$

Appendix C

The stress field near the fracture tip in an orthotropic body in the coordinate system x-y-z (see Figure 6.1) is given as,

$$\sigma_x = \frac{K_I}{\sqrt{2\pi r}} \mathrm{Re}\left[\frac{\mu_1\mu_2}{\mu_1-\mu_2}\left(\frac{\mu_2}{\sqrt{\cos\omega+\mu_2\sin\omega}} - \frac{\mu_1}{\sqrt{\cos\omega+\mu_1\sin\omega}} \right)\right] + \frac{K_{II}}{\sqrt{2\pi r}} \mathrm{Re}\left[\frac{1}{\mu_1-\mu_2}\left(\frac{\mu_2^{\,2}}{\sqrt{\cos\omega+\mu_2\sin\omega}} - \frac{\mu_1^{\,2}}{\sqrt{\cos\theta+\mu_1\sin\omega}} \right)\right] \quad \text{(C.1)}$$

$$\sigma_y = \frac{K_I}{\sqrt{2\pi r}} \mathrm{Re}\left[\frac{1}{\mu_1-\mu_2}\left(\frac{\mu_1}{\sqrt{\cos\omega+\mu_2\sin\omega}} - \frac{\mu_2}{\sqrt{\cos\omega+\mu_1\sin\omega}} \right)\right] + \frac{K_{II}}{\sqrt{2\pi r}} \mathrm{Re}\left[\frac{1}{\mu_1-\mu_2}\left(\frac{1}{\sqrt{\cos\omega+\mu_2\sin\omega}} - \frac{1}{\sqrt{\cos\omega+\mu_1\sin\omega}} \right)\right] \quad \text{(C.2)}$$

$$\sigma_{xy} = \frac{K_I}{\sqrt{2\pi r}} \mathrm{Re}\left[\frac{\mu_1\mu_2}{\mu_1-\mu_2}\left(\frac{1}{\sqrt{\cos\omega+\mu_1\sin\omega}} - \frac{1}{\sqrt{\cos\omega+\mu_2\sin\omega}} \right)\right] + \frac{K_{II}}{\sqrt{2\pi r}} \mathrm{Re}\left[\frac{1}{\mu_1-\mu_2}\left(\frac{\mu_1}{\sqrt{\cos\omega+\mu_1\sin\omega}} - \frac{\mu_2}{\sqrt{\cos\omega+\mu_2\sin\omega}} \right)\right] \quad \text{(C.3)}$$

where K_I and K_{II} are mode-1 and mode-2 stress intensity factors, μ_1 and μ_2 are complex roots of the characteristic equation (Eq C.6) with positive imaginary parts. The above equations can be transformed to polar coordinates r and ω using Eq. A.4

$$\sigma_{\omega\omega} = \frac{\sigma_x+\sigma_y}{2} - \frac{\sigma_x-\sigma_y}{2}\cos 2\omega - \sigma_{xy}\sin 2\omega$$
$$\sigma_{r\omega} = -\frac{\sigma_x-\sigma_y}{2}\sin 2\omega + \sigma_{xy}\cos 2\omega \quad \text{(C.4)}$$

The near tip normal and shear displacement field is given as

$$u_s(r,\omega) = K_I\sqrt{\frac{2r}{\pi}}\,\mathrm{Re}\left[\frac{(\mu_1 p_2\lambda_2 - \mu_2 p_1\lambda_1)}{\mu_1-\mu_2}\right] + K_2\sqrt{\frac{2r}{\pi}}\,\mathrm{Re}\left[\frac{(p_2\lambda_2 - p_1\lambda_1)}{\mu_1-\mu_2}\right]$$
$$u_n(r,\omega) = K_I\sqrt{\frac{2r}{\pi}}\,\mathrm{Re}\left[\frac{(\mu_1 q_2\lambda_2 - \mu_2 q_1\lambda_1)}{\mu_1-\mu_2}\right] + K_2\sqrt{\frac{2r}{\pi}}\,\mathrm{Re}\left[\frac{(q_2\lambda_2 - q_1\lambda_1)}{\mu_1-\mu_2}\right] \quad \text{(C.5)}$$

where

$$p_i = b_{11}\mu_i^2 + b_{12} - b_{16}\mu_i$$
$$q_i = b_{12}\mu_i + \frac{b_{22}}{\mu_i} - b_{26} \quad \text{(C.6)}$$
$$\lambda_i = \sqrt{\cos\omega + \mu_i \sin\omega}$$
$$i = (1,2)$$

The following material constants are given in the coordinate system 1-2-3 (see Figure 6.1).

$$a_{11} = \frac{1}{E_1}, a_{22} = \frac{1}{E_2}, a_{33} = \frac{1}{E_3}, a_{12} = \frac{-\nu_{21}}{E_2} = \frac{-\nu_{12}}{E_1}, a_{13} = \frac{-\nu_{31}}{E_3} = \frac{-\nu_{13}}{E_1}, a_{23} = \frac{-\nu_{32}}{E_3} = \frac{-\nu_{23}}{E_2}, a_{66} = \frac{1}{G_{13}}$$

Using the above definitions and plane strain condition we define b_{ij}

$$b_{ij} = a_{ij} - \frac{a_{i3}a_{j3}}{a_{33}}$$

The above constants are used to solve the following characteristic equation

$$b_{11}\mu^4 - 2b_{16}\mu^3 + (2b_{12} + b_{66})\mu^2 - 2b_{26}\mu + b_{22} = 0 \quad \text{(C.7)}$$